

CARBON SEQUESTRATION IN CHRYSOTILE MINE TAILINGS

by

SIOBHAN ALEXANDRA WILSON

B.Sc., McMaster University, 2003

A THESIS SUBMITTED IN PARTIAL FULFILMENT OF  
THE REQUIREMENTS FOR THE DEGREE OF

MASTER OF SCIENCE

in

THE FACULTY OF GRADUATE STUDIES

Geological Sciences

THE UNIVERSITY OF BRITISH COLUMBIA

November 2005

© Siobhan Alexandra Wilson, 2005

**ABSTRACT**

Active sequestration of atmospheric carbon dioxide (CO<sub>2</sub>) is occurring in chrysotile mine tailings at Clinton Creek, Yukon and Cassiar, British Columbia. Hydrated magnesium carbonate minerals develop in mine tailings as a natural consequence of the weathering process within the residues. Magnesium, leached from silicate minerals, reacts with dissolved CO<sub>2</sub> and bicarbonate in rainwater, precipitating carbonates at the surface of tailings upon evaporation of pore fluids and in near-surface environments with possible mediation by photosynthetic microbes. Increased reaction rates are observed in the tailings environment due to fine grain size resulting from mineral processing. Mine tailings may therefore represent the optimal environment in which to pursue mineral sequestration.

Stable carbon and oxygen isotopes and radiogenic carbon are used to confirm an atmospheric source for CO<sub>2</sub> in recently-precipitated carbonate efflorescences in mine tailings. X-ray powder-diffraction studies demonstrate that CO<sub>2</sub> is crystallographically bound within the hydrated magnesium carbonate minerals nesquehonite [MgCO<sub>3</sub>·3H<sub>2</sub>O], dypingite [Mg<sub>5</sub>(CO<sub>3</sub>)<sub>4</sub>(OH)<sub>2</sub>·5H<sub>2</sub>O], hydromagnesite [Mg<sub>5</sub>(CO<sub>3</sub>)<sub>4</sub>(OH)<sub>2</sub>·4H<sub>2</sub>O], and lansfordite [MgCO<sub>3</sub>·5H<sub>2</sub>O]. Quantitative phase analysis with the Rietveld method for X-ray powder-diffraction is used to determine the modal abundance of hydrated magnesium carbonates in mine tailings. Isotopic-fingerprinting and the Rietveld method are an effective verification protocol for carbon sequestration in mine tailings.

**TABLE OF CONTENTS**

Abstract.....	ii
Table of Contents.....	iii
List of Tables.....	v
List of Figures.....	vi
List of Abbreviations.....	ix
List of Symbols.....	x
Preface.....	xii
Acknowledgements.....	xiv
CHAPTER I: Introduction.....	1
1.1 Introduction and Motivation for Study.....	1
1.2 References.....	5
CHAPTER II: Mineralogical characterization of magnesium-carbonate precipitates in chrysotile mine tailings.....	6
2.1 Introduction.....	6
2.2 Characterization of Tailings Material.....	7
2.2.1 Field Localities.....	7
2.2.2 Sampling Methodology.....	11
2.3 Experimental Techniques for Characterization of Tailings.....	13
2.3.1 Qualitative X-ray Powder Diffraction.....	13
2.3.2 Scanning Electron Microscopy.....	14
2.3.3 Grain Size Analysis.....	15
2.3.4 Bulk Geochemistry.....	16
2.4 Results of Bulk Tailings Characterization.....	16
2.4.1 Bulk Mineralogy.....	16
2.4.2 Asbestos Mineral Content.....	18
2.4.3 Carbonate Precipitate in Bulk Tailings Samples.....	19
2.4.4 Grain Size Analysis.....	21
2.5 Hydrated Magnesium Carbonate Mineralogy.....	23
2.6 Modes of Occurrence and Mechanisms of Formation.....	30

---

## TABLE OF CONTENTS

---

2.7 Interpretation of Experimental Results.....	38
2.8 References.....	44
 CHAPTER III: Isotopic Characterization of Magnesium-Carbonate Precipitates.....	49
3.1 Introduction.....	49
3.2 Experimental Method.....	49
3.2.1 Light Stable Isotopes.....	49
3.2.2 Radiogenic Carbon Fingerprinting.....	50
3.2.3 Surface Area Analysis.....	51
3.3 Results of Isotopic Investigation.....	51
3.3.1 Stable Carbon and Oxygen Isotopes.....	51
3.3.2 Radiogenic Carbon.....	54
3.4 Determination of the Source of Carbon.....	56
3.5 The Source for Cations.....	63
3.6 References.....	67
 CHAPTER IV: Verifying and quantifying carbon fixation in minerals from serpentine-rich mine tailings using the Rietveld method with X-ray powder diffraction data.....	70
4.1 Introduction.....	70
4.1.1 Sample Localities.....	75
4.2 Experimental Methods.....	77
4.2.1 Sample Preparation and Data Collection.....	77
4.2.2 Motivation for Using the Rietveld Method.....	82
4.2.3 Rietveld Refinement and Quantitative Phase Analysis.....	86
4.3 Results and Discussion.....	91
4.3.1 Synthetic Mine Tailings.....	91
4.3.2 Natural Mine Tailings.....	100
4.4 References.....	111
 CHAPTER V: Conclusions.....	119
 Appendix A: Whole Rock Geochemistry for Clinton Creek and Cassiar.....	122
 Appendix B: X-ray Powder Diffraction Data for Qualitative Analysis.....	125
 Appendix C: Sieving Data.....	197



**LIST OF TABLES**

TABLE 2.1:	Empirical formulae for hydrated magnesium carbonate minerals.....	29
TABLE 2.2:	Mineralogy and mode of carbonate occurrence.....	31
TABLE 3.1:	Mineralogical and isotopic data for carbonate samples.....	52
TABLE 3.2:	Estimates for surface area of mineral phases in bulk tailings samples.....	66
TABLE 4.1:	Compositions of synthetic serpentinite mine tailings renormalized to exclude fluorite spike.....	79
TABLE 4.2:	Sources of crystal structure data for Rietveld refinement.....	87
TABLE 4.3:	Results of quantitative phase analysis of synthetic serpentinite mine tailings.....	92
TABLE 4.4:	Results of quantitative phase analysis of natural serpentinite mine tailings renormalized to exclude 10% fluorite spike.....	101
TABLE 4.5:	Estimated amounts of atmospheric CO <sub>2</sub> crystallographically bound in serpentinite mine tailings.....	109

---

**LIST OF FIGURES**

FIGURE 1.1: Location of Clinton Creek, YT, and Cassiar, BC.....	3
FIGURE 2.1: Location of Clinton Creek, YT, and Cassiar, BC.....	8
FIGURE 2.2: Collapse of the northern lobe of the Wolverine tailings pile at Clinton Creek.....	9
FIGURE 2.3: Modes of carbonate occurrence at Clinton Creek and Cassiar.....	12
FIGURE 2.4: Back-scattered electron image of actinolite grains in sample 04CA0401.....	20
FIGURE 2.5: Results of grain size analysis for two typical samples of tailings.....	22
FIGURE 2.6: Mass fractions of fibrous and non-fibrous tailings materials for each size fraction used in wet-sieving for sample 04CC1401.....	24
FIGURE 2.7: Percent of tailings to pass through each sieve for sample 04CC1401.....	25
FIGURE 2.8: H <sub>2</sub> O-MgO-CO <sub>2</sub> compositional ternary for the hydrated magnesium carbonate minerals.....	28
FIGURE 2.9: Variation in habit and intensity of backscattered electrons between nesquehonite and dypingite/hydromagnesite phases in vertical crust sample 04CC0201B.....	33
FIGURE 2.10: Distinguishing between hydromagnesite/dypingite and nesquehonite in thin section with EDS.....	34
FIGURE 2.11: Secondary electron (SE) and Back-scattered electron (BSE) images of spire samples 04CC0702 and 04CC0902 and vertical crusts 04CC0201B and 04CC0703.....	35
FIGURE 2.12: Secondary electron (SE) and Back-scattered electron (BSE) images of spire samples 04CC0702 and 04CC0902 and vertical crust 04CC0106.....	36

## LIST OF FIGURES

---

FIGURE 2.13: Zonation of hydrated magnesium carbonate minerals in crusts and spires.....	39
FIGURE 2.14: Best-case scenario model for hydrated magnesium carbonate formation in mine tailings.....	41
FIGURE 2.15: Mechanisms of formation for the four modes of occurrence.....	43
FIGURE 3.1: Stable oxygen and carbon isotope data by mode of carbonate occurrence and mineralogy.....	53
FIGURE 3.2: Worst-case scenario for carbonate stability in mine tailings.....	60
FIGURE 3.3: Best-case scenario model for hydrated magnesium carbonate formation in mine tailings.....	61
FIGURE 3.4: Variation of $\delta^{13}\text{C}$ with $\text{F}^{14}\text{C}$ for seven samples from Cassiar and Clinton Creek.....	62
FIGURE 4.1: Locations of Clinton Creek, Yukon, Cassiar, British Columbia, and Atlin, British Columbia.....	72
FIGURE 4.2: Modes in which hydrated magnesium carbonate minerals have been identified at Clinton Creek, Yukon and Cassiar, British Columbia.....	76
FIGURE 4.3: Abundance of serpentine from Rietveld refinement versus nominal abundance for three different concentrations of the fluorite spike (9, 10, and 11% $\text{CaF}_2$ ).....	90
FIGURE 4.4: Rietveld refinement plot, ACMIX70.....	94
FIGURE 4.5: Modal abundances from Rietveld refinement versus nominal abundances in synthetic serpentinites.....	95
FIGURE 4.6: Absolute (wt.%) error in estimates for all minerals versus the abundance of that mineral in a sample.....	96
FIGURE 4.7: Relative and absolute (wt.%) error in Rietveld estimates of hydromagnesite abundance for all synthetic samples.....	97
FIGURE 4.8: Refinement results used to determine the percent magnesite contamination in the “pure” hydromagnesite sample.....	99

---

FIGURE 4.9: Rietveld refinement plot of a chrysotile mine residue from Clinton Creek, YT (04CC0703).....	103
FIGURE 4.10: Detailed mineralogy for modal occurrences of hydrated magnesium carbonate crusts in serpentine-rich mine tailings.....	105
FIGURE 4.11: Evolution of magnesium-carbonate mineral phases and bound carbon per mole cation ( $\text{Mg}^{2+}$ ) during dehydration in a mine-tailings carbon-disposal site.....	108

**LIST OF ABBREVIATIONS**

AMS	Accelerator Mass Spectrometry
BP	Before Present
BSE	Back-Scattered Electron
EDS	Energy-Dispersive Spectrometry or Energy-Dispersive Spectrum
PCIGR	Pacific Centre for Isotopic and Geochemical Research
SE	Secondary Electron
SEM	Scanning Electron Microscope or Scanning Electron Microscopy
VPDB	Vienna Pee Dee Belemnite
VSMOV	Vienna Standard Mean Ocean Water
XRD	X-ray Diffractometer or X-ray Diffractometry
XRPD	X-ray Powder Diffractometer or X-ray Powder Diffractometry
yBP	Years Before Present

**LIST OF SYMBOLS****Non-Greek**

$^{14}\text{C}$	Carbon-14
$A$	Amount of amorphous phase
$\text{Ca}$	Calcium
$\text{CO}_2$	Carbon dioxide
$ F $	Refined structure factor
$ F_{\text{calculated}} $	Calculated structure factor
$F^{14}\text{C}$	Fraction Modern Carbon
$i$	Index for intensity measurements
$I$	Intensity of scattered X-rays
$M$	Mass of formula unit
$\text{Mg}$	Magnesium
$r$	index for mineral phases
$R_s$	Amount of spike, $s$ , determined by Rietveld refinement
$s$	Spike phase
$S$	Rietveld scale factor
$S_y$	Least-squares residual for Rietveld fit
$t$	Number of mineral phases in a refined sample
$V$	Volume of unit cell

---

## LIST OF SYMBOLS

---

$w_i$	Weight on least squares residual, $S_y$
$w_s$	Weighed amount of spike, $s$
$W_r$	Relative weight fraction of phase $r$
wt. %	Weight-percent
$y_{ci}$	Calculated intensity at the $i^{th}$ step in an X-ray diffractogram
$y_i$	Measured intensity at the $i^{th}$ step in an X-ray diffractogram
$Z$	Number of formula units per cell

### Greek

$\delta^{13}C$	Delta Carbon-13
$\delta^{18}O$	Delta Oxygen-18
$\theta$	Scattering angle for X-rays

## PREFACE

This work is composed of three body chapters, one of which has been accepted for publication pending minor revisions, and two of which are in preparation for publication.

Chapter II outlines the detailed characterization of mineral assemblages, grain size, and mode of carbonate occurrence in the mine tailings from Clinton Creek and Cassiar. Samples for the 2003 field season were collected by Gregory M. Dipple, R.G. Anderson, and M. Mihalynuk. Dry-sieving was done by Elizabeth Castle. Wet-sieving on two samples was done with the assistance of James Thom and Joanne Woodhouse.

Chapter III is a discussion of isotope data for carbonate precipitates from chrysotile mine tailings. A method for fingerprinting the source of carbon dioxide tapped in the precipitation of calcium and magnesium-carbonates is given. Stable isotope analyses and radiocarbon dating were performed by Janet Gabites and Beta Analytic Radiocarbon Dating Laboratory, respectively. Surface area analysis using the BET N-gas adsorption isotherm technique was done by James Thom.

Chapter IV has been accepted for publication in the *American Mineralogist*, pending minor revisions, under the title "Verifying and quantifying carbon fixation in minerals from serpentine-rich mine tailings using the Rietveld method with X-ray powder diffraction data". It is co-authored by Drs. Mati Raudsepp and Gregory M. Dipple. This chapter describes a new technique, for use with the Rietveld method for X-ray powder diffraction data, which overcomes the previously unresolved barriers to



quantitative phase analysis in samples containing disordered minerals. This new approach to the Rietveld method allows CO<sub>2</sub>-sequestration in mineral carbonates to be quantified in serpentine-rich mine tailings. M. Raudsepp provided valuable technical advice and suggestions. G.M. Dipple, who initiated the project, provided oversight on applications and general concepts.

Drs. Gregory M. Dipple and Mati Raudsepp initiated this line of research, secured funding, and supervised this project.

## ACKNOWLEDGEMENTS

This research was funded by Natural Sciences and Engineering Research Council of Canada Discovery Grants held by G.M. Dipple and M. Raudsepp, by the Yukon Geological Survey, and the British Columbia Ministry of Energy, Mines and Petroleum Resources.

I would like to thank Grant Abbott from the Yukon Geological Survey and Hugh Copland from the Yukon Department of Energy, Mines, and Resources for their interest in this project. Bob Anderson from the Geological Survey of Canada provided samples from Clinton Creek and valuable advice. Mitch Mihalynuk from the British Columbia Ministry of Energy, Mines and Petroleum Resources provided samples from Cassiar. Ernie Hatzl of Cassiar Jade Contracting Inc. provided access and accommodations at Cassiar during the 2003 and 2004 field seasons. Arnt Kern supplied invaluable advice pertaining to the use of the Pawley method. Thanks to Marcia Yu and Andrea De Souza for training in Raman microspectroscopy and to Michael Blades for granting access to his laboratory facilities. Thanks to James Thom for advice and for grain size and surface area data. Lyle Hansen shared his programming expertise in Matlab. Joanne Woodhouse and Elizabeth Castle provided expert laboratory assistance. Thanks to Gordon Southam and Ian Power for discussion and advice regarding the geomicrobiological aspects of this study.

I would like to thank Elisabetta Pani for providing me with training in the use of the X-ray diffractometer and scanning electron microscope and for being an example

## ACKNOWLEDGEMENTS

---

of stoicism and grace under pressure. Thanks to Uli Mayer for advice, constructive criticism, and for serving on my advisory committee. Thanks to Dominique Weis for serving on my examination committee and for sharing her expertise in the field of isotope geochemistry. Many thanks to Greg Dipple and Mati Raudsepp for guidance, for getting me involved in such a fascinating project, and for helping me to become a better scientist. Thanks to Greg for teaching me to always keep the “big picture” in mind and to Mati for impressing upon me the importance of precision and detail in research.

Thanks to Gareth Chalmers, Sarah Gordee, Lyle Hansen, Steve Johnston, Cathy Lovekin, Diana Moscu, Kirsten Parker, Daniel Ross, Swati Singh, Reza Tafti, James Thom, Stuart Sutherland, and all the graduate students in the Department of Earth and Ocean Sciences at UBC for tea, sympathy, and excellent times. My gratitude goes to F.D. Spike for inspiration.

Thanks especially to Jesse, my parents, and Min for their patience and for everything else.

**CHAPTER I:*****Introduction*****1.1 INTRODUCTION AND MOTIVATION FOR STUDY**

The combustion of fossil fuels currently accounts for greater than 80% of global energy use (Goldberg *et al.* 2001). Although alternative energy sources such as nuclear fission, wind, and solar power are available, it is unlikely that increased reliability on these methods of energy production will significantly reduce greenhouse gas emissions in the near future. As national dependence on fossil fuels is unlikely to diminish in the next fifty years, the sequestration of anthropogenic carbon dioxide (CO<sub>2</sub>) may be required to meet Canada's commitment to the Kyoto Protocols. Several methods of CO<sub>2</sub> sequestration including storage in coal seams, in oil and gas reservoirs, in the ocean and saline aquifers, and in mineral carbonates have been proposed (Office of Fossil Energy 2004). Of these schemes, mineral carbonation provides the most stable and environmentally benign means of fixing anthropogenic CO<sub>2</sub> (Lackner *et al.* 1995; Lackner 2003).

Mineral carbonation is a process by which kaolinite-serpentine minerals and olivine are artificially altered to carbonate minerals as a means of binding carbon dioxide in mineral form (Lackner *et al.* 1995). Carbon dioxide bound in carbonates is potentially trapped within the crystal structure of these minerals on a geologic timescale. A large-scale industrial process for mineral carbonation has been under development by the

Mineral Sequestration Working Group affiliated with the U.S. Department of Energy (Goldberg *et al.* 2001). Carbonation of kaolinite-serpentine group minerals in ultramafic mine tailings has only recently been recognized as a natural analogue of the industrial process (Huot *et al.* 2003). Furthermore, enhanced carbonation in mine tailings may provide a potential implementation of the mineral carbonation process.

The primary goals of this research project have been to document the mineralogy and the modes in which carbonation occurs in mine tailings, to identify the environmental controls upon natural carbonation, to determine the sources for carbon dioxide and magnesium tapped during carbonate formation, and to establish whether net sequestration is occurring in the tailings from two abandoned chrysotile mines at Clinton Creek, Yukon and Cassiar, British Columbia (Fig. 1.1). The outcomes of this study include a first detailed description of low-temperature carbonate alteration in ultramafic mine tailings, a method for X-ray powder diffraction data that allows for the quantification of carbon dioxide sequestration with mineral carbonation, and a means by which to fingerprint the source of carbon tapped in the precipitation of modern carbonates using stable and radiogenic isotopes of carbon.

Chapter II provides a detailed account of the mineralogy, modes of occurrence, and methods of formation for carbonate alteration in mine tailings. The hydrated magnesium carbonate minerals lansfordite, nesquehonite, dypingite, and hydromagnesite and the calcium carbonate minerals calcite and aragonite are determined to be developing *in situ* in the ultramafic mine tailings. Five distinct modes of carbonate mineralization

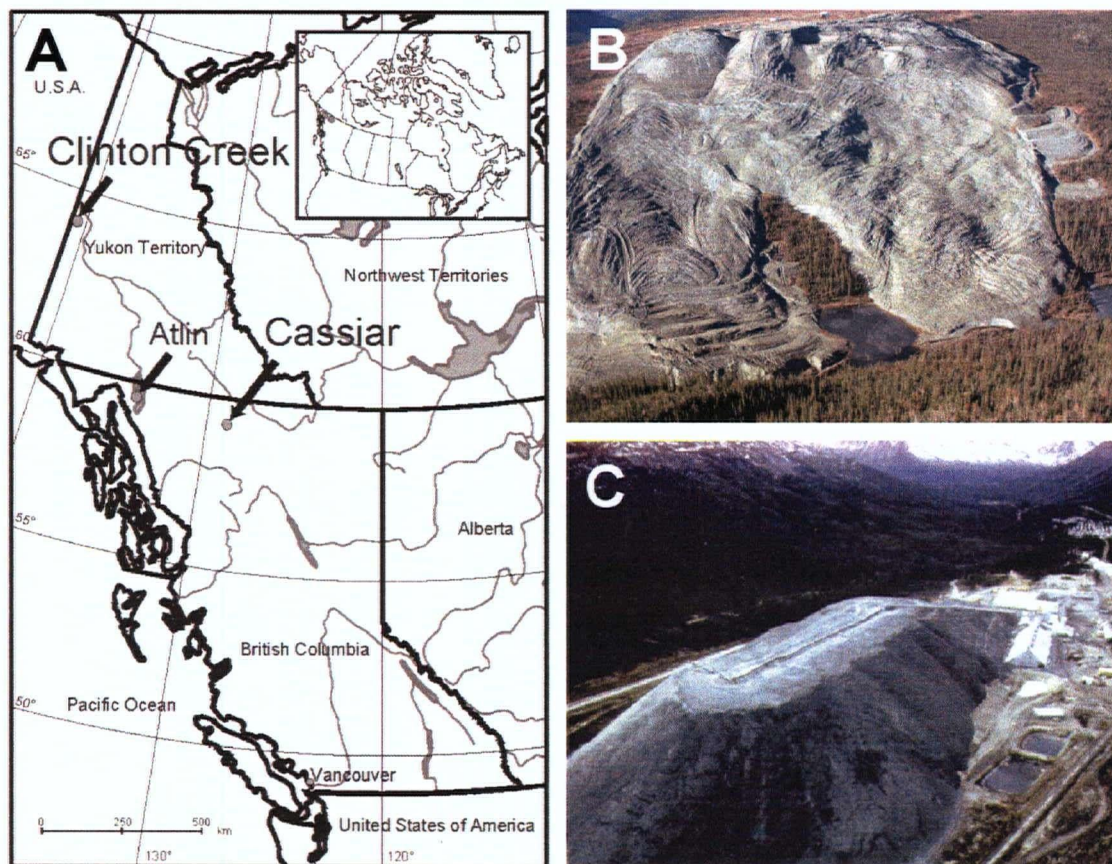


FIGURE 1.1: Location of Clinton Creek, YT, and Cassiar, BC (A). The tailings pile at Clinton Creek is shown in B (trees for scale) and the tailings at Cassiar in C (road for scale).

are documented: Efflorescences or "crusts" on vertical surfaces, spire-like structures on horizontal surfaces, coatings on cobbles, disseminated cements, and linings in runoff streams.

Chapter III discusses the use of stable and radiogenic isotope geochemistry to identify the sources for carbon and cations tapped in the precipitation of carbonates in mine tailings environments. Using stable isotope data for carbon and oxygen and radiogenic carbon dating, an atmospheric source for carbon is identified for the hydrated magnesium carbonates, while the calcium carbonates are determined to have reprecipitated from bedrock.

Chapter IV has been accepted for publication by the American Mineralogist, pending minor revisions. This chapter describes a quantitative method for determining the amount of carbon dioxide that has been crystallographically bound in mineral carbonates in serpentine-rich mine tailings. This procedure employs a variant of the Rietveld method for X-ray powder diffraction data, in which kaolinite-serpentine group minerals are modeled as amorphous phases to account for structural disorder. This method is developed and optimized for a series of synthetic chrysotile and antigorite mine tailings and later implemented on a number of natural mine tailings samples from Clinton Creek and Cassiar.

A discussion of the implications of the results presented in Chapters II, III, and IV is given in Chapter V.

## 1.2 REFERENCES

- Goldberg, P., Chen, Z.-Y., O'Connor, W., Walters, R., and Ziock, H. (2001) CO<sub>2</sub> Mineral Sequestration Studies in US. In the Proceedings of the First National Conference on Carbon Sequestration. Retrieved in 2004 from the National Energy Technology Laboratory of the U.S. Department of Energy Website: [http://www.netl.doe.gov/publications/proceedings/01/carbon\\_seq/6c1.pdf](http://www.netl.doe.gov/publications/proceedings/01/carbon_seq/6c1.pdf).
- Huot, F., Beaudoin, G., Hebert, R. Constantin, M., Bonin, G., and Dipple, G. (2003) Evaluation of Southern Quebec asbestos residues for CO<sub>2</sub> sequestration by mineral carbonation; preliminary results. Joint Annual Meeting of the Geological and Mineralogical Associations of Canada.
- Lackner, K.S. (2003) Climate change: A guide to CO<sub>2</sub> sequestration. *Science*, 300, 1677-1678.
- Lackner, K.S., Wendt, C.H., Butt, D.P., Joyce, G.L., and Sharp, D.H. (1995) Carbon dioxide disposal in carbonate minerals. *Energy*, 20, 1153-1170.
- Office of Fossil Energy. (2005, June 1) Carbon Sequestration R& D. Retrieved October 22, 2005 from the U.S. Department of Energy: <http://www.fossil.energy.gov/programs/sequestration/index.html>.



**CHAPTER II:*****Mineralogical characterization of magnesium-carbonate precipitates in chrysotile mine tailings*****2.1 INTRODUCTION**

The carbonation of kaolinite-serpentine group minerals in ultramafic mine tailings is one potential implementation of the mineral carbonation process (Huot *et al.* 2003). Carbonation of historical mine residues could provide the dual benefit of destroying the fine fibre content of tailings and binding atmospheric greenhouse gases in the process. CO<sub>2</sub> futures or credit trading could also provide a revenue stream for implementing the industrial process. Futures of CO<sub>2</sub> sequestration currently trade for about US\$ 2.50 per tonne (\$/tCO<sub>2</sub>) at the Chicago Climate Exchange (2005), while long-term forecasts approach US\$ 100/tCO<sub>2</sub> (Ciorba *et al.* 2001). On October 25, 2003, a system for emissions trading between member nations came into effect in the EU, under the auspices of Directive 2003/87/EC. Limitations on production of greenhouse gases within the EU were implemented January 1, 2005. Polluters that exceed set emissions caps are fined €40 per tonne of excess CO<sub>2</sub>. This fine will increase to €100/tCO<sub>2</sub> in 2008. EU emissions allowances currently trade for about €23/tCO<sub>2</sub> through Carbon Pool Europe (Climate Corporation 2005). The discovery that some chrysotile mine residues are spontaneously carbonating presents an opportunity to study a natural analogue to the industrial carbonation process that is currently under development by the Mineral

Sequestration Working Group affiliated with the U.S. Department of Energy (Goldberg *et al.* 2001). Additionally, *in situ* acceleration of mineral carbonation in the tailings environment could render large mining operations CO<sub>2</sub>-neutral.

A thorough investigation of the mineralogy of carbonate alteration in serpentinite tailings piles is a necessary first step toward understanding and accelerating uptake of CO<sub>2</sub> in mine tailings. In this chapter, we identify the mineral phases precipitating in these tailings environments and describe the mechanisms by which they form.

## **2.2 CHARACTERIZATION OF TAILINGS MATERIAL**

### **2.2.1 Field Localities**

The Clinton Creek chrysotile deposit is a partially carbonate-altered serpentinitized peridotite (Htoon 1979). The Clinton Creek Mine, situated near Dawson City, Yukon Territory (Fig. 2.1), operated from 1967 to 1978 (Htoon 1979). A total of 16 Mt of chrysotile ore were extracted from the four open pit mines at Clinton Creek during this eleven year period. In addition to the ore, 60 Mt of waste rock and 10 Mt of tailings were produced as a by-product of the mining process (EMAN-North 2003). The tailings pile, situated on a topographic high overlooking Wolverine Creek, slumped into the creek in two stages: The southern lobe of the pile dammed the creek in the early 1970s followed by the northern lobe which destabilized in 1986 (Fig. 2.2). Because most of the

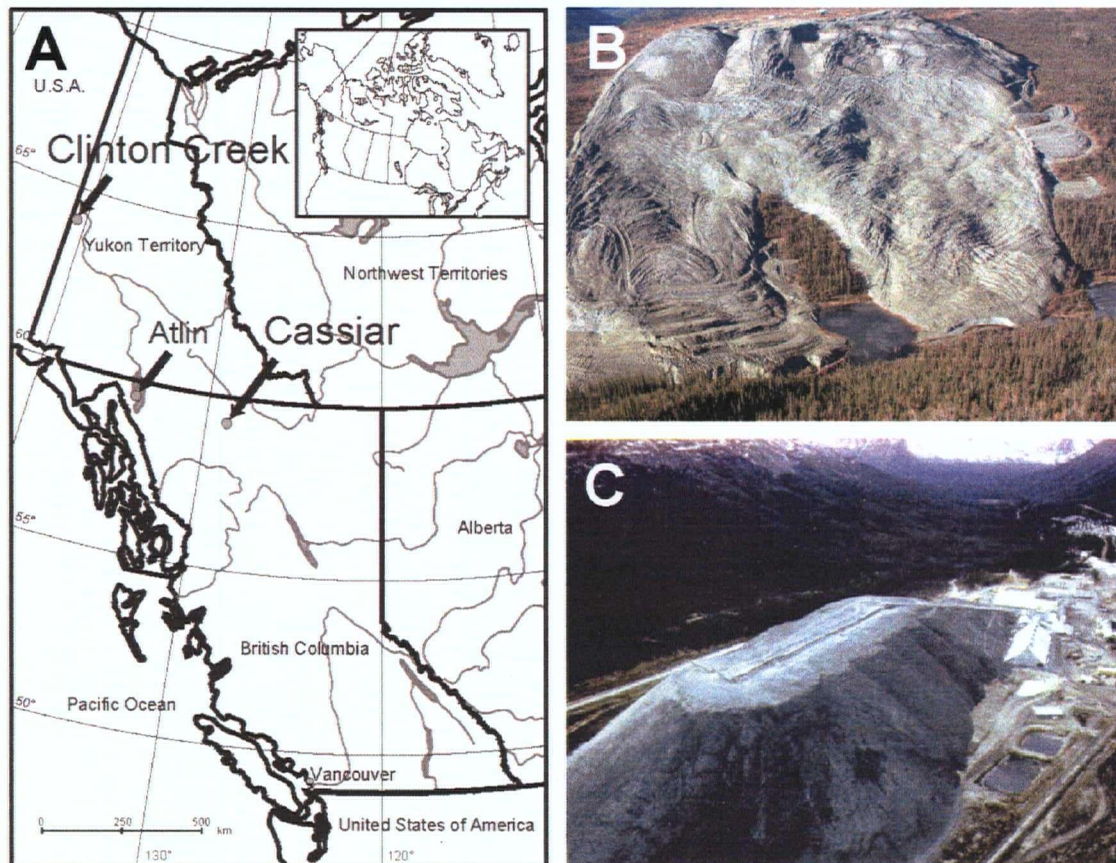


FIGURE 2.1: Location of Clinton Creek, YT, and Cassiar, BC (A). The tailings pile at Clinton Creek is shown in B (trees for scale) and the tailings at Cassiar in C (road for scale).



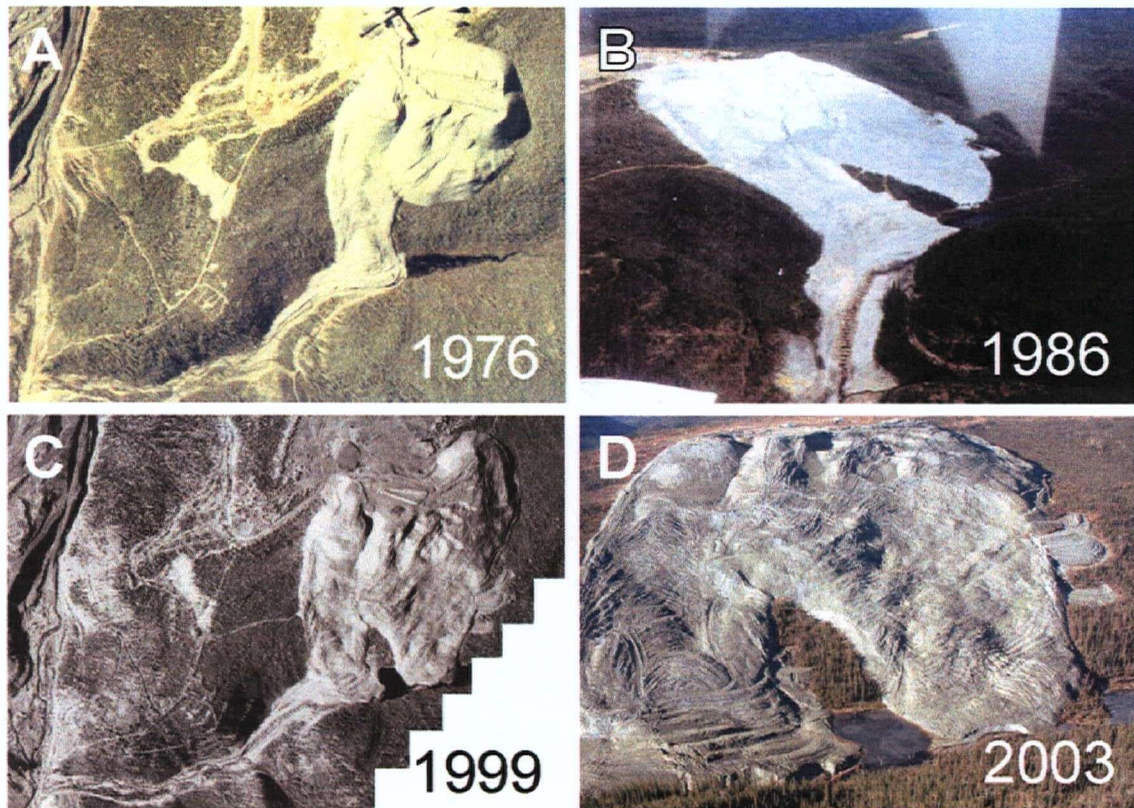


FIGURE 2.2: Collapse of the northern lobe of the Wolverine tailings pile at Clinton Creek. The southern lobe of the tailings pile (left-most lobe in all photos) has already dammed Wolverine Creek by 1976 (A). The northern lobe (right-most lobe) of the tailings pile slumps into the creek in 1986 (B). Terracing features and roads on the tailings surface, added in the 1990s, have not changed from 1999 to 2003 (C and D). No new large-scale slumping features have developed since 1999. (Photographs courtesy of the Yukon Geological Survey.)

sampling done at Clinton Creek was carried out on the surface of these two lobes, it allows us to constrain the age of carbonate alteration at the surface of the tailings pile. Carbonates that have developed on the southern lobe must have formed later than 1974, after the first episode of slope instability, while carbonates on the northern lobe must have formed later than 1986. In an effort to mitigate instability in the tailings pile, the lower sections of the northern and southern lobes were reworked into a series of terraces. Carbonates that have developed on these terrace structures are likely to have formed no earlier than the 1990s when the terraces were initially constructed. Tailings at Clinton Creek are characterized by short-fibre chrysotile and serpentinite cobbles containing massive serpentine and minor amounts of magnetite, calcite, dolomite, magnesite, quartz, clinochlore, and pyroaurite.

The chrysotile deposit at Cassiar, British Columbia, forms part of a serpentinitized harzburgite tectonite (Wicks and O'Hanley 1988). Cassiar is located approximately 130 km north of Dease Lake, BC (Fig. 2.1). During the 39-year operational lifetime of the mine, from 1953 to 1992, 17 Mt of mine tailings were produced. These tailings were stored outdoors in an elongate pile. Beginning in 1993, the mine underwent a six-year process of renovation and revitalization. By January 2000 commercial production of chrysotile had been renewed. Mining proceeded until December 25, 2000 when the mill was severely damaged by fire (MINFILE 2005). Tailings are composed primarily of short-fibre chrysotile and cobbles of massive serpentine with minor magnetite, clinochlore, and occasional quartz and carbonates.

Hydrated magnesium carbonate and calcium carbonate minerals occur in five distinct modes in the mine tailings at Clinton Creek and Cassiar: 1) as crusts on vertical surfaces, 2) as carbonate spires on horizontal tailings surfaces, 3) as thin crusts (< 1 mm in thickness) on serpentinite cobbles, 4) as a fine-grained disseminated cement between tailings grains, and 5) as precipitates lining the beds of ephemeral runoff streams (Fig. 2.3). Vertical carbonate crusts, spires, coated cobbles, and cements composed of hydrated magnesium carbonates are abundant at Clinton Creek. Vertical hydrated magnesium carbonate crusts, calcium-carbonate cobble-coatings, and stream linings have been observed at Cassiar. Hydrated magnesium carbonate mineralization is easily recognised by its off-white colour, colloform habit, and reactivity with dilute hydrochloric acid (10% HCl). Calcium-carbonate cobble-coatings and stream-bed precipitates are also recognizable by their off-white colour and reactivity with dilute HCl.

### **2.2.2 Sampling Methodology**

The samples under study were collected during the 2003 and 2004 summer field seasons. In 2003, 23 samples were taken from Clinton Creek at the surface of the tailings pile by R. Anderson. Forty samples from Cassiar were taken at depths varying from 0 to 1.7 m below the surface of the tailings pile. Sampling at Cassiar was done by M. Mihalynuk, G. Dipple, and R. Anderson. These samples can be characterized as crust-like material, loose tailings, or bulk samples, collected by shovel or auger. Having set



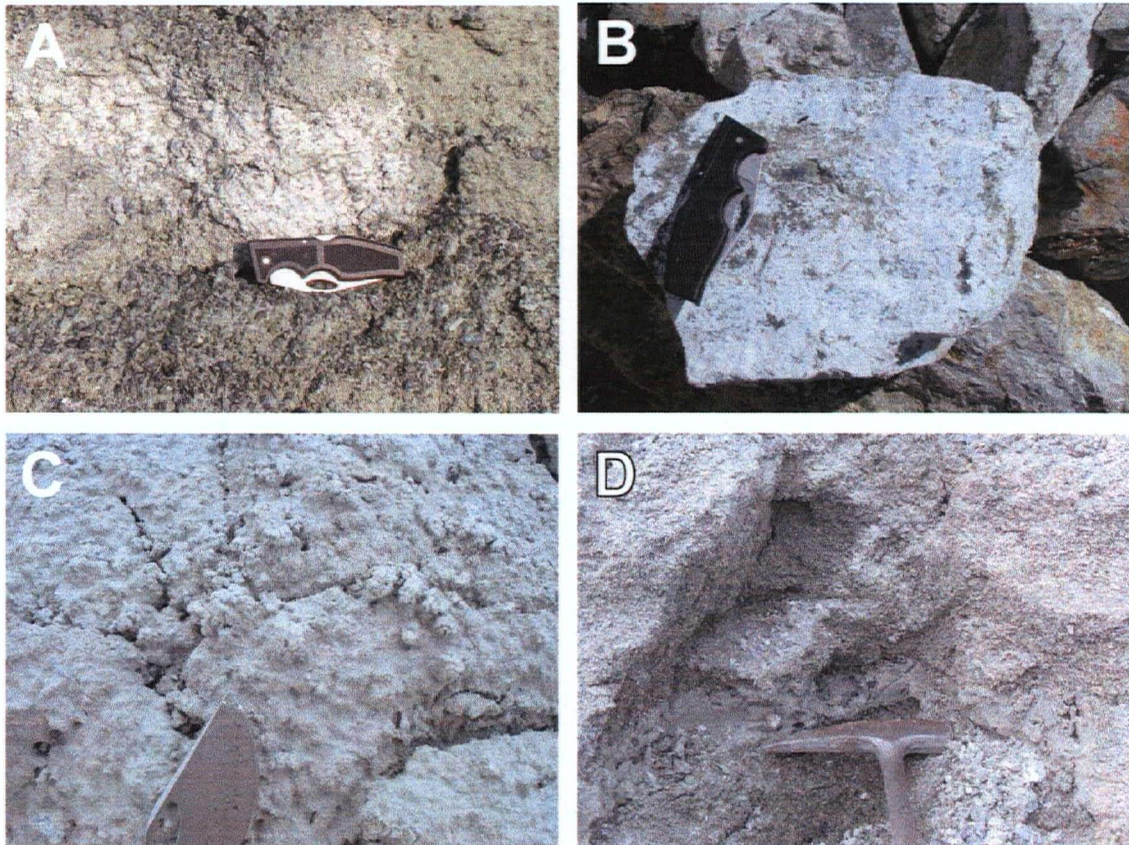


FIGURE 2.3: Modes of carbonate occurrence at Clinton Creek and Cassiar. A) Crusts on vertical surfaces, B) thin coatings on cobbles, C) spires on horizontal surfaces, and D) disseminated carbonate cement.

some early constraints on the appearance and occurrence of hydrated magnesium carbonate minerals in mine tailings, the goal of the 2004 field season was to find and sample carbonate-rich crusts. During this season, 19 samples of surface tailings and 11 samples from the waste rock pile were collected from Clinton Creek. Fourteen samples were collected from the surface of the tailings pile and one sample was collected from the waste rock pile at Cassiar.

## **2.3 EXPERIMENTAL TECHNIQUES FOR CHARACTERIZATION OF TAILINGS**

### **2.3.1 Qualitative X-ray Powder Diffraction**

Mineral phases were identified with X-ray powder diffraction (XRPD). Finely-ground aliquots of sample were smear-mounted onto petrographic slides with ethanol and allowed to dry at room temperature. XRPD data for mineral identification were collected with a scanning step of  $0.04^\circ 2\theta$  and counting time of 2s/step on a Siemens D5000  $\theta$ - $2\theta$  diffractometer over a range of  $3$ - $70^\circ 2\theta$  with each scan taking 55 minutes. Constituent mineral phases were identified with reference to the ICDD PDF-4 database using DIFFRAC<sup>plus</sup> EVA (Bruker AXS 2004a). The normal-focus Cu X-ray tube was operated at 40 kV and 40 mA. Samples from the 2003 field season were scanned for amphibole asbestos to a detection limit of less than 0.2 wt.%. A scanning step of  $0.02^\circ 2\theta$  and a counting time of 10 s/step over a range of  $9$ - $11^\circ 2\theta$  were used, taking approximately 17



minutes. In order to detect hydrated magnesium carbonate minerals at low abundance, a scanning step of  $0.04^\circ 2\theta$  and a counting time of 40 s/step over a range of  $12-17^\circ 2\theta$  were used, giving a scan time of 1 hour and 24 minutes.

### **2.3.2 Scanning Electron Microscopy**

Characterization of carbonate crust habits and textural relations between carbonate phases was carried out using the Philips XL-30 Scanning Electron Microscope (SEM), equipped with a Princeton Gamma-Tech Energy Dispersive X-ray Spectrometer (EDS) system, in the Department of Earth and Ocean Sciences at UBC. Secondary electron imaging was used to observe the surface morphology of carbonate crusts while back-scattered electron imaging was used to observe textural relations in thin section. Energy dispersive X-ray spectroscopy (EDS) was used for the identification of minerals and to distinguish between magnesium carbonate phases. Two samples of vertical crusts (04CC0201B and 04CC0703) and two carbonate spires (04CC0702 and 04CC0901) from Clinton Creek were impregnated with epoxy and thin-sectioned for petrographic analysis. Additionally, small segments of carbonate crusts and coatings were mounted on aluminum stubs for imaging mineral habit with the SEM.

### 2.3.3 Grain Size Analysis

Grain size analysis was performed by dry-sieving, on 40 samples from Cassiar and 20 samples from Clinton Creek, collected during the 2003 field season. Standard sieve sizes ranging from 16 mm to 0.053 mm were used. Chrysotile-rich samples do not give particularly accurate grain size data due to the fibrous nature of the mineral. Long fibres do not pass easily through sieves and as such are generally included in larger size fractions which do not reflect the size and higher surface area associated with fibres.

A separate method of wet sieving, developed by James Thom at the Department of Earth and Ocean Sciences at UBC, was used to determine the “fibre fraction” of one bulk sample from each locality. Accounting for the fibre fraction allows for improved quantification of grain size and surface area within chrysotile-rich samples. Improved estimates for surface area allow for better estimates of the available cross-section for chemical reaction of the serpentine minerals. For each locality, the bulk sample was dry-sieved and bundles of fibres were hand-picked from the larger size fractions. The remaining, predominantly non-fibrous material was washed in deionised water in an ultrasonic bath and mechanically stirred to disaggregate small fibres. The fibre-rich water was decanted from the bath and passed through filter-cloth to collect the fine fibre fraction. Tailings from individual size fractions and the filtered fibres were placed under a drying hood for 96 hours and weighed on an electronic balance once dry.

### **2.3.4 Bulk Geochemistry**

Bulk geochemical analysis of 22 samples from Clinton Creek and Cassiar was done by McGill Geochemical Laboratories. Samples were analysed for major element oxides, Ni, V, Zn and volatiles (Appendix A). Analyses were done by X-ray fluorescence using a Philips PW2440 spectrometer with a 60 kV rhodium end-window X-ray tube. Bulk geochemical data do not distinguish bedrock carbonate from carbonate efflorescences.

## **2.4 RESULTS OF BULK TAILINGS CHARACTERIZATION**

### **2.4.1 Bulk Mineralogy**

Samples from the tailings pile at Clinton Creek are characterized by kaolinite-serpentine group minerals, chrysotile in particular, with minor magnetite, calcite, dolomite, magnesite, quartz, clinocllore, and pyroaurite (refer to Appendix B for complete mineralogical data). Carbonate crusts, spires, and cobble coatings which were analysed separately from the underlying tailings material generally contain hydrated magnesium carbonate phases. Nesquehonite, dypingite, and hydromagnesite, with occasional lansfordite, have been identified at Clinton Creek. The presence of nesquehonite and dypingite has been documented at Cassiar. Samples taken at water level from the artificial lake in the waste rock pile were found to contain the hydrated

sulphate minerals epsomite and hexahydrite. Hexahydrite was also observed in two vertical carbonate crusts in the tailings pile. The most likely source of the sulphur in these minerals is the pyrite present in the carbonaceous argillite that underlies the Clinton Creek valley (Htoon 1979). Calcite, dolomite, magnesite, and pyroaurite are abundant in the bedrock at Clinton Creek. The presence of pyroaurite [a hydrotalcite group mineral which can be produced in association with the infiltration of serpentinites by a CO<sub>2</sub>-rich fluid (Grguric *et al.* 2001)], and evidence for acid intrusion during the Latest Cretaceous to Earliest Tertiary documented by Htoon (1979), seem to indicate that the tailings from Cassiar and Clinton Creek are mineralogically distinct. Furthermore, silica-carbonate veining has replaced cryptocrystalline serpentine and fibrous chrysotile along fractures (Htoon 1979). Based on Htoon's (1979) observations of talc-magnesite-silica alteration of serpentinite at Clinton Creek, some of the bedrock has undergone post-serpentinization alteration to listwanite.

Tailings at Cassiar are composed primarily of kaolinite-serpentine group minerals (predominantly chrysotile) with minor magnetite, clinochlore, and occasional quartz and carbonates (mostly dolomite). Thin coatings of aragonite ± calcite have been found on serpentinite cobbles in both the tailings and the waste rock. In one instance, a thin film of calcite + aragonite was found lining the periphery of a small stream flowing through the waste rock pile.

### 2.4.2 Asbestos Mineral Content

During the past two decades, research into the carcinogenic properties of asbestiform minerals has shown that exposure to amphibole asbestos poses a greater health hazard than exposure to chrysotile (Langer 2001). Prolonged exposure to high doses of both chrysotile and amphibole asbestos (*e.g.*, tremolite-actinolite, grunerite, riebeckite, and anthophyllite) is known to cause mesothelioma, asbestosis, and lung cancer in humans (Langer 2001). Pulmonary tissues retain chrysotile asbestos to a much lesser degree than amphibole asbestos, completely independent of the degree of exposure. The Mg-ions in chrysotile are easily leached from the surface of fibres under the slightly acidic conditions found in lung fluids. Mg-depleted fibres have a higher solubility and can be cleared from the lungs at an increased rate, accounting for the relatively short-lived biopersistence of chrysotile (Johnson and Mossman 2001).

A recent study shows that the typical amphibole content of chrysotile ore from the Jeffrey Mine, Asbestos, Québec is less than 2.5 wt.% (Williams-Jones *et al.* 2001). Despite the low amphibole content of the ore, the same study showed an average distribution of 72 wt.% fibrous tremolite and 26 wt.% chrysotile in the lungs of miners and millers from this locality (Williams-Jones *et al.* 2001). Previous studies at other chrysotile mines and in laboratory mammals have found similar results (*e.g.*, Johnson and Mossman 2001; Williams-Jones *et al.* 2001). Since amphibole asbestos fibres have a residence half-life in lung tissue on the order of years, compared to months for chrysotile, the length of *in vivo* exposure to the pathogen is significantly longer (Johnson and

Mossman 2001). Thus, exposure to amphibole asbestos is likely to pose a greater health risk than exposure to chrysotile.

Four of the fifty-seven samples analysed for amphibole asbestos from Cassiar were found to contain an amphibole mineral when analysed with XRPD. No amphibole phases were detected in Clinton Creek samples to a detection limit of approximately 0.2 wt.%. Grains of the amphibole mineral were analysed using energy dispersion spectroscopy (EDS) on the scanning electron microscope (SEM). EDS revealed that the amphibole in question is non-fibrous actinolite  $[\text{Ca}_2(\text{Mg,Fe})_5\text{Si}_8\text{O}_{22}(\text{OH})_2]$ , which is consistent with the presence of nephrite jade at the Cassiar mine (Fig. 2.4). The absence of fibrous amphiboles implies that the likelihood of serious illness resulting from working with Cassiar tailings is greatly reduced in comparison to tailings with amphibole-asbestos content.

### **2.4.3 Carbonate Precipitate in Bulk Tailings Samples**

XRPD scans of bulk tailings samples have identified the hydrated magnesium carbonate minerals nesquehonite, dypingite, and hydromagnesite at Clinton Creek and Cassiar by XRPD. Detailed mineralogical data are given in Appendix B. The high-sensitivity XRD scans performed on bulk tailings samples from the 2003 field season do not allow for the determination of hydromagnesite versus dypingite because both minerals share several major peaks and the intensities of their characteristic reflections

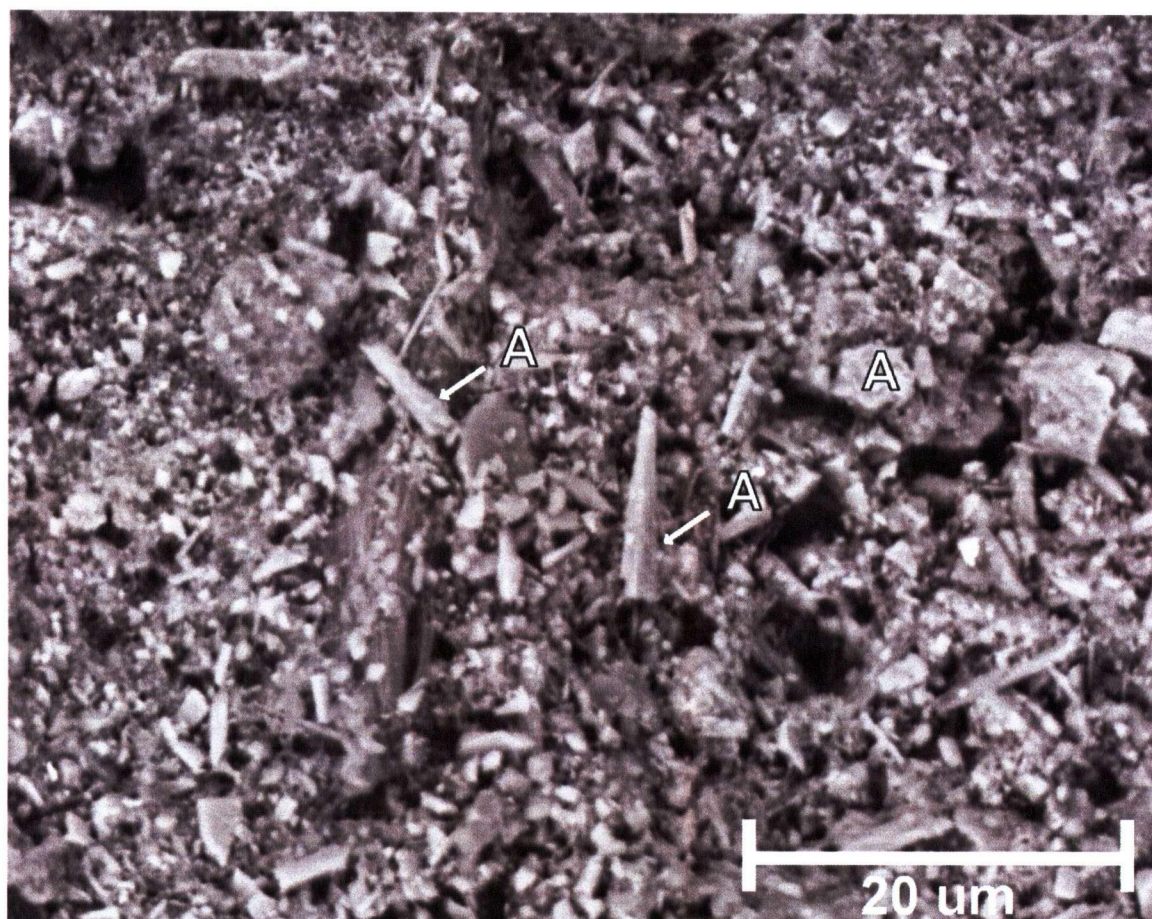


FIGURE 2.4: Back-scattered electron image of actinolite grains in sample 04CA0401. Actinolite grains detected by XRPD in several samples from Cassiar have been determined by back-scattered SEM imaging to be non-fibrous. A – Actinolite.

are typically below detection. As such, these minerals are identified as “either/or” in the 2003 samples (Appendix B), except for the occasional case in which sufficient carbonate material was available for separate analysis or for particularly carbonate-rich samples of bulk tailings. Samples from the 2004 field season were selected for carbonate abundance rather than bulk determination of tailings mineralogy. With more carbonate material available for analysis, carbonate phases are readily identified; dypingite and hydromagnesite become distinguishable and low abundances of lansfordite can be detected.

#### **2.4.4 Grain Size Analysis**

Twenty bulk samples from Clinton Creek and 40 from Cassiar were analyzed for grain size using standard sieve techniques (refer to Appendix C for detailed results). The conclusions of this analysis are threefold: 1) Although the samples were heterogeneous, they were generally composed of sand to cobble-sized grains (Udden-Wentworth scale) at both localities; 2) no significant difference in grain size between crust-like materials at the surface of the tailings pile and loose or bulk materials was observed (Fig. 2.5), which implies that carbonate precipitation is not solely a function of grain size, and 3) the medium to fine sand fraction of most samples from Cassiar comprises approximately 10 wt.%. At Clinton Creek, the fine sand to silt fraction represents the finest 10 wt.% of most samples.



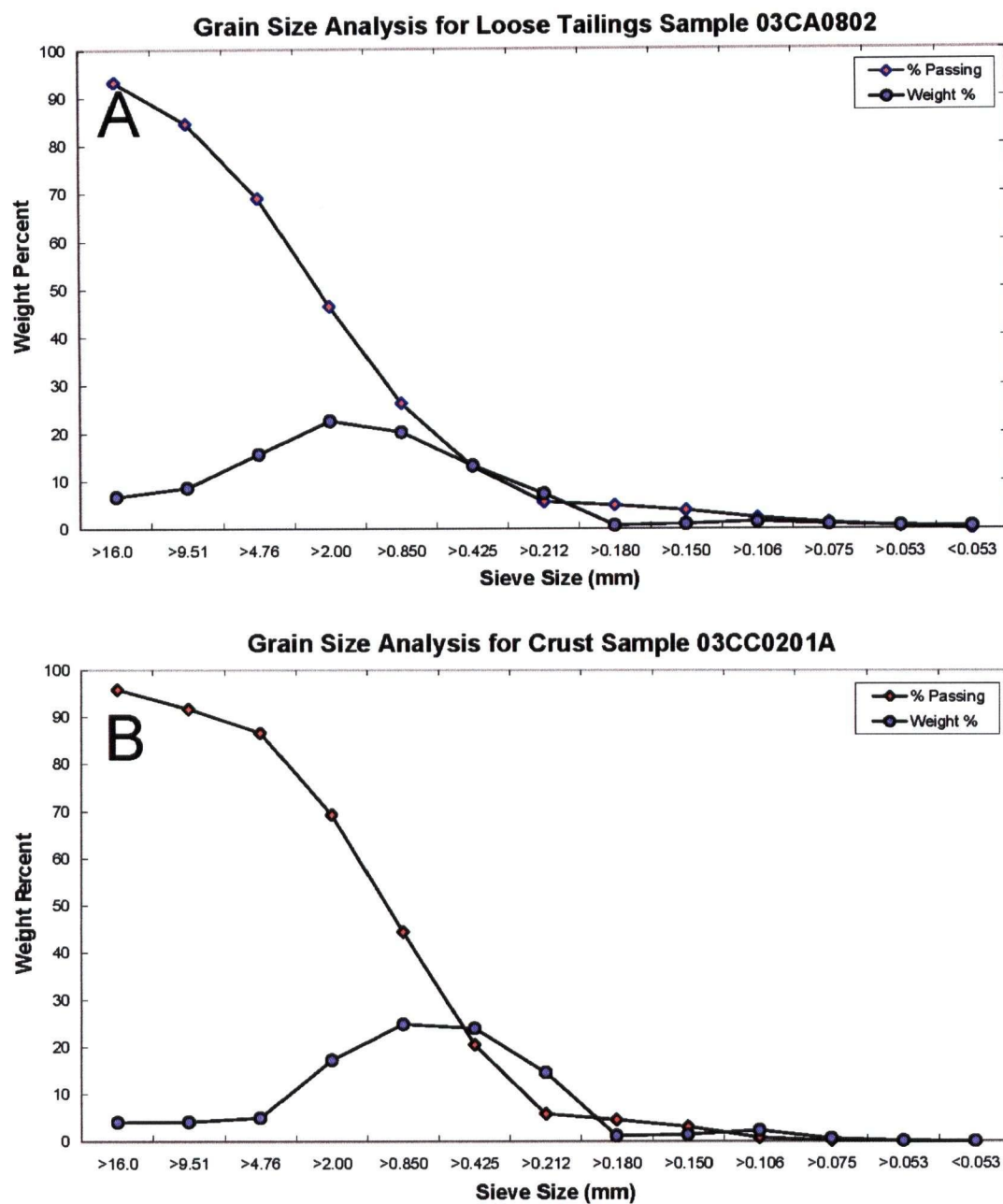


FIGURE 2.5: Results of grain size analysis for two typical samples of tailings. No significant difference in grain size distribution is observed between carbonate-free 03CA0802 (A) and the carbonate-rich tailings sample 03CC0201A (B).

Wet-sieving was done for sample 04CC1401 – a bulk tailings sample from Clinton Creek. The fine fibres from each size fraction were decanted, dried, and weighed, yielding the result that  $6.8 \pm 0.3$  wt.% of the bulk sample consisted of fine fibres of chrysotile. The breakdown for each size fraction, by weight, is shown in Figure 2.6. What is most notable about the results of wet-sieving is that over 50 wt.% of the fine fibres in the sample were decanted from the coarse sand to cobble size fractions (Fig. 2.7). These fibres were loosely adhered to the surfaces of cobbles and cemented between grains of sand. The fine fibres from the bulk tailings sample from Cassiar (03CA1601) constituted 10.9 wt.% of the bulk sample, 56.9% of which fibres were decanted from the coarse sand to cobble size fractions (J. Thom, pers. comm.).

## **2.5 HYDRATED MAGNESIUM CARBONATE MINERALOGY**

The efficiency of the natural carbonation of serpentine minerals to produce hydrated magnesium carbonates is an important aspect of this study, as it has implications for CO<sub>2</sub> sequestration within mine tailings. Carbonate mineral species differ in terms of thermodynamic stability and sequestration potential. Lansfordite, nesquehonite, dypingite, hydromagnesite, and aragonite have been identified at Clinton Creek and nesquehonite, dypingite, aragonite, and calcite have been observed at Cassiar. There is a possibility that other magnesium carbonate species with varying states of hydration are occurring at both sites in amounts below detection by XRPD.

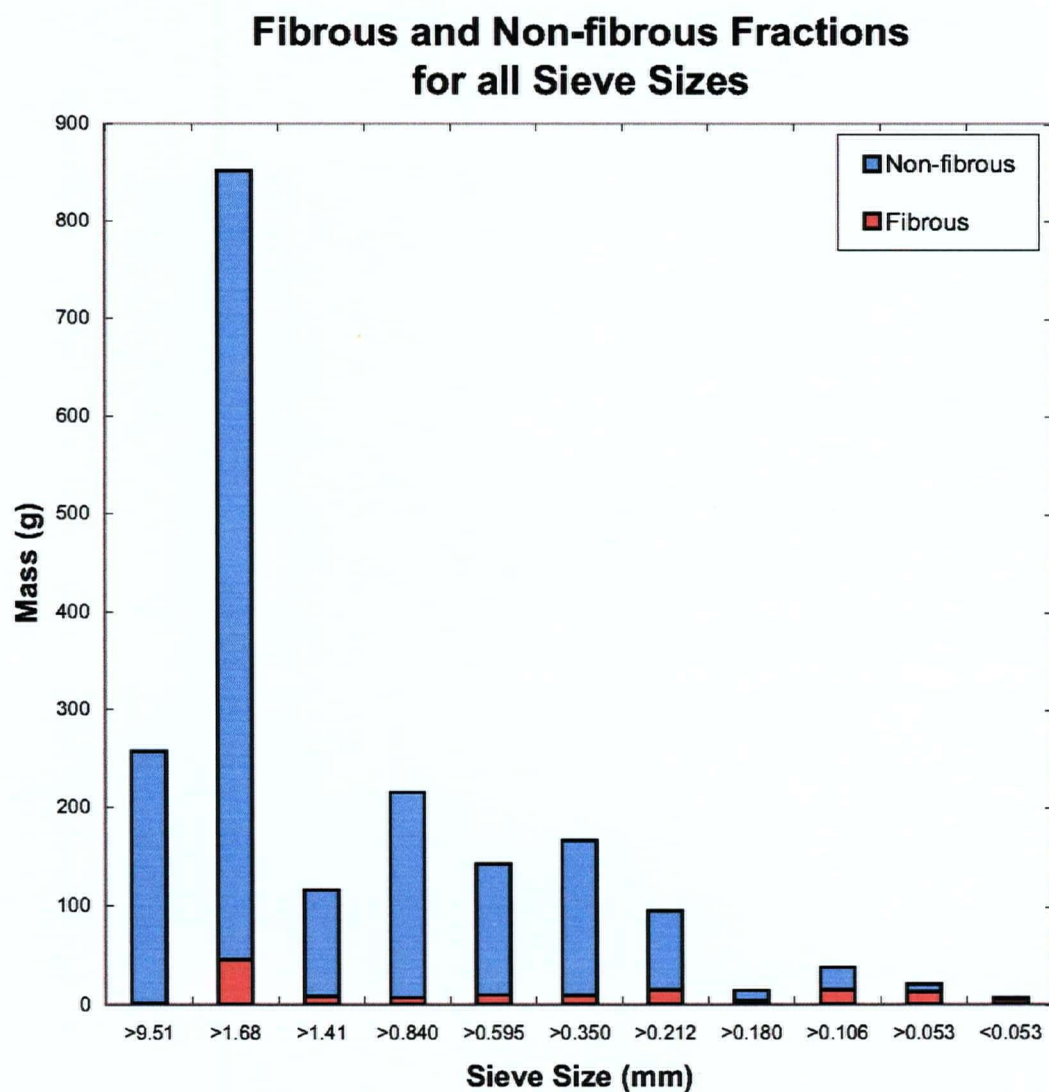


FIGURE 2.6: Mass fractions of fibrous and non-fibrous tailings materials for each size fraction used in wet-sieving for sample 04CC1401.

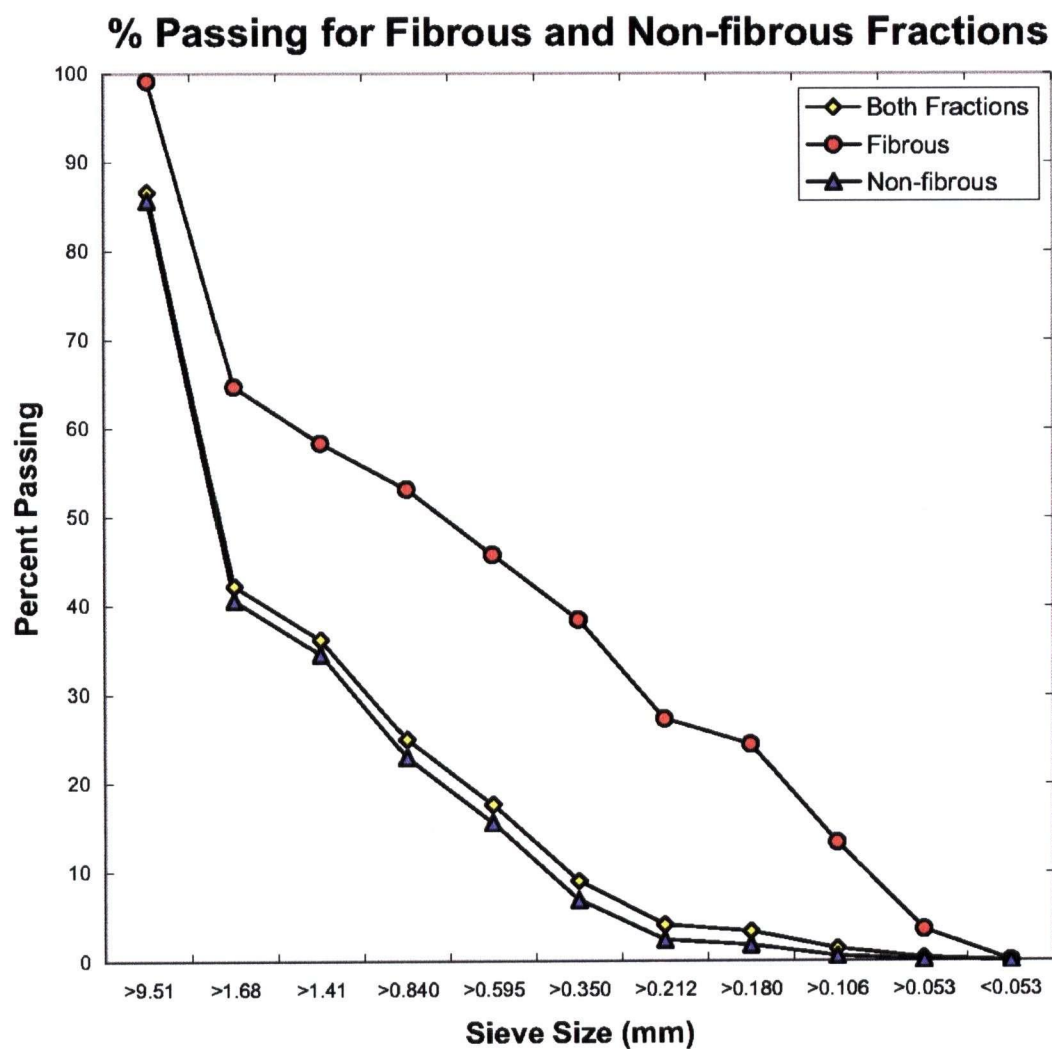


FIGURE 2.7: Percent of tailings to pass through each sieve for sample 04CC1401. More than 50 wt.% of the fine chrysotile fibres are found in the coarse sand to cobble fractions.

The hydrated magnesium carbonate minerals can be organized into three groups based on their chemical formulae (after Canterford *et al.* 1984):

- 1)  $\text{MgCO}_3 \cdot x\text{H}_2\text{O}$ , for integral values of  $x$  greater than zero. The first group consists of those minerals whose formulae are composed of magnesite ( $\text{MgCO}_3$ ) with variable waters of hydration. Three such minerals are known to occur in nature: Barringtonite is  $\text{MgCO}_3 \cdot 2\text{H}_2\text{O}$  (Nashar 1965), nesquehonite is  $\text{MgCO}_3 \cdot 3\text{H}_2\text{O}$  (Stephan and MacGillavry 1972), and lansfordite is  $\text{MgCO}_3 \cdot 5\text{H}_2\text{O}$  (Hill *et al.* 1982). Stability of these minerals tends to decrease with increasing  $\text{H}_2\text{O}$  (*e.g.*, Langmuir 1965; Hill *et al.* 1982; Garvie 2003).
- 2)  $\text{Mg}_2(\text{CO}_3)(\text{OH})_2 \cdot x\text{H}_2\text{O}$ , for integral values of  $x$  greater than zero. The second group of hydrated magnesium carbonate minerals is distinguished from the first by the addition of hydroxyl groups or a brucite-like formula component,  $\text{Mg}(\text{OH})_2$ . Artinite [ $\text{Mg}_2(\text{CO}_3)(\text{OH})_2 \cdot 3\text{H}_2\text{O}$ ] is the only known member of this group (Canterford *et al.* 1984).
- 3)  $\text{Mg}_5(\text{CO}_4)(\text{OH})_2 \cdot x\text{H}_2\text{O}$ , for integral values of  $x$  in the range of 4 to 11. Five minerals have been identified as belonging to this group, four of which have been confirmed to occur in nature: Hydromagnesite with  $x = 4$  (Akao and Iwai 1977), dypingite with  $x = 5$  (Raade 1970), giorgiosite with  $x = 6$  (Canterford *et al.* 1984), and yoshikawaite with  $x = 8$  (Suzuki and Ito 1973). Protohydromagnesite, characterized by  $x = 11$ , has only been identified in synthetic samples (Davies and Bubula 1973).

The values for waters of hydration,  $x$ , have been drawn from the most recent formula determinations from oxide weight-percent data by Canterford *et al.* (1984).

The formation of the magnesium carbonate minerals barringtonite, nesquehonite, lansfordite, and magnesite optimizes the sequestration of atmospheric CO<sub>2</sub>. This can be demonstrated by inspection of the H<sub>2</sub>O-MgO-CO<sub>2</sub> compositional ternary for hydrated magnesium carbonates (Fig. 2.8) or simply by inspection of the general formulae for the three mineral groups (Table 2.1). The ratio of CO<sub>2</sub> to Mg per formula unit of the Group 2 and 3 minerals is always less than 1 (*i.e.*, CO<sub>2</sub>/Mg < 1), while that for the Group 1 minerals is equal to 1 (*i.e.*, CO<sub>2</sub>/Mg = 1). The carbon dioxide to cation ratio for calcite and aragonite is also unity (*i.e.*, CO<sub>2</sub>/Ca = 1), implying similarly high capacity for sequestration as the Group 1 minerals. In terms of the amount of dissolved cation required, Group 1 minerals, calcite, and aragonite are more efficient hosts for CO<sub>2</sub>.

Lansfordite is unstable at atmospheric pressure above 10 °C (Langmuir 1965), at which temperature it dehydrates to nesquehonite. Nesquehonite decomposes to hydromagnesite *via* a series of metastable intermediate phases above 55 °C (*e.g.*, Dell and Weller 1959; Kazakov *et al.* 1959; Langmuir 1965; Davies and Bubela 1973). Dypingite is the most commonly observed intermediate phase in the decomposition of nesquehonite to hydromagnesite in nature and in the laboratory (*e.g.*, Davies and Bubela 1973; Canterford *et al.* 1984; Inaba *et al.* 1985). Canterford *et al.* (1984) have speculated that the decomposition of nesquehonite may proceed *via* several pathways dependent upon differing environmental controls. Mineralogy of observed intermediate phases varies between decomposition experiments and between site localities in the literature.

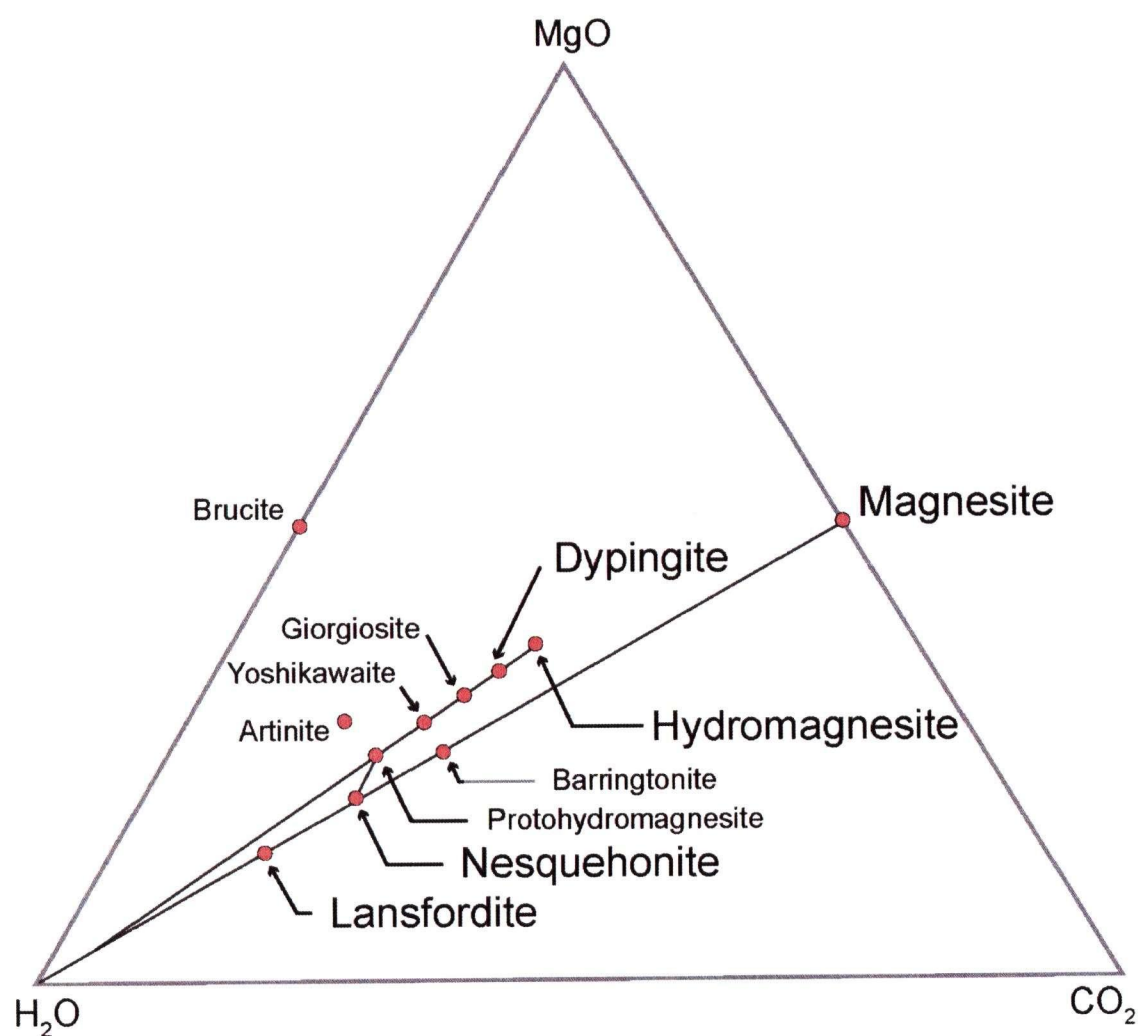


FIGURE 2.8:  $\text{H}_2\text{O}$ - $\text{MgO}$ - $\text{CO}_2$  compositional ternary for the hydrated magnesium carbonate minerals, after Canterford *et al.* (1984).

TABLE 2.1: Empirical formulae for hydrated magnesium carbonate minerals.

MINERAL SPECIES	CHEMICAL FORMULA
Group 1	$\text{MgCO}_3 \cdot x\text{H}_2\text{O}$
Barringtonite	$\text{MgCO}_3 \cdot 2\text{H}_2\text{O}$
Nesquehonite	$\text{MgCO}_3 \cdot 3\text{H}_2\text{O}$
Lansfordite	$\text{MgCO}_3 \cdot 5\text{H}_2\text{O}$
Group 2	$\text{Mg}_2(\text{CO}_3)(\text{OH})_2 \cdot x\text{H}_2\text{O}$
Artinite	$\text{Mg}_2(\text{CO}_3)(\text{OH})_2 \cdot 3\text{H}_2\text{O}$
Group 3	$\text{Mg}_5(\text{CO}_3)_4(\text{OH})_2 \cdot x\text{H}_2\text{O}$
Hydromagnesite	$\text{Mg}_5(\text{CO}_3)_4(\text{OH})_2 \cdot 4\text{H}_2\text{O}$
Dypingite	$\text{Mg}_5(\text{CO}_3)_4(\text{OH})_2 \cdot 5\text{H}_2\text{O}$
Giorgiosite	$\text{Mg}_5(\text{CO}_3)_4(\text{OH})_2 \cdot 6\text{H}_2\text{O}$ or $\text{Mg}_5(\text{CO}_3)_4(\text{OH})_2 \cdot 5\text{H}_2\text{O}$
Yoshikawaite	$\text{Mg}_5(\text{CO}_3)_4(\text{OH})_2 \cdot 8\text{H}_2\text{O}$
Protohydromagnesite	$\text{Mg}_5(\text{CO}_3)_4(\text{OH})_2 \cdot 11\text{H}_2\text{O}$



## 2.6 MODES OF OCCURRENCE AND MECHANISMS OF FORMATION

Nesquehonite, dypingite, and hydromagnesite are abundant at Clinton Creek while lansfordite remains scarce. Nesquehonite and dypingite have been identified in tailings materials from Cassiar. Aragonite precipitates are found at both localities as thin crusts on the surface of cobbles.

A correlation between mode of carbonate occurrence and carbonate species has been identified from XRD data (Table 2.2). Carbonate crusts and spires generally contain nesquehonite, dypingite, and hydromagnesite. Lansfordite has been found to occur in some vertical crusts. Crusts vary in composition from mostly nesquehonite with minor dypingite  $\pm$  hydromagnesite to dypingite  $\pm$  nesquehonite  $\pm$  hydromagnesite. The nesquehonite  $\pm$  dypingite  $\pm$  hydromagnesite crusts are more common. Cobble coatings are almost exclusively dypingite or aragonite  $\pm$  calcite with one case of dypingite + hydromagnesite from Clinton Creek. Disseminated carbonate cements are composed entirely of hydromagnesite. The bed of one ephemeral runoff stream in the waste rock pile at Cassiar was found to be lined by a coating of calcite + aragonite.

Zonation of carbonate phases in spires and vertical crusts is readily observed in thin section with back-scattered SEM imaging. In thin section, nesquehonite can be differentiated from dypingite and hydromagnesite by habit, slight variation in the intensity of backscattered electrons (*i.e.*, nesquehonite appears darker as a result of its

TABLE 2.2: Mineralogy and mode of carbonate occurrence.

MODE OF OCCURRENCE	CARBONATE MINERALOGY	
	Magnesium Carbonates	Calcium Carbonates
Vertical Crusts	Nesquehonite ± Dypingite ± Hydromagnesite	
Horizontal Spires	Nesquehonite ± Dypingite ± Hydromagnesite	
Cobble Coatings	Dypingite ± Hydromagnesite	Aragonite ± Calcite
Disseminated Cements	Hydromagnesite	
Stream Linings		Aragonite ± Calcite

lower density), and a small but detectable increase in the ratio of the intensities of the C to Mg K $\alpha$  X-ray peaks in energy dispersion spectra (Fig. 2.9 for habit and “colour” and Fig. 2.10 for EDS). As a result of their similar chemical composition, density, and habit, dypingite and hydromagnesite are indistinguishable with SEM.

Back-scattered electron (BSE) images of spire samples 04CC0702 and 04CC0902 and vertical crusts 04CC0201B and 04CC0703 in thin section reveal the zonation of hydrated magnesium carbonate phases which cannot be seen in secondary electron (SE) images of the surfaces of crusts and spires (Figs. 2.11 and 2.12). Dypingite and/or hydromagnesite are abundant at depth within vertical crust and spire samples. Fine-grained, radiating crystals of dypingite and/or hydromagnesite have nucleated on the surfaces of serpentinite grains, forming a cement between them (Fig. 2.11A). Because nesquehonite is the primary phase at the surface of crust and spire samples, it is not usually possible to observe the habit and topography of dypingite and hydromagnesite crystals using secondary electrons; but similar habits have been observed in dypingite coating serpentinite cobbles. Dypingite commonly forms rosette-like structures at the surface of cobbles at Clinton Creek (Fig. 2.11B). The fine-grained dypingite/hydromagnesite observed in thin section can be interpreted as a cross-section through rosettes which have formed at depth rather than at the surface of a cobble. Grains of hydrated magnesium carbonate minerals are frequently observed infilling fissures in serpentinite grains (Fig. 2.11C). This appears to be the result of silicate dissolution, as the pieces of these grains cannot be reassembled without obvious loss of material. Fracture patterns which do not reflect dissolution are also common (Fig. 2.11D). The

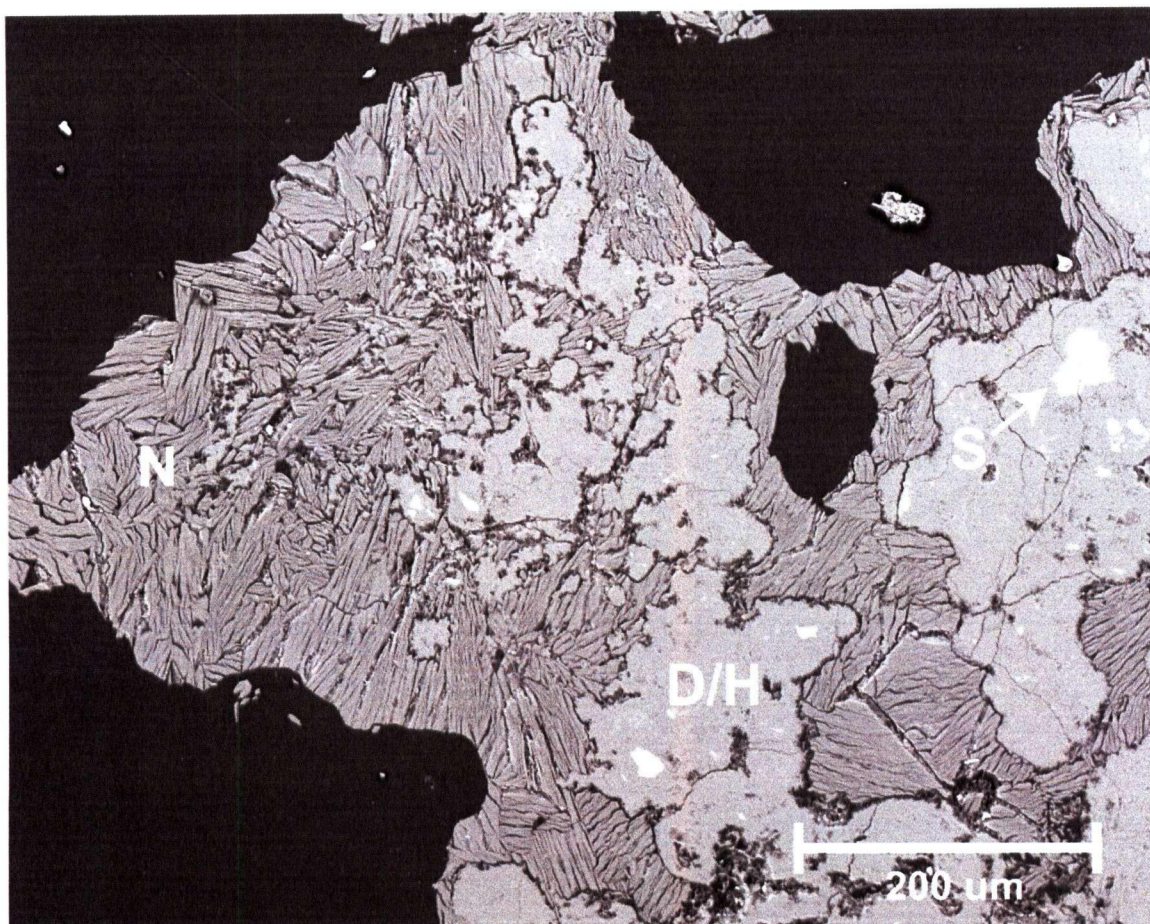


FIGURE 2.9: Variation in habit and intensity of backscattered electrons between nesquehonite and dypingite/hydromagnesite phases in vertical crust sample 04CC0201B. N – characteristic bladed crystals of nesquehonite. D/H – finely crystalline rosette-like masses of dypingite and/or hydromagnesite. S – serpentine grains.



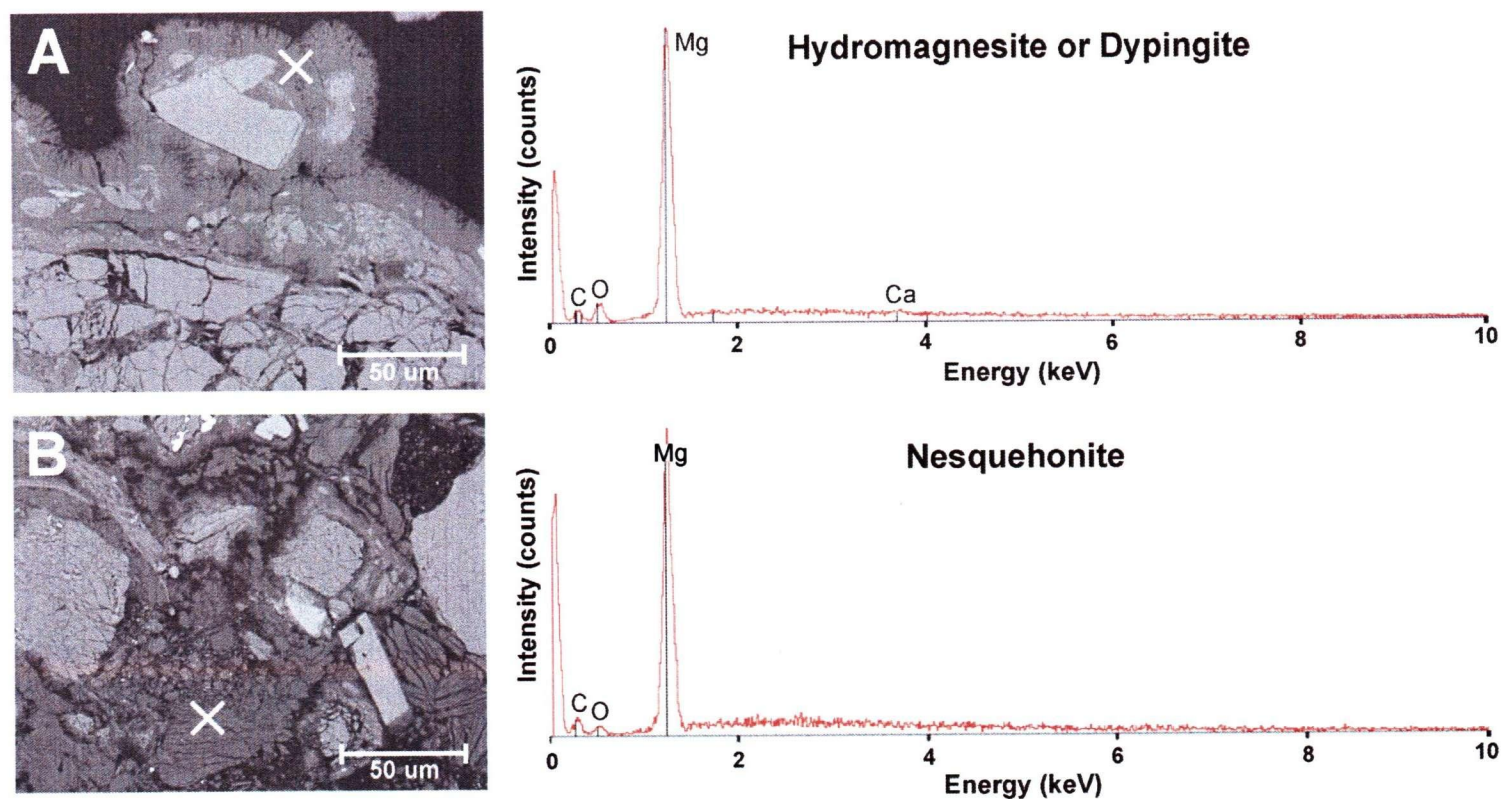


FIGURE 2.10: Distinguishing between hydromagnesite/dypingite (A) and nesquehonite (B) in thin section with EDS. The lower density of nesquehonite and the slightly higher ratio of the C:Mg peaks can be used to distinguish it from other hydrated magnesium carbonates. Spectra were collected in semi-quantitative mode for 180 s. Xs mark the points at which EDS were taken.

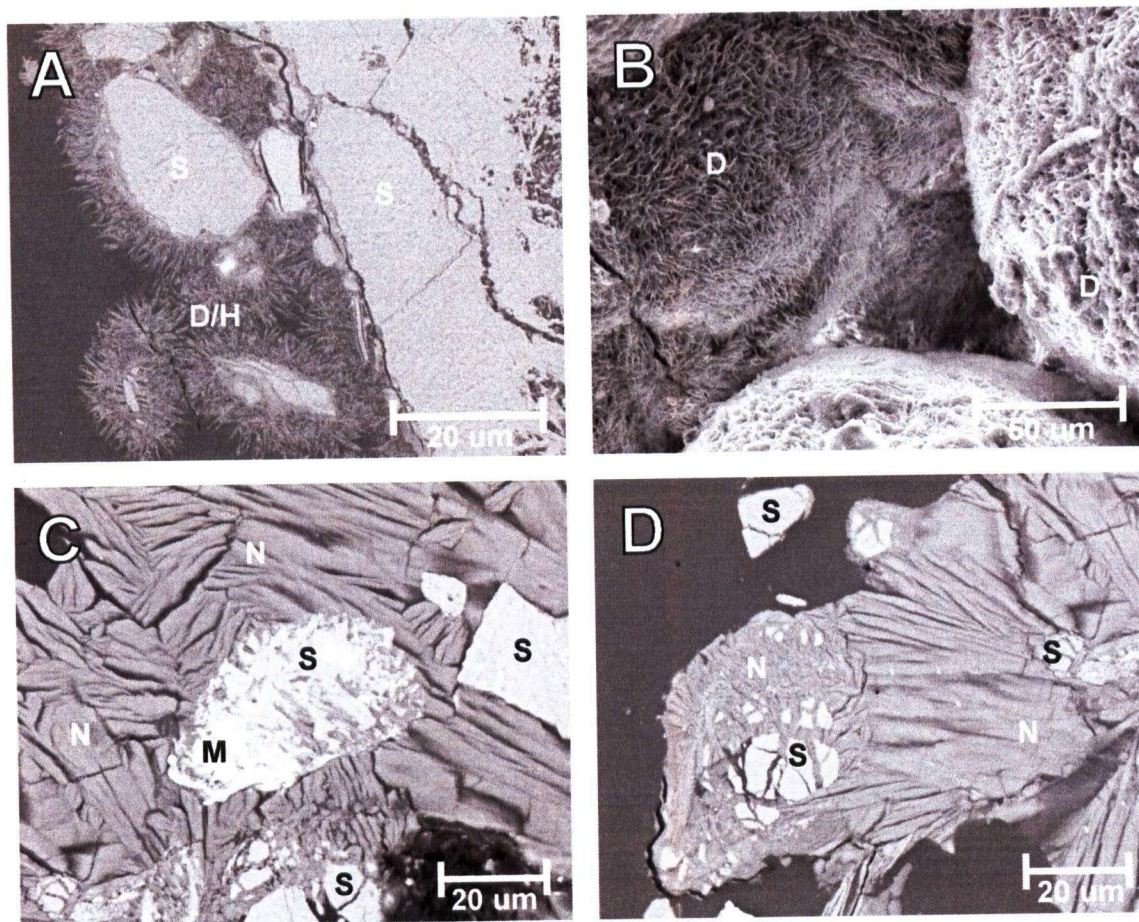


FIGURE 2.11: Secondary electron (SE) and back-scattered electron (BSE) images of spire sample 04CC0702, vertical crust 04CC0201B, and cobble 04CC0601B-CB. A) BSE image of cross-section through dypingite/hydromagnesite rosettes on surfaces of serpentinite grains at depth in 04CC0201B. B) Dypingite rosettes in SE as seen on the surface of cobble sample 04CC0601B-CB. C) Nesquehonite infilling dissolution fissures in a serpentinite grain near the spire surface in 04CC0702 (BSE). D) Formation of nesquehonite may subject serpentinite grains to a type of freeze-thaw action which could lead to the type of fissuring seen in here in 04CC0702 (BSE). N – nesquehonite. D/H – dypingite and/or hydromagnesite. D – dypingite. S – serpentine grains. M – magnetite.



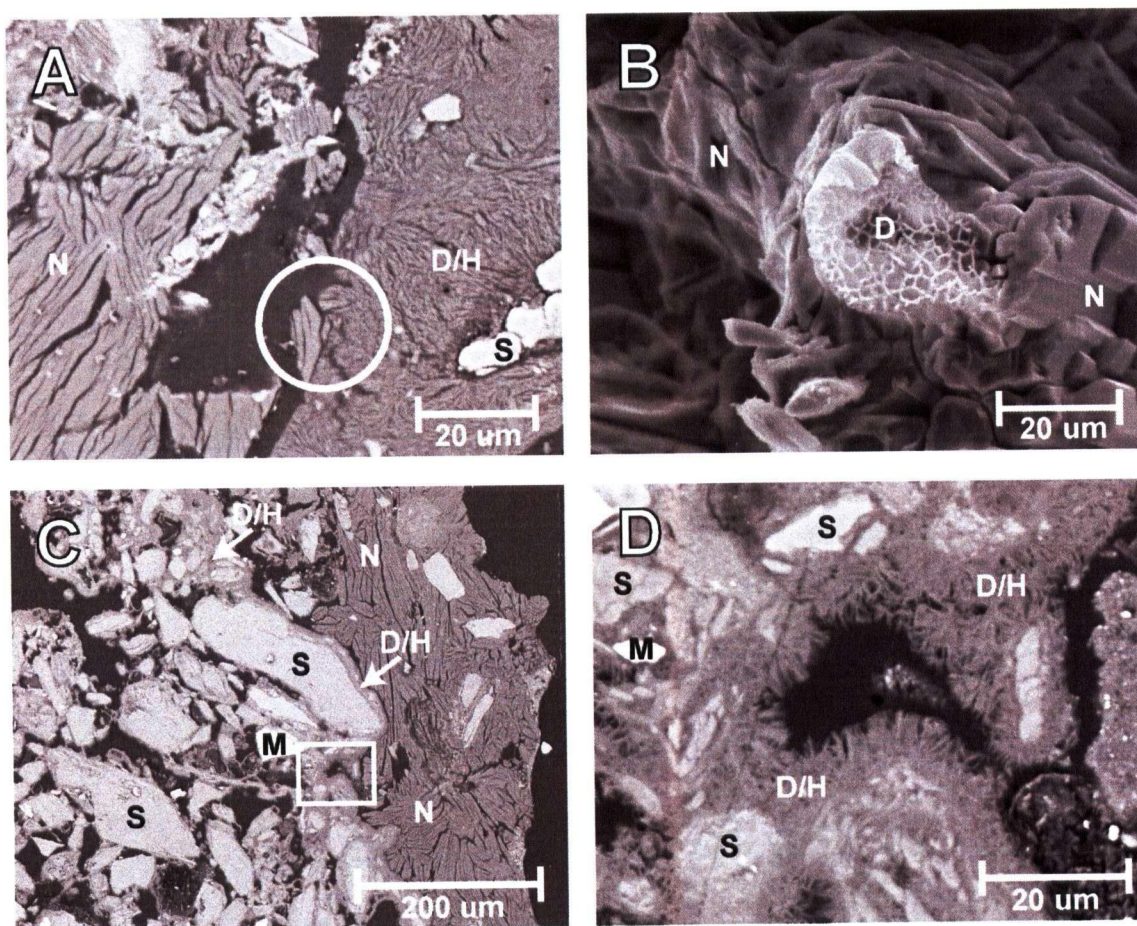


FIGURE 2.12: Secondary electron (SE) and back-scattered electron (BSE) images of spire samples 04CC0702 and 04CC0902 and vertical crust 04CC0106. A) Interface between nesquehonite and dypingite/hydromagnesite phases in 04CC0902 (BSE). The circled region may be evidence of a dehydration front. B) View of a nesquehonite-dypingite contact in 04CC0106 (SE). C) BSE image of nesquehonite at the surface of sample 04CC0702. Boxed region is shown in D) Dypingite/hydromagnesite rosettes nucleating on serpentine grains at depth. N – nesquehonite. D/H – dypingite and/or hydromagnesite. D – dypingite. S – serpentine grains. M – magnetite.

latter textures could be indicative of a type of freeze-thaw action occurring within serpentinite grains, by which lansfordite or nesquehonite precipitate at low temperatures, causing serpentinite grains to fracture.

There are few intact interfaces between the nesquehonite caps at the surfaces of the crusts and spires and the dypingite/hydromagnesite at depth. Some interfaces are continuous (*e.g.*, Fig. 2.12A), but most are broken by gaps ranging from 100 to 500  $\mu\text{m}$  between the nesquehonite caps and the rosette-covered serpentinite grains. This effect may simply have resulted during the manufacture of the thin sections; else, it may be indicative of a volume loss within the sample. Volume could have been lost from either the evaporation of adsorbed water in chrysotile fibres or from dehydration of nesquehonite. The region circled in Figure 2.12A is suggestive of a dehydration front, but most continuous interfaces between the nesquehonite and dypingite/hydromagnesite do not show evidence of replacement textures. Contacts between the mineral species can occasionally be seen outside of thin sections in vertical crusts (Fig. 2.12B), but the textural relationships do not provide definitive support for a particular interpretation. Regardless of the formational relationship between the magnesium carbonate phases, the zonation is consistent in crusts and spires with nesquehonite at the surface (Fig. 2.12C) and dypingite and/or hydromagnesite at depth (Figs. 2.12C and D).

It is possible that a differential in pore-water evaporation or chemistry may be the cause of zonation within carbonate crusts and spires. Qualitative XRPD results for other samples of vertical crusts and spires indicate that they often contain all of nesquehonite, dypingite, and hydromagnesite. Dypingite is a metastable mineral phase, which can be



created as nesquehonite transforms to hydromagnesite (Davies and Bubela 1973; Canterford *et al.* 1984; Inaba *et al.* 1985). Hydromagnesite in the tailings at Clinton Creek may be a product of the decomposition of nesquehonite forming in contact with the atmosphere. If so, decomposition of nesquehonite in mine tailings would not appear to be a function of humidity, but rather a function of age, with the metastable minerals forming at the interface between the tailings and the atmosphere, and the older carbonate precipitates decomposing to increasingly stable mineral phases at depth (Fig. 2.13). The SEM data are inconclusive, and may suggest that the zonation of minerals within carbonate crusts and spires is controlled by water chemistry and temperature or progressive decomposition of nesquehonite to dypingite and hydromagnesite.

## 2.7 INTERPRETATION OF EXPERIMENTAL RESULTS

Observations of the occurrence patterns of the hydrated magnesium carbonate minerals at Clinton Creek and Cassiar imply that they have developed *in situ*, rather than having been inherited from bedrock through the mining process. The precipitation of carbonate crusts is a surface phenomenon, which is most likely driven by evaporation and/or freeze-out. The development of disseminated carbonate cements may be a near-surface pedogenic process. Marked differences in the mineralogy of the modes of occurrence indicate that there may be several reaction pathways by which mineral

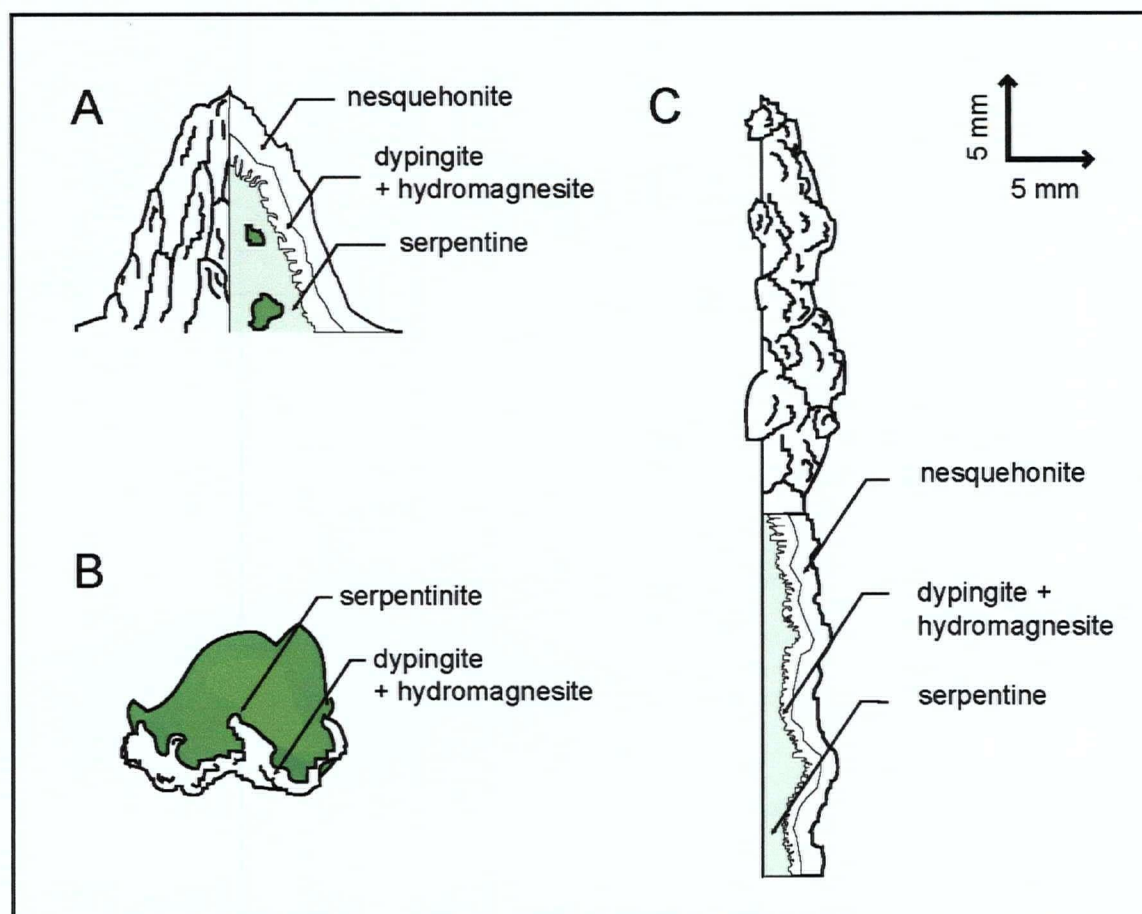


FIGURE 2.13: Zonation of hydrated magnesium carbonate minerals in crusts and spires. A) Carbonate spire capped by nesquehonite with dypingite + hydromagnesite at depth, B) serpentinite cobble with coating of dypingite, and C) vertical crust with nesquehonite at the surface and dypingite + hydromagnesite at depth.

sequestration is occurring in the residues. As such, it is likely that there are multiple routes by which the rate of precipitation could be increased for enhanced carbonation.

The most likely means by which hydrated magnesium carbonate crusts are developing in the mine residues at Clinton Creek and Cassiar is outlined in Figure 2.14. Carbon dioxide and bicarbonate, dissolved in rain water, come into contact with mine residues. Magnesium is leached from the tailings and carried, in aqueous solution by evaporation and upward flow, to the surface of the tailings piles, where carbonates are precipitated through evaporation and/or freeze-out.

Carbonation is much less abundant at Cassiar than at Clinton Creek due to comparatively less favourable hydrological conditions within the tailings pile. At Clinton Creek, pore waters may be channelled through regions of higher permeability within the tailings. It is possible that fine-grained tailings materials retain moisture, essentially trapping it in place until solar heat induces evaporation and/or wicking to the surface of the pile. Carbonation is limited at Cassiar, because the tailings are contained within a steeply-sloping, compact pile. The core of the tailings pile is frozen year round (Ernie Hatzl, pers. comm.), hastening the run-off of rainwater through the pile and limiting dissolution of magnesium to the upper few metres of material. Regular, steeply-sloping sides shorten the residence time of pore waters in the tailings pile at Cassiar, providing little chance for silicate weathering and precipitation of carbonate at the surface. The bulk sample from Clinton Creek (04CC1401) was taken from the base of the tailings pile near the water table. Pore waters flowing through the sampled surface are rich in dissolved  $\text{Mg}^{2+}$ ,  $\text{HCO}_3^-$ , and  $\text{CO}_3^{2-}$ , having passed through

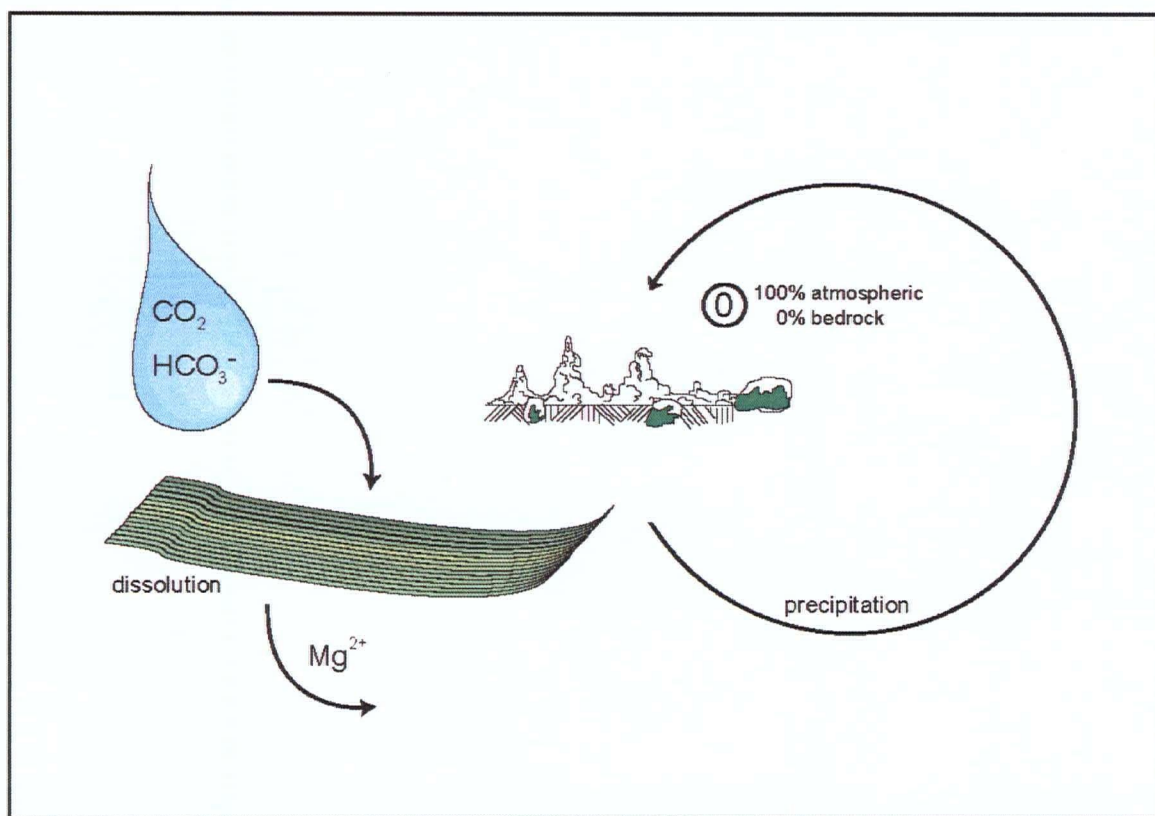


FIGURE 2.14: Best-case scenario model for hydrated magnesium carbonate formation in mine tailings.

much of the hummocky terrain that has been produced by slumping in the tailings pile. As a result, tailings from this sampling location are rich in Mg-carbonate cement.

The development of magnesium carbonate crusts within mine tailings may be structurally controlled by the positions of relatively more permeable horizons within the tailings. Where flux of  $\text{Mg}^{2+}$  and  $\text{HCO}_3^-$  ion-rich pore waters is high at vertical outlets in a tailings pile, vertical crusts are more likely to develop by evaporation or freeze-out of these fluids (Fig. 2.15). Regions with high moisture retention capacity, high pore water residence time, and higher Mg-concentration are also potential controls on precipitation. Pore waters, flowing through permeable horizons near the tailings surface, are subject to wicking by chrysotile fibres. Redirection of pore water to horizontal surfaces by wicking leads to the development of carbonate spires. Carbonate crusts on cobbles may form by local dissolution of serpentine and direct reprecipitation of Mg-carbonates onto the cobble surface or by nucleation of mineral precipitates from the out-flowing tailings waters. Cobble coatings, when observed on a single grain surface, are frequently on the underside, suggesting long contact with moisture from the tailings pile. As cobbles are dislodged from their original sites of deposition, the previously uncoated surfaces receive increased exposure to surface water, also developing coatings. Disseminated hydromagnesite cements likely form in regions of the tailings pile characterized by fine grain size and high pore-water residence times.

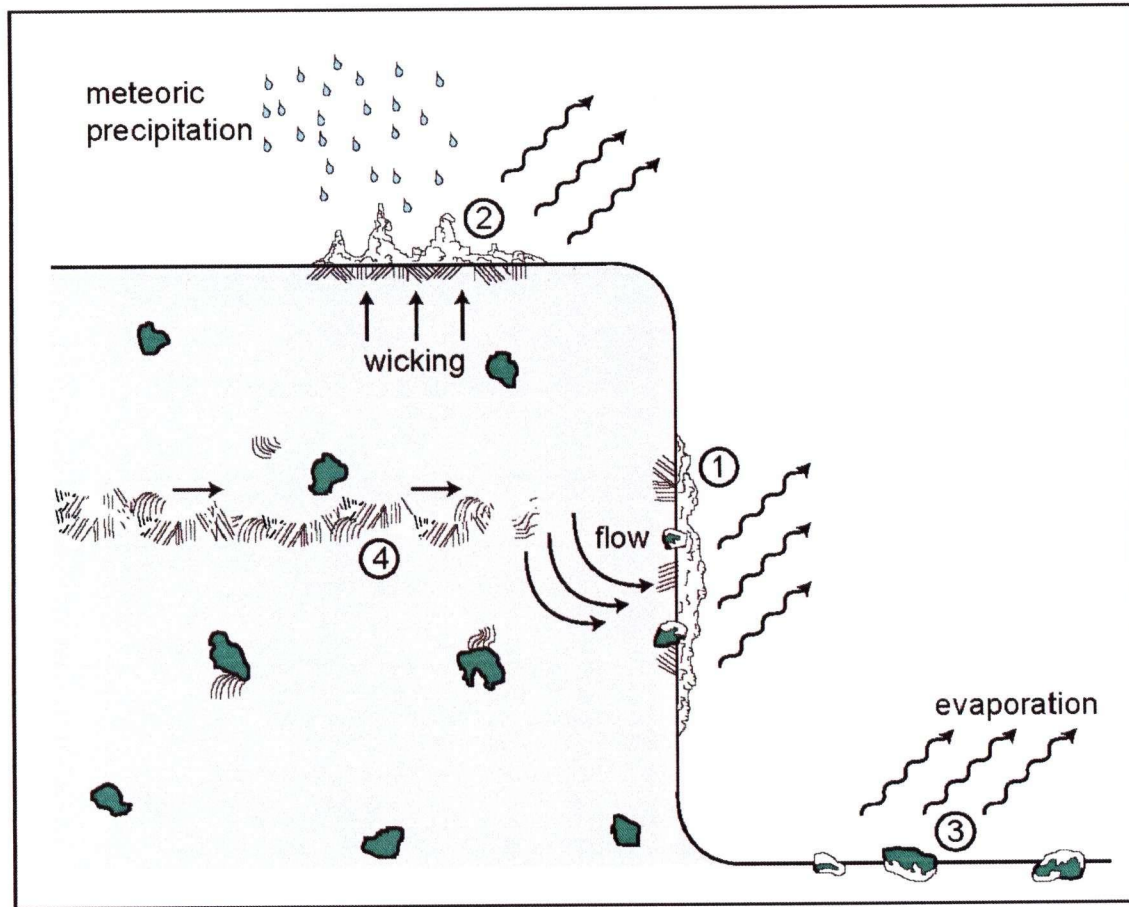


FIGURE 2.15: Mechanisms of formation for the four modes of occurrence: 1) Vertical crusts, 2) carbonate spires, 3) cobble coatings, and 4) disseminated cement.

An alternate explanation for the simultaneous occurrence of multiple hydrated magnesium carbonate phases may be the direct precipitation of separate phases without having to invoke decomposition as a mechanism of formation. Possible cyanobacterially-mediated precipitation of magnesite has been observed in the laboratory by Thompson and Ferris (1990); however, direct precipitation of magnesite is thought to be kinetically inhibited in most lacustrine environments (refer to Zedef *et al.* 2000 for a brief review). Zedef *et al.* (2000) and Renaut and Long (1989) have observed direct precipitation of hydromagnesite in playa environments. It has been proposed by Renaut and Long (1989) that salinity and the Mg/Ca ionic ratio of lake water control which magnesium carbonate phases precipitate from solution. Similar controls may be active in the mine tailings environment. Precipitation of specific mineral species may be seasonally variable based on water chemistry or temperature.

## 2.8 REFERENCES

- Akao, M. and Iwai, S. (1977) The hydrogen bonding of hydromagnesite. *Acta Crystallographica*, Section B: Structural Crystallography and Crystal Chemistry, B33, 1273-1275.
- BRUKER AXS (2004a) EVA V. 10.0: Release 2004 – User's Manual. Bruker AXS, Karlsruhe, Germany.

- Canterford, J.H., Tsambourakis, G., and Lambert, B. (1984) Some observations on the properties of dypingite,  $\text{Mg}_5(\text{CO}_3)_4(\text{OH})_2 \cdot 5\text{H}_2\text{O}$ , and related minerals. *Mineralogical Magazine*, 48, 437-442.
- Chicago Climate Exchange (2005) Chicago Climate Exchange Market Data. Retrieved September 2005 from the Chicago Climate Exchange Website: <http://www.chicagoclimateexchange.com/trading/marketData.html>.
- Ciorba, U., Lanza, A., and Pauli, F. (2001) Kyoto Protocol and emission trading: does the US make a difference? Fondazione Eni Enrico Mattei, Milan.
- Climate Corporation (2005)  $\text{CO}_2$  Climate Pool: The EU ETS: Facts and Figures. Retrieved September 2005 from the Climate Corporation Website: <http://www.climatecorp.com>.
- Davies, P.J. and Bubela, B. (1973) The transformation of nesquehonite into hydromagnesite: *Chemical Geology*, 12, 289-300.
- Dell, R.M. and Weller, S.W. (1959) The thermal decomposition of nesquehonite,  $\text{MgCO}_3 \cdot 3\text{H}_2\text{O}$ , and magnesium ammonium carbonate,  $\text{MgCO}_3(\text{NH}_4)_2\text{CO}_3 \cdot 4\text{H}_2\text{O}$ . *Transactions of the Faraday Society*, 55, 2203-2220.
- EMAN-North. (2003) Northern Contaminants Program: Local Contaminants Sources (Yukon): Clinton Creek Mine. Retrieved in 2004 from the Ecological Monitoring and Assessment Network for Northern Canada Website, Government of Canada: <http://www.emannorth.ca/ic/ds014/clinton.cfm>.
- Garvie, L.A.J. (2003) Decay-induced biomineralization of the saguaro cactus (*Carnegiea gigantea*). *American Mineralogist*, 88, 1879-1888.



- Goldberg, P., Chen, Z.-Y., O'Connor, W., Walters, R., and Ziock, H. (2001) CO<sub>2</sub> Mineral Sequestration Studies in US. In the Proceedings of the First National Conference on Carbon Sequestration. Retrieved in 2004 from the National Energy Technology Laboratory of the U.S. Department of Energy Website: [http://www.netl.doe.gov/publications/proceedings/01/carbon\\_seq/6c1.pdf](http://www.netl.doe.gov/publications/proceedings/01/carbon_seq/6c1.pdf).
- Grguric, B.A., Madsen, I.C., and Pring, A. (2001) Woodallite, a new chromium analogue of iowaite from the Mount Keith nickel deposit, Western Australia. *Mineralogical Magazine*, 65, 427-435.
- Hill, R.J., Canterford, J.H., and Moyle, F.J. (1982) New data for lansfordite. *Mineralogical Magazine*, 46, 453-457.
- Htoon, M. (1979) Geology of the Clinton Creek asbestos deposit, Yukon Territory. M.Sc. Thesis, University of British Columbia, Vancouver, British Columbia.
- Huot, F., Beaudoin, G., Hebert, R. Constantin, M., Bonin, G., and Dipple, G. (2003) Evaluation of Southern Quebec asbestos residues for CO<sub>2</sub> sequestration by mineral carbonation; preliminary results. Joint Annual Meeting of the Geological and Mineralogical Associations of Canada.
- Inaba, S., Minakawa, T., and Noto, Shigetoshi. (1985) Nesquehonite and dypingite from Shiraki, Mie Prefecture, Japan, 34, 281-287.
- Johnson, N.F. and Mossman, B.T. (2001) Dose, dimension, durability and biopersistence of chrysotile asbestos. In *The Health Effects of Chrysotile Asbestos: Contribution of Science to Risk-Management Decisions*, Canadian Mineralogist Special Publication 5, 145-154.

- Kazakov, A.V., Tikhomirova, M.M., and Plotonkova, V.I. (1959) The system of carbonate equilibria. *International Geology Review*, 1, 1-39.
- Langer, A.M. (2001) Health experience of some U.S. and Canadian workers exposed to asbestos: foundation for risk assessment. In *The Health Effects of Chrysotile Asbestos: Contribution of Science to Risk-Management Decisions*, Canadian Mineralogist Special Publication 5, 9-20.
- Langmuir, D. (1965) Stability of carbonates in the system MgO-CO<sub>2</sub>-H<sub>2</sub>O. *Journal of Geology*, 73, 730-754.
- MINFILE (2005) Cassiar, 104P 005. Retrieved April 2005 from the BC Ministry of Energy and Mines MINFILE Digital Data Website: <http://www.em.gov.bc.ca/cf/minfile/search/search.cfm?mode=capbib&minfilno=104P%20%20005>.
- Nashar, B. (1965) Barringtonite, a new hydrous MgCO<sub>3</sub> from Barrington Tops, New South Wales, Australia. *Mineralogical Magazine*, 34, 370-372.
- Raade, G. (1970) Dypingite, a new hydrous basic carbonate of magnesium, from Norway. *American Mineralogist*, 55, 1457-1465.
- Renaut, R.W. and Long, P.R. (1989) Sedimentology of the saline lakes of the Cariboo Plateau, Interior British Columbia, Canada. *Sedimentary Geology*, 64, 239-264.
- Stephan, G.W. and MacGillavry, C.H. (1972) The crystal structure of nesquehonite, MgCO<sub>3</sub>·3H<sub>2</sub>O. *Acta Crystallographica*, B28, 1031-1033.
- Suzuki, J. and Ito, M. (1973) New magnesium carbonate hydrate mineral Mg<sub>5</sub>(CO<sub>3</sub>)<sub>4</sub>(OH)<sub>2</sub>·8H<sub>2</sub>O, from Yoshikawa, Aichi Prefecture, Japan. *Ganseki Kobutsu Kosho Gakkaishi*, 68, 353-361.

- Wicks, F.J. and O'Hanley, D.S. (1988) Serpentine Minerals: Structures and Petrology. In Hydrous Phyllosilicates (Exclusive of Micas), edited by S.W. Bailey, Reviews in Mineralogy, Vol. 19 (Mineralogical Society of America), 91-167.
- Williams-Jones, A.E., Normand, C., Clark, J.R., Vali, H., Martin, R.F., Dufresne, A., and Nayeibzadeh, A. (2001) Controls of amphibole formation in chrysotile deposits: evidence from the Jeffrey Mine, Asbestos, Québec. In The Health Effects of Chrysotile Asbestos: Contribution of Science to Risk-Management Decisions, Canadian Mineralogist Special Publication 5, 89-104.
- Zedef, V., Russell, M.J., Fallick, A.E., and Hall, A.J. (2000) Genesis of vein stockwork and sedimentary magnesite and hydromagnesite deposits in the ultramafic terranes of Southwestern Turkey: A stable isotope study. Economic Geology, 95, 429-446.

**CHAPTER III:*****Isotopic characterization of magnesium-carbonate precipitates*****3.1 INTRODUCTION**

The source of CO<sub>2</sub> tapped in the formation of carbonate minerals can be determined using stable and radiogenic isotope techniques. In this chapter, isotope data for samples from the abandoned chrysotile mines at Clinton Creek, Yukon, and Cassiar, British Columbia are used to determine the sources for carbon and cations accessed in the precipitation of carbonates. Isotopic characterization of carbonate precipitates provides confirmation of net sequestration of carbon. The results of this analysis can be used with quantitative phase analysis (Chapter 4; Wilson *et al.* 2006) to give an initial estimate for the sequestration capacity of ultramafic mine tailings.

**3.2 EXPERIMENTAL METHOD****3.2.1 Light Stable Isotopes**

The fractionation of light stable isotopes in minerals can be used to identify the reservoir or reservoirs from which the constituent elements were drawn.  $\delta^{13}\text{C}$  and  $\delta^{18}\text{O}$  data (Craig 1959) for carbonate minerals can be used to identify the source of carbon

tapped during their precipitation (*eg.*, Kralik *et al.* 1989; Zedef *et al.* 2000; Deines 2004). As such, the fractionation of carbon and oxygen in hydrated magnesium carbonates and calcium carbonates can be used to determine whether atmospheric CO<sub>2</sub> is being crystallographically trapped in mine tailings. Stable carbon and oxygen isotope compositions were determined for 41 samples from Clinton Creek and Cassiar by J. Gabites using a Thermo Finnigan DeltaPlus XL LS-IRMS at the Pacific Centre for Isotopic and Geochemical Research (PCIGR), UBC. Carbonate samples (weighing from 10 to 100 mg) were treated with phosphoric acid in sealed gas exetainers after having been flushed with helium. The CO<sub>2</sub> produced in the reaction was carried by continuous flow of helium into the mass spectrometer. Carbon dioxide gas and calcite of known isotopic composition were run with the samples as reference standards to correct for machine fractionation. Raw values for  $\delta^{18}\text{O}/\delta^{16}\text{O}$  were corrected for fractionation between phosphoric acid and calcite or phosphoric acid and magnesite (for all Mg-carbonates). Replicate analyses were done on five samples to assess the reproducibility of the data. Measurement errors were determined from the averages of multiple analyses of NBS standards 18 and 19.

### **3.2.2 Radiogenic Carbon Fingerprinting**

Radiogenic carbon dates for five Mg-carbonate crust samples from Clinton Creek and Cassiar, three Ca-carbonate crusts from Cassiar were obtained with Accelerator Mass

Spectrometric (AMS) dating by Beta Analytic Radiocarbon Dating Laboratory in Miami, Florida. Samples underwent no laboratory pre-treatment prior to analysis.

### **3.2.3 Surface Area Analysis**

Surface-area analysis was done on A65-grade chrysotile from Cassiar with the BET N-gas adsorption isotherm technique using a Micromeritics ASAP 2010 surface area analyser in the Department of Earth and Ocean Sciences, at UBC.

## **3.3 RESULTS OF ISOTOPIC INVESTIGATION**

### **3.3.1 Stable Carbon and Oxygen Isotopes**

The  $\delta^{13}\text{C}$  results for carbonate samples from Clinton Creek and Cassiar (Table 3.1 and Fig. 3.1) vary from -8‰ to 15‰ (VPDB), with  $\delta^{18}\text{O}$  values ranging from 12‰ to 29‰ (VSMOW). A relationship between mineralogy, mode of carbonate occurrence, and  $\delta^{13}\text{C}$  is observed in the isotope data. Bedrock carbonate-rich samples from both sites yield  $\delta^{13}\text{C}$  values in the range of -8.0‰ to 0.7‰ (VPDB) and  $\delta^{18}\text{O}$  values between 12‰ and 16‰. These samples are mostly bedrock dolomite from Cassiar and magnesite from Clinton Creek. It is notable that the aragonite and calcite cobble coatings and streambed precipitates plot in the same region of  $\delta^{18}\text{O}$ - $\delta^{13}\text{C}$ -space as the bedrock carbonates. Bulk

TABLE 3.1: Mineralogical and isotopic data for carbonate samples.

SAMPLE	MODE	MAJOR PHASE <sup>†</sup>	MINOR PHASES <sup>†</sup>	$\delta^{13}\text{C}$	$2\sigma_{\delta^{13}\text{C}}$	$\delta^{18}\text{O}$	$2\sigma_{\delta^{18}\text{O}}$	$\text{F}^{14}\text{C}$ or $^{14}\text{C}^*$ DATE
03CC01A	Bulk*	Dyp/Hymag	Dol, Mags, Pyro	3.322	0.128	19.854	0.094	
03CC01B	Crust	Nesq	Dyp, Cal, Mags, Pyro	14.528	0.092	25.699	0.063	1.114 ± 0.006
03CC01C	Bulk*	Dyp	Mags, Pyro	-0.025	0.137	17.568	0.098	
03CC0201A	Bulk*	Hymag	Dol, Mags, Pyro	-2.159	0.277	16.280	0.207	
03CC0401B	Cobble	Dyp	Mags, Pyro	8.638	0.173	18.176	0.126	
03CC0601B	Bulk	Dyp/Hymag	Mags, Pyro	4.306	0.204	19.522	0.124	
03CC0701A	Bulk*	Nesq	Dol, Mags, Pyro	-5.141	0.482	15.518	0.342	
03CC1001A	Bulk*	Dyp/Hymag	Cal, Dol, Mags, Pyro	3.871	0.147	20.493	0.141	
04CC0104	Bedrock	Mags	Pyro	-7.994	0.070	15.066	0.104	> 46 kyBP
04CC0105	Cobble	Dyp, Hymag, Pyro		-1.617	0.208	19.021	0.132	1.026 ± 0.005
04CC0106	Crust	Nesq	Dyp	7.489	0.139	20.820	0.143	
04CC0107-CA	Cobble	Arag		0.022	0.107	15.605	0.143	
04CC0108-CA	Cobble	Arag	Pyro	0.687	0.108	15.123	0.159	
04CC0109	Cobble	Dyp	Pyro	1.957	0.191	20.754	0.289	
04CC0111	Crust	Not detected		-3.200	0.324	13.136	0.374	
04CC0201A	Crust	Nesq	Dyp, Lans, Pyro	10.369	0.236	25.215	0.196	
04CC0202A	Crust	Dyp		9.828	0.227	27.711	0.135	
04CC0301	Bedrock	Mags	Dol	-6.809	0.170	15.837	0.119	
04CC0401-CA	Cobble	Dyp	Mags, Pyro	-1.454	0.076	17.419	0.103	
04CC0601A	Crust	Dyp	Mags, Pyro	4.431	0.147	20.693	0.120	1.156 ± 0.006
04CC0601B-CA	Cobble	Hymag, Dyp?	Pyro	2.074	0.192	22.966	0.220	
04CC0601B-CB	Cobble	Dyp		6.610	0.107	20.969	0.106	
04CC0701	Crust	Nesq	Dyp, Hymag, Pyro	10.447	0.077	22.114	0.060	
04CC0701	Crust	Nesq	Dyp, Hymag, Pyro	10.062	0.086	22.024	0.164	
04CC0702	Spire	Nesq	Dyp, Hymag	7.799	0.172	23.502	0.145	
04CC0703	Crust	Nesq	Dyp, Hymag	13.185	0.296	23.896	0.214	
04CC0703	Crust	Nesq	Dyp, Hymag	13.597	0.146	23.772	0.087	
04CC0703-nesq	Crust	Nesq	Dyp, Hymag	13.320	0.098	22.574	0.103	
04CC0703-hymag	Crust	Hymag	Dyp, Nesq	4.330	0.066	18.302	0.096	
04CC0901	Crust	Dyp, Pyro		6.678	0.181	28.495	0.171	
04CC1001	Crust	Nesq	Dyp/Hymag, Mags	11.256	0.276	24.821	0.208	
04CC1101	Crust	Nesq	Dyp/Hymag	12.530	0.146	23.991	0.116	
04CC1201	Crust	Dyp, Hymag	Mags	3.481	0.264	22.537	0.253	
04CC1301	Bedrock	Mags	Dol	-4.481	0.109	15.664	0.046	
04CC1301	Bedrock	Mags	Dol	-4.344	0.069	15.448	0.061	
04CC1401	Bulk	Hymag	Mags/Pyro	-5.565	0.102	16.180	0.130	
03CA1601	Bulk	Cal/Dol		-2.119	0.233	18.847	0.301	
04CA0101	Crust	Arag		-7.017	0.515	12.842	0.658	2790 ± 40 yBP
04CA0202-CA	Cobble	Cal/Dol						1560 ± 40 yBP
04CA0202-CB	Cobble	Cal/Arag		-0.509	0.134	13.875	0.133	
04CA0202-CC	Cobble	Cal/Dol		0.474	0.477	15.057	0.326	
04CA0202-CC	Cobble	Cal/Dol		0.736	0.252	15.530	0.180	
04CA0202-CD	Cobble	Cal/Arag		0.351	0.318	14.889	0.310	
04CA0202-CD	Cobble	Cal/Arag		0.720	0.080	15.799	0.111	
04CA0301-CA	Cobble	Cal	MC	-5.576	0.188	12.098	0.179	
04CA0601	Crust	Nesq	Dyp	8.429	0.137	26.519	0.191	1.072 ± 0.005
04CA1001	Stream	Cal	Arag	-3.543	0.168	12.636	0.180	9840 ± 40 yBP

\* Denotes major contamination by bedrock carbonates due to extremely low concentration of hydrated magnesium carbonate material

† Arag – Aragonite, Cal – Calcite, Dol – Dolomite, Dyp – Dypingite, Hymag – Hydromagnesite, Lans – Lansfordite, Mags – Magnesite, MC – Monohydrocalcite, Nesq – Nesquehonite, Pyro – Pyroaurite.

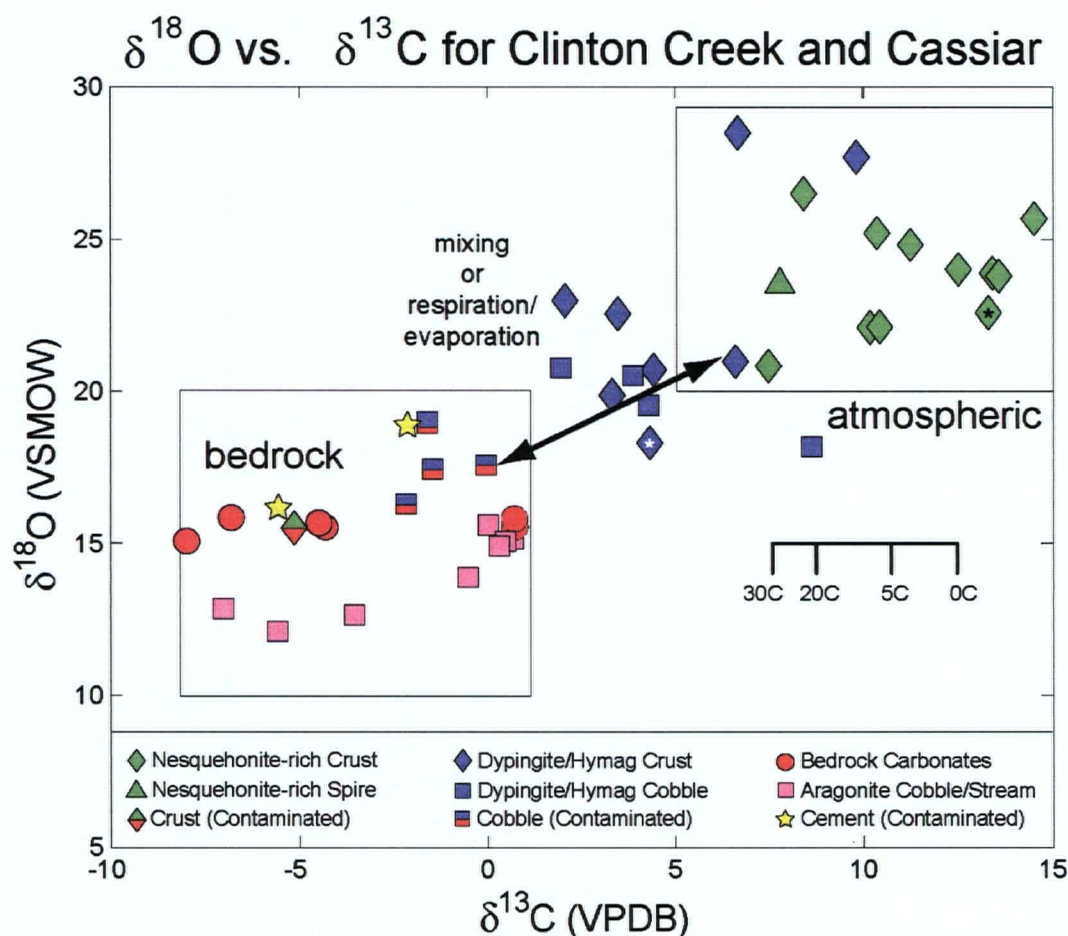


FIGURE 3.1: Stable oxygen and carbon isotope data by mode of carbonate occurrence and mineralogy. Temperature effect for fractionation of carbon is calculated after the method of Deines (2004) for magnesite. The scale for temperature fractionation is given for the typical range of non-freezing temperatures at Clinton Creek and Cassiar. The symbols marked with asterisks represent data collected for the nesquehonite and dypingite/hydromagnesite zones in sample 04CC0703.  $2\sigma$  measurement errors are smaller than the symbols employed.



tailings containing hydromagnesite cement or minor hydrated Mg-carbonates from Clinton Creek tend to plot in this region as well. These samples all contain a significant amount of pyroaurite  $\pm$  magnesite contamination which could lead to a reduction in  $\delta^{13}\text{C}$ . Generally, dypingite cobble coatings and vertical crusts are isotopically heavier than bedrock carbonates, being characterized by  $-2.1\text{‰} \leq \delta^{13}\text{C} \leq 6.7\text{‰}$  and  $16\text{‰} \leq \delta^{18}\text{O} \leq 28\text{‰}$ . Nesquehonite-rich spires and vertical crusts are further-enriched in both  $\delta^{13}\text{C}$  and  $\delta^{18}\text{O}$ , falling in the range of  $4.3\text{‰} \leq \delta^{13}\text{C} \leq 15\text{‰}$  and  $24\text{‰} \leq \delta^{18}\text{O} \leq 29\text{‰}$ .

### 3.3.2 Radiogenic Carbon

Radiogenic  $^{14}\text{C}$  can be used as an indicator for modern precipitation of carbonate minerals. Due to the artificial enrichment of atmospheric  $^{14}\text{C}$  caused by nuclear testing in the mid-twentieth century (the so-called “Bomb Effect”), minerals precipitated from atmospheric  $\text{CO}_2$  will contain a greater proportion of  $^{14}\text{C}$  than the 1950 AD reference standard (Reimer *et al.* 2004). Radiogenic carbon dating relies upon the relative proportion of radiogenic to stable isotopes in a sample to be less than or equal to the 1950 reference ratio in order to obtain ages. Values of this ratio in excess of the reference can only be expressed as a fraction of the modern value (*i.e.*, the value for 1950). The level of bomb  $^{14}\text{C}$  in the atmosphere reached a global equilibrium in the late 1960s (Telegadas 1971), significantly decreasing the difference between  $^{14}\text{C}$  readings from distant sampling locations. The amount of  $^{14}\text{C}$  in the atmosphere has been steadily decreasing due primarily to exchange with the Earth’s oceans (Rafter and Fergusson

1957) and by dilution from the Suess Effect (Suess 1955). As such, younger carbonate precipitates will have increasingly lower values of  $F^{14}\text{C}$  (*i.e.*, the Fraction Modern Carbon, as defined by Reimer *et al.* 2004).

There is potential that more than one source of carbon is being tapped in the precipitation of modern carbonate minerals. For instance, a hydrated magnesium carbonate mineral may contain 95% atmospheric carbon and 5% carbon derived from the dissolution of bedrock carbonates. Most bedrock is older than 40 ka, containing  $^{14}\text{C}$  below detection limits, and cannot be dated with radiocarbon techniques – as such it is considered to effectively contain zero  $^{14}\text{C}$ . Because the amount of  $^{14}\text{C}$  in the atmosphere has been decreasing over the past forty years, dilution of the  $^{14}\text{C}$  content of a modern carbonate sample gives a lower value for  $F^{14}\text{C}$  and consequently a younger date of precipitation.

Radiogenic  $^{14}\text{C}$  analysis of hydrated magnesium carbonate samples from Clinton Creek and Cassiar provides values of  $F^{14}\text{C}$  ranging from 1.02 to 1.15 for cobble coatings and vertical crusts. These results suggest a post-1950 (*i.e.*,  $F^{14}\text{C} > 1$ ) date of formation for carbonate minerals and confirm that carbonate precipitation occurred after mining. Although analysis yields modern atmospheric signatures, minor dilution of modern  $^{14}\text{C}$  by bedrock carbonate may be occurring in these samples.

The negligible amount of  $^{14}\text{C}$  remaining in the magnesite sample from Clinton Creek (04CC0104) implies that it is bedrock carbonate, likely having formed from listwanite alteration of the serpentinite. The aragonite/calcite samples from Cassiar (04CA0101, 04CA0202-CA, and 04CA1001) give radiocarbon dates corresponding to

precipitation  $2790 \pm 40$  years before present (yBP),  $1560 \pm 40$  yBP, and  $9840 \pm 40$  yBP, respectively. Despite the radiocarbon dates associated with the Ca-carbonate samples, field observations suggest that their formation was recent.

### 3.4 DETERMINATION OF THE SOURCE OF CARBON

There exist three sources for carbon in mine tailings, one or more of which may have been tapped during mineral carbonation: 1) Bedrock carbon from mined carbonates; 2) Atmospheric carbon from meteoric precipitation, and 3) Organic carbon from mined organic sediments or microbial pathways.

The fractionation of the stable isotopes of carbon and oxygen in carbonate minerals can be used to identify the source of  $\text{CO}_2$  tapped in the precipitation of these minerals. Negative values for  $\delta^{13}\text{C}$  in the range of  $+1\text{‰}$  to  $-8\text{‰}$  with  $\delta^{18}\text{O}$  between  $10\text{‰}$  and  $20\text{‰}$  often reflect the isotopic compositions of metamorphic (bedrock) magnesite (Kralik *et al.* 1989; Hansen 2005). Moderately high, positive values of  $\delta^{13}\text{C}$  and  $\delta^{18}\text{O}$  are typical of carbonates that have formed at low-temperature from atmosphere-derived  $\text{CO}_2$  (*e.g.*, Kralik *et al.* 1989; Zedef *et al.* 2000). The temperature-dependence of the carbon fractionation effect in magnesium carbonates (Fig. 3.1) was calculated using the theoretical results of Deines (2004), using magnesite in equilibrium with the atmosphere ( $-8\text{‰} \leq \delta^{13}\text{C} \leq -7\text{‰}$ ) as a proxy for the hydrated magnesium carbonates. Temperature-dependence of carbon fractionation covers the range of values from  $\sim 7\text{‰}$  to  $\sim 12\text{‰}$  for 0-

30 °C (Fig. 3.1), spanning the typical range of non-freezing temperature conditions for Clinton Creek and Cassiar.

Surface precipitates with abnormally low  $\delta^{13}\text{C}$ -values in the range of 0‰ to 5‰ and with  $\delta^{18}\text{O}$  between 18‰ and 24‰ have been documented by Knauth *et al.* (2003). Knauth *et al.* (2003) have described  $\delta^{13}\text{C}$ -depletion in atmospherically-sourced caliche on basaltic lava flows in the San Francisco volcanic field, Arizona, USA. In the course of their studies, Knauth *et al.* (2003) identified an isotopic distinction between pedogenic calcitic caliche that had developed in heavily weathered basaltic soils and subaerial calcitic caliche on recent (< 900 yBP) basaltic flows. Pedogenic caliche gave rise to values of  $-9\text{‰} \leq \delta^{13}\text{C} \leq -4\text{‰}$  and  $13\text{‰} \leq \delta^{18}\text{O} \leq 32\text{‰}$ , while subaerial caliche was characterized by  $4\text{‰} \leq \delta^{13}\text{C} \leq 15\text{‰}$  and  $24\text{‰} \leq \delta^{18}\text{O} \leq 32\text{‰}$ .

A positive correlation between  $\delta^{18}\text{O}$  and  $\delta^{13}\text{C}$  is observed for caliche developed on basalts at three locations in Arizona. A correlation between  $\delta^{18}\text{O}$  and  $\delta^{13}\text{C}$  data for pedogenic caliche has also been observed by Schlesinger *et al.* (1998), who argue that the isotopically heaviest samples formed when the soil horizon experienced the greatest exposure to atmospheric  $\text{CO}_2$  and during times of significant water loss due to evaporation. They suggested that covariation reflects a transition to soil atmospheres increasingly dominated by microbial  $\text{CO}_2$  at depth with soil waters that are less affected by evaporative enrichment in  $^{18}\text{O}$ .

Knauth *et al.* (2003) speculate that the isotopically intermediate caliche developed within the soil horizon in contact with respired carbon and with less exposure

to the atmosphere than the subaerial caliche (which developed in an evaporative environment, drawing exclusively on the atmospheric carbon reservoir).

From inspection of Figure 3.1, most nesquehonite-rich crust and spire samples can be interpreted as having an atmospheric source of  $\text{CO}_2$ , based on enrichment in  $\delta^{13}\text{C}$  and  $\delta^{18}\text{O}$ . Most data for nesquehonite-rich samples fall into the range of values explained by temperature-dependent fractionation. Samples for which the major carbonate phases include calcite, aragonite, dolomite, magnesite, and pyroaurite give typical bedrock to organic signatures. Crusts and cobble coatings contaminated by bedrock carbonate plot within or near the region populated by the bedrock carbonate samples. This result is consistent with the bedrock carbonate content observed in X-ray diffractograms for these samples. Uncontaminated dypingite  $\pm$  hydromagnesite crusts and cobbles plot in a distinct region that could reflect either a mixing line between atmospheric carbon and bedrock carbon sources or an atmospheric source with an intermediate-caliche or soil-like signature. In the former case, dissolution of bedrock carbonates may play a role in the precipitation of dypingite. Under this interpretation, for each mole of bedrock carbonate consumed in reaction at low temperatures, one mole of atmospheric  $\text{CO}_2$  is required to precipitate new carbonate (Faure 1986). As such, the relative scarcity of bedrock carbonate at Cassiar may be a contributing factor to the less-than vigorous rate of carbonation in the tailings pile. In the case that hydrated magnesium carbonate phases are being reprecipitated from dissolved bedrock carbonate, one mole of atmospheric  $\text{CO}_2$  would be required to precipitate one mole of hydrated magnesium carbonate. With each cycle of dissolution and reprecipitation, the bedrock

carbon would be diluted by an additional 50% atmospheric carbon (Fig. 3.2). Although this model for precipitation has the potential to bind as much atmospheric carbon as the model for 100%-atmospheric precipitation (Fig. 3.3), it does not lead to a net increase in mineralogically-bound CO<sub>2</sub>. Precipitation at the end of each dissolution cycle releases an amount of bedrock carbon equal to the amount of atmospheric carbon trapped.

The ambiguity in the  $\delta^{13}\text{C}$  data for dypingite can be resolved using radiogenic  $^{14}\text{C}$ . Fraction modern values above unity correspond distinctly to modern atmospheric CO<sub>2</sub>. As a result, samples containing dissolved bedrock carbonate will give  $F^{14}\text{C} < 1$ . Sample data fall within two isotopically distinct fields when  $\delta^{13}\text{C}$  is plotted against  $F^{14}\text{C}$  (Fig. 3.4). The first field is populated by bedrock carbon (with  $F^{14}\text{C} = 0$  and  $\delta^{13}\text{C} < 0$ ) and aragonite/calcite precipitates (with  $F^{14}\text{C} \leq 0.5$  and  $\delta^{13}\text{C} < 0$ ). The second field contains two uncontaminated crusts of nesquehonite, one uncontaminated crust of dypingite, and one dypingite/hydromagnesite crust with minor pyroaurite contamination. Despite the wide spread in  $\delta^{13}\text{C}$ -values, these hydrated magnesium carbonate samples all have modern atmospheric  $^{14}\text{C}$ -signatures. No clear trend between bedrock and hydrated magnesium carbonates is detectable, while a mixing line is clearly present between bedrock and Ca-carbonate precipitates. The lack of a mixing trend between the modern and bedrock populations suggests that precipitation of hydrated magnesium carbonate efflorescences is not driven by the dissolution of bedrock carbonate. Hydrated magnesium carbonate efflorescences have tapped the atmospheric carbon reservoir. Depletion in  $^{13}\text{C}$  is microbially mediated, giving rise to soil-like stable isotope signatures. The marked differences in mineralogy and isotopic signatures observed in Mg-carbonate

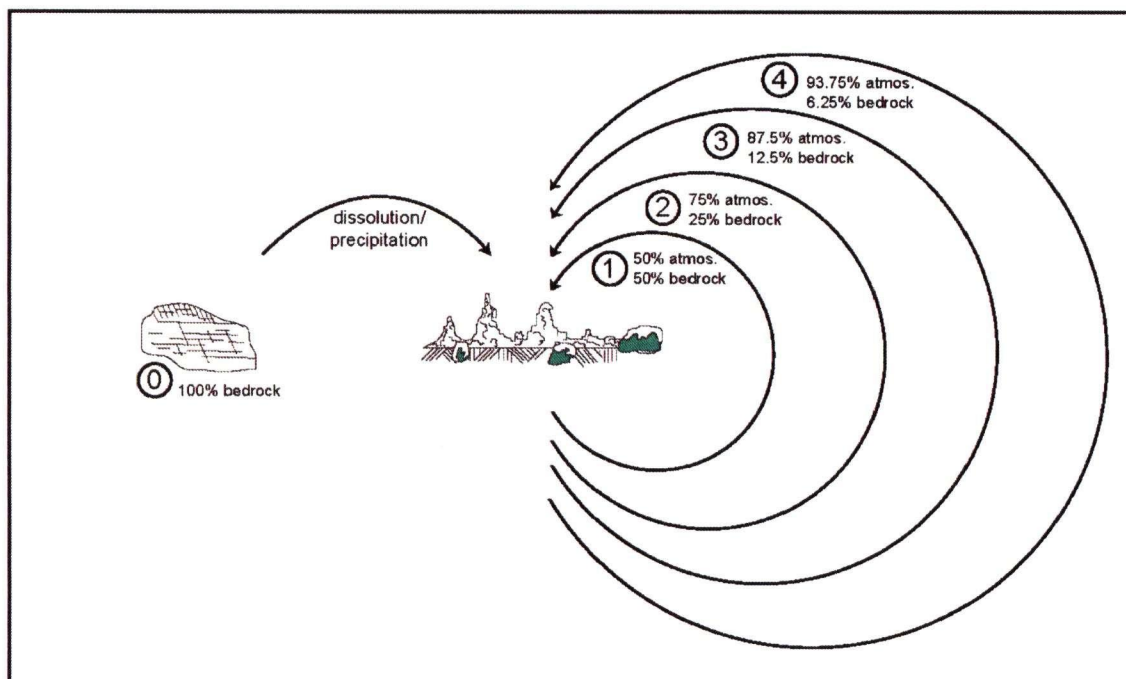


FIGURE 3.2: Worst-case scenario for carbonate stability in mine tailings: Carbonate efflorescences may precipitate cyclically from dissolved bedrock carbonate minerals. With each cycle, the original bedrock  $^{14}\text{C}$ -signature becomes increasingly enriched by addition of atmospheric carbon. After six or seven cycles, such carbonate could be indistinguishable from carbonate precipitated directly from atmospheric carbon.

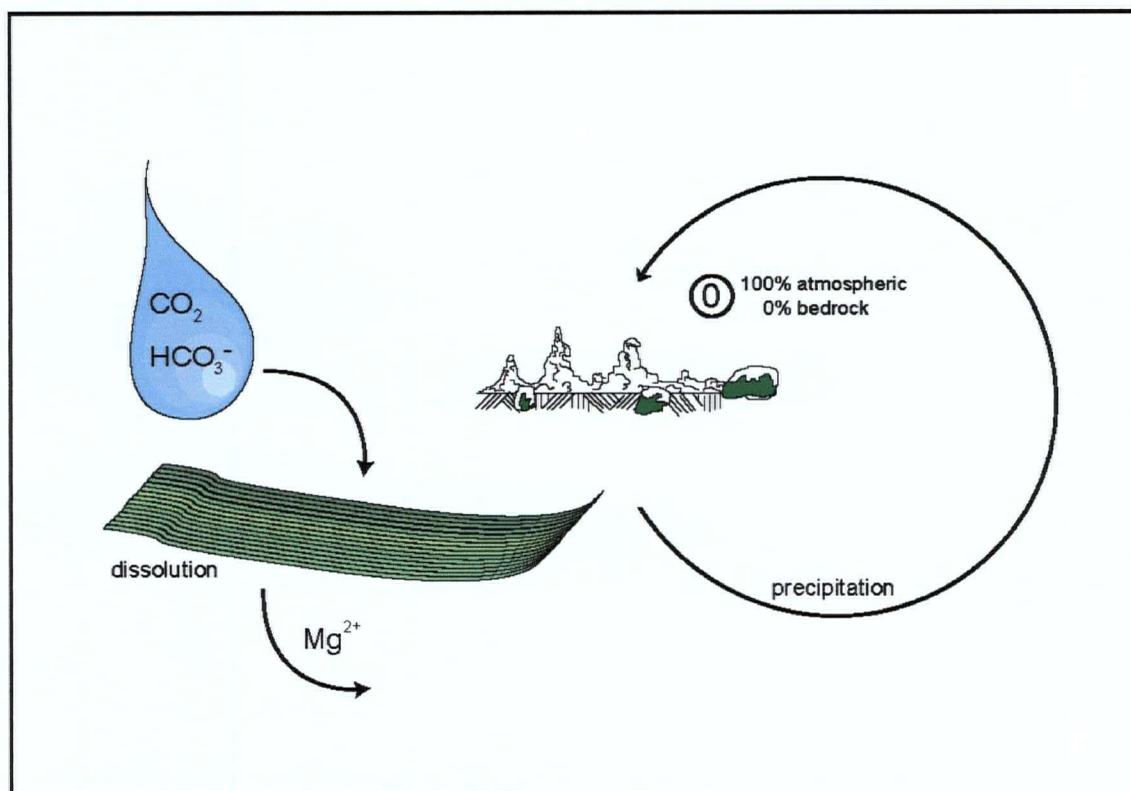


FIGURE 3.3: Best-case scenario model for hydrated magnesium carbonate formation in mine tailings. An atmospheric source of carbon dioxide and a bedrock silicate source for magnesium guarantee sequestration of carbon.



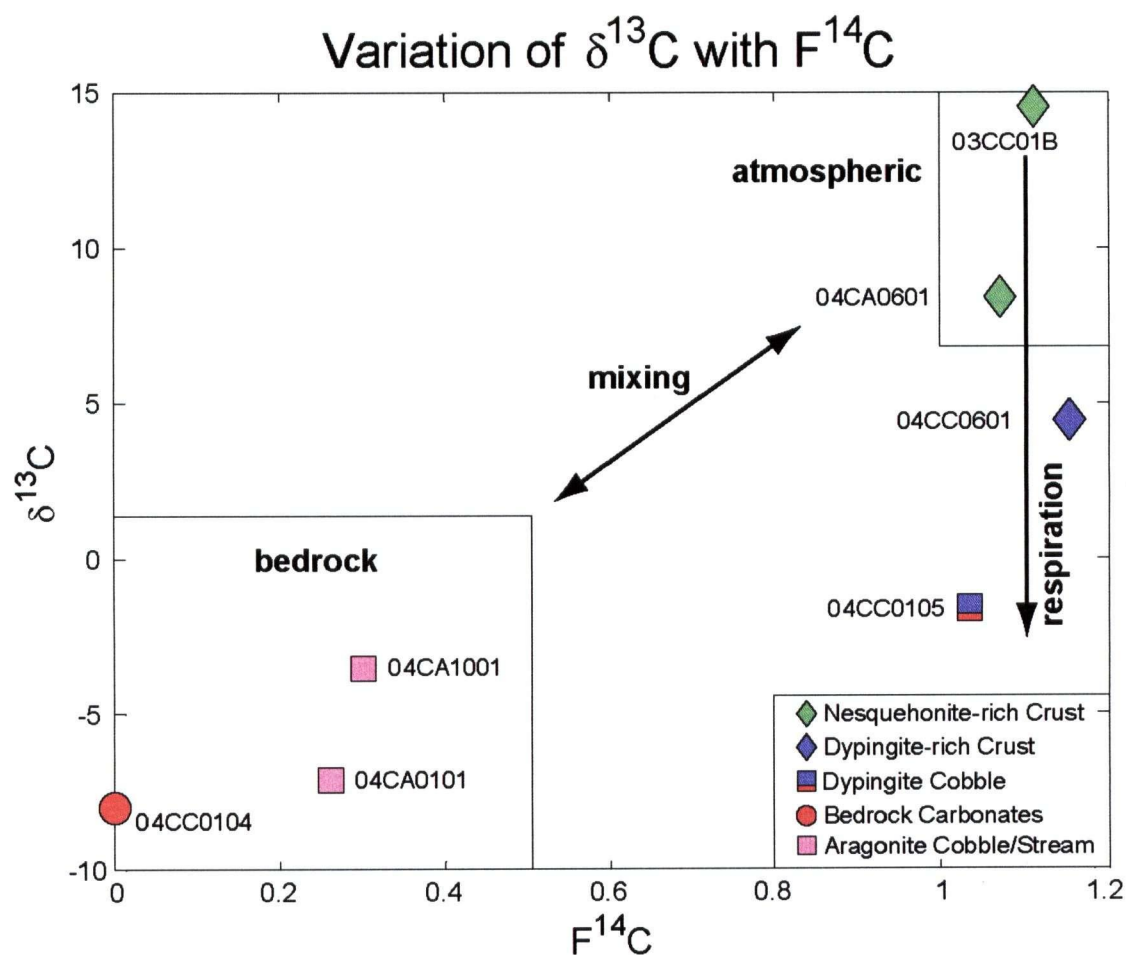


FIGURE 3.4: Variation of  $\delta^{13}\text{C}$  with  $F^{14}\text{C}$  for seven samples from Cassiar and Clinton Creek. No mixing line is present between the bedrock and atmospheric carbonate samples, indicating that the precipitation of hydrated magnesium carbonates is not driven by the dissolution of bedrock carbonate.

precipitates at Clinton Creek and Cassiar reflect at least two separate pathways for formation: An abiotic, atmospheric pathway for lansfordite and nesquehonite and a microbially-mediated pathway for dypingite and hydromagnesite. Microbially-mediated precipitation of hydromagnesite and magnesite has been proposed by Renaut and Stead (1991) and Braithwaite and Zedef (1996). Power and Southam (2005) have shown that hydromagnesite and/or dypingite precipitate in association with cyanobacteria in Mg-rich water, whereas under similar yet abiotic conditions, only nesquehonite forms.

The high cost associated with radiocarbon dating precludes its regular use as a diagnostic tool. Ideally, stable carbon and oxygen isotope techniques can be calibrated to reflect the definitive results provided by radiocarbon dating for confirmation of an atmospheric source for carbon. In terms of calibrating stable isotope data for the identification of modern, atmospheric carbonate minerals, values for  $\delta^{13}\text{C} \geq 7\text{‰}$  with  $\delta^{18}\text{O} \geq 20\text{‰}$  can be considered definitive evidence of an atmospheric origin for  $\text{CO}_2$ , while values in the range of  $2\text{‰} \leq \delta^{13}\text{C} \leq 7\text{‰}$  and  $17\text{‰} \leq \delta^{18}\text{O} \leq 20\text{‰}$  are very likely indicative of atmospheric carbon. Samples giving values of  $\delta^{13}\text{C} < 2\text{‰}$  with  $\delta^{18}\text{O} < 17\text{‰}$  may be either bedrock or atmospheric carbonates contaminated by bedrock carbonate.

### 3.5 THE SOURCE FOR CATIONS

Final confirmation that the dissolution of bedrock carbonate does not drive the precipitation of carbonate efflorescences must come from the identification of the cation

source. Should the cations be sourced from dissolved bedrock carbonate, one molecule of  $\text{CO}_2$  would be released during dissolution of bedrock carbonate for every molecule bound in the reprecipitated mineral. Although a carbonate that has been through several cycles of dissolution and reprecipitation could give an atmospheric carbon signature (Fig. 3.2), no additional sequestration occurs for a bedrock source of cations.

The only available sources for the  $\text{Ca}^{2+}$  in calcium carbonate precipitates are bedrock dolomite and calcite. Calcium carbonate precipitates are isotopically distinct from the hydrated magnesium carbonates in  $\delta^{13}\text{C}$ ,  $\delta^{18}\text{O}$ , and  $\text{F}^{14}\text{C}$ . These samples plot on a mixing line between bedrock and atmospheric populations (Fig. 3.4), defining the isotopic field for bedrock dissolution. Calcium-carbonate precipitates are strictly the result of the reprecipitation of bedrock carbonate.

Several bedrock sources exist for  $\text{Mg}^{2+}$  in hydrated magnesium carbonate precipitates: dolomite, magnesite, chrysotile, antigorite, and lizardite. Sequestration can only occur in magnesium carbonates for a silicate source of magnesium. Although silicate minerals typically dissolve more slowly than carbonates in mine tailings environments (*e.g.*, Nesbitt and Jambor 1998), surface area, grain size, mineral content, porewater composition and pH, and deviation from equilibrium conditions have a significant effect on the total amount of dissolution.

A simple model can be developed to estimate the order of magnitude difference in geometric surface area between magnesium-bearing carbonate grains and the surface area of the serpentine-group weight fraction in a bulk tailings sample. Geometric surface area is used to estimate an upper limit for reactive surface area, which is typically smaller

than geometric and BET surface areas. Approximating tailings grains as cubes with perfectly smooth surfaces and assuming zero porosity (*i.e.*, perfect packing), an approximation of the surface area per gram of material can be calculated for typical sieve-size fractions (as in Chapter 2). The median value for successive sieve sizes was used to approximate the grain size for the smaller of two size fractions. From this value, the surface area per gram of the tailings grains can be estimated (Table 3.2).

BET N-gas absorption isotherm grain size analysis of chrysotile fibres from Cassiar gives a surface area of  $17.45 \text{ m}^2/\text{g}$  (J. Thom, pers. comm.). The fibres provide an increase in surface area of 4 orders of magnitude over the area calculated for grains of medium sand (Udden-Wentworth scale). The non-fibrous fraction of sample 04CC1401 from Clinton Creek (which was wet-sieved for grain size analysis in Chapter 2) has a surface area on the order of  $1.8 \times 10^{-3} \text{ m}^2/\text{g}$ . The non-fibrous fraction for sample 03CC1601 from Cassiar gives a surface area on the order of  $2.4 \times 10^{-3} \text{ m}^2/\text{g}$ . The fibrous fraction of the same bulk samples has a surface area of  $17.45 \text{ m}^2/\text{g}$  – an increase of 4 orders of magnitude. Although the contribution of massive, non-fibrous serpentine generally outweighs that of chrysotile fibres by an order of magnitude, its contribution to surface area is comparatively small and can be neglected in further calculations.

Assuming negligible microporosity in the carbonate grains in the tailings, and using the grain size distribution (Chapter 2) and mineral composition (Chapter 4, Wilson *et al.* 2006) from 04CC1401 (Table 3.2), the average surface area per gram of magnesium carbonate in a typical sample of bulk tailings is in the range of  $0.0020 \text{ g}/\text{cm}^2$ . The surface area per gram of chrysotile fibres is 4 orders of magnitude larger than that

TABLE 3.2: Estimates for surface area of mineral phases in bulk tailings samples.

	Size Fraction (mm)	Fraction Mass (g)	Mean Grain Size (mm)	Surface Area per Grain (m <sup>2</sup> )	Volume per Grain (m <sup>3</sup> )	Grains per g of Tailings (g <sup>-1</sup> )	Area per Gram (m <sup>2</sup> /g)	Area for Mg-Silicates (m <sup>2</sup> /g)	Area for Carbonates (m <sup>2</sup> /g)	Area for Other Phases (m <sup>2</sup> /g)	Area per Size Fraction (m <sup>2</sup> )	Total Area (m <sup>2</sup> )
03CA1601	> 16.0	199.7	1.60x10 <sup>-2</sup>	8.04x10 <sup>-4</sup>	2.14x10 <sup>-6</sup>	1.67x10 <sup>-1</sup>	1.34x10 <sup>-4</sup>	2.34x10 <sup>-2</sup>	6.85x10 <sup>-4</sup>	2.62x10 <sup>-3</sup>	2.67x10 <sup>-2</sup>	11.3
	> 9.50	377.3	1.28 x10 <sup>-2</sup>	5.11x10 <sup>-4</sup>	1.09x10 <sup>-6</sup>	3.29x10 <sup>-1</sup>	1.68x10 <sup>-4</sup>	5.56x10 <sup>-2</sup>	1.62x10 <sup>-3</sup>	6.2x10 <sup>-3</sup>	6.34x10 <sup>-2</sup>	
	> 4.76	854.7	7.13 x10 <sup>-3</sup>	1.60x10 <sup>-4</sup>	1.90x10 <sup>-7</sup>	1.88	3.01x10 <sup>-4</sup>	2.25x10 <sup>-1</sup>	6.58x10 <sup>-3</sup>	2.52x10 <sup>-2</sup>	2.57x10 <sup>-1</sup>	
	>2.00	953.7	3.38 x10 <sup>-3</sup>	3.59x10 <sup>-5</sup>	2.02x10 <sup>-8</sup>	1.77x10 <sup>1</sup>	6.34x10 <sup>-4</sup>	5.30x10 <sup>-1</sup>	1.55x10 <sup>-2</sup>	5.93x10 <sup>-2</sup>	6.05x10 <sup>-1</sup>	
	>0.850	758.5	1.43 x10 <sup>-3</sup>	6.38x10 <sup>-6</sup>	1.52x10 <sup>-9</sup>	2.36x10 <sup>2</sup>	1.50x10 <sup>-3</sup>	9.99x10 <sup>-1</sup>	2.92x10 <sup>-2</sup>	1.12x10 <sup>-1</sup>	1.14	
	>0.425	343.5	6.38 x10 <sup>-4</sup>	1.28x10 <sup>-6</sup>	1.36x10 <sup>-10</sup>	2.63x10 <sup>3</sup>	3.36x10 <sup>-3</sup>	1.01	2.96x10 <sup>-2</sup>	1.13x10 <sup>-1</sup>	1.15	
	>0.212	256.7	3.19x10 <sup>-4</sup>	3.19x10 <sup>-7</sup>	1.69x10 <sup>-11</sup>	2.11x10 <sup>4</sup>	6.73x10 <sup>-3</sup>	1.51	4.42x10 <sup>-2</sup>	1.69x10 <sup>-1</sup>	1.73	
	>0.150	97.4	1.81x10 <sup>-4</sup>	1.03x10 <sup>-7</sup>	3.10x10 <sup>-12</sup>	1.15x10 <sup>5</sup>	1.18x10 <sup>-2</sup>	1.01	2.95x10 <sup>-2</sup>	1.13x10 <sup>-1</sup>	1.15	
	>0.106	93.7	1.28x10 <sup>-4</sup>	5.15x10 <sup>-8</sup>	1.10x10 <sup>-12</sup>	3.25x10 <sup>5</sup>	1.67x10 <sup>-2</sup>	1.37	4.02x10 <sup>-2</sup>	1.54x10 <sup>-1</sup>	1.57	
	>0.075	75.1	9.05x10 <sup>-5</sup>	2.57x10 <sup>-8</sup>	3.88x10 <sup>-13</sup>	9.20x10 <sup>5</sup>	2.37x10 <sup>-2</sup>	1.56	4.55x10 <sup>-2</sup>	1.74x10 <sup>-1</sup>	1.78	
	>0.053	53.9	6.40x10 <sup>-5</sup>	1.29x10 <sup>-8</sup>	1.37x10 <sup>-13</sup>	2.60x10 <sup>6</sup>	3.35x10 <sup>-2</sup>	1.58	4.62x10 <sup>-2</sup>	1.77x10 <sup>-1</sup>	1.80	
	<0.053	68.9	5.30x10 <sup>-5</sup>	8.82x10 <sup>-9</sup>	7.79x10 <sup>-14</sup>	4.58x10 <sup>6</sup>	4.04x10 <sup>-2</sup>	2.44	7.13x10 <sup>-2</sup>	2.73x10 <sup>-1</sup>	2.79	
	<b>Fibre</b>						17.45					8856
04CC1401	>9.51	255.8	9.51x10 <sup>-3</sup>	2.84x10 <sup>-4</sup>	4.50x10 <sup>-7</sup>	7.93x10 <sup>-1</sup>	2.25x10 <sup>-4</sup>	5.09x10 <sup>-2</sup>	1.78x10 <sup>-3</sup>	4.93x10 <sup>-3</sup>	5.76x10 <sup>-2</sup>	3.36
	>1.68	807.1	5.60x10 <sup>-3</sup>	9.83x10 <sup>-5</sup>	9.17x10 <sup>-8</sup>	3.89	3.83x10 <sup>-4</sup>	2.73x10 <sup>-1</sup>	9.55x10 <sup>-3</sup>	2.6x10 <sup>-2</sup>	3.09x10 <sup>-1</sup>	
	>1.41	107.3	1.55x10 <sup>-3</sup>	7.50x10 <sup>-6</sup>	1.93x10 <sup>-9</sup>	1.85x10 <sup>2</sup>	1.39x10 <sup>-3</sup>	1.31x10 <sup>-1</sup>	4.60x10 <sup>-3</sup>	1.27x10 <sup>-2</sup>	1.49x10 <sup>-1</sup>	
	>0.840	208.4	1.13x10 <sup>-3</sup>	3.98x10 <sup>-6</sup>	7.45x10 <sup>-10</sup>	4.79x10 <sup>2</sup>	1.90x10 <sup>-3</sup>	3.51x10 <sup>-1</sup>	1.23x10 <sup>-2</sup>	3.40x10 <sup>-2</sup>	3.97x10 <sup>-1</sup>	
	>0.595	132.1	7.18x10 <sup>-4</sup>	1.62x10 <sup>-6</sup>	1.93x10 <sup>-10</sup>	1.85x10 <sup>3</sup>	2.99x10 <sup>-3</sup>	3.49x10 <sup>-1</sup>	1.22x10 <sup>-2</sup>	3.38x10 <sup>-2</sup>	3.95x10 <sup>-1</sup>	
	>0.350	155.8	4.73x10 <sup>-4</sup>	7.01x10 <sup>-7</sup>	5.52x10 <sup>-11</sup>	6.47x10 <sup>3</sup>	4.54x10 <sup>-3</sup>	6.24x10 <sup>-1</sup>	2.18x10 <sup>-2</sup>	6.05x10 <sup>-2</sup>	7.07x10 <sup>-1</sup>	
	>0.212	80.7	2.81x10 <sup>-4</sup>	2.48x10 <sup>-7</sup>	1.16x10 <sup>-11</sup>	3.07x10 <sup>4</sup>	7.63x10 <sup>-3</sup>	5.44x10 <sup>-1</sup>	1.90x10 <sup>-2</sup>	5.27x10 <sup>-2</sup>	6.15x10 <sup>-1</sup>	
	>0.180	10.5	1.96x10 <sup>-4</sup>	1.21x10 <sup>-7</sup>	3.94x10 <sup>-12</sup>	9.06x10 <sup>4</sup>	1.09x10 <sup>-2</sup>	1.01x10 <sup>-1</sup>	3.55x10 <sup>-3</sup>	9.83x10 <sup>-3</sup>	1.15x10 <sup>-1</sup>	
	>0.106	22.6	1.43x10 <sup>-4</sup>	6.42x10 <sup>-8</sup>	1.53x10 <sup>-12</sup>	2.33x10 <sup>5</sup>	1.50x10 <sup>-2</sup>	2.99x10 <sup>-1</sup>	1.05x10 <sup>-2</sup>	2.90x10 <sup>-2</sup>	3.39x10 <sup>-1</sup>	
	>0.053	7.6	7.95x10 <sup>-5</sup>	1.99x10 <sup>-8</sup>	2.63x10 <sup>-13</sup>	1.36x10 <sup>6</sup>	2.70x10 <sup>-2</sup>	1.81x10 <sup>-1</sup>	6.33x10 <sup>-3</sup>	1.75x10 <sup>-2</sup>	2.05x10 <sup>-1</sup>	
	<0.053	1.9	5.30x10 <sup>-5</sup>	8.82x10 <sup>-9</sup>	7.79x10 <sup>-14</sup>	4.58x10 <sup>6</sup>	4.04x10 <sup>-2</sup>	6.79x10 <sup>-2</sup>	2.37x10 <sup>-3</sup>	6.58x10 <sup>-3</sup>	7.68x10 <sup>-2</sup>	
	<b>Fibre</b>						17.45					2272

for the magnesium carbonates. The large surface area from which Mg can be leached in chrysotile fibres and the distinct atmospheric signature in the  $\delta^{13}\text{C}$  and  $\delta^{14}\text{C}$  data for hydrated magnesium carbonates indicate that chrysotile is the primary source for  $\text{Mg}^{2+}$  in magnesium carbonate precipitates. It can be concluded from the stable and radiogenic isotope data and the estimate for surface area that dissolution of bedrock carbonate does not drive the precipitation of hydrated magnesium carbonate minerals. Sequestration of atmospheric  $\text{CO}_2$  is occurring in chrysotile mine tailings at Clinton Creek and Cassiar.

### 3.6 REFERENCES

- Braithwaite, C.J.R. and Zedef, V. (1996) Hydromagnesite stromatolites and sediments in alkaline lake, Salda Golu, Turkey. *Journal of Sedimentary Research*, 66, 991-1002.
- Craig, H. (1957) Isotopic standards for carbon and oxygen and correction factors for mass-spectrometric analysis of carbon dioxide. *Geochimica et Cosmochimica Acta*, 12, 133-149.
- Deines, P. (2004) Carbon isotope effects in carbonate systems. *Geochimica et Cosmochimica Acta*, 68, 2659-2679.
- Faure, G. (1986) *Principles of isotope geology*. New York, John Wiley & Sons, Inc.

- Hansen, L.D. (2005) Geologic setting of listwanite, Atlin, B.C.: Implications for carbon dioxide sequestration and lode-gold mineralization. M.Sc. Thesis, University of British Columbia, Vancouver, British Columbia.
- Knauth, L.P., Brilli, M., and Klonowski, S. (2003) Isotope Geochemistry of Caliche Developed on Basalt. *Geochimica et Cosmochimica Acta*, 67(2), 185-195.
- Kralik, M., Aharon, P., Schroll, E., and Zachmann, D. (1989) Carbon and oxygen isotope systematics of magnesites: a review. *Monograph Series on Mineral Deposits* (Ed. G. Friedrich), 28, 197-223.
- Melezhik, V.A., Fallick, A.E., Medvedev, P.V., and Makarikhin, V.V. (2001) Palaeoproterozoic magnesite: lithological and isotopic evidence for playa/sabkha environments. *Sedimentology*, 48, 379-397.
- Nesbitt, H.W. and Jambor, J.L. (1998) Role of mafic minerals in neutralizing ARD, demonstrated using a chemical weathering methodology. In *Modern Approaches to Ore and Environmental Mineralogy* (Cabri, L.J. and Vaughan, D.J., Eds.), Mineralogical Association of Canada Short Course Series, 27, 403-421.
- Power, I.M. and Southam, G. (2005) Carbon dioxide sequestration through enhanced weathering of chrysotile mine tailings and subsequent microbial precipitation of magnesium carbonates. *Goldschmidt 2005*, Moscow, Idaho.
- Rafter, T.A. and Fergusson, G.J. (1957) Atom bomb effect – recent increase in the carbon-14 content of the atmosphere, biosphere, and surface water of the oceans. *New Zealand Journal of Science and Technology, Section A: Agricultural Research Section*, 38, 871-883.

- Reimer, P.J., Brown, T.A., and Reimer, R.W. (2004) Discussion: Reporting and calibration of post-bomb  $^{14}\text{C}$  data. *Radiocarbon*, 46, 1299-1304.
- Renaut, R.W. and Stead, D. (1991) Recent magnesite-hydromagnesite sedimentation in the playa basins of the Cariboo Plateau, British Columbia. *Geological Fieldwork (BCGSB)*, Paper 1991-1, 279-288.
- Schlesinger, W.H., Mario, G.M., and Fonteyn, P.J. (1998) Stable isotope ratios and dynamics of caliche in desert soils. In *Stable Isotopes in Ecological Research* (Rundel, P.W., Ehleringer, J.R., and Nagy, K.A., Eds.), 307-317. Springer-Verlag, New York.
- Suess, H.E. (1955) Radiocarbon concentration in modern wood. *Science*, 122, 415-417.
- Telegadas, K. (1971) The seasonal atmospheric distribution and inventories of excess carbon-14 from March 1955 to July 1969. U.S. Atomic Energy Commission Report HASL-243.
- Wilson, S.A., Raudsepp, M., and Dipple, G.M. (2006) Verifying and quantifying carbon fixation in minerals from serpentine-rich mine tailings using the Rietveld method with X-ray powder diffraction data. *American Mineralogist*, In review.
- Zedef, V., Russell, M.J., Fallick, A.E., and Hall, A.J. (2000) Genesis of vein stockwork and sedimentary magnesite and hydromagnesite deposits in the ultramafic terranes of Southwestern Turkey: A stable isotope study. *Economic Geology*, 95, 429-446.



**CHAPTER IV:*****Verifying and quantifying carbon fixation in minerals from serpentine-rich mine tailings using the Rietveld method with X-ray powder diffraction data*****4.1 INTRODUCTION**

The release of anthropogenic greenhouse gases (*e.g.*, CO<sub>2</sub>, CH<sub>4</sub>, N<sub>2</sub>O, and SO<sub>2</sub>) into the atmosphere has been linked to environmental degradation and global climate change (IPCC 2001). Production of atmospheric pollutants, CO<sub>2</sub> in particular, is associated with the combustion of fossil fuels - which accounts for as much as 90% of greenhouse gas emissions in the past 20 years (IPCC 2001). It is expected that development and implementation of new carbonless sources of energy will require another 50 to 100 years (*e.g.*, Lackner 2003; Pacala and Socolow 2004), during which time fossil fuels will see continued widespread use (Lackner 2003). Current models require that atmospheric CO<sub>2</sub> levels be stabilized on this timescale in order to curtail irreversible climate change (Pacala and Socolow 2004). Carbon dioxide sequestration or disposal is an essential component in the international effort to stabilize CO<sub>2</sub> emissions. Of the proposed sequestration schemes, mineral sequestration represents the most geologically stable and environmentally benign method for carbon disposal (Lackner *et al.* 1995). Mineral sequestration mimics natural silicate weathering processes which bind CO<sub>2</sub> in carbonate minerals. An estimated 87% of the Earth's carbon, or  $9.2 \times 10^{16}$  tonnes, is bound in carbonate minerals (Sundquist 1985). Kump *et al.* (2000) have predicted

that, given a timescale of  $10^6$  years, carbonate minerals will be the ultimate sink for anthropogenic  $\text{CO}_2$ . Mineral sequestration seeks to accelerate this natural process.

Carbonate minerals in mine tailings are of general interest for their role in suppressing acid generation (*e.g.*, Jambor and Blowes 1991; Blowes *et al.* 1998). Carbonate precipitates were observed in tailings from the Kidd Creek copper-zinc mine near Timmins, Ontario, Canada in 2000 (Al *et al.* 2000). Similar carbonation phenomena have been observed in tailings from the Lower Williams Lake uranium mine near Elliot Lake, Ontario (Paktunc and Davé 2002), and in tailings from the chrysotile mines at Thetford, Québec (Huot *et al.* 2003), Clinton Creek, Yukon (Wilson *et al.* 2003), and Cassiar, British Columbia (Wilson *et al.* 2005). The carbon bound in many tailings environments may not have an atmospheric origin, but the data presented in Chapter 3 indicate that the millions of tonnes of serpentinite tailings from the abandoned chrysotile mining operations at Clinton Creek, Yukon Territory, and Cassiar, British Columbia, Canada (Fig. 4.1) are actively fixing atmospheric  $\text{CO}_2$  in mineral carbonates. The magnesium-carbonate minerals dypingite, hydromagnesite, nesquehonite, and more rarely, lansfordite, are forming *in situ* at the surface of the tailings piles at these historical mine sites.

The hydrated magnesium carbonate minerals found at Cassiar and Clinton Creek are of interest as they have potential for long-term storage of greenhouse gases (Lackner *et al.* 1995; Lackner 2003). In this chapter we discuss the mineralogy of magnesium carbonates at Clinton Creek and Cassiar and develop a quantitative method for carbonate



FIGURE 4.1: Locations of Clinton Creek, Yukon, Cassiar, British Columbia, and Atlin, British Columbia.

determination in serpentine-rich mine tailings. The isotopic data and implications for fingerprinting the source of carbon are discussed in Chapter 3.

Carbonate crusts are observed in mine tailings within months of tailings deposition, indicating that mineral sequestration in chrysotile tailings can be a rapid process (Huot *et al.* 2003). The rapidity and extent of carbonate formation in mine tailings is almost certainly linked to the vast increases in silicate mineral surface area that are a direct result of mineral processing. Acceleration of the carbonation process in historical and active mining operations could be used to render large mining operations CO<sub>2</sub>-neutral and may help to reduce the greenhouse gas content of the atmosphere on a global scale.

Quantification of the amount of atmospheric carbon sequestered in geologic samples from Clinton Creek and Cassiar will give an estimate for the sequestration capacity of ultramafic mine tailings in general and will provide a framework for the development of standard policies related to the trading of CO<sub>2</sub> emissions for enhanced mineral sequestration at mine sites. Standard bulk geochemical measures of CO<sub>2</sub> abundance cannot be used to quantify mineral trapping as they cannot distinguish between carbonate phases, nor can they discriminate between the sources of carbon - bedrock, atmospheric, or industrial. Stable and radiogenic fingerprinting of carbon can be used to identify which carbonate minerals in a geological sample are the sinks for atmospheric, industrial, or bedrock carbon. Quantitative phase analysis using the Rietveld method provides a measure of the weight-percent contribution of each carbonate mineral in a sample. From this measure, the amount of CO<sub>2</sub> stored in atmosphere-

derived carbonate minerals can be determined. Quantitative phase analysis is therefore essential to verification and quantification of carbon disposal *via* mineral sequestration.

In order to develop and test a practical method of quantitative phase analysis for serpentinites, a series of synthetic serpentinite mine tailings of typical and known composition were prepared by weighing and mixing pure mineral constituents. At issue here is that kaolinite-serpentine group minerals generally exhibit planar disorder and thus cannot be fitted by diffraction patterns calculated from the ideal structures which is the basis of the Rietveld method (Rietveld 1967, 1969). A previous study made use of a combined reference intensity ratio and Rietveld method to measure serpentine abundance (Gualtieri and Artioli 1995). If, however, the experimental pattern of the disordered phase can be fitted independently by some means and if a known weight of a spike of an extraneous phase is added to the sample, the amount of serpentine in the sample could be measured as if it were an amorphous phase. Spikes have been used successfully as internal standards for largely amorphous materials (*e.g.*, Gualtieri 2000; De La Torre *et al.* 2001; Orlhac *et al.* 2001), but have not been applied to disordered crystalline phases. We seek to develop a standardless method that is applicable to most geological samples containing a disordered mineral phase. For this study, we used annealed  $\text{CaF}_2$  as a spike and fitted the diffraction pattern of the disordered kaolinite-serpentine group mineral with the Pawley method (Pawley 1981). This procedure was subsequently applied to samples of tailings from the mines at Cassiar and Clinton Creek. We propose that the Rietveld method with X-ray powder-diffraction data can be used to accurately quantify the amount of carbonation occurring in serpentinite mine tailings.

#### 4.1.1 Sample Localities

The Clinton Creek chrysotile deposit is a partially carbonate-altered serpentized peridotite (Htoon 1979). The Clinton Creek Mine, situated near Dawson City, Yukon Territory, operated from 1967 to 1978 (Htoon 1979). A total of 16 Mt of chrysotile ore were extracted from the four open pit mines at Clinton Creek during this eleven year period. In addition to the ore, 60 Mt of waste rock and 10 Mt of tailings were produced as a by-product of the mining process (EMAN-North 2003). Tailings materials are characterized by short-fibre chrysotile and serpentinite cobbles containing massive serpentine and minor amounts of magnetite, calcite, dolomite, magnesite, quartz, clinocllore, and pyroaurite. Carbonate mineral formation occurs in four distinct modes at Clinton Creek: crusts on vertical surfaces (composed of nesquehonite, dypingite, hydromagnesite, and occasional lansfordite), carbonate spires on horizontal tailings surfaces (composed of nesquehonite, dypingite, and hydromagnesite and caused by wicking-up of pore fluids), as thin crusts of dypingite ( $< 1$  mm in thickness) on serpentinite cobbles, and as a disseminated cement of hydromagnesite in bulk tailings (Fig. 4.2). Carbonate crusts are abundant and easily recognised by their off-white color, coloform habit, and reactivity with dilute hydrochloric acid (10 % HCl).

The chrysotile deposit at Cassiar, British Columbia, forms part of a serpentized harzburgite tectonite (Wicks and O'Hanley 1988). Cassiar is located approximately 130 km north of Dease Lake, BC. During the 39-year operational lifetime of the mine, from 1953 to 1992, 17 Mt of mine tailings were produced. These tailings were stored outdoors

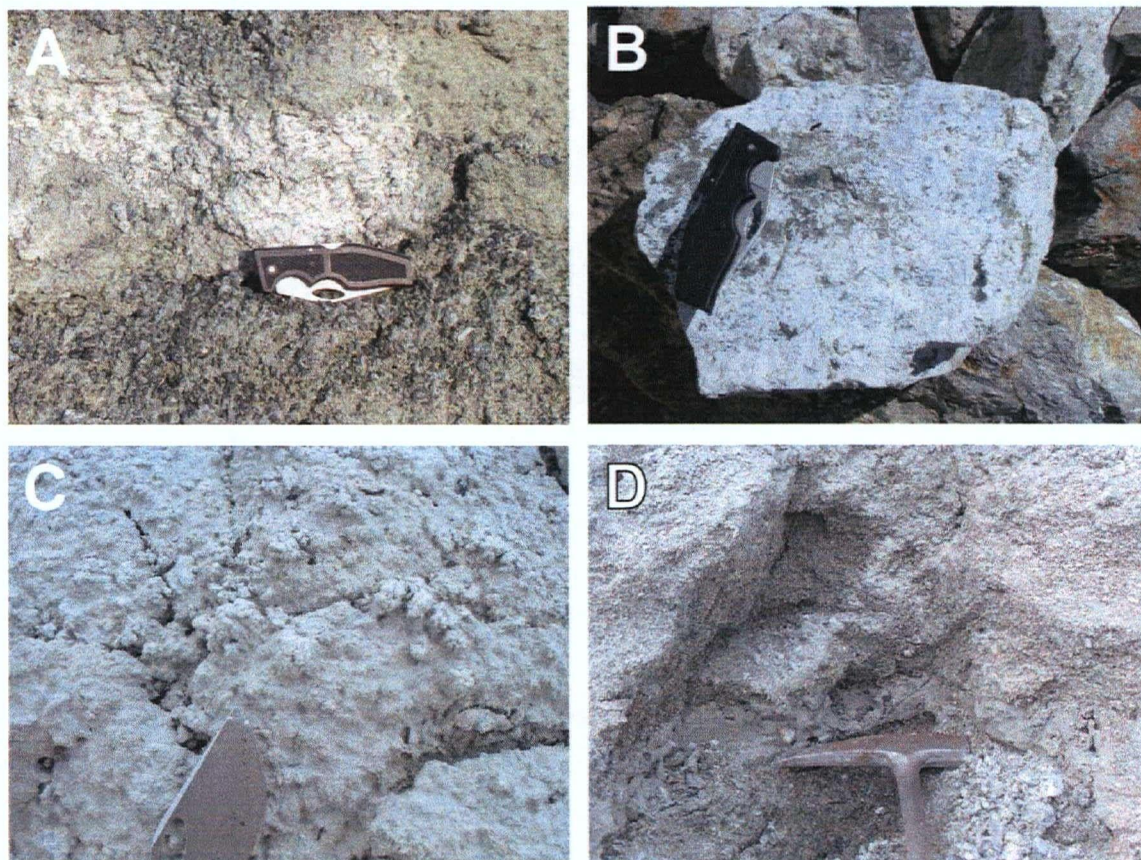


FIGURE 4.2: Modes in which hydrated magnesium carbonate minerals have been identified at Clinton Creek, Yukon and Cassiar, British Columbia: A) nesquehonite/dypingite crust from Cassiar, B) dypingite on cobble from Clinton Creek, C) nesquehonite/dypingite/hydromagnesite spires from Clinton Creek, and D) disseminated hydromagnesite cement from Clinton Creek.

in an elongate pile. Beginning in 1993, the mine underwent a six-year process of renovation and revitalization. By January 2000 commercial production of chrysotile had been renewed. Mining proceeded until December 25, 2000 when the mill was severely damaged by fire (MINFILE, 2005). Tailings are composed primarily of short-fibre chrysotile with cobbles of massive serpentine with minor magnetite, clinochlore, and occasional quartz and carbonates. The carbonate minerals nesquehonite and dypingite form crusts on vertical tailings surfaces at Cassiar.

## **4.2 EXPERIMENTAL METHOD**

### **4.2.1 Sample Preparation and Data Collection**

Twenty-four mixtures of pure mineral samples were prepared to simulate serpentinite mine tailings. Minerals commonly found in the tailings at Clinton Creek and Cassiar were used: kaolinite-serpentine group (antigorite and chrysotile), magnetite, quartz, calcite, dolomite, magnesite, and hydromagnesite.

Mixtures of pure mineral samples were prepared to simulate serpentinite mine tailings. Minerals commonly found in the tailings at Clinton Creek and Cassiar were used: kaolinite-serpentine group (antigorite and chrysotile), magnetite, quartz, calcite, dolomite, magnesite, and hydromagnesite. As sufficient amounts of pure nesquehonite, dypingite, and lansfordite (also present in the mine tailings at Clinton Creek and Cassiar)



were not available, and well-crystallized, synthetic hydrated magnesium carbonates are difficult to manufacture (Davies and Bubela 1973; Klopogge *et al.* 2003), hydromagnesite was used in their place. Samples of the constituent minerals were checked for purity using X-ray powder diffraction. Kaolinite-serpentine group minerals were identified positively as chrysotile and antigorite using X-ray powder diffraction and dispersive Raman microspectroscopy according the method of Rinaudo *et al.* (2003). All components, with the exception of hydromagnesite, were greater than 99% pure. Rietveld analysis showed that the hydromagnesite had partially decomposed to 4.8 wt.% magnesite.

Three identical stock mixtures (A1, C1 and AC1) were prepared with the relevant phases exclusive of serpentine in the following abundances: magnetite (40 wt.%), quartz (20 wt.%), calcite (10 wt.%), dolomite (10 wt.%), magnesite (10 wt.%), and hydromagnesite (10 wt.%). Each mixture was ground under anhydrous ethanol with synthetic corundum grinding elements for 10 minutes in a McCrone micronising mill to reduce the mean grain size and to ensure homogenization. Stock mixtures were dried at room temperature under a fume hood and were disaggregated with an agate mortar and pestle when dry. From each of the identical 6-phase mineral mixtures, series of 5 synthetic serpentinite samples each were produced by adding serpentine as follows. Antigorite and chrysotile were added in amounts of 10, 30, 50, 70 and 90 wt.% to mixtures A1 and C1, "AMIX" and "CMIX" series, respectively (Table 4.1). A third series ("ACMIX" series) was prepared by adding both chrysotile and antigorite to mixture AC1 in amounts 5, 15, 25, 35 and 45 wt.%. A spike of annealed  $\text{CaF}_2$  was added

TABLE 4.1: Compositions of synthetic serpentinite mine tailings renormalized to exclude fluorite spike.

Phase (wt.%)	Stock Mix	SERPMIX10	SERPMIX30	SERPMIX50	SERPMIX70	SERPMIX90	HMIX1	HMIX2	HMIX3	HMIX4	HMIX5	HMIX6	HMIX7	HMIX8	HMIX9
Chrysotile		10.00	30.00	50.00	70.00	90.00	90.00	80.00	50.00	80.00	45.00	70.00	60.00		
Magnetite	40.00	36.00	28.00	20.00	12.00	4.00				10.00	5.00	5.00	5.00	0.00	10.00
Quartz	20.00	18.00	14.00	10.00	6.00	2.00						5.00	5.00	49.67	40.00
Calcite	10.00	9.00	7.00	5.00	3.00	1.00						5.00	5.00	9.93	10.00
Dolomite	10.00	9.00	7.00	5.00	3.00	1.00								10.60	10.00
Magnesite	10.48	9.43	7.33	5.24	3.14	1.05	0.48	0.95	2.39	0.48	2.39	0.72	1.19	10.88	10.95
Hydromagnesite	9.52	8.57	6.67	4.76	2.86	0.95	9.52	19.05	47.62	9.52	47.62	14.28	23.81	18.92	19.05
Total	100.00	100.00	100.00	100.00	100.00	100.00	100.00	100.00	100.00	100.00	100.00	100.00	100.00	100.00	100.00

to each sample such that it constituted 10 wt.% of the renormalized weight. Although low abundances of antigorite or chrysotile are not found in serpentinite mine tailings, they were used in this study to define the limitations of the method. The synthetic samples were ground under anhydrous ethanol in the McCrone micronising mill for an additional 7 minutes to reduce the grain size of the serpentine phases and to homogenize the samples. The fourth, and final, series ("HMIX" series) consisted of 9 weighed mixtures, 7 of which represented more realistic mineral abundances and 2 of which contained no serpentine (Table 4.1). These samples were prepared individually, rather than from a stock mixture. As with the previous 15 samples, a 10 wt.% spike of  $\text{CaF}_2$  was added to each HMIX sample. The HMIX series samples were ground for 10 minutes in the McCrone micronising mill. The grinding times were chosen to minimize the degradation of the serpentine structure while optimizing particle-size reduction. Samples were dried at room temperature and disaggregated with an agate mortar and pestle.

In addition, two specimens of tailings from Cassiar and eight specimens from Clinton Creek were prepared to assess the method on real mine tailings. Two samples from a hydromagnesite playa in Atlin, BC were also included to demonstrate Rietveld refinements on carbonate-rich samples that lack serpentine. Samples were left in a drying hood for 48 hours and were then homogenized mechanically with a spatula. A five kilogram aliquot was taken from a bulk sample (weighing in excess of 20 kg) from each locality. These large aliquots were dried and homogenized prior to division into smaller, more workable aliquots for X-ray powder diffraction. An aliquot of each sample was powdered using a tungsten carbide ringmill. A 10 wt.% spike of annealed  $\text{CaF}_2$  was

added to 3.00 g of each sample of tailings and the mixture was ground under ethanol for 10 minutes in the micronising mill.

Samples were mounted in a back-loading aluminum cavity holder of the design described by Raudsepp and Pani (2003). Preferred orientation of inequant crystallites was minimized by covering the top of the cavity with a sheet of ground glass and loading powdered samples against the roughened surface. To further inhibit preferred orientation of crystallites, particularly those of chrysotile, the surface of each sample was serrated with a razor blade along two axes: one parallel to the axis of the diffractometer goniometer and the second in the perpendicular direction. X-ray powder diffraction data were collected on a Siemens D5000  $\theta$ - $2\theta$  diffractometer with a step size of  $0.04^\circ 2\theta$  and counting time of 1s/step over a range of  $3$ - $90^\circ 2\theta$ . The normal-focus Cu X-ray tube was operated at 40 kV and 40 mA.

Conventional quantitative modal analysis with X-ray powder diffraction data is performed through the integration of peak intensities and calibrated using internal standards. This is an awkward method due to the difficulty inherent in the preparation of standards displaying similar materials properties (*i.e.*, crystallinity, composition, and microabsorption) to the minerals in a sample. The overlap of Bragg reflections in complex patterns, such as those for geological samples, makes it extremely difficult to locate peaks suitable for integration of intensity. Although deconvolution protocols can be used to account for peak overlap in modern whole-pattern profile fitting, the use of internal standards is still prerequisite. New imaging technology has brought about a renaissance in the field of point counting; however such methods are limited by grain

size, time constraints, and the high cost of experimental accuracy. (Raudsepp and Pani 2003) Normative calculations depend upon assumptions made from ideal mineral assemblages based on mass-balance calculations, and as such are indirect and fairly inaccurate for minerals that do not preferentially partition trace to minor abundance elements (Dipple *et al.* 2002; Raudsepp and Pani 2003).

#### **4.2.2 Motivation for Using the Rietveld Method**

The Rietveld method is a standardless, full-profile method for quantitative phase analysis which can be applied to diffraction patterns collected using conventional laboratory diffractometers (Rietveld 1967, 1969). Essentially, the Rietveld method is a least squares refinement which is carried out until a best fit is obtained between the entire experimental powder diffraction pattern and the entire calculated pattern for a mineral or mixture of minerals. What makes the Rietveld method so useful is that it provides feedback between an ever-improving model for crystal structure and the assignment of observed intensities for overlapping Bragg reflections (Young 1993). In all other quantitative refinement methodologies the assignment of Bragg reflections to observed intensities and the structure refinement depending on this assignment are non-interacting processes. The quantity to be minimized in the Rietveld least squares refinement is the

least squares residual (for a best fit to all intensities,  $y_i$ , simultaneously):

$$s_y = \sum_i w_i (y_i - y_{ci})^2 \quad (4.1)$$

where  $s_y$  is the least squares residual for the least squares fit,  $w_i = 1/y_i$  is a weight on the residual,  $y_i$  is the observed intensity at the  $i^{\text{th}}$  step in the acquired XRPD pattern, and  $y_{ci}$  is the calculated intensity at the  $i^{\text{th}}$  step. (Young 1993)

The relative masses of the constituent mineral phases in a specimen can be calculated using the relation:

$$W_r = \frac{S_r(ZMV)_r}{\sum_i S_i(ZMV)_i} \quad (4.2)$$

where  $W_r$  is the relative weight fraction of the  $r^{\text{th}}$  mineral phase in a mixture of  $t$ -many phases,  $S$  is the Rietveld scale factor,  $Z$  is the number of formula units per unit cell of the mineral in question,  $M$  is the mass of the formula unit, and  $V$  is the volume of the unit cell (Hill and Howard 1987). This relation holds for well-crystallized phases, but becomes less accurate for samples containing amorphous, nanocrystalline, or disordered phases.

Structural models for crystalline materials, derived from the literature, are only directly applicable to simple structures and minerals for which the degree of solid solution is negligible (Gualtieri 2000). Complex minerals, such as clays and serpentines,

which are strongly affected by planar disorder, will cause under or overestimates of the scale factor during a standard Rietveld refinement, leading to a misestimate of the mineral content in the sample. However, the addition of a known weight of a spike of an extraneous phase (*e.g.*,  $\text{CaF}_2$ ) and the use of structureless profile fitting of the serpentine pattern allows the measurement of the amount of serpentine in the sample as if it were an amorphous phase.

During refinement, amorphous and nanocrystalline components are usually included in the background model and subtracted out of the pattern (Raudsepp and Pani 2003). The crystalline phases are subsequently normalized to 100%. For a specimen to which a spike has been added, there will be a discrepancy between the known weight percent of the spike and the amount calculated with the Rietveld method. This discrepancy can be used to determine the amount of amorphous material in the specimen with the relation:

$$A = \frac{1 - W_s / R_s}{100 - W_s} \cdot 10^4 \% \quad (4.3)$$

where  $A$  (%) is the amount of amorphous phase in the specimen,  $W_s$  (%) is the weighed amount of spike, and  $R_s$  (%) is the amount of spike determined by Rietveld analysis (Gualtieri 2000; De La Torre *et al.* 2001).

An appropriate amount of spike must be chosen such that it contributes significantly to the overall pattern signal without dominating the other phases in the

specimen. A recent study has shown that the relative error on the amorphous content of a specimen increases as the percent content of the spike decreases and that 10% spike gives a sufficiently high signal without drowning out the rest of the pattern (Gualtieri 2000). A spike of approximately 10% is typically recommended as a good compromise between resolution of intensities and accuracy of estimation for the amorphous phase (Bish and Post 1993; Gualtieri 2000).

Structureless profile fitting with the Pawley method helps to provide an estimate of the amount of a disordered mineral phase in a specimen (Pawley 1981). The Pawley method is a variation on the standard Rietveld method. It differs in that the location of each Bragg reflection is held fixed, while the peak intensities are permitted to vary. The Pawley method resembles, yet should not be confused with, the Le Bail method for structureless profile fitting. The distinguishing feature of the Le Bail method being the initial definition of the structure factors,  $|F|$  (*i.e.*, the sum of the scattering vectors for all atoms in a unit cell), assigned to the Bragg peaks for the hypothetical crystal structures used in the refinement. Iterations are begun with a set of arbitrarily identical values of  $|F|$  rather than using the  $|F_{\text{calculated}}|$  values used in the standard Rietveld method or the refinable peak heights used in the Pawley method (Le Bail 1988; Le Bail 2002). The Pawley and Le Bail methods constrain the positions of the Bragg reflections in an X-ray diffraction pattern according to crystal data for the relevant phases but do not use structural data to fit the peak intensities. Due to the effects of structural disorder and preferred orientation on Bragg intensities, it is necessary to use a method for structureless fitting to obtain a direct estimate of the amount of serpentine in a spiked specimen.



Essentially, fitting with the Pawley method allows the disordered phase to be subtracted from the pattern as a part of the background curve. The wt.% abundance of the disordered phase is then calculated as a function of the overestimate of the spike phase using (4.3).

#### **4.2.3 Rietveld Refinement and Quantitative Phase Analysis**

Rietveld refinements were done with Rietveld refinement software Topas Version 3 (Bruker AXS 2004b) using the fundamental parameters approach (Cheary and Coelho 1992). Sources of crystal structure data for the constituent phases are listed in Table 4.2. To avoid the unpredictable effect of planar disorder on the diffraction patterns of the serpentine minerals, the Pawley method (Pawley 1981) was used to extract peak intensities independently of atomic scattering from the powder diffraction patterns of pure chrysotile and antigorite. The extracted intensities with the appropriate space groups and cell dimensions of antigorite and chrysotile were subsequently used to fit the serpentine component in the powder diffraction patterns of the mixtures as a peak phase using the Pawley method. As the relative intensities of peaks during Pawley refinement are not constrained by atomic scattering, the relative intensities of the peaks for the serpentine were initially held constant to avoid the interference of serpentine peaks with peaks from the other phases. After the correct fitting of these peaks, the relative intensities of the serpentine peaks were refined. In order to provide an estimate of the

TABLE 4.2: Sources of crystal structure data for Rietveld refinement.

Mineral	Source
Antigorite	Uehara (1998)
Brucite	Catti <i>et al.</i> (1995)
Calcite	Maslen <i>et al.</i> (1995)
Chrysotile	Falini <i>et al.</i> (2004)
Dolomite	Ross and Reeder (1992)
Fluorite	Batchelder and Simmons (1964)
Hydromagnesite	Akao and Iwai (1977)
Magnesite	Markgraf and Reeder (1985)
Magnetite	Tsukimura <i>et al.</i> (1997)
Nesquehonite	Giester <i>et al.</i> (2000)
Palygorskite	Chisholm (1992)
Pyroaurite	Olowe (1995)
Quartz	Glinnemann <i>et al.</i> (1992)

combined abundance of serpentine, both antigorite and chrysotile structures were used as a basis to fit serpentine in samples containing both phases.

Backgrounds for samples containing chrysotile, or both chrysotile and antigorite, were modelled using third-order Chebychev polynomials with an additional  $1/x$  term to aid in the fitting of the background curve at low angles of diffraction. Second-order Chebychev polynomials were adequate to model the background for samples in which antigorite was the only serpentine phase. The zero error, Lorentzian crystallite size, strain and cell parameters were refined for all phases. Preferred orientation of phases other than serpentine was corrected for using the method of March and Dollase (March 1932; Dollase 1986). Contamination from the corundum grinding elements of the micronising mill accounted for less than 1% of most samples and was not treated as an additional phase in refinements.

All Rietveld refinements were done assuming a 10 wt.% spike. In order to model the effects that weighing error for the spike may have had on results, refined abundances were recalculated using an exaggerated weighing error of  $\pm 10\%$  relative. Refinement results were recalculated and renormalized for each sample using the method of Gualtieri (2000), assuming spike abundances of 9 and 11%. As observed by Gualtieri (2000), the amorphous phase is underestimated with the assumption of an increased abundance of the spike phase. The absolute and relative error on the estimation of the serpentine phase decrease as the amount of that phase increases. The 10% overestimate of the spike leads to an underestimate of the disordered phase, while a 10% underestimate leads to a

general overestimate. The converse holds for all other phases in the mixture, as the refined weights are compelled to increase by the normalization criterion (Fig. 4.3).

To correct for microabsorption, a Brindley radius of 2.5  $\mu\text{m}$  was used for all phases (Brindley 1945). Scanning electron microscopy showed that the radii of carbonate particles were seldom greater than 2.5  $\mu\text{m}$ , while particles of magnetite and quartz frequently exceeded this value. The radii of approximately one-half of magnetite and quartz particles are within the range 3.0 to 5.0  $\mu\text{m}$ . These observations suggest that the harder minerals are more resistant to particle-size reduction *via* milling. Serpentine particles, chrysotile in particular, were significantly larger than those for other phases with most particle radii falling within the range of 5.0 – 7.5  $\mu\text{m}$ . The serpentines were the only phases in the mixtures to be ground for less than 17 minutes, as grinding times in excess of 10 minutes were found to cause deterioration of the crystal structure. Laser-diffraction based particle-size analysis gave average particle diameters of 3.40  $\mu\text{m}$  ( $r = 1.70 \mu\text{m}$ ) and 4.00  $\mu\text{m}$  ( $r = 2.00 \mu\text{m}$ ) for the antigorite stock mixture ("A1") and the 50 wt.% antigorite sample ("AMIX50"), respectively. Based on observations in the scanning electron microscope, the results of the laser-diffraction based analyses, and the fact that an accurate estimate of particle size for each phase is not practical, a Brindley radius of 2.5  $\mu\text{m}$  was taken to be representative of a typical mixture.

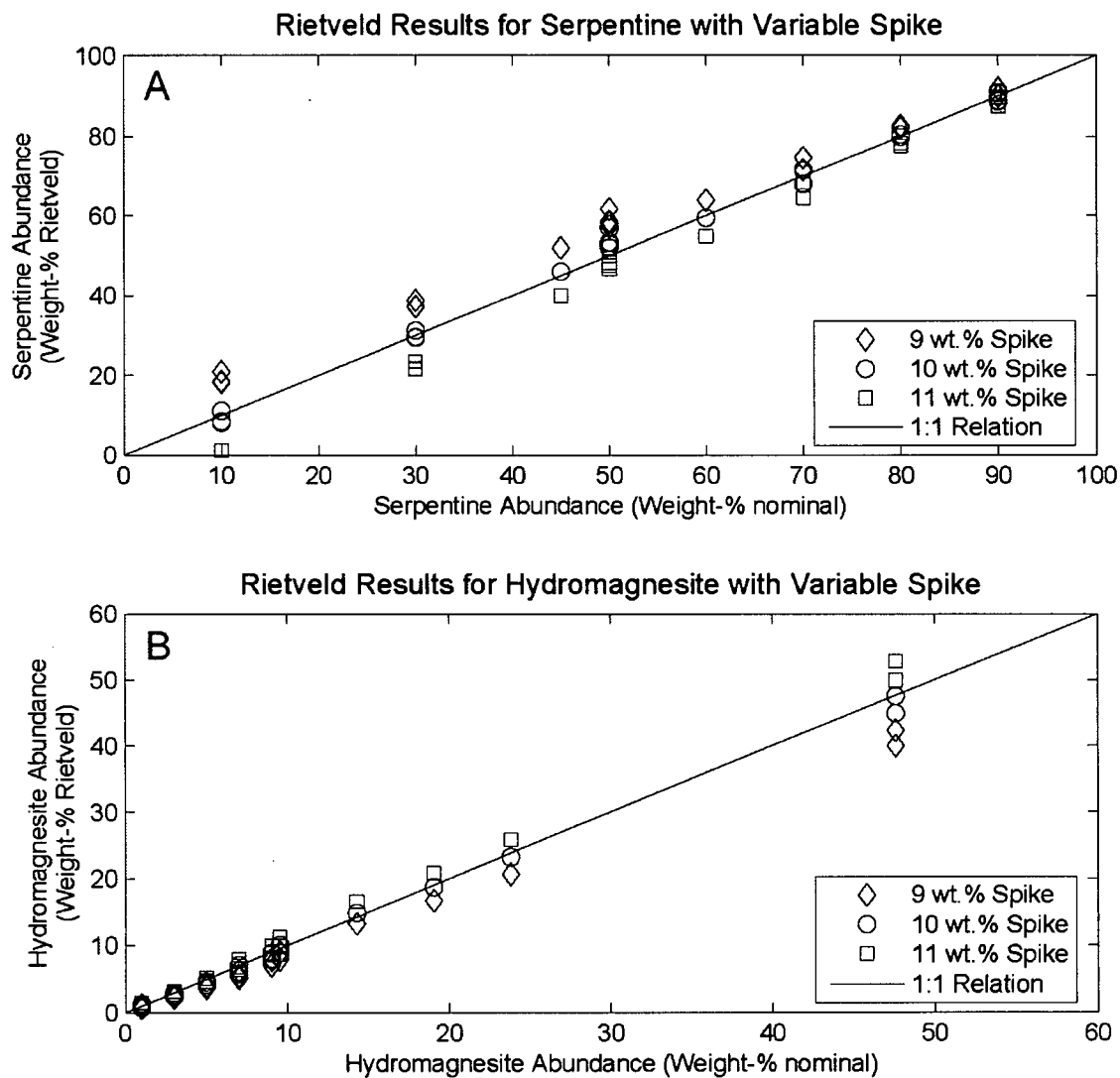


FIGURE 4.3: Abundance of serpentine from Rietveld refinement versus nominal abundance for three different concentrations of the fluorite spike (9, 10, and 11%  $\text{CaF}_2$ ): (A) serpentine; (B) hydromagnesite.

## 4.3 RESULTS AND DISCUSSION

### 4.3.1 Synthetic Mine Tailings

Results of quantitative phase analysis for the synthetic serpentine mine tailings are displayed in Table 4.3 and Figures 4.3, 4.4, and 4.5. Measured abundance versus the nominal abundance for most phases deviates slightly from the ideal 1:1 trend (Fig. 4.5). The deviation results at least in part from the large increase in relative error for the refinements of minor phases. Raudsepp *et al.* (1999) and Dipple *et al.* (2002) report that for the conditions of data collection used in our laboratory, the relative error increases rapidly for measurements of concentrations below 6 wt.%. While the relative error is high for phases of less than approximately 6 wt.%, the absolute errors are small (Fig. 4.6). The relationship between absolute and relative errors is typical for measurements of hydromagnesite (Fig. 4.7). The relative error in the amount of hydromagnesite increases with decreasing abundance, but the corresponding absolute error is well within the range for estimates of mineral binding of CO<sub>2</sub>. A 5% relative error can be expected on estimates of hydromagnesite content for abundances greater than 10 wt.%. Relative error is expected to increase as hydromagnesite abundance approaches the 1 wt.% detection limit of our X-ray data. A relative error of 10 to 15% is expected for hydromagnesite abundances less than 10 wt.%. Thus, precise and accurate estimates of hydrated magnesium carbonate abundance can be made for samples containing

TABLE 4.3: Results of quantitative phase analysis of synthetic serpentinite mine tailings.

Phase (wt.%)	AMIX10	AMIX30	AMIX50	AMIX70	AMIX90	CMIX10	CMIX30	CMIX50	CMIX70	CMIX90	ACMIX10	ACMIX30
Chrysotile	8.45	29.38	53.40	71.49	90.66	11.11	31.20	52.08	67.93	88.92	8.15	29.58
difference	1.55	0.62	3.40	1.49	0.66	1.11	1.20	2.08	2.07	1.08	1.85	0.42
Magnetite	37.79	27.90	18.26	12.18	3.83	34.11	26.28	18.54	10.79	3.38	37.65	26.81
difference	1.79	0.10	1.74	0.18	0.17	1.89	1.72	1.46	1.21	0.62	1.65	1.19
Quartz	17.19	14.11	10.57	5.97	2.16	16.60	13.90	9.79	5.99	2.25	16.88	13.55
difference	0.81	0.11	0.57	0.03	0.16	1.40	0.10	0.21	0.01	0.25	1.12	0.46
Calcite	7.81	7.20	3.15	1.95	0.35	9.73	7.37	4.85	4.51	1.36	8.63	6.88
difference	1.19	0.20	1.85	1.05	0.65	0.73	0.37	0.15	1.51	0.36	0.37	0.12
Dolomite	9.51	6.91	3.82	3.57	1.20	9.33	6.82	4.40	3.09	1.41	8.88	8.24
difference	0.51	0.09	1.18	0.57	0.20	0.33	0.18	0.60	0.09	0.41	0.12	1.24
Magnesite	11.28	8.69	6.18	2.35	0.75	11.22	8.26	6.08	4.81	1.90	10.98	7.91
difference	1.85	1.35	0.94	0.79	0.30	1.79	0.93	0.84	1.66	0.85	1.55	0.58
Hydromagnesite	7.97	5.82	4.61	2.48	1.05	7.90	6.17	4.26	2.88	0.77	8.83	7.04
difference	0.60	0.85	0.15	0.37	0.10	0.68	0.50	0.50	0.02	0.18	0.26	0.38
Total	100.00	100.00	100.00	100.00	100.00	100.00	100.00	100.00	100.00	100.00	100.00	100.00
$\chi^2$	1.76	1.89	2.15	1.89	2.20	1.20	1.17	1.14	1.19	1.26	1.37	1.31
R <sub>wp</sub>	8.08	8.22	8.33	7.10	6.80	9.45	8.27	7.67	7.37	6.95	8.19	7.03

\*  $\chi^2$  is the reduced chi-squared statistic for the least-squares fit.

† R<sub>wp</sub> is the weighted pattern index, a function of the least-squares residual.

TABLE 4.3 (Continued): Results of quantitative phase analysis of synthetic serpentinite mine tailings.

Phase (wt.%)	ACMIX50	ACMIX70	ACMIX90	HMIX1	HMIX2	HMIX3	HMIX4	HMIX5	HMIX6	HMIX7	HMIX8	HMIX9
Chrysotile	57.00	71.57	88.68	90.80	80.47	52.83	79.87	46.02	68.03	59.38		
difference	7.00	1.57	1.32	0.80	0.47	2.83	0.13	1.02	1.97	0.62		
Magnetite	14.96	10.95	3.89				8.70	4.45	4.64	4.74		10.45
difference	5.04	1.06	0.11				1.30	0.55	0.36	0.26		0.45
Quartz	9.88	5.82	2.24						5.37	4.73	50.61	41.19
difference	0.12	0.18	0.24						0.37	0.27	0.94	1.19
Calcite	4.44	2.82	1.81						6.00	5.78	9.64	9.57
difference	0.56	0.18	0.81						1.00	0.78	0.29	0.43
Dolomite	6.27	3.26	1.02								10.96	10.05
difference	1.27	0.26	0.02								0.37	0.05
Magnesite	3.23	3.01	1.07	0.32	0.77	2.27	1.38	2.01	1.08	2.16	11.24	11.68
difference	2.01	0.14	0.02	0.16	0.18	0.12	0.90	0.38	0.37	0.97	0.36	0.73
Hydromagnesite	4.22	2.58	1.28	8.89	18.76	44.90	10.05	47.52	14.88	23.22	17.54	17.07
difference	0.54	0.28	0.33	0.64	0.29	2.71	0.53	0.09	0.60	0.59	1.38	1.98
Total	100.00	100.00	100.00	100.00	100.00	100.00	100.00	100.00	100.00	100.00	100.00	100.00
$\chi^2$	1.25	1.30	1.40	1.37	1.40	1.47	1.21	1.43	1.32	1.27	1.67	1.43
R <sub>wp</sub>	6.07	5.79	5.37	7.09	7.19	7.25	7.12	7.62	7.38	7.26	9.49	9.56

\*  $\chi^2$  is the reduced chi-squared statistic for the least-squares fit.

† R<sub>wp</sub> is the weighted pattern index, a function of the least-squares residual.



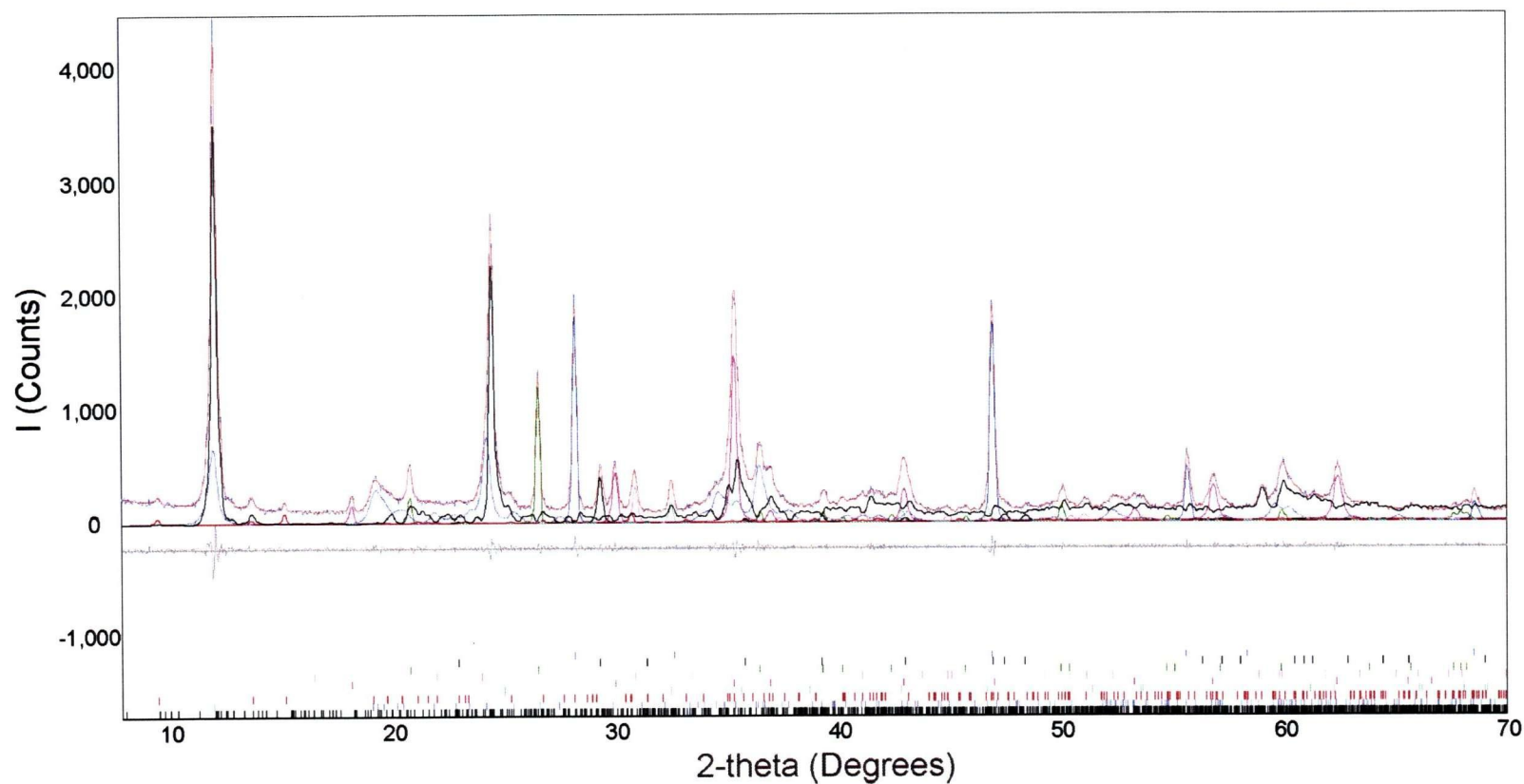


FIGURE 4.4: Rietveld refinement plot, ACMIX70. Uppermost line - observed data overlain by calculated pattern; black line below - residual pattern; vertical lines - positions of Bragg reflections for each phase; curves under the observed and calculated patterns - calculated patterns of each phase. Axes are intensity (counts) versus  $2\theta$  (degrees).

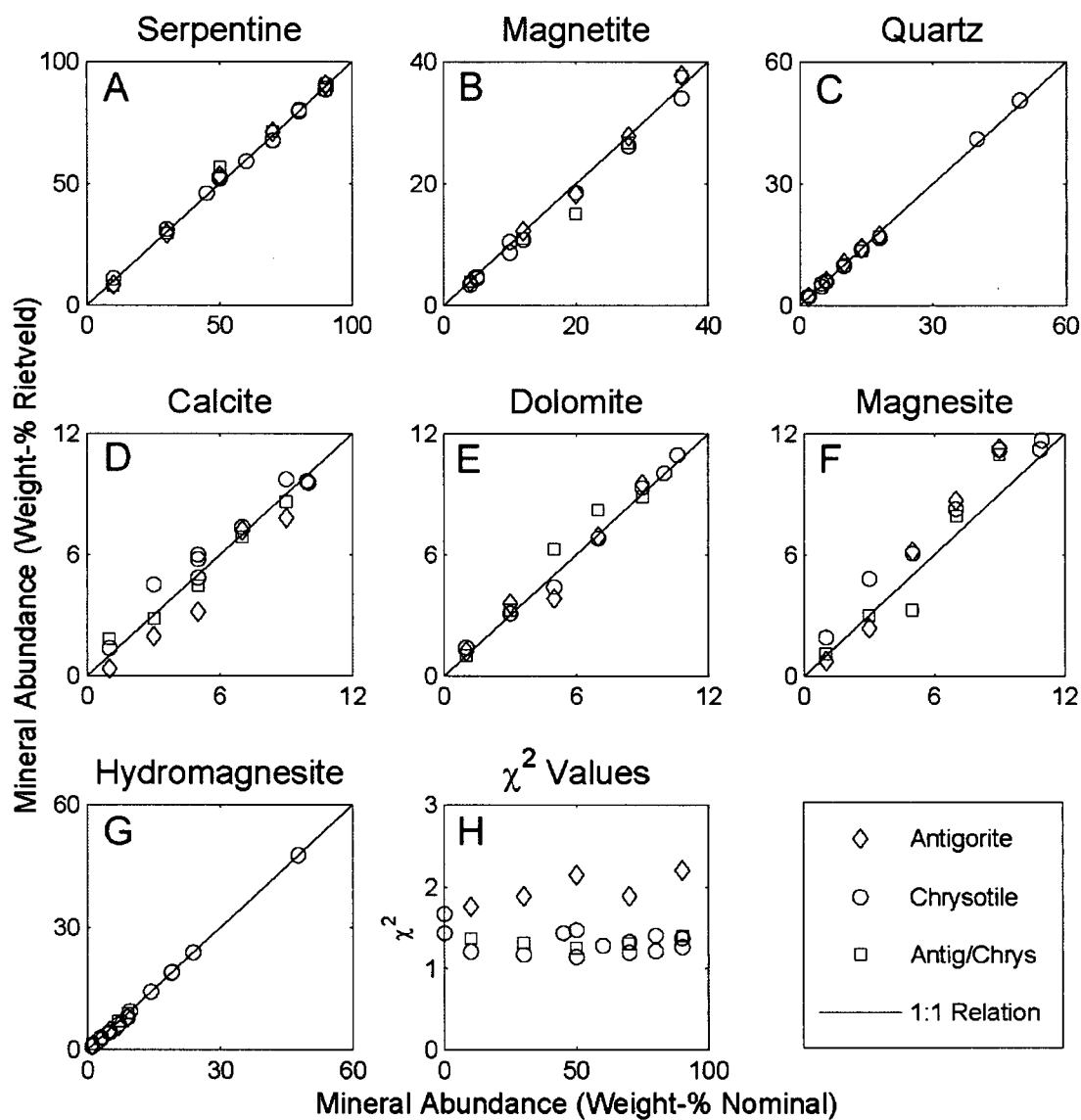


FIGURE 4.5: Modal abundances from Rietveld refinement versus nominal abundances in synthetic serpentinites.

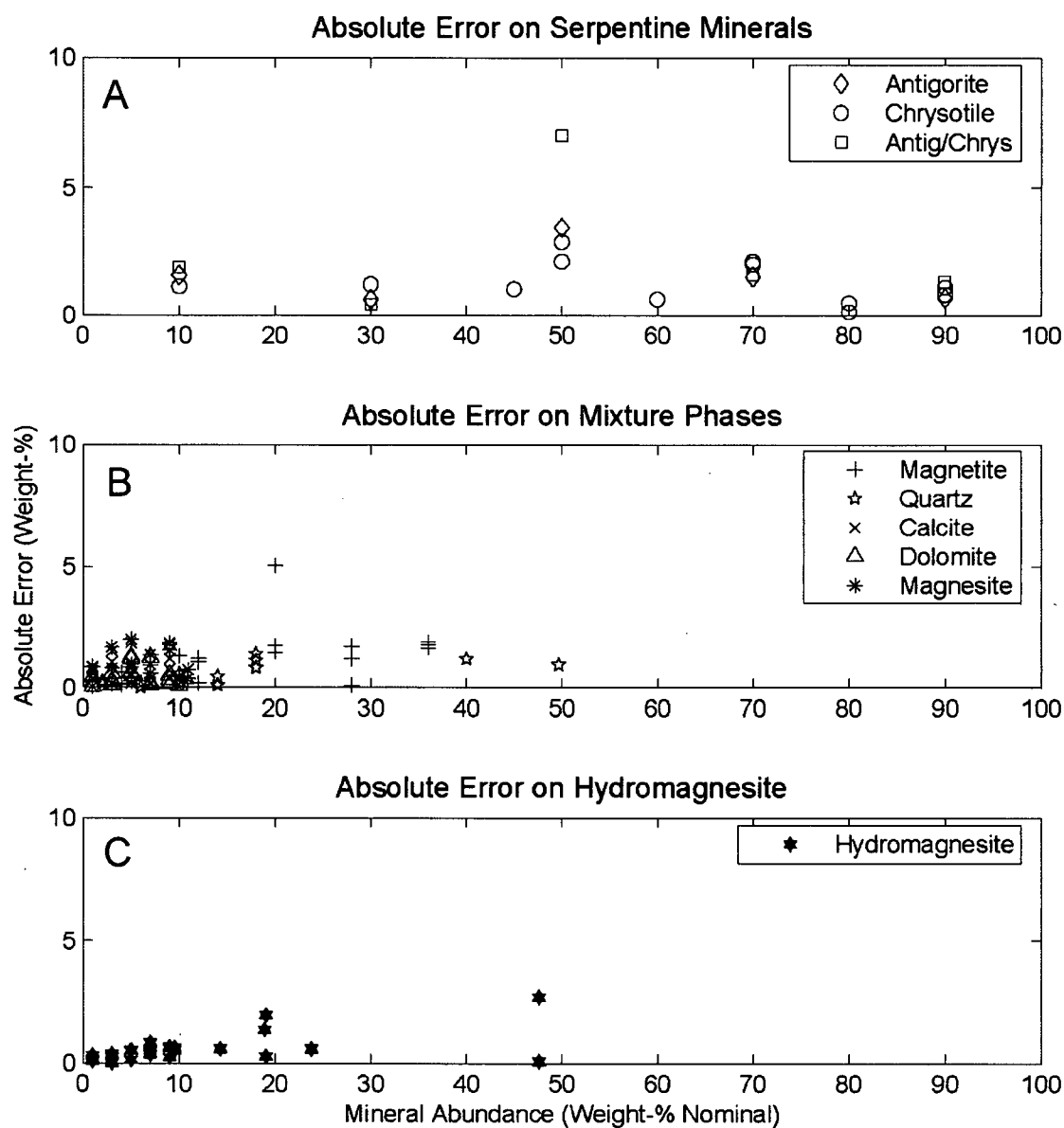


FIGURE 4.6: Absolute (wt.%) error in estimates for all minerals versus the abundance of that mineral in a sample.

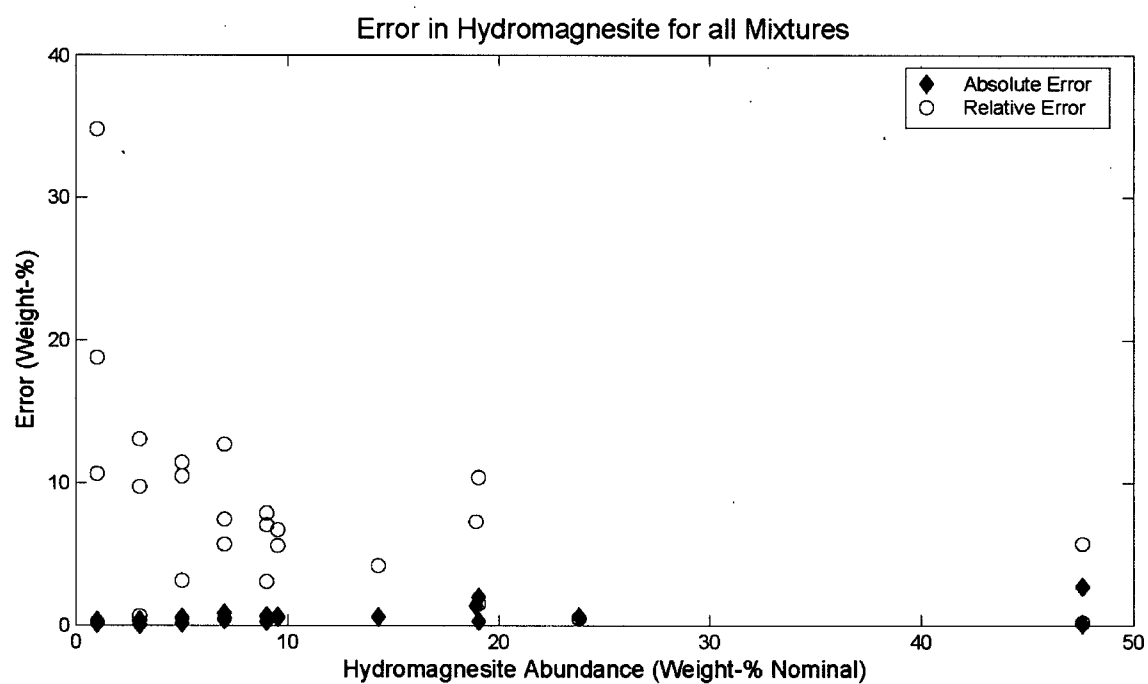


FIGURE 4.7: Relative and absolute (wt.%) error in Rietveld estimates of hydromagnesite abundance for all synthetic samples.

disordered mineral phases such as kaolinite-serpentine group minerals. Note that the type of serpentine used in the weighed mixtures has no significant effect on the results of the Rietveld refinement (Figs. 4.5A and 4.6A). We do not know why the abundance of hydromagnesite is consistently underestimated at low abundances. It was initially thought that the original hydromagnesite used in the mixtures was not entirely crystalline; however, Rietveld refinements of pure hydromagnesite do not show evidence of significant deterioration of crystallinity with increased grinding time during preparation of the mixtures. Preferred orientation of hydromagnesite crystallites could also lead to severe underestimates of modal abundance, although this had largely been accounted for. The data, as reported in Table 4.3 and Figures 4.4-4.7, has already been corrected to account for the 4.8 % magnesite impurity in the hydromagnesite, a correction which failed to adequately explain the misestimates obtained for these two minerals. To determine whether the hydromagnesite was becoming nanocrystalline with increased grinding time, conventional Rietveld refinements were done on the XRPD data collected after 0, 7, and 17 minutes of grinding in the micronising mill (Fig. 4.8). The relative intensities of the hydromagnesite and magnesite patterns do not change with grinding, although the absolute intensities decreased as a result of the dilution effect (caused by contamination from the corundum grinding elements). These underestimates may be an artefact of the Pawley fitting procedure or the result of amorphous content in the  $\text{CaF}_2$  spike. As such, there is no need for concern that estimates of carbonate abundance are being compromised by deterioration of crystallinity due to grinding.

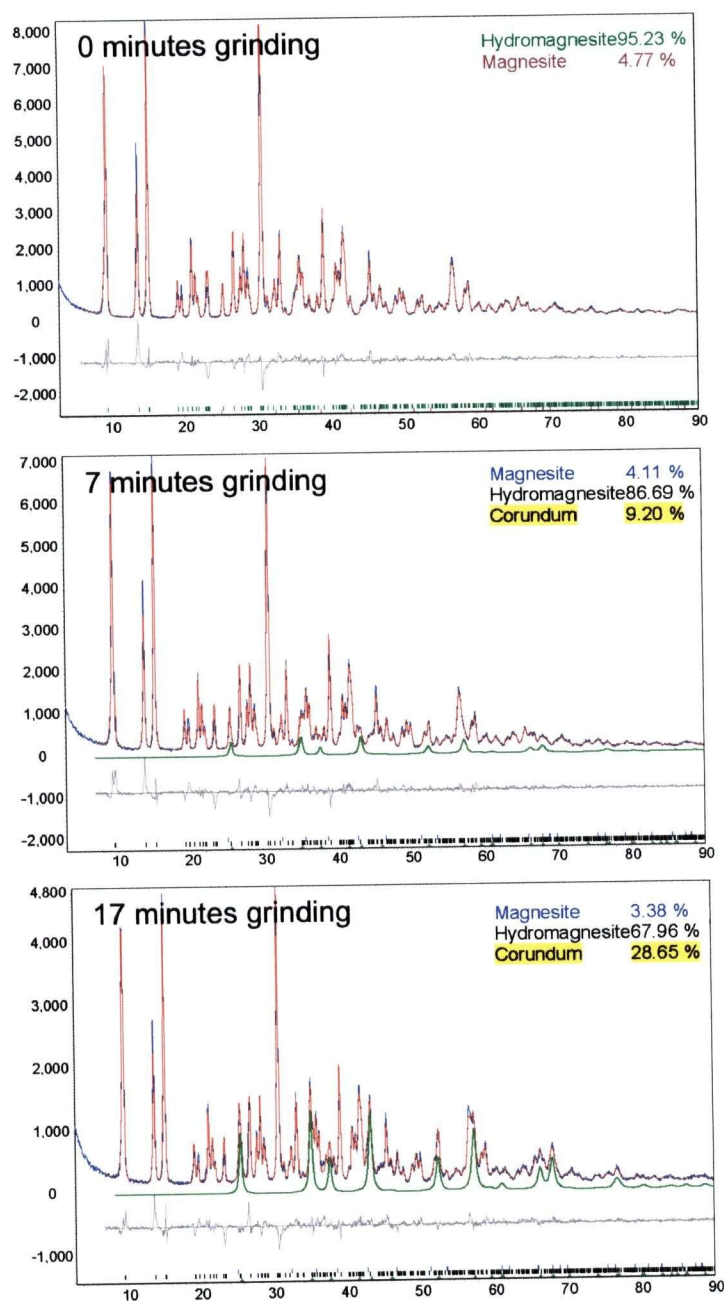


FIGURE 4.8: Refinement results used to determine the percent magnesite contamination in the “pure” hydromagnesite sample. Relative abundances of hydromagnesite and magnesite remain identical, with increased grinding, to within 5% relative. The curve within the observed pattern represents corundum contamination due to grinding.

Accurate determination of carbonate mineral abundances in synthetic geological samples bodes well for implementing the Rietveld method as a standard for assessing carbonate precipitation in mine tailings. Furthermore, this procedure can be applied to the measurement of acid neutralization potential of carbonate minerals in acid-generating mine tailings containing disordered mineral phases.

#### **4.3.2 Natural Mine Tailings**

Two samples of mine tailings from Cassiar, BC (04CA0601 and 03CA1601), and six samples from Clinton Creek, YT (04CC0702, 04CC0703, 04CC1001, 04CC1201, 04CC1401, and 05CC8) were analyzed using the method developed for synthetic serpentinites. Samples 03CA1601 and 04CC1401 are samples of bulk tailings. Samples 04CA0601, 04CC0703, 04CC1001, and 04CC1201 are from vertical carbonate crusts. 04CA0702 is a carbonate spire and 05CC8 is a sample containing disseminated carbonate cement. In addition, two samples from a hydromagnesite playa in Atlin, BC, were analyzed as an example of natural hydrated magnesium carbonate samples lacking serpentine. The results of quantitative phase analysis are given in Table 4.4.

Bulk samples from Clinton Creek and Cassiar contain serpentine in excess of 80 wt.% (Table 4.4). Where present, dolomite, magnesite, quartz, and pyroaurite constitute minor components; magnetite concentrations range from 5.1 to 8.1 wt.%. Bulk geochemical data for most samples give  $\text{Fe}_2\text{O}_3$  values in the range of 5 to 9 %, which is consistent with the results from Rietveld refinement, assuming that most of the iron was

TABLE 4.4: Results of quantitative phase analysis of natural serpentinite mine tailings renormalized to exclude 10% fluorite spike.

Locality	Cassiar	Cassiar	Clinton Creek	Clinton Creek	Clinton Creek	Clinton Creek	Clinton Creek	Clinton Creek	Clinton Creek	Clinton Creek	Atlin	Atlin
Predominant serpentinite phase	Chrysotile	Chrysotile	Chrysotile	Chrysotile	Chrysotile	Chrysotile	Chrysotile	Chrysotile	Chrysotile	Chrysotile	None	None
Mode	Bulk	Vertical Crust	Bulk	Spire	Spire Cap	Vertical Crust	Crust Cap	Vertical Crust	Vertical Crust	Cement	Playa	Playa
Phase	03CA1601	04CA0601	04CC1401	04CC0702	04CC0702	04CC0703	04CC0703	04CC1001	04CC1201	05CC8	03ATC3-A	03ATC3-I
Serpentine	87.62	89.42	88.35	77.95	59.49	81.33	32.34	81.13	83.33	77.30		
Palygorskite				1.63	4.37		2.82	1.17	1.52	1.52		
Magnetite	6.74	5.10	8.06	4.46	1.78	6.85	2.22	4.90	5.29	3.09		
Quartz	3.07		0.50	1.13	0.46	0.63	0.48	0.35	0.82			
Dolomite	2.56											
Magnesite			0.77			1.36		1.53	2.22	7.12	9.42	1.41
Nesquehonite	n/d	5.48	n/d	5.89	15.04	1.81	46.95	5.05				
Hydromagnesite	n/d	n/d	2.18	8.43	17.48	7.72	12.25	5.39	5.84	8.72	90.58	98.59
Pyroaurite			0.14	0.51	1.38	0.30	2.94	0.48		1.38		
Brucite									0.98	0.87		
Total	100.00	100.00	100.00	100.00	100.00	100.00	100.00	100.00	100.00	100.00	100.00	100.00
$\chi^2$	1.40	1.21	1.35	1.14	1.32	1.22	1.29	1.24	1.23	1.26	2.02	2.26
$R_{wp}$	8.06	6.77	7.74	6.37	7.05	6.92	6.47	7.01	7.04	7.02	8.87	9.71

\*  $\chi^2$  is the reduced chi-squared statistic for the least-squares fit.

†  $R_{wp}$  is the weighted pattern index, a function of the least-squares residual.

‡ n/d means that the mineral phase was not detected above the 1 wt.% limit.



partitioned into magnetite during serpentinization of the original peridotite (Wicks and Whittaker 1977).

The sample of bulk tailings from Cassiar (03CA1601) contains no detectable hydrated magnesium carbonate minerals to a detection limit of 1 wt.%, whereas the sample of bulk tailings from Clinton Creek (04CC1401) contains 2.2 wt.% hydromagnesite. The disseminated cement from Clinton Creek, 05CC8, contains 8.72 wt.% hydromagnesite. If the entire tailings pile at Clinton Creek contains hydromagnesite at the lower abundance found for 04CC1401, then a total of 82 000 tonnes of CO<sub>2</sub> bound within minerals at this site.

The crust samples (04CA0601, 04CC0703, 04CC1001, and 04CC1201) contain more than 5 wt.% hydrated magnesium carbonate minerals. These crusts, grown on vertical tailings surfaces, are readily identified in the field as hydrated carbonates based on colour, habit, and reaction to dilute HCl. The crust sampled from the tailings at Cassiar contains 5.5 wt.% nesquehonite. Sample 04CC0703 from Clinton Creek contains 7.7 wt.% hydromagnesite and 1.8 wt.% nesquehonite (Fig. 4.9). Analysis of the top 1 to 2 mm of sample 04CC0703 shows that it contains 47 wt.% nesquehonite and 12 wt.% hydromagnesite. The same trend is observed in the carbonate spire sample, 04CC0702 (and for 04CC1001 and 04CC1201); with increasing depth, below the surface of the carbonate crust or spire, hydromagnesite becomes more abundant than nesquehonite. Trace dypingite (below 1 wt.%) is observed in x-ray powder diffraction patterns for all the carbonate crust and spire samples. Dypingite is a metastable mineral phase, which can be created as nesquehonite decomposes to hydromagnesite (Davies and

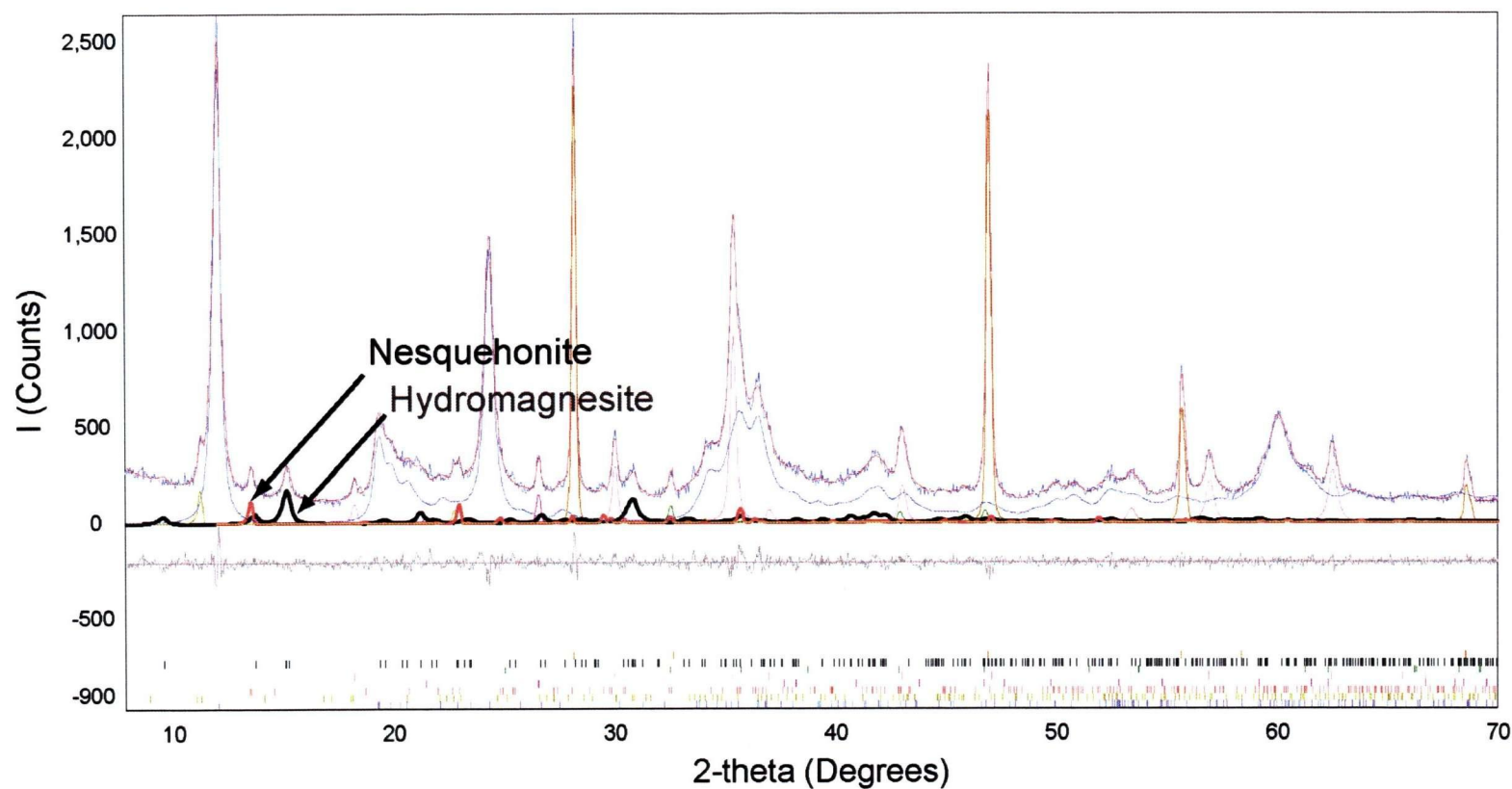


FIGURE 4.9: Rietveld refinement plot of a chrysotile mine residue from Clinton Creek, YT (04CC0703). Uppermost lines - observed data overlain by calculated pattern; black line below - residual pattern; vertical lines - positions of Bragg reflections for each phase; curves under the observed and calculated patterns - calculated patterns of each phase. Axes are intensity (counts) versus  $2\theta$  (degrees).

Bubela 1973; Canterford *et al.* 1984). Hydromagnesite in the tailings at Clinton Creek may be a product of the decomposition of nesquehonite forming in contact with the atmosphere. Decomposition of nesquehonite in mine tailings does not appear to be a function of humidity, but rather a function of age, with the metastable minerals forming at the interface between the tailings and the atmosphere, and the older carbonate precipitates dehydrating to increasingly stable mineral phases at depth (Fig. 4.10).

The core samples taken from the hydromagnesite swamp in Atlin, BC, both contained in excess of 90 wt.% hydromagnesite. A modern sample, 03ATC3-A, was taken from the top of the core at the surface of the swamp. 03ATC3-I was taken from a section 50.5 cm beneath the surface. A clear trend toward decreasing magnesite abundance with depth has been observed at Atlin, with sample 03ATC3-A possessing the most magnesite in the core and 03ATC3-I having the least. A series of previous studies of hydromagnesite playas located on the Cariboo Plateau, interior British Columbia, indicates that magnesite commonly becomes more abundant at depth within hydromagnesite mudflats on the periphery of alkaline playas, while magnesite dominates at the surface of modern lacustrine deposits during the summer months when the playas have desiccated (*e.g.*, Renaut and Long 1989; Renaut 1990; Renaut and Stead 1991). Possible cyanobacterially-mediated precipitation of magnesite has been observed in the laboratory by Thompson and Ferris (1990); however, direct precipitation of magnesite is thought to be kinetically inhibited in most lacustrine environments (refer to Zedef *et al.* 2000 for a brief review). The increased weight-percent abundance of magnesite at the

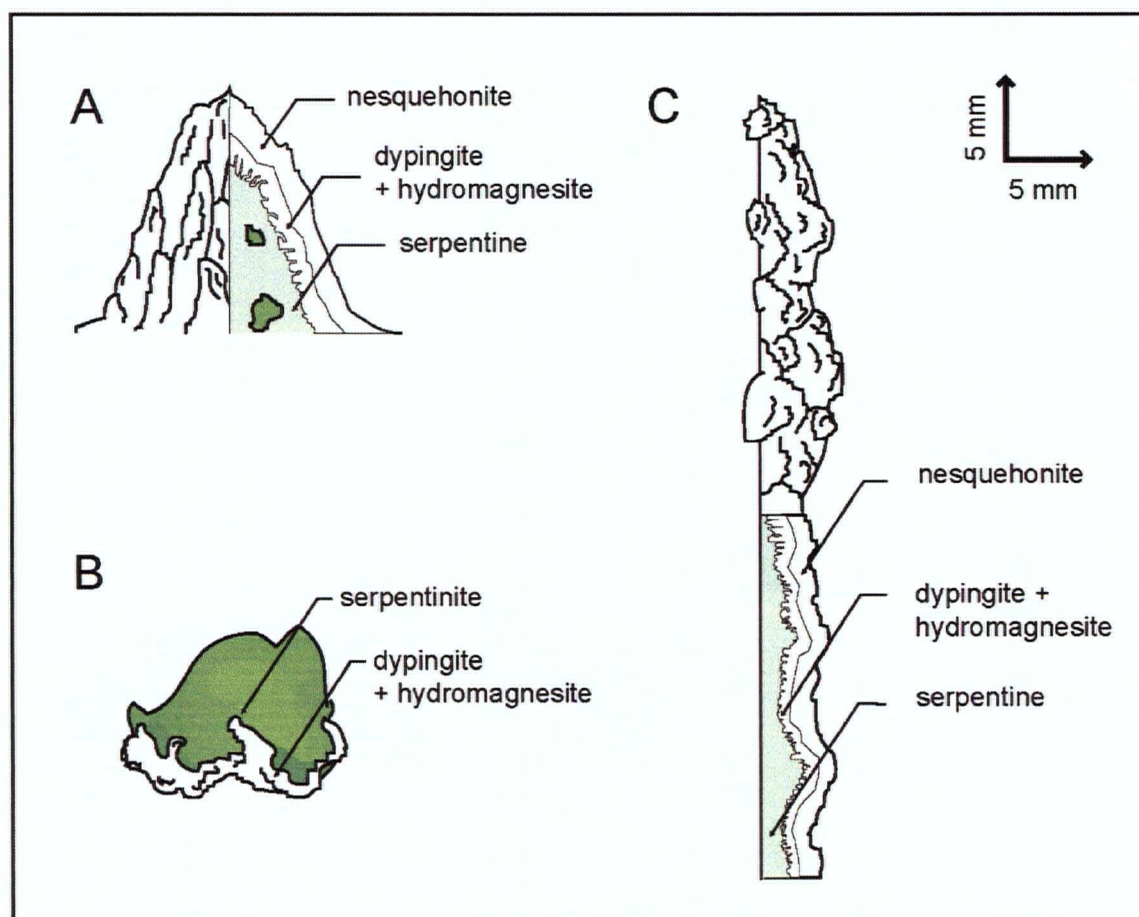


FIGURE 4.10: Detailed mineralogy for modal occurrences of hydrated magnesium carbonate crusts in serpentine-rich mine tailings: A) carbonate spire from horizontal tailings surface, B) crust on serpentinite cobble, and C) carbonate crust from vertical tailings surface.

surface of the Atlin playas may be the result of dehydration of hydromagnesite in contact with the atmosphere.

Hydromagnesite playas, like those found in Atlin, represent an analogue to the potential end-state of mineral carbonates in serpentinite mine tailings. These natural carbon sinks provide valuable insight into the long-term stability of hydrated magnesium carbonate minerals and the environmental impact of carbon disposal in mine tailings. Playa deposits at Atlin conformably overly glacial sediments (Grant 1987), suggesting an early Holocene age. Furthermore, a decrease in  $^{14}\text{C}$  content with depth in the Atlin playa deposits is consistent with hydromagnesite precipitation over the past several thousand years (Wilson and Dipple, unpublished data).

Possible evidence of decomposition of hydromagnesite to magnesite has been observed at depth within the playas of the Cariboo Plateau of interior British Columbia (Renaut and Stead 1991) and at the surface of the playas in Atlin. Morphological and isotopic similarities between modern hydromagnesite playas at Salda Gölü, western Turkey, and sedimentary magnesite deposits at Hirsizdere, Turkey, and Bela Stena, Serbia, may be demonstrative of large-scale diagenetic alteration of hydromagnesite to magnesite (Braithwaite and Zedef 1996; Zedef *et al.* 2000). The magnesite deposits at Hirsizdere are interbedded with Pliocene lacustrine sediments, indicating long-term stability of sedimentary magnesite on a geologic timescale. Provided that hydromagnesite playas generally dewater at depth, this process is analogous to the transformation of nesquehonite to dypingite followed by dehydration to hydromagnesite

(or dehydration of lansfordite to nesquehonite, which transforms to dypingite, etc.) with increasing depth within serpentinite mine tailings (Fig. 4.11).

Transformation of nesquehonite to magnesite in mine tailings would allow CO<sub>2</sub> to be stored in a mineral phase which is potentially stable on a timescale of millions of years. Disposal of CO<sub>2</sub> in magnesite optimizes both the thermodynamic stability and amount of bound carbon: nesquehonite, lansfordite, and magnesite have a CO<sub>2</sub> to Mg ratio of 1 per formula unit, while dypingite and hydromagnesite have a ratio of 4/5. During the decomposition of nesquehonite, one CO<sub>2</sub> molecule per formula unit is liberated to produce the more stable hydromagnesite phase. The optimal ratio of CO<sub>2</sub>:Mg is regained upon decomposition to magnesite. Magnesite production is widespread within hydromagnesite playas, and will likely be the end-product of mineral sequestration in serpentinite mine tailings.

The amount of atmospheric CO<sub>2</sub> that has been crystallographically bound in mineral form can be estimated from the Rietveld results for weight-percent abundance of hydrated magnesium carbonates (Table 4.5). A conservative estimate for total bound CO<sub>2</sub> can also be estimated using the refinement results for 03CC1601 for Cassiar and using 05CC8 and 04CC1401 to set the upper and lower limits, respectively, on bound CO<sub>2</sub> at Clinton Creek. As has been previously stated, a 5 to 15 % relative error is likely to apply to these estimates. This high degree of accuracy cannot be readily obtained with other methods of quantitative phase analysis.

Application of this method to other geologic systems should be approached with due caution. The Rietveld method for X-ray powder diffraction can only be used

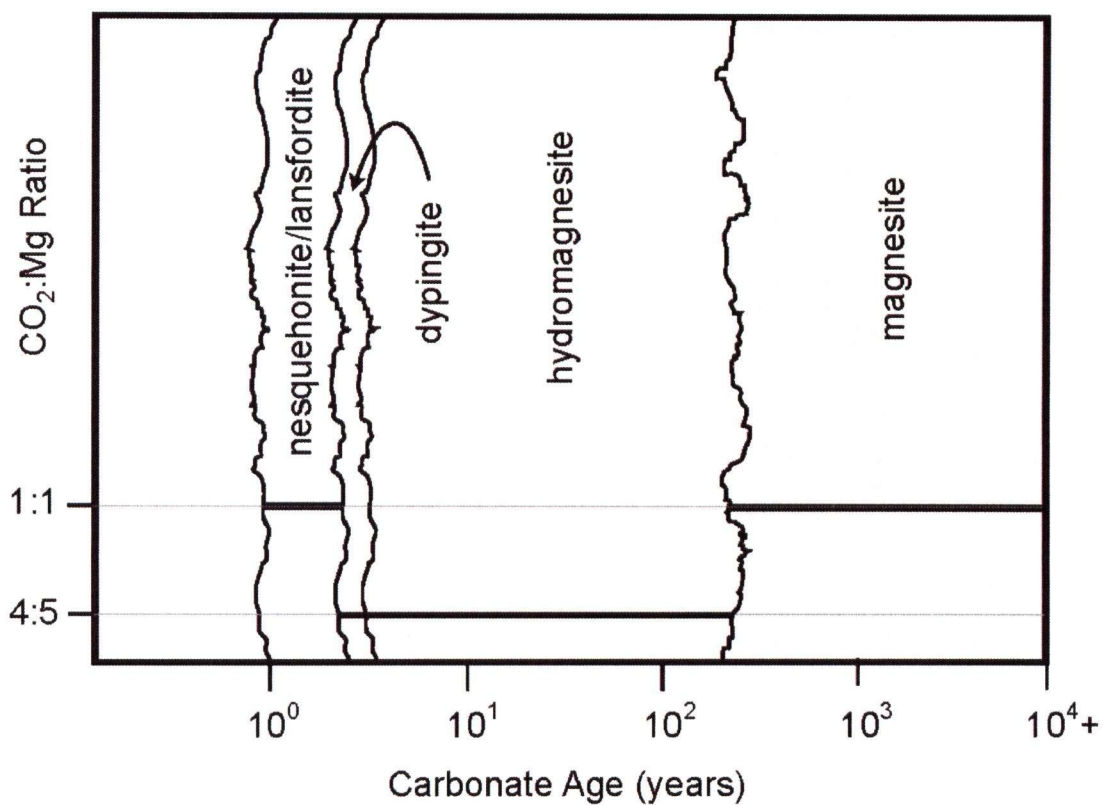


FIGURE 4.11: Evolution of magnesium-carbonate mineral phases and bound carbon per mole cation ( $\text{Mg}^{2+}$ ) during dehydration in a mine-tailings carbon-disposal site.

TABLE 4.5: Estimated amounts of atmospheric CO<sub>2</sub> crystallographically bound in serpentinite mine tailings.

Sample	Occurrence Type	CO <sub>2</sub> Sequestered (g/kg tailings)	CO <sub>2</sub> Potentially Sequestered (in tailings pile)
04CA1601	Bulk	<3.8	<64.6 kt <sup>†</sup>
04CA0601	Vertical Crust	17.4	
04CC1401	Bulk	8.2	82.0 kt <sup>‡</sup>
04CC0702	Spire	50.5	
04CC0703	Vertical Crust	34.8	
05CC8	Cement	32.8	328 kt <sup>‡</sup>

\* Where the upper limit on the amount of sequestration occurring in 04CA1601 has been calculated from the 1% detection limit.

† For 17 Mt of mine tailings at Cassiar, BC.

‡ For 10 Mt of mine tailings at Clinton Creek, YT.



indirectly as a tool for elemental analysis. As such, estimation of bound CO<sub>2</sub> is only feasible for phases with minor solid solution. Successful characterization of the tailings from Cassiar and Clinton Creek is due in part to the negligible solid solution to which the hydrated magnesium carbonate minerals are subject. This method does not account for additional amorphous phases and cannot be used to quantify more than one disordered phase per sample. The use of the Pawley method for complicated mineral phases may cause low-abundance mineral phases to be underestimated in refinements. Misestimates of disordered phases are likely to occur at low abundance (i.e., <5 wt.%) due to limitations in the fundamental parameters approach and preferred orientation corrections, and the way in which complex Pawley phases usurp peaks from other phases. The effect of grinding time on the crystallinity of ordered phases should be considered prior to application of this method to any geological or synthetic samples.

The efficacy and accuracy with which this refinement procedure can be applied to serpentine-rich samples allows for improved characterisation of many tailings materials. Carbon disposal *via* carbonation of serpentine minerals can be accurately quantified using the Rietveld method.

#### 4.4 REFERENCES

- Akao, M. and Iwai, S. (1977) The hydrogen bonding of hydromagnesite. *Acta Crystallographica*, Section B: Structural Crystallography and Crystal Chemistry, B33, 1273-1275.
- Al, T.A., Martin, C.J., and Blowes, D.W. (2000) Carbonate-mineral/water interactions in sulfide-rich mine tailings. *Geochimica et Cosmochimica Acta*, 64, 3933-3948.
- Batchelder, D.N. and Simmons, R.O. (1964) Lattice constants and thermal expansivities of silicon and of calcium fluoride between 6 and 322 °K. *Journal of Chemical Physics*, 41, 2324-2329.
- Bish, D.L. and Post, J.B. (1993): Quantitative mineralogical analysis using the Rietveld full-pattern fitting method. *American Mineralogist*, 78, 932-940.
- Blowes, D.W., Jambor, J.L., and Hanton-Fong, C.J. (1998) Geochemical, mineralogical and microbiological characterization of a sulphide-bearing carbonate-rich gold-mine tailings impoundment, Joutel, Québec. *Applied Geochemistry*, 13, 687-705.
- Braithwaite, C.J.R. and Zedef, V. (1996) Hydromagnesite stromatolites and sediments in alkaline lake, Salda Golu, Turkey. *Journal of Sedimentary Research*, 66, 991-1002.
- Brindley, G.W. (1945) The effect of grain or particle size on X-ray reflections from mixed powders and alloys, considered in relation to the quantitative determination of crystalline substances by X-ray methods. *Philosophy Magazine*, 36, 347-369.

- 
- BRUKER AXS (2004b) Topas V. 3.0: General Profile and Structure Analysis Software for Powder Diffraction Data. Bruker AXS, Germany.
- Canterford, J.H., Tsambourakis, G., and Lambert, B. (1984) Some observations on the properties of dypingite,  $\text{Mg}_5(\text{CO}_3)_4(\text{OH})_2 \cdot 5\text{H}_2\text{O}$ , and related minerals. *Mineralogical Magazine*, 48, 437-442.
- Catti, M., Ferraris, G., Hull, S., and Pavese, A. (1995) Static compression and H-disorder in brucite,  $\text{Mg}(\text{OH})_2$ , to 11 GPa: a powder neutron diffraction study. *Physics and Chemistry of Minerals*, 22, 200-206.
- Cheary, R.W. and Coelho, A.A. (1992) A fundamental parameters approach to X-ray line-profile fitting. *Journal of Applied Crystallography*, 25, 109-121.
- Chisholm, J.E. (1992) Powder-diffraction patterns and structural models for palygorskite. *Canadian Mineralogist*, 30, 61-73.
- Davies, P.J. and Bubela, B. (1973) The transformation of nesquehonite into hydromagnesite: *Chemical Geology*, 12, 289-300.
- De La Torre, A.G., Bruque, S., and Aranda, M.A.G. (2001) Rietveld quantitative amorphous content analysis. *Journal of Applied Crystallography*, 34, 196-202.
- Dipple, G.M., Raudsepp, M., and Gordon, T.M. (2002) Assaying wollastonite in skarn. In *Industrial Minerals in Canada*, Canadian Institute of Mining, Metallurgy and Petroleum Special Volume, 53, 303-312.
- Dollase, W.A. (1986) Correction of intensities for preferred orientation in powder diffractometry: application of the March model. *Journal of Applied Crystallography*, 19, 267-72.
-

- EMAN-North. (2003) Northern Contaminants Program: Local Contaminants Sources (Yukon): Clinton Creek Mine. Retrieved in 2004 from the Ecological Monitoring and Assessment Network for Northern Canada Website, Government of Canada: <http://www.emannorth.ca/ic/ds014/clinton.cfm>.
- Falini, F., Foresti, E., Gazzano, M., Gualtieri, A.F., Leoni, M., Lesci, I.G., and Roveri, N. (2004) Tubular-Shaped Stoichiometric Chrysotile Nanocrystals. *Chemistry – A European Journal*, 10, 3043-3049.
- Giester, G., Lengauer, C.L., and Rieck, B. (2000) The crystal structure of nesquehonite,  $\text{MgCO}_3 \cdot 3\text{H}_2\text{O}$ , from Lavrion, Greece. *Mineralogy and Petrology*, 70, 153-163.
- Glinnemann, J., King, H.E., Jr., Schulz, H., Hahn, T., La Placa, S.J., and Dacol, F. (1992) Crystal structures of the low-temperature quartz-type phases of silica and germanium dioxide at elevated pressure. *Zeitschrift fuer Kristallographie*, 198, 177-212.
- Grant, B. (1987) Magnesite, brucite and hydromagnesite occurrences in British Columbia. Province of British Columbia, Ministry of Energy, Mines and Petroleum Resources, Victoria, British Columbia, Open File, 1987-13.
- Gualtieri, A.F. and Artioli, G. (1995) Quantitative determination of chrysotile asbestos in bulk materials by combined Rietveld and RIR method. *Powder Diffraction*, 10, 269-277.
- Gualtieri, A.F. (2000) Accuracy of XRPD QPA using the combined Rietveld – RIR method. *Journal of Applied Crystallography*, 33, 267-278.

- Hill, R.J. and Howard, C.J. (1987) Quantitative phase analysis from neutron powder diffraction data using the Rietveld method. *Journal of Applied Crystallography*, 20, 467-474.
- Htoon, M. (1979) Geology of the Clinton Creek asbestos deposit, Yukon Territory. M.Sc. Thesis, University of British Columbia, Vancouver, British Columbia.
- Huot, F., Beaudoin, G., Hebert, R. Constantin, M., Bonin, G., and Dipple, G. (2003) Evaluation of Southern Quebec asbestos residues for CO<sub>2</sub> sequestration by mineral carbonation; preliminary results. Joint Annual Meeting of the Geological and Mineralogical Associations of Canada.
- IPCC (2001) Climate Change 2001: The Scientific Basis (Contribution of Working Group I to the Third Assessment Report of the Intergovernmental Panel on Climate Change). Retrieved August 2005 from the Website of the IPCC Secretariat, Geneva: [http://www.grida.no/climate/ipcc\\_tar/wg1/index.htm](http://www.grida.no/climate/ipcc_tar/wg1/index.htm).
- Jambor J.L. and Blowes D.W. (1991) Mineralogical study of low-sulphide, high-carbonate, arsenic-bearing tailings from the Delnite minesite, Timmins, Ontario. In Proceedings of the 2<sup>nd</sup> International Conference on the Abatement of Acidic Drainage (Montréal, Québec) 4, 173-197.
- Kloprogge, J.T., Martens, W.N., Nothdurft, L., Duong, L.V., and Webb, G.E. (2003) Low temperature synthesis and characterization of nesquehonite. *Journal of Materials Science Letters*, 22, 825-829.
- Kump, L.R., Brantley, S.L., and Arthur, M.A. (2000) Chemical weathering, atmospheric CO<sub>2</sub>, and climate. *Annual Review of Earth and Planetary Sciences*, 28, 611-667.

- Lackner, K.S. (2003) Climate change: A guide to CO<sub>2</sub> sequestration. *Science*, 300, 1677-1678.
- Lackner, K.S., Wendt, C.H., Butt, D.P., Joyce, G.L., and Sharp, D.H. (1995) Carbon dioxide disposal in carbonate minerals. *Energy*, 20, 1153-1170.
- Le Bail, A., Duroy, J., and Fourquet, J.L. (1988) Ab-initio structure determination of LiSbWO<sub>6</sub> by X-ray powder diffraction. *Materials Research Bulletin*, 23, 447-452.
- Le Bail, A. (2002) Le Bail method full saga. Retrieved January 2005 from the ALB Crystallography Website: <http://sdpd.univ-lemans.fr>.
- March, A. (1932) Mathematische theorie der regelung nach der korngestalt bei affiner deformation. *Zeitschrift für Kristallographie*, 81, 285-297.
- Markgraf, S.A. and Reeder, R.J. (1985) High-temperature structure refinements of calcite and magnesite. *American Mineralogist*, 70, 590-600.
- Maslen, E.N., Streltsov, V.A., Streltsova, N.R., and Ishizawa, N. (1995) Electron density and optical anisotropy in rhombohedral carbonates. III. Synchrotron x-ray studies of CaCO<sub>3</sub>, MgCO<sub>3</sub> and MnCO<sub>3</sub>. *Acta Crystallographica, Section B: Structural Science*, B51, 929-939.
- MINFILE (2005) Cassiar, 104P 005. Retrieved April 2005 from the BC Ministry of Energy and Mines MINFILE Digital Data Website: <http://www.em.gov.bc.ca/cf/minfile/search/search.cfm?mode=capbib&minfilno=104P%20%20005>.
- Olowe, A. (1995) Crystal structures of pyroaurite and sjogrenite. *Advances in X-Ray Analysis*, 38, 749-755.

- Orlhac, X., Fillet, C., Deniard, P., Dulac, A.M., and Brec, R. (2001) Determination of the crystallized fractions of a largely amorphous multiphase material by the Rietveld method. *Journal of Applied Crystallography*, 34, 114-118.
- Pacala, S. and Socolow, R. (2004) Stabilization wedges: solving the climate problem for the next 50 years with current technologies. *Science*, 305, 968-972.
- Paktunc, A.D. and Davé, N.K. (2002) Formation of secondary pyrite and carbonate minerals in the Lower Williams Lake tailings basin, Elliot Lake, Ontario, Canada. *American Mineralogist*, 87, 593-602.
- Pawley, G.S. (1981) Unit-cell refinement from powder diffraction scans. *Journal of Applied Crystallography*, 14, 357-361.
- Raudsepp, M., Pani, E., and Dipple, G.M. (1999) Measuring mineral abundance in skarn. I. The Rietveld method using X-ray powder-diffraction data. *The Canadian Mineralogist*, 37, 1-15.
- Raudsepp, M., and Pani, E. (2003) Application of Rietveld analysis to environmental mineralogy. In *Environmental Mineralogy of Mine Wastes* (Jambor, J.L., Blowes, D.W., and Ritchie, A.I.M., Eds.), Mineralogical Association of Canada Short Course, 31, 165-180.
- Renaut, R.W. (1990) Recent carbonate sedimentation and brine evolution in the saline lake basins of the Cariboo Plateau, British Columbia, Canada. *Hydrobiologia*, 197, 67-81.
- Renaut, R.W. and Long, P.R. (1989) Sedimentology of the saline lakes of the Cariboo Plateau, Interior British Columbia, Canada. *Sedimentary Geology*, 64, 239-264.

- Renaut, R.W. and Stead, D. (1991) Recent magnesite-hydromagnesite sedimentation in the playa basins of the Cariboo Plateau, British Columbia. Geological Fieldwork (BCGSB), Paper 1991-1, 279-288.
- Rietveld, H.M. (1967) Line profiles of neutron powder-diffraction peaks for structure refinement. *Acta Crystallographica*, 22, 151-152.
- Rietveld, H.M. (1969) A profile refinement method for nuclear and magnetic structures. *Journal of Applied Crystallography*, 2, 65-71.
- Rinaudo, C., Gastaldi, D., and Bulluso, E. (2003) Characterization of chrysotile, antigorite and lizardite by FT-Raman spectroscopy. *Canadian Mineralogist*, 41, 883-890.
- Ross, N.L. and Reeder, R.J. (1992) High-pressure structural study of dolomite and ankerite. *American Mineralogist*, 77, 412-421.
- Sundquist, E.T. (1985) Geological perspectives on carbon dioxide and the carbon cycle. In *The Carbon Cycle and Atmospheric CO<sub>2</sub>: Natural Variations Archean to Present*, (E.T. Sundquist and W.S. Broecker, Eds.) *Geophysical Monographs*, 32, 5-60.
- Thompson, J.B. and Ferris, F.G. (1990) Cyanobacterial precipitation of gypsum, calcite, and magnesite from natural alkaline lake water. *Geology*, 18, 995-998.
- Tsukimura, K., Sasaki, S., Kimizuka, N. (1997) Cation distributions in nickel ferrites. *Japanese Journal of Applied Physics, Part 1: Regular Papers, Short Notes & Review Papers*, 36, 3609-3612.



- Uehara, S. (1998) TEM and XRD study of antigorite superstructures. *Canadian Mineralogist*, 36, 1595-1605.
- Wicks, F.J. and O'Hanley, D.S. (1988) Serpentine Minerals: Structures and Petrology. In *Hydrous Phyllosilicates (Exclusive of Micas)*, edited by S.W. Bailey, *Reviews in Mineralogy*, Vol. 19 (Mineralogical Society of America), 91-167.
- Wicks, F.J. and Whittaker, E.J.W. (1977) Serpentine textures and serpentinization. *Canadian Mineralogist*, 14, 459-488.
- Wilson, S.A., Dipple, G.M., Anderson, R.G. and Raudsepp, M. (2003) Characterization of Clinton Creek mine residues and their suitability for CO<sub>2</sub> sequestration. *Yukon Geoscience Forum*.
- Wilson, S.A., Thom, J.M., Dipple, G.M., Raudsepp, M., and Anderson, R.G. (2005) Towards sustainable mining: uptake of greenhouse gases by mine tailings. *British Columbia and Yukon Chamber of Mines, Cordilleran Roundup*.
- Young, R.A. (1993) Introduction to the Rietveld Method. In *The Rietveld Method* (R.A. Young, Ed.), International Union of Crystallography, Oxford University Press, Great Britain.
- Zedef, V., Russell, M.J., Fallick, A.E., and Hall, A.J. (2000) Genesis of vein stockwork and sedimentary magnesite and hydromagnesite deposits in the ultramafic terranes of Southwestern Turkey: A stable isotope study. *Economic Geology*, 95, 429-446.

**CHAPTER V:*****Conclusions***

Atmospheric carbon dioxide is being crystallographically bound in hydrated magnesium carbonate minerals in the mine tailings piles at Clinton Creek, Yukon and Cassiar, B.C. Although the rate of natural mineral carbonation in mine tailings is trivial to the global carbon cycle, study of this process provides valuable insight into the pathways by which mineral carbonation occurs.

Metastable Mg-carbonate minerals grow as efflorescences on vertical and horizontal tailings surfaces, as coatings on cobbles of serpentinite, and as disseminated cements within the tailings. Magnesium cations are derived from weathering of chrysotile fibres and carbon dioxide and bicarbonate are brought into contact with Mg-rich solutions through dissolution in meteoric water. Precipitation of lansfordite and nesquehonite occurs subaerially by evaporation and/or freeze-out, at the surface of the mine tailings, giving rise to atmospheric values for  $\delta^{13}\text{C}$  and an evaporative  $\delta^{18}\text{O}$  signature. At depth within the tailings piles, within crusts and spires, and on the sheltered surfaces of serpentinite cobbles, dypingite and hydromagnesite are forming. These minerals precipitate under less extreme evaporative conditions and within an increasingly  $^{12}\text{C}$ -rich microbial atmosphere. The covariation in  $\delta^{13}\text{C}$  and  $\delta^{18}\text{O}$  values displayed for carbonate samples from Clinton Creek and Cassiar is representative of a transition between the subaerial, environment in which lansfordite and nesquehonite develop and the  $^{13}\text{C}$ -depleted, microbially-mediated environments in which dypingite

and hydromagnesite form. Isotopic fingerprinting has confirmed that the ultimate source of carbon dioxide for all hydrated magnesium carbonates is the atmosphere.

It may be feasible to modify historical and active tailings environments to increase the rate and scale of carbonation to achieve appreciable uptake of atmospheric CO<sub>2</sub>. One possibility is to mill the tailings more finely to increase surface area and thereby accelerate the rate of silicate dissolution. More thorough mechanical separation of individual fibres and fine milling of massive serpentine could increase the rate of silicate dissolution and CO<sub>2</sub> uptake from the atmosphere.

It may also be possible to mediate precipitation of magnesium carbonates with salinity, Mg/Ca ratios, and microbes; tailings environments may be re-engineered accordingly, driving carbonation reactions toward more stable phases such as hydromagnesite and magnesite. Skimming of carbonate crusts from the surface of tailings and subsequent indoor storage may become necessary in environments with high annual precipitation as a measure to prevent dissolution. Also, by uncovering fresh tailings surfaces it is likely to renew more vigorous reaction with the atmosphere.

The Rietveld method for X-ray powder diffraction data provides a precise and accurate means by which the amount of carbon dioxide bound in carbonate minerals can be quantified (Chapter 4). The characteristic planar disorder associated with the serpentine-kaolinite group minerals has been overcome using structureless pattern fitting and a mineral spike to model the disordered minerals as amorphous phases. The accuracy and precision of this refinement method has been tested using synthetic serpentine-rich mine tailings of known composition. Estimates of the abundance of

hydrated magnesium carbonates in these tailings have a precision of 5 to 15% relative for mineral species present in amounts greater than 10 wt.%. The application of this method to natural tailings samples from Clinton Creek and Cassiar has allowed for precise estimates of carbonate mineral content and crystallographically-bound atmospheric CO<sub>2</sub>. Rietveld results for mine tailings have been compared to mineralogically similar samples from a carbonate playa at Atlin, British Columbia. Possible dehydration of metastable hydrated magnesium carbonate phases to geologically stable minerals in mine tailings and carbonate playa lakes is representative of long-term stability of the products of mineral sequestration in mine tailings. Furthermore, evidence for microbially-mediated precipitation of dypingite and hydromagnesite in mine tailings suggests that mineral carbonation reactions can be driven to produce more stable hydrated magnesium carbonate phases in regions of high photosynthetic activity.

The Rietveld method for quantitative phase analysis and isotopic fingerprinting are an effective verification protocol for carbon storage in mine tailings. Stable and radiogenic isotopes confirm an atmospheric source for CO<sub>2</sub> and the Rietveld method quantifies crystallographic trapping.

The goal of this research has been to provide an initial characterization of natural mineral carbonation processes in the mine tailings environment and to introduce a procedure by which sequestration of atmospheric and anthropogenic carbon dioxide can be both confirmed and quantified. The next step in developing a framework for economically feasible, large-scale carbon sequestration in mine tailings will be to apply the results of this work to demonstration projects in active mining environments.

**APPENDIX A:*****Whole-rock geochemistry for Clinton Creek and Cassiar***

Bulk geochemical analysis was done on 22 samples from Cassiar and 21 samples from Clinton Creek for major element oxides, Ni, V, Zn and volatiles (Tables A1 and A2). The most striking distinction between the tailings samples from the two localities is the difference in CO<sub>2</sub> content. Carbon dioxide abundance at Cassiar ranges from  $0.29 \pm 0.01$  % to  $1.06 \pm 0.01$  %, while reaching values high as  $5.38 \pm 0.01$  % at Clinton Creek and averaging  $2.78 \pm 0.01$  %.

The high bedrock carbonate content of the tailings at Clinton Creek is expressed in the results for bulk geochemical analysis and carbon dioxide content can be quantified from these data. There is however, no means by which to determine the source; bedrock carbon, anthropogenic carbon, and atmospheric carbon are indistinguishable. The source of carbon must be identified by the fractionation of light stable isotopes, as has been done with carbon and oxygen (Chapter 3). The amount of atmospherically-derived carbon crystallographically-bound within carbonate mineral phases cannot be determined from these data, necessitating the use of the Rietveld method (Chapter 4).

TABLE A1: Bulk geochemical analyses for Cassiar. Results for the abundance of major element oxides are expressed as weight-percent values. Trace element abundances and detection limits are expressed in parts per million (ppm). The total iron present in each sample has been recalculated as Fe<sub>2</sub>O<sub>3</sub>. 3 $\sigma$  detection limits have been employed.

Sample	SiO <sub>2</sub>	TiO <sub>2</sub>	Al <sub>2</sub> O <sub>3</sub>	Fe <sub>2</sub> O <sub>3</sub>	MnO	MgO	CaO	Na <sub>2</sub> O	K <sub>2</sub> O	P <sub>2</sub> O <sub>5</sub>	Cr <sub>2</sub> O <sub>3</sub>	Ni	V	Zn	LOI	Total	CO <sub>2</sub> (%)	H <sub>2</sub> O-	H <sub>2</sub> O+
MMI03-1-1	39.33	0.021	1.37	7.83	0.082	38.09	0.19	0.12	0.12	0.011	4010	2028	44	13	12.97	100.74	0.32	2.62	11.09
MMI03-1-2	38.56	0.018	1.00	8.00	0.094	39.31	0.04	0.07	0.02	0.008	3592	2174	41	12	13.16	100.86	0.47	2.92	14.09
MMI03-1-3	38.47	0.024	1.14	9.14	0.100	38.35	0.04	0.07	0.04	0.009	4141	2214	38	21	12.79	100.81	0.35	2.62	10.66
MMI03-1-4	38.40	0.018	0.98	8.57	0.092	39.13	0.02	0.05	0.01	0.008	3618	2216	38	7	13.03	100.90	0.42	2.50	10.97
MMI03-1-5	38.01	0.016	0.99	9.09	0.087	38.75	0.03	0.03	0.01	0.008	3650	2279	42	9	13.14	100.76	0.35	2.79	10.98
MMI03-1-6	38.03	0.021	1.09	8.63	0.104	38.73	0.07	0.09	0.02	0.009	4582	2236	42	29	13.26	100.74	0.41	2.95	11.81
MMI03-1-7	38.23	0.019	1.05	8.73	0.103	38.83	0.10	0.05	0.01	0.008	4212	2246	42	20	13.07	100.85	0.35	3.06	11.88
MMI03-1-8	38.09	0.018	0.98	9.16	0.095	38.70	0.04	0.10	0.01	0.009	3503	2281	39	11	13.11	100.90	0.40	2.98	10.82
MMI03-1-9	38.28	0.025	1.10	9.99	0.101	37.77	0.12	0.08	0.05	0.009	3980	2295	45	20	12.79	100.95	0.40	1.18	9.93
MMI03-1-10	38.04	0.017	0.96	8.48	0.094	38.95	0.07	0.06	0.01	0.008	2959	2248	37	<d/l	13.43	100.64	0.48	0.91	9.51
MMI03-1-11	38.43	0.017	1.10	7.91	0.087	39.10	0.05	0.07	0.01	0.008	3609	2265	42	4	13.35	100.72	0.38	0.84	9.77
MMI03-1-12	38.58	0.028	1.18	8.86	0.093	38.30	0.22	0.07	0.02	0.009	3459	2261	42	8	12.96	100.90	0.33	2.05	10.07
03CA03-02	38.51	0.021	1.03	8.10	0.091	39.08	0.04	0.06	0.02	0.008	4062	2261	42	20	13.03	100.63	0.33	0.71	11.18
03CA06-01	39.55	0.022	1.11	7.36	0.094	38.55	0.10	0.05	0.04	0.011	3308	2166	43	7	13.29	100.73	0.66	0.37	11.65
03CA06-02	39.04	0.025	1.12	7.96	0.086	38.85	0.05	0.06	0.02	0.009	3422	2214	46	6	12.95	100.74	0.32	1.69	11.11
03CA06-03	39.22	0.031	1.22	7.69	0.094	38.76	0.16	0.05	0.02	0.009	3784	2260	44	12	12.76	100.62	0.34	2.24	10.35
03CA07-01	38.52	0.018	1.03	8.45	0.095	38.60	0.03	0.10	0.03	0.009	3338	2181	39	6	13.18	100.62	0.53	1.76	11.19
03CA07-02	38.73	0.019	1.08	8.23	0.100	38.77	0.02	0.09	0.03	0.010	4185	2231	41	30	13.03	100.76	0.46	0.09	11.60
03CA08-01	38.77	0.025	1.15	8.40	0.104	38.28	0.11	0.09	0.04	0.011	3597	2205	40	16	13.20	100.77	1.06	4.16	9.55
03CA08-02	38.36	0.021	1.07	9.13	0.101	38.15	0.06	0.08	0.03	0.010	3978	2341	40	21	12.93	100.58	0.42	0.33	17.28
03CA09-01	38.79	0.018	0.98	7.47	0.096	38.98	0.04	0.08	0.03	0.011	2787	2261	39	35	13.86	100.87	0.67	2.33	8.80
03CA09-02	38.12	0.015	0.94	9.04	0.092	38.84	0.03	0.04	0.01	0.008	3790	2130	38	13	13.13	100.86	0.29	0.35	9.90
Detection Limits	60	35	120	30	30	95	15	75	25	35	15	3	10	2	100		0.01%		

TABLE A2: Bulk geochemical analyses for Clinton Creek. Abundances of major element oxides are expressed as weight-percent values. Trace element abundances and detection limits are expressed in parts per million (ppm). The total iron present in each sample has been recalculated as Fe<sub>2</sub>O<sub>3</sub>. 3 $\sigma$  detection limits have been employed.

Sample	SiO <sub>2</sub>	TiO <sub>2</sub>	Al <sub>2</sub> O <sub>3</sub>	Fe <sub>2</sub> O <sub>3</sub>	MnO	MgO	CaO	Na <sub>2</sub> O	K <sub>2</sub> O	P <sub>2</sub> O <sub>5</sub>	Cr <sub>2</sub> O <sub>3</sub>	Ni	V	Zn	LOI	Total	CO <sub>2</sub> (%)	H <sub>2</sub> O-	H <sub>2</sub> O+
03CC01-A	36.62	0.030	0.93	7.90	0.093	38.82	0.50	0.04	0.01	0.009	4238	2288	33	12	15.16	100.77	2.71	0.48	10.38
03CC01-B	52.47	0.019	0.68	5.31	0.074	26.81	0.55	0.06	0.04	0.010	4867	1741	29	2	13.22	99.91	4.23	2.14	7.77
03CC01-C	37.81	0.044	1.31	7.19	0.100	37.45	0.52	0.07	0.04	0.012	4072	2090	34	21	15.20	100.37	3.08	0.67	9.53
03CC01-D	36.91	0.042	1.14	9.11	0.100	37.51	0.76	0.08	0.02	0.010	3976	2256	41	14	14.18	100.49	2.00	1.63	10.49
03CC0201A	33.76	0.026	0.71	9.09	0.098	37.72	0.82	0.09	0.02	0.009	4980	2539	23	9	17.48	100.58	5.21	1.83	10.92
03CC0201B	36.57	0.026	0.90	8.91	0.100	38.70	0.17	0.07	0.01	0.008	4191	2392	33	20	14.50	100.63	1.89	0.23	10.52
03CC0301A	36.77	0.054	1.32	8.24	0.078	36.80	1.25	0.07	0.09	0.019	2660	2260	36	<d/l	15.39	100.58	3.30	0.72	9.80
03CC0301B	35.86	0.029	1.13	6.90	0.066	39.45	0.18	0.06	0.01	0.009	25350	2315	45	41	14.26	100.73	1.47	0.34	8.92
03CC0401A	37.51	0.052	1.27	8.61	0.083	37.60	0.71	0.09	0.05	0.016	2423	2192	36	<d/l	14.47	100.92	1.97	3.22	9.86
03CC0401B	38.81	0.031	0.91	6.62	0.108	39.50	0.20	0.05	0.02	0.010	4185	2359	36	20	13.73	100.65	0.64	2.03	9.93
03CC0501A	36.71	0.037	1.02	8.38	0.074	38.26	0.53	0.06	0.04	0.013	2424	2136	34	<d/l	14.94	100.52	2.04	0.81	10.74
03CC0601A	37.04	0.046	1.12	8.02	0.090	38.36	0.61	0.04	0.03	0.013	3732	2614	34	<d/l	14.75	100.76	2.61	1.38	10.36
03CC0601B	36.72	0.036	1.05	8.50	0.099	38.58	0.36	0.06	0.01	0.010	3856	2373	39	9	14.70	100.75	1.51	0.77	9.23
03CC0701A	37.04	0.066	1.59	8.41	0.079	36.16	0.75	0.10	0.07	0.026	2140	2127	42	<d/l	15.86	100.58	5.38	0.62	9.60
03CC0701B	36.73	0.063	1.52	8.91	0.081	36.40	1.11	0.11	0.05	0.019	2192	2181	38	<d/l	14.85	100.28	2.95	3.51	9.99
03CC0801A	36.66	0.053	1.34	9.17	0.085	37.14	0.92	0.09	0.04	0.015	2579	2185	37	<d/l	14.73	100.72	2.94	3.05	9.76
03CC0801B	35.76	0.045	1.00	9.40	0.095	37.92	0.70	0.10	0.02	0.011	3841	2291	31	2	15.26	100.93	3.40	1.15	9.28
03CC0901A	36.85	0.058	1.42	9.21	0.083	36.98	0.87	0.08	0.05	0.018	2198	2129	40	<d/l	14.76	100.81	3.01	2.62	10.09
03CC0901B	39.13	0.039	0.69	5.27	0.058	39.63	0.51	0.07	0.01	0.011	4956	2596	21	<d/l	13.97	100.14	1.43	1.25	9.19
03CC1001A	35.04	0.038	1.09	9.19	0.088	37.22	1.15	0.07	0.03	0.014	2651	2329	37	<d/l	15.97	100.40	4.11	1.55	9.70
03CC1001B	36.10	0.036	1.01	8.89	0.087	38.12	0.75	0.08	0.02	0.010	2982	2325	33	<d/l	15.16	100.80	2.47	3.42	10.43
Detection Limits	60	35	120	30	30	95	15	75	25	35	15	3	10	2	100		0.01%		

**APPENDIX B:*****X-ray powder diffraction data for qualitative analysis*****SUMMARY OF MINE TAILINGS MINERALOGY**

The samples under study were collected during the 2003 and 2004 summer field seasons. In 2003, 23 samples were taken from Clinton Creek at the surface of the tailings pile by Bob Anderson. Bob Anderson, Gregory M. Dipple, and Mitch Mihalynuk collected forty samples from Cassiar at depths varying from 0 to 1.7 m below the surface of the tailings pile. These samples can be characterized as crust-like material, loose tailings, or bulk auger samples. Because samples were not specifically selected for carbonate mineral content, modal abundance of carbonate phases is low in the 03CC, 03CA, and MMI03 series of samples.

Having set some early constraints on the appearance and the occurrence of hydrated magnesium carbonate minerals in mine residues, the goal of the 2004 field season was to find and sample carbonate-rich crusts. During this season, 19 samples of surface tailings and 11 samples from the waste rock pile were collected from Clinton Creek. Fourteen samples were collected from the surface of the tailings pile and one sample was collected from the waste rock pile at Cassiar.

Mineralogical data, collected with XRPD and analysed using the ICDD PDF-4 Database in Bruker AXS Eva 10.0 software, are summarized in Tables B1, B2, B3, and



B4. X-ray powder diffractograms for all smear-mounted samples and two back-mounted Rietveld samples are ordered by sample name in Figures B1 through B120.

TABLE B1: Mineralogy of Cassiar samples collected during the 2003 field season.

Variety	Sample	Amphibole? (Actinolite)	Hydrated Magnesium Carbonates								Serpentine	Magnetite	Quartz	Chlorite	Brucite	Mica	Calcite	Dolomite	Magnesite	Siderite	Aragonite	Sample
			Confirmed Present?	Artinite	Barringtonite	Dypingite	Giorgosite	Hydromagnesite	Lansfordite	Nesquehonite												
Bulk Auger Samples	MMI03-1-1	none									+	+	+				+				+	MMI03-1-1
	MMI03-1-2	none									+	+	+	+								MMI03-1-2
	MMI03-1-3	none									+	+	+	+								MMI03-1-3
	MMI03-1-4	none									+	+										MMI03-1-4
	MMI03-1-5	none									+	+		+								MMI03-1-5
	MMI03-1-6	none									+	+	+	+			+					MMI03-1-6
	MMI03-1-7	none									+	+										MMI03-1-7
	MMI03-1-8	none									+	+	+	+								MMI03-1-8
	MMI03-1-9	none									+	+	+	+								MMI03-1-9
	MMI03-1-10	none									+	+		+								MMI03-1-10
	MMI03-1-11	none									+	+										MMI03-1-11
	MMI03-1-12	none									+	+	+	+				+				MMI03-1-12

+ Confirmed present by XRD  
 ? Near detection limit  
 † Non-fibrous actinolite  
 \* Major phase in sample

TABLE B1 (continued): Mineralogy of Cassiar samples collected during the 2003 field season.

Variety	Sample	Amphibole? (Actinolite)	Hydrated Magnesium Carbonates							Serpentine	Magnetite	Quartz	Chlorite	Brucite	Smectite/Montmorillonite	Calcite	Dolomite	Magnesite	Siderite	Aragonite	Sample
			Confirmed Present?	Artinite	Barringtonite	Dypingite	Giorgiosite	Hydromagnesite	Lansfordite	Nesquehonite											
Crust Samples	03CA01-02	none										+				+	+				03CA01-02
	03CA02-02	?									+	+									03CA02-02
	03CA04-02	none	?								+	+	+		+		+				03CA04-02
	03CA05-01	none									+	+									03CA05-01
	03CA05-02	none									+	+	+								03CA05-02
	03CA06-01	none									+	+	+								03CA06-01
	03CA08-01	none									+	+	+								03CA08-01
	03CA09-01	none									+	+	+					+			03CA09-01
	03CA11-01	none									+	+	+								03CA11-01
	03CA12-01	none									+	+									03CA12-01
	03CA15-01	none									+	+	+								03CA15-01

+ Confirmed present by XRD  
 ? Near detection limit  
 † Non-fibrous actinolite  
 \* Major phase in sample

TABLE B1 (continued): Mineralogy of Cassiar samples collected during the 2003 field season.

Variety	Sample	Amphibole? (Actinolite)	Hydrated Magnesium Carbonates							Serpentine	Magnetite	Quartz	Chlorite	Brucite	Diaspore	Calcite	Dolomite	Magnesite	Siderite	Aragonite	OPX	Sample
			Confirmed Present?	Artinite	Barringtonite	Dypingite	Giorgiosite	Hydromagnesite	Lansfordite	Nesquehonite												
Bulk (Loose Tailings) Samples	03CA02-01	none									+	+	+		+	+						03CA02-01
	03CA03-01	none									+	+	+									03CA03-01
	03CA03-02	none									+	+	+				+					03CA03-02
	03CA03-03	+									+	+	+									03CA03-03
	03CA03-04	none									+	+		+								03CA03-04
	03CA03-05	+									+	+	+	+								03CA03-05
	03CA04-01	none									+	+	+									03CA04-01
	03CA06-02	none									+	+	+	+								03CA06-02
	03CA06-03	none									+	+	+		+							03CA06-03
	03CA07-01	none									+	+	+									03CA07-01
	03CA07-02	none									+	+	+	+								03CA07-02
	03CA08-02	none									+	+	+									03CA08-02
	03CA09-02	none									+	+	+									03CA09-02
	03CA14-01	none									+	+										03CA14-01
	03CA15-02	none									+	+	+	+			+				+	03CA15-02
	03CA16-01	none									+	+	+				+				+	03CA16-01

+ Confirmed present by XRD  
 ? Near detection limit  
 + Non-fibrous actinolite  
 \* Major phase in sample

TABLE B2: Mineralogy of Cassiar samples collected during the 2004 field season. 04CA0601 is the only sample from Cassiar which has been found to contain hydrated magnesium carbonate minerals.

Variety	Sample	Amphibole? (Actinolite)	Hydrated Magnesium Carbonates								Serpentine	Magnetite	Quartz	Chlorite	Mica	Talc	Feldspar	Calcite	Dolomite	Magnesite	Aragonite	Monohydrocalcite	Smeectite/Montmorillonite	OPX	Sample
			Confirmed Present?	Artinite	Barringtonite	Dypingite	Giorgiosite	Hydromagnesite	Lansfordite	Nesquehonite															
Cobble Samples	04CA02-02A	+									+	+	+	+				+						+	04CA02-02A
	04CA02-02B	none									+	+						+							04CA02-02B
	04CA02-02C	none									+	+	+	+				+	+						04CA02-02C
	04CA02-02D	none									+	+	+					+			+				04CA02-02D
	04CA03-01A	none									+	+	+		+		+				+	+			04CA03-01A
	04CA03-02	+									+	+	+	+		+			+		+				04CA03-02
	04CA04-01	+									+	+									+				04CA04-01

+ Confirmed present by XRD  
 ? Near detection limit  
 † Non-fibrous actinolite  
 \* Major phase in sample



TABLE B2 (continued): Mineralogy of Cassiar samples collected during the 2004 field season. 04CA0601 is the only sample from Cassiar which has been found to contain hydrated magnesium carbonate minerals.

Variety	Sample	Amphibole? (Actinolite)	Hydrated Magnesium Carbonates								Serpentine	Magnetite	Quartz	Chlorite	Brucite	Talc	Feldspar	Calcite	Dolomite	Magnesite	Aragonite	Monohydrocalcite	Smectite/Montmorillonite	OPX	Sample
			Confirmed Present?	Artinite	Barringtonite	Dypingite	Giorgiosite	Hydromagnesite	Lansfordite	Nesquehonite															
Crust Samples	04CA01-01	none									+	+	+											+	04CA01-01
	04CA02-01	none									+	+	+												04CA02-01
	04CA02-04	none									+	+												+	04CA02-04
	04CA05-01	none									+	+													04CA05-01
	04CA06-01	none	+			+				+	+	+											+		04CA06-01
	04CA08-01	none									+	+													04CA08-01
	04CA09-01	none									+	+													04CA09-01
	04CA10-01	none									+	+						+			+				04CA10-01
Soil Samples	04CA02-03	none									+	+	+					+							04CA02-03
Mud Samples	04CA07-01	none									+	+													04CA07-01
	04CA07-02	none									+	+													04CA07-02

+ Confirmed present by XRD  
 ? Near detection limit  
 † Non-fibrous actinolite  
 \* Major phase in sample

TABLE B3: Mineralogy of Clinton Creek samples collected during the 2003 field season.

Variety	Sample	Amphibole? (Actinolite)	Hydrated Magnesium Carbonates							Serpentine	Magnetite	Quartz	Chlorite	Brucite	Mica	Talc	Calcite	Dolomite	Magnesite	Aragonite	Pyroaurite	Smectite/Montmorillonite Group	Sample
			Confirmed Present?	Artinite	Barringtonite	Dypingite	Giorgiosite	Hydromagnesite	Lansfordite	Nesquehonite													
Crust Samples	03CC01B	none	+			+				+	+	+						+	+		+		03CC01B
	03CC0201A	none	+					+			+	+						+	+		+		03CC0201A
	03CC0501A	none									+	+	+					+	+		+		03CC0501A
	03CC0601A	none									+	+	+	+				+	+		+		03CC0601A
	03CC0701A	none	+							+	+	+	+					+	+		+	+	03CC0701A
	03CC0801A	none									+	+	+				+	+	+		+		03CC0801A
	03CC0901A	none									+	+	+					+	+				03CC0901A
	03CC1001A	none	+			+		+			+	+	+				+	+	+		+		03CC1001A

+ Confirmed present by XRD  
 + Either or both phases denoted by this symbol are present  
 ? Near detection limit  
 † Non-fibrous actinolite  
 \* Major phase in sample

TABLE B3 (continued): Mineralogy of Clinton Creek samples collected during the 2003 field season.

Variety	Sample	Amphibole? (Actinolite)	Hydrated Magnesium Carbonates							Serpentine	Magnetite	Quartz	Chlorite	Brucite	Mica	Talc	Calcite	Dolomite	Magnesite	Aragonite	Pyroaurite	Smectite/Montmorillonite Group	Sample
			Confirmed Present?	Artinite	Barringtonite	Dypingite	Giorgiosite	Hydromagnesite	Lansfordite	Nesquehonite													
Bulk (Loose Tailings) Samples	03CC01A	none	+			+		+			+	+						+	+		+		03CC01A
	03CC01C	none	+			+				+	+	+						+	+				03CC01C
	03CC01D	none	+			+				+	+	+					+	+	+		+		03CC01D
	03CC0201B	none	+			+		+			+	+						+	+		+		03CC0201B
	03CC0301A	none									+	+	+				+	+	+		+	+	03CC0301A
	03CC0301B	none	+			+		+			+	+		+							+	+	03CC0301B
	03CC0401A	none									+	+	+					+	+		+	+	03CC0401A
	03CC0601B	none	+			+		+			+	+	+						+		+	+	03CC0601B
	03CC0701B	none									+	+	+					+	+				03CC0701B
	03CC0801B	none	+			+		+			+	+	+				+	+	+		+		03CC0801B
	03CC0901B	none									+	+					+	+	+		+		03CC0901B
	03CC1001B	none	+			+		+			+	+	+				+	+	+		+		03CC1001B
Mixture	03CC0401B	none	+			+					+	+	+						+		+	+	03CC0401B

+ Confirmed present by XRD  
 + Either or both phases denoted by this symbol are present  
 ? Near detection limit  
 † Non-fibrous actinolite  
 \* Major phase in sample



TABLE B4: Mineralogy of Clinton Creek samples collected during the 2004 field season and one sample from the 2005 season.

Variety	Sample	Amphibole? ( <i>Actinolite</i> )	Hydrated Magnesium Carbonates							Serpentine	Magnetite	Quartz	Chlorite	Brucite	Calcite	Dolomite	Magnesite	Aragonite	Pyroaurite	Hexahydrite	Epsomite	Gypsum	Smectite/Montmorillonite Group	Sample
			Confirmed Present?	<i>Artinite</i>	<i>Barringtonite</i>	<i>Dypingite</i>	<i>Giorgosite</i>	<i>Hydromagnesite</i>	<i>Lansfordite</i>	<i>Nesquehonite</i>														
Cobble Samples	04CC0104	none								+							+		+					04CC0104
	04CC0105	none	+			+		+		+	+								+					04CC0105
	04CC0107	none								+	+							+					+	04CC0107
	04CC0108	none								+	+	+						+	+				+	04CC0108
	04CC0109	none	+			+				+	+								+				+	04CC0109
	04CC0301	none								+						+	+							04CC0301
	04CC0401	none	+			+				+	+						+		+				+	04CC0401
	04CC1301	none								+						+	+							04CC1301
Bulk Samples	04CC1401	none	+					+		+	+	+					+		+					04CC1401
	05CC8	none	+					+		+	+			+			+		+				+	05CC8

+ Confirmed present by XRD  
 ? Near detection limit  
 † Non-fibrous actinolite  
 \* Major phase in sample

TABLE B4 (continued): Mineralogy of Clinton Creek samples collected during the 2004 field season.

Variety	Sample	Amphibole? ( <i>Actinolite</i> )	Hydrated Magnesium Carbonates							Serpentine	Magnetite	Quartz	Chlorite	Brucite	Calcite	Dolomite	Magnesite	Aragonite	Pyroaurite	Hexahydrite	Epsomite	Gypsum	Smectite/Montmorillonite Group	Sample
			Confirmed Present?	<i>Artinite</i>	<i>Barringtonite</i>	<i>Dypingite</i>	<i>Giorgiosite</i>	<i>Hydromagnesite</i>	<i>Lansfordite</i>	<i>Nesquehonite</i>														
Crust Samples	04CC0106	none	+			+				+	+	+											+	04CC0106
	04CC0111	none								+		+	+							+		+	+	04CC0111
	04CC0201A	none	+			+			+	+	+								+					04CC021A
	04CC0201B	none	+			+			+	+	+													04CC021B
	04CC0202A	none	+			+				+										+	+			04CC022A
	04CC0202B	none	+			+				+										+	+			04CC022B
	04CC0601A	none	+			+				+	+	+					+		+					04CC0601A
	04CC0601B-CA	none	+			+		+		+	+	+							+				+	04CC0601B-CA
	04CC0601B-CB	none	+			+				+													+	04CC0601B-CB

+ Confirmed present by XRD  
 ? Near detection limit  
 † Non-fibrous actinolite  
 \* Major phase in sample

TABLE B4 (continued): Mineralogy of Clinton Creek samples collected during the 2004 field season.

Variety	Sample	Amphibole? ( <i>Actinolite</i> )	Hydrated Magnesium Carbonates								Serpentine	Magnetite	Quartz	Chlorite	Brucite	Calcite	Dolomite	Magnesite	Aragonite	Pyroaurite	Hexahydrite	Epsomite	Gypsum	Smectite/Montmorillonite Group	Sample
			Confirmed Present?	<i>Artinite</i>	<i>Barringtonite</i>	<i>Dypingite</i>	<i>Giorgiosite</i>	<i>Hydromagnesite</i>	<i>Lansfordite</i>	<i>Nesquehonite</i>															
Crust Samples	04CC0701	none	+			+		+		+	+									+				+	04CC0701
	04CC0703	none	+			+		+		+	+														04CC0703
	04CC0901	none	+			+					+	+								+	+				04CC0901
	04CC1001	none	+			+		+		+	+	+					+								04CC1001
	04CC1101	none	+			+		+		+	+														04CC1101
	04CC1201	none	+			+		+		+	+	+					+			+				+	04CC1201
Chrysotile Mat Samples	04CC0101	none									+	+	+	+		+	+		+					+	04CC0101
	04CC0102	none									+	+		+		+	+								04CC0102
Chrysotile	04CC0110	none									+														04CC0110
Spire & Q-tip Samples	04CC0702	none	+			+		+		+	+	+								+				+	04CC0702
	04CC0801	none	+			+				+	+	+	+							+					04CC0801
	04CC0902	none	+			+		+		+	+	+	+				+	+						+	04CC0902

+ Confirmed present by XRD  
 ? Near detection limit  
 † Non-fibrous actinolite  
 \* Major phase in sample

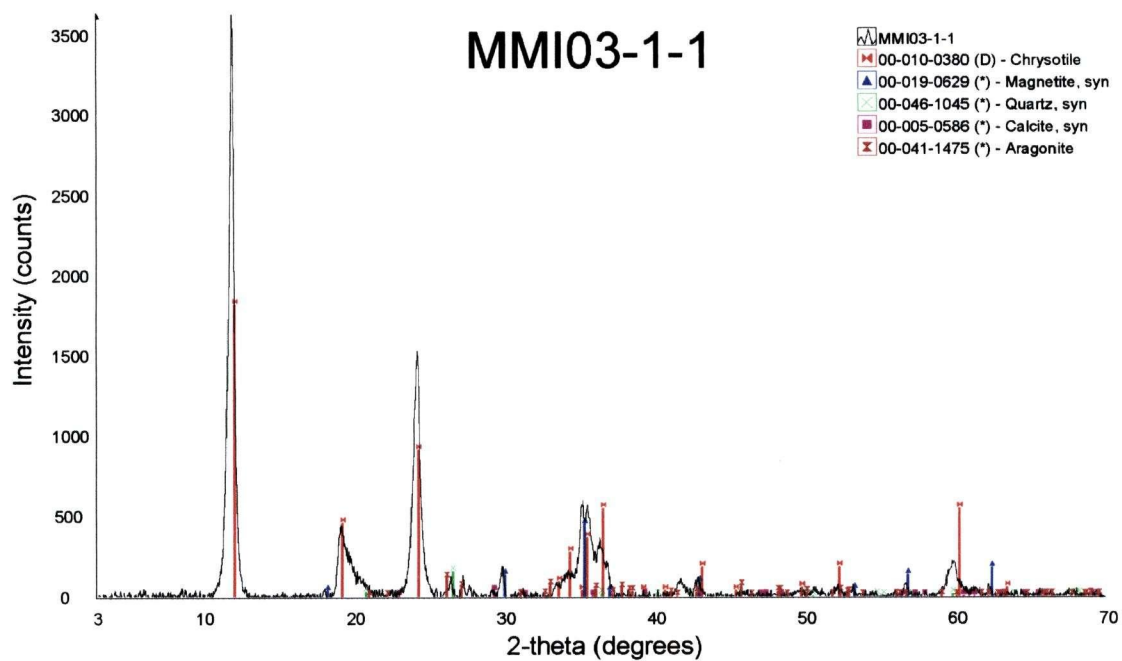


FIGURE B1: X-ray diffractogram for MMI03-1-1.

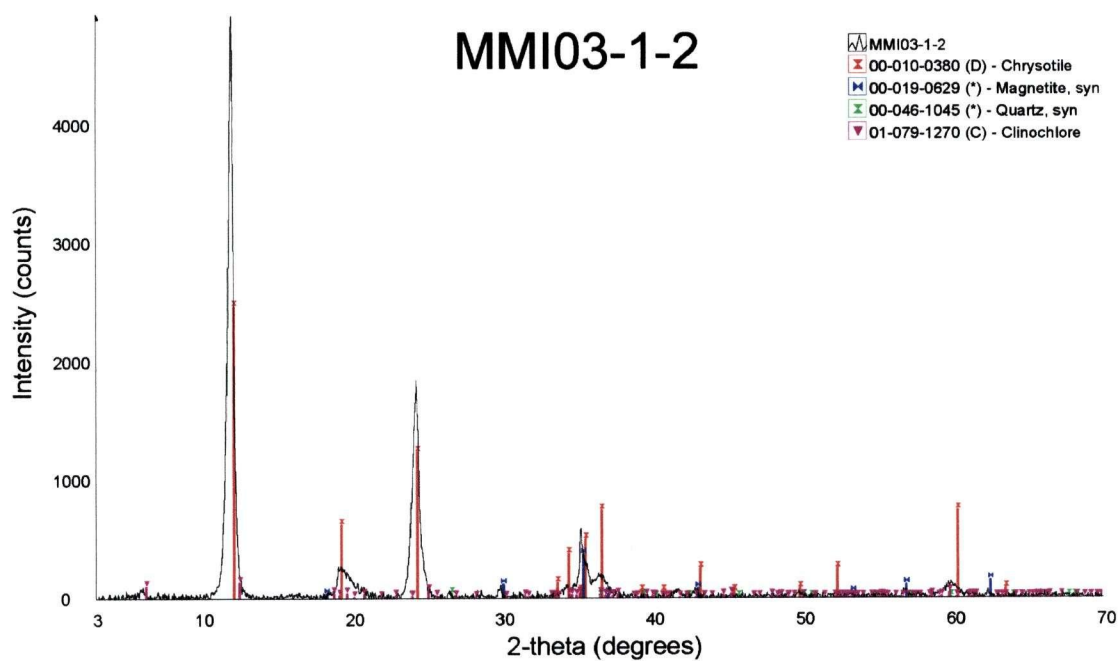


FIGURE B2: X-ray diffractogram for MMI03-1-2.

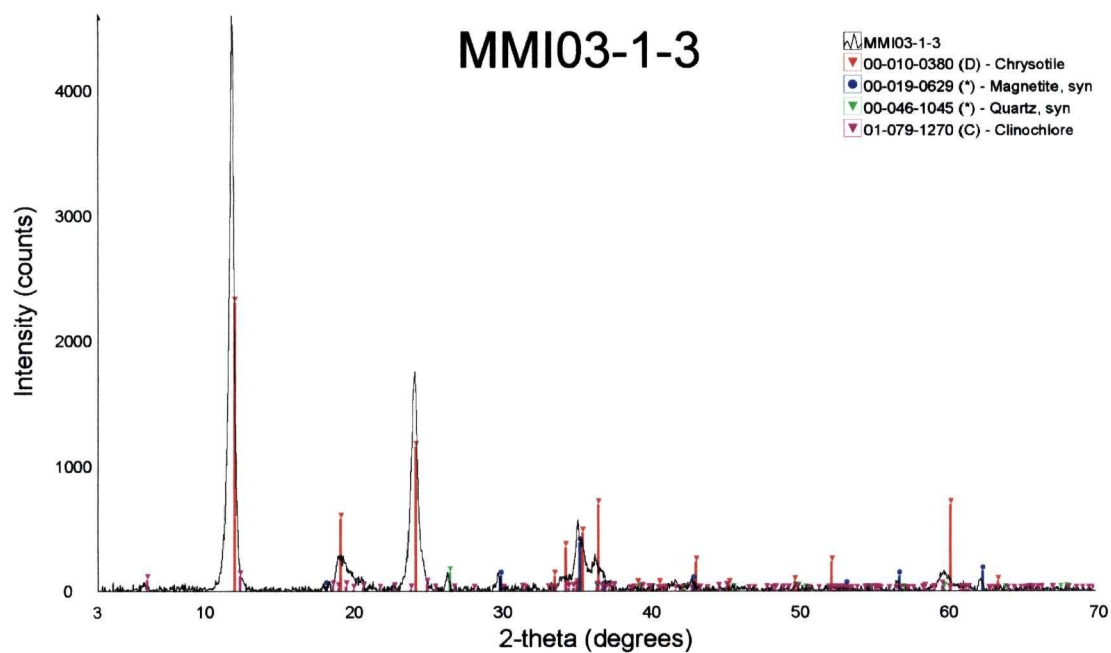


FIGURE B3: X-ray diffractogram for MMI03-1-3.

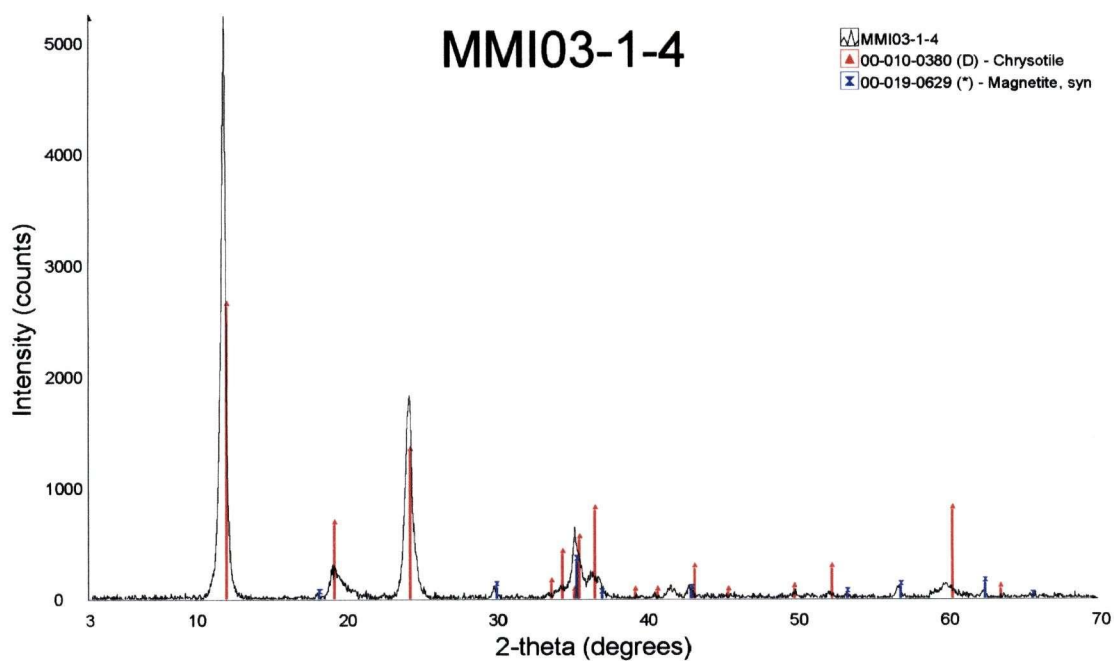


FIGURE B4: X-ray diffractogram for MMI03-1-4.



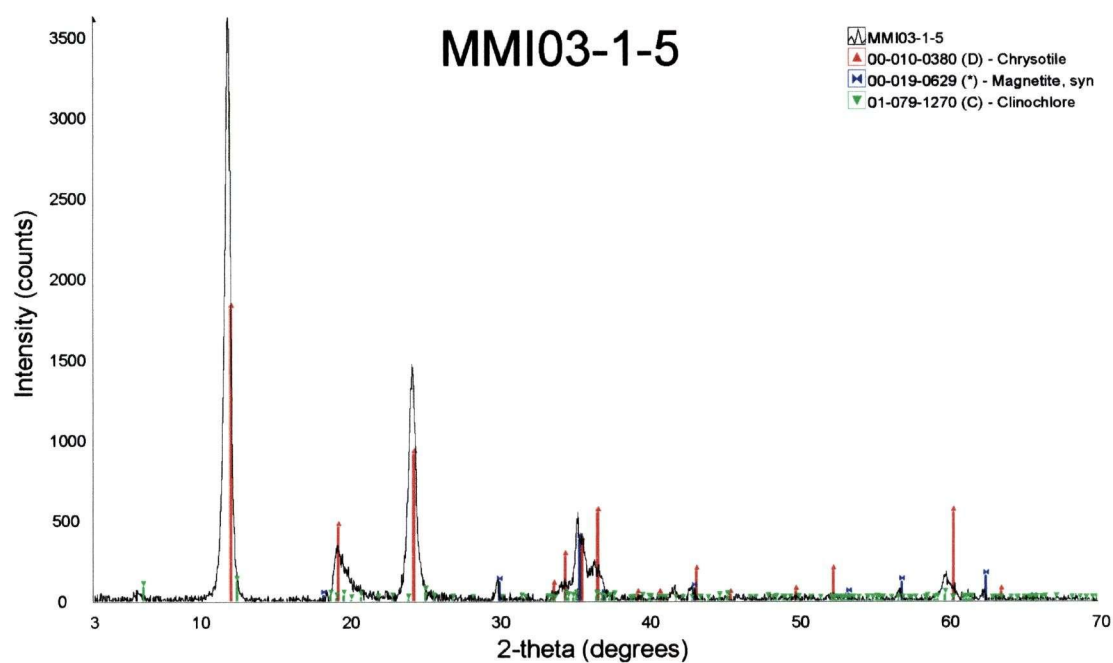


FIGURE B5: X-ray diffractogram for MMI03-1-5.

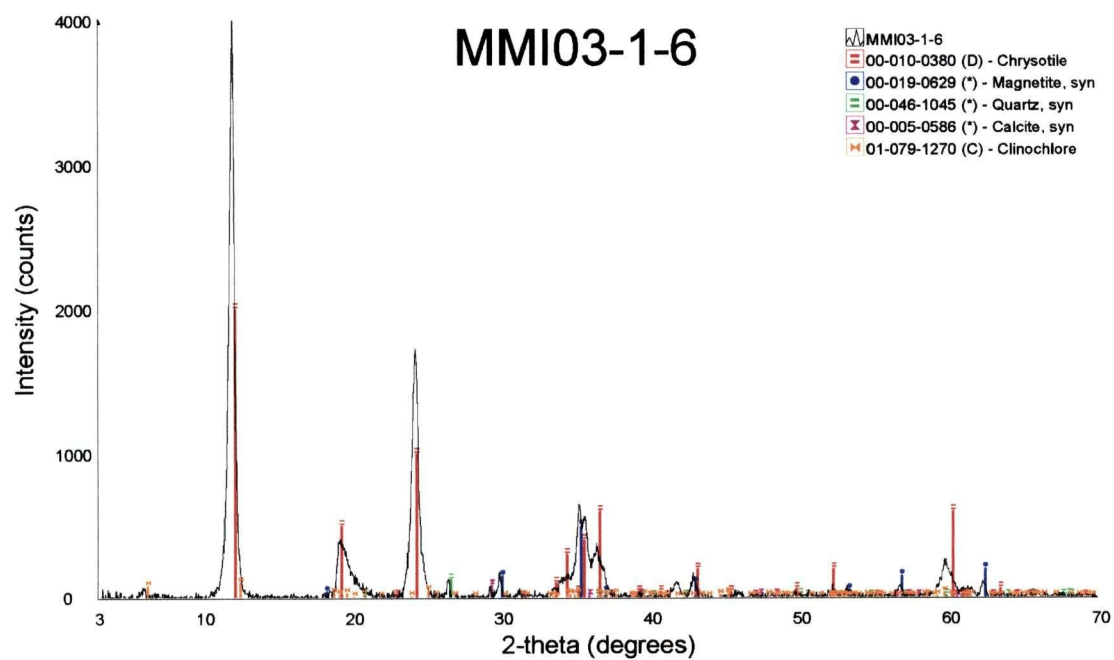


FIGURE B6: X-ray diffractogram for MMI03-1-6.

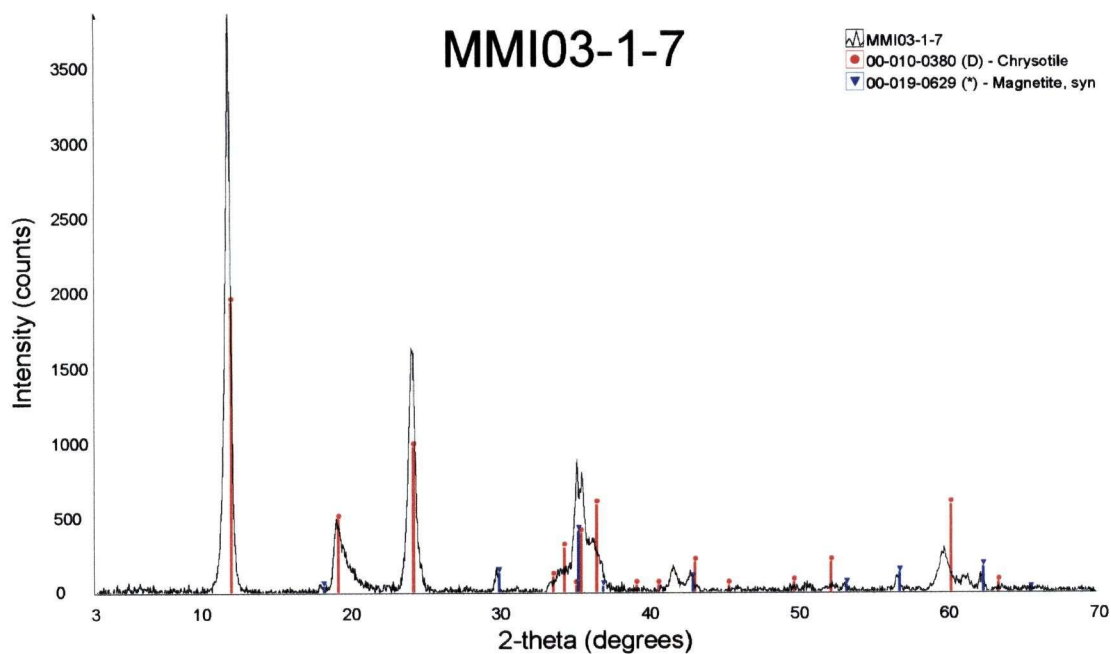


FIGURE B7: X-ray diffractogram for MMI03-1-7.

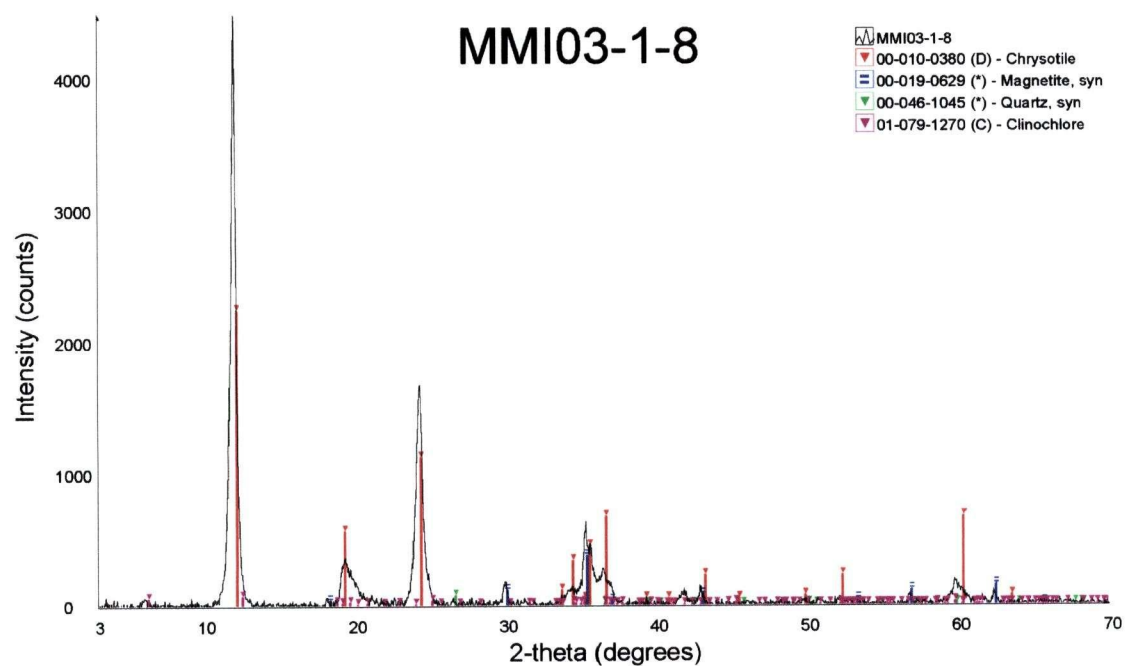


FIGURE B8: X-ray diffractogram for MMI03-1-8.

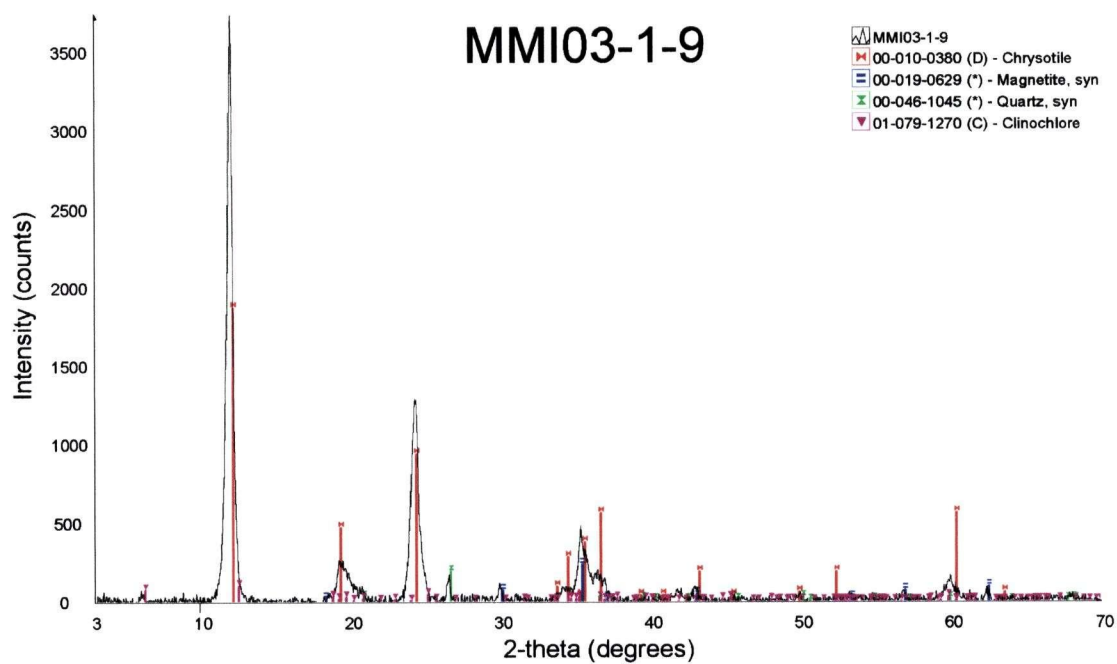


FIGURE B9: X-ray diffractogram for MMI03-1-9.

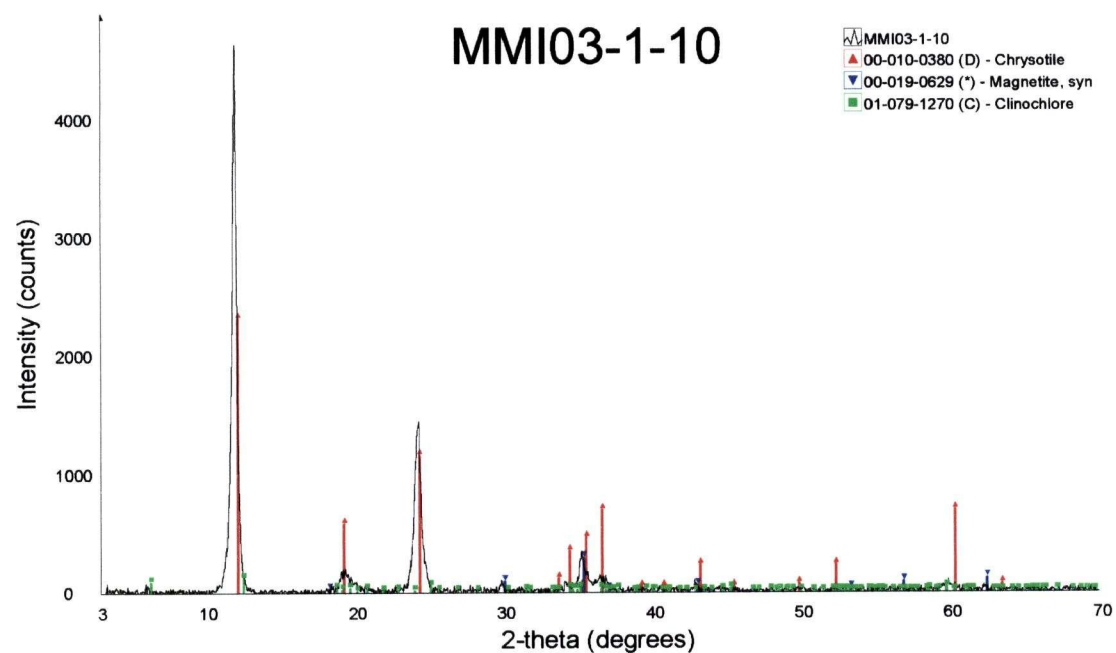


FIGURE B10: X-ray diffractogram for MMI03-1-10.



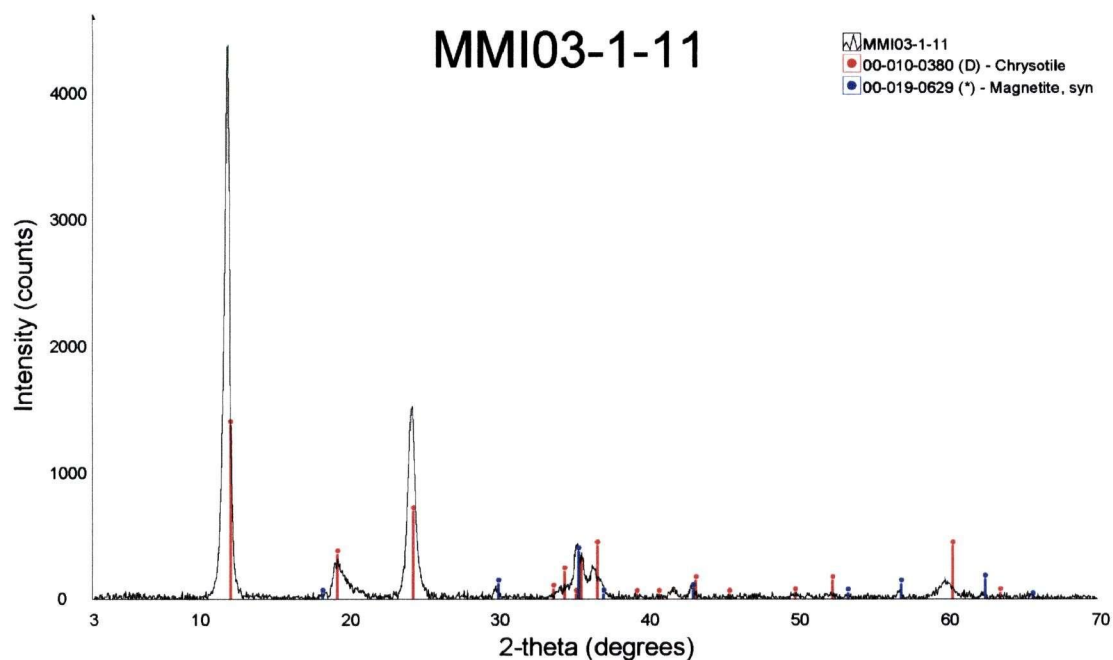


FIGURE B11: X-ray diffractogram for MMI03-1-11.

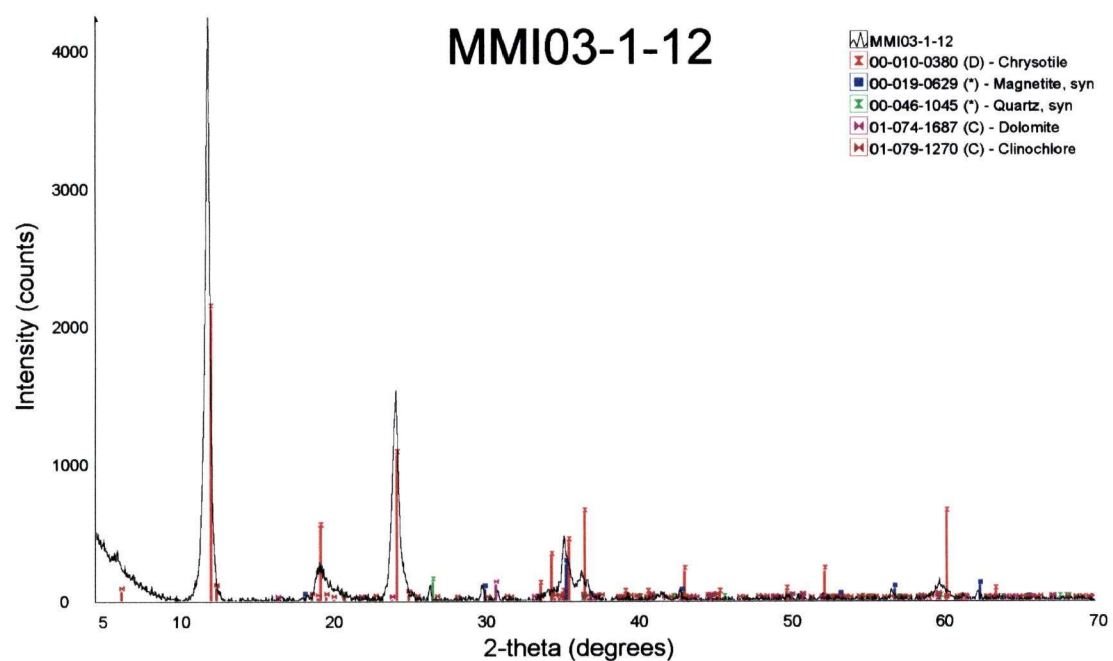


FIGURE B12: X-ray diffractogram for MMI03-1-12.

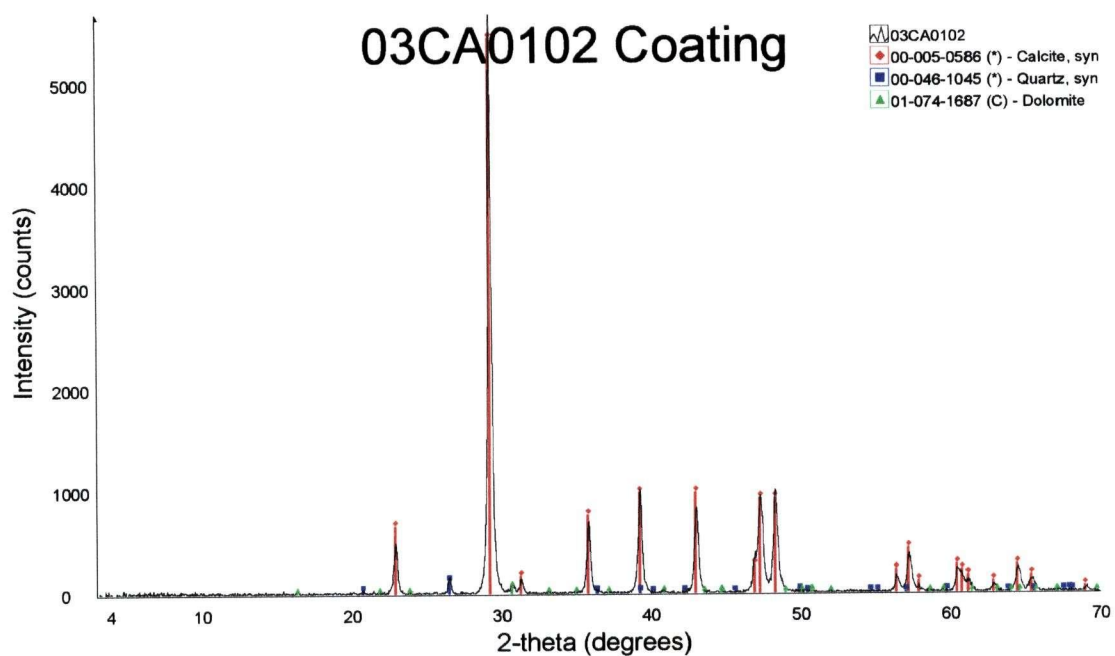


FIGURE B13: X-ray diffractogram for calcite coating on 03CA0102.

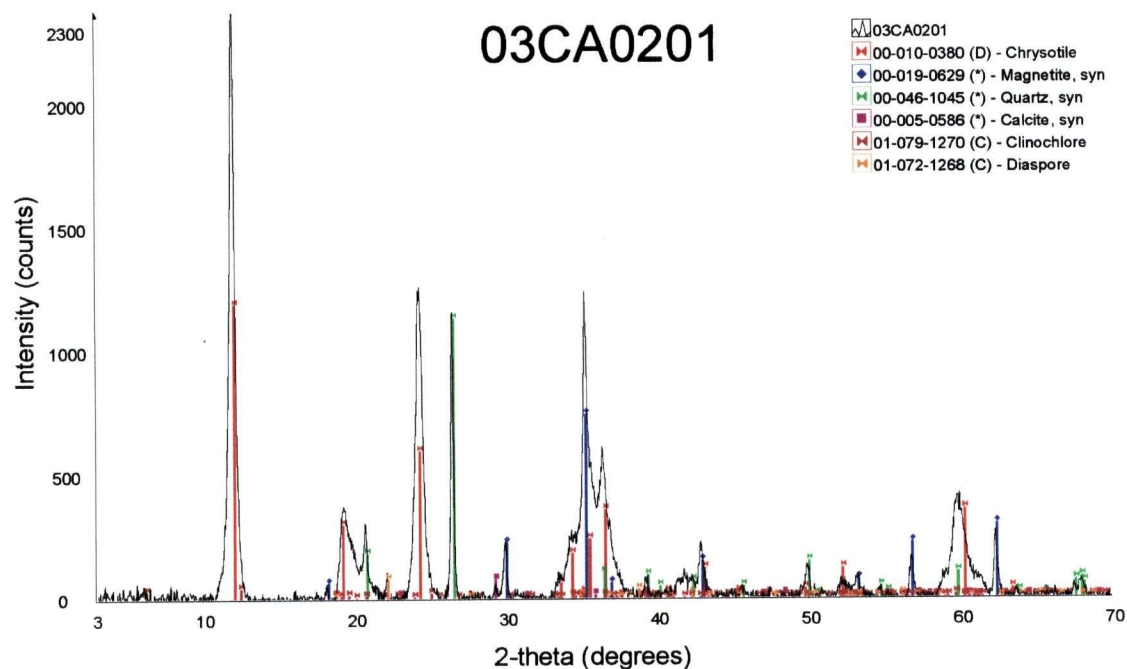


FIGURE B14: X-ray diffractogram for 03CA0201.

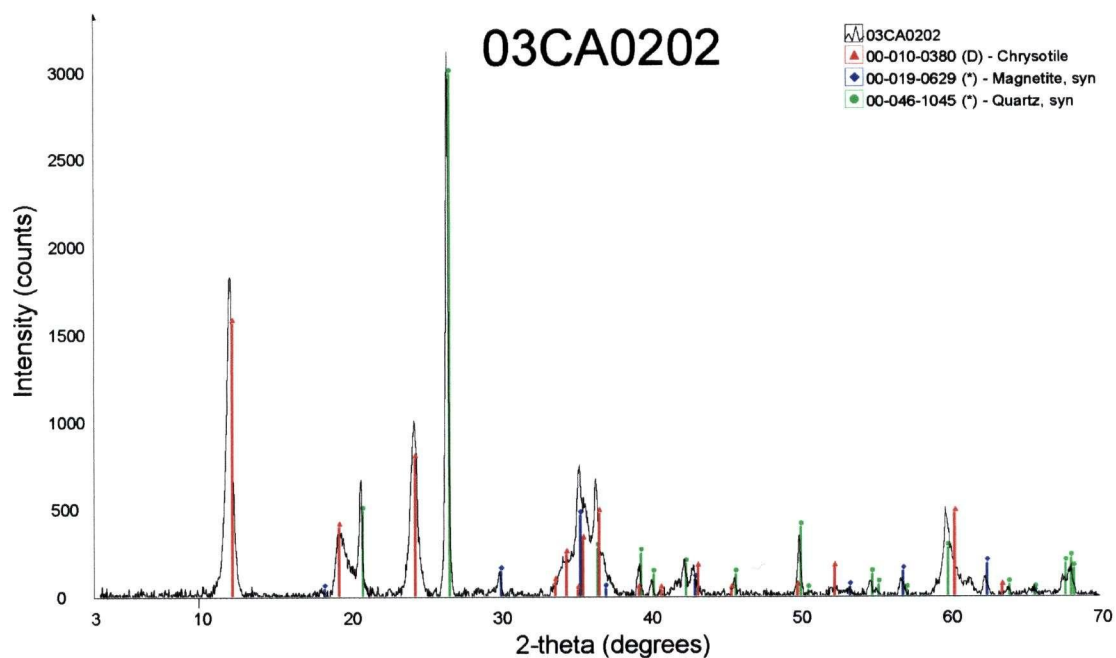


FIGURE B15: X-ray diffractogram for 03CA0202.

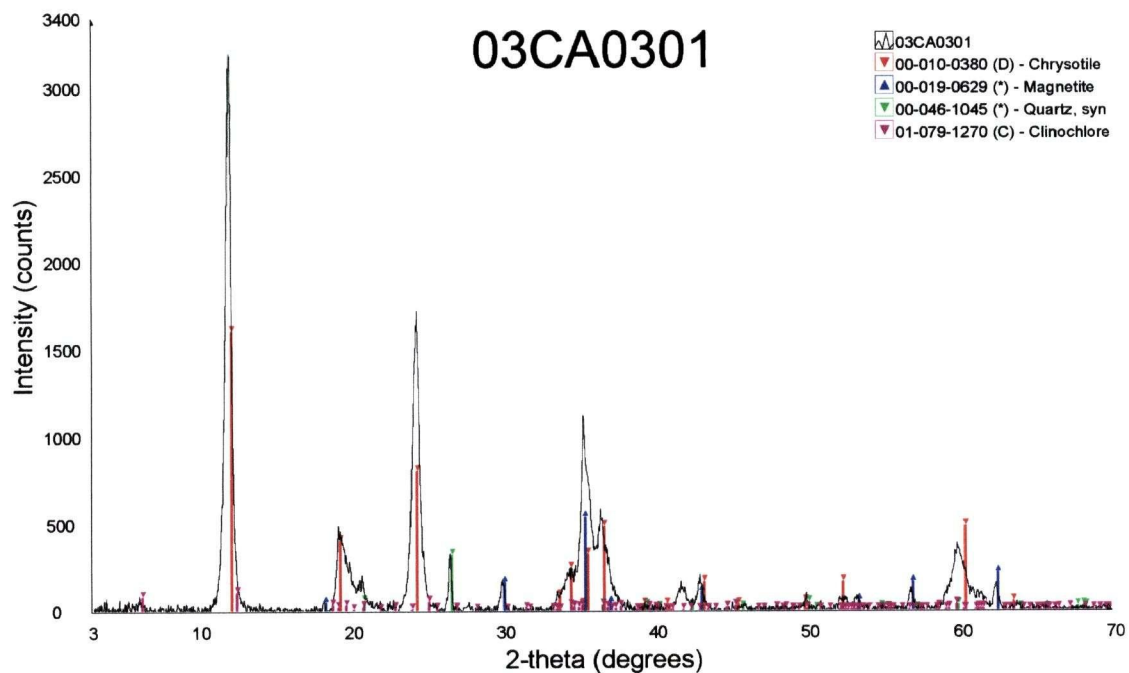


FIGURE B16: X-ray diffractogram for 03CA0301.

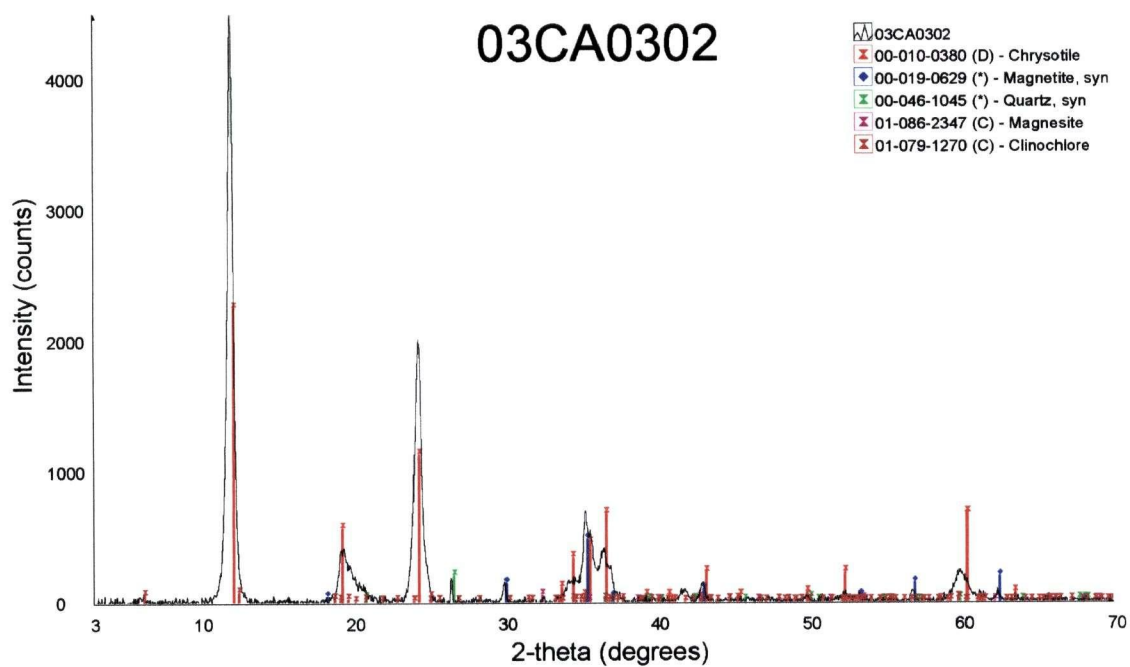


FIGURE B17: X-ray diffractogram for 03CA0302.

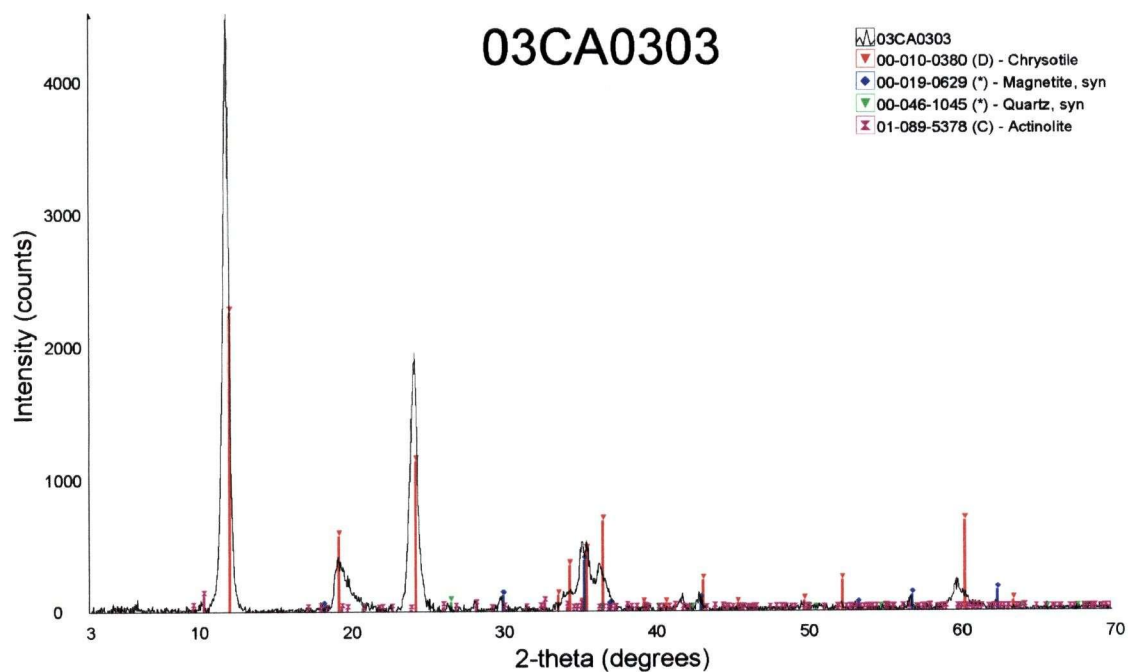


FIGURE B18: X-ray diffractogram for 03CA0303.

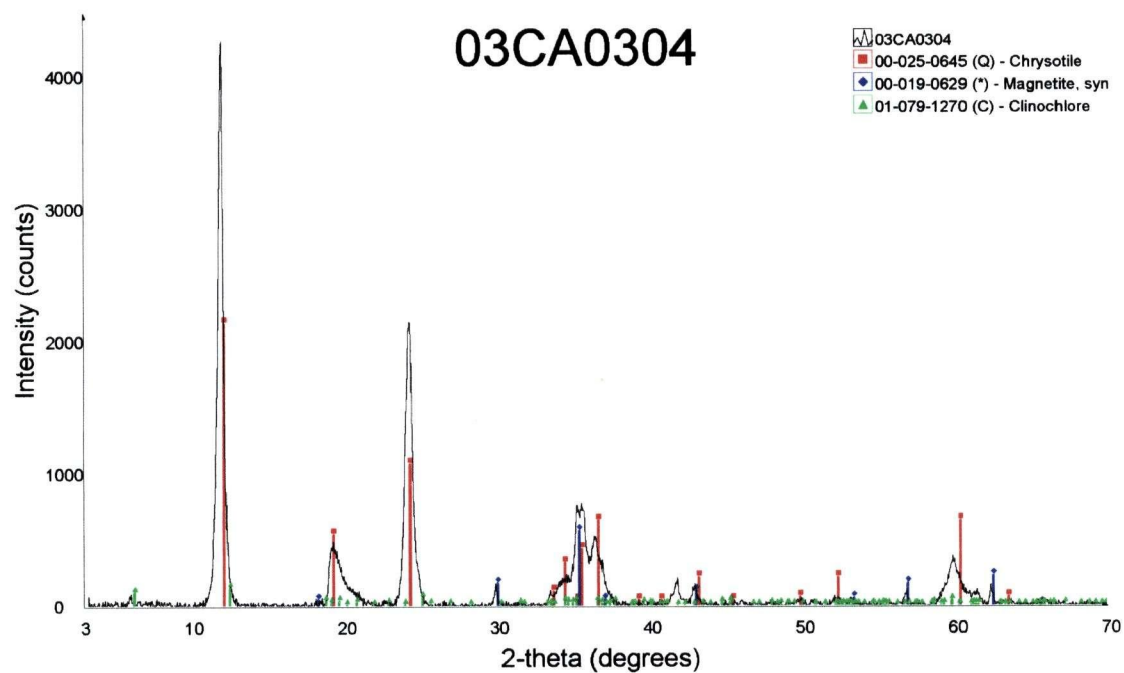


FIGURE B19: X-ray diffractogram for 03CA0304.

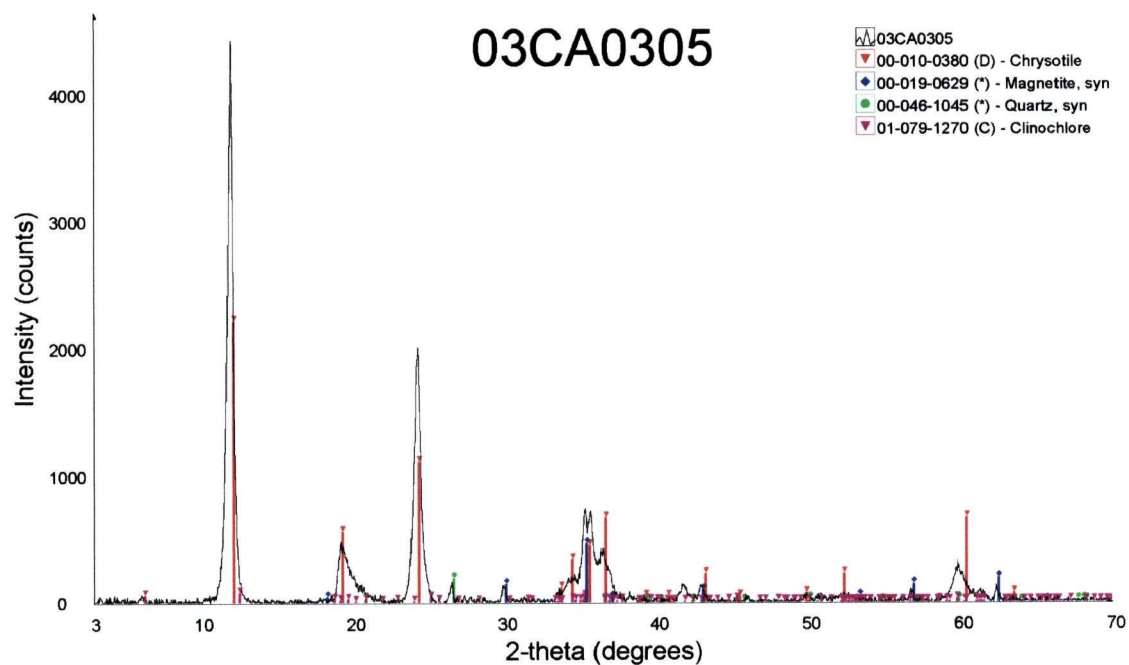


FIGURE B20: X-ray diffractogram for 03CA0305.

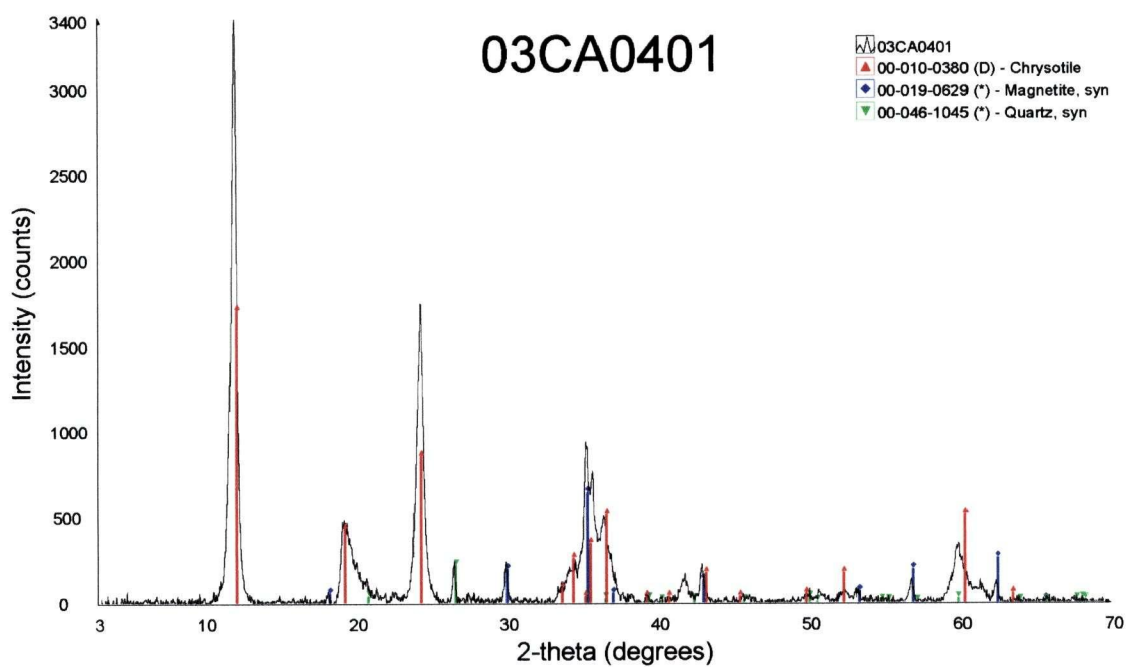


FIGURE B21: X-ray diffractogram for 03CA0401.

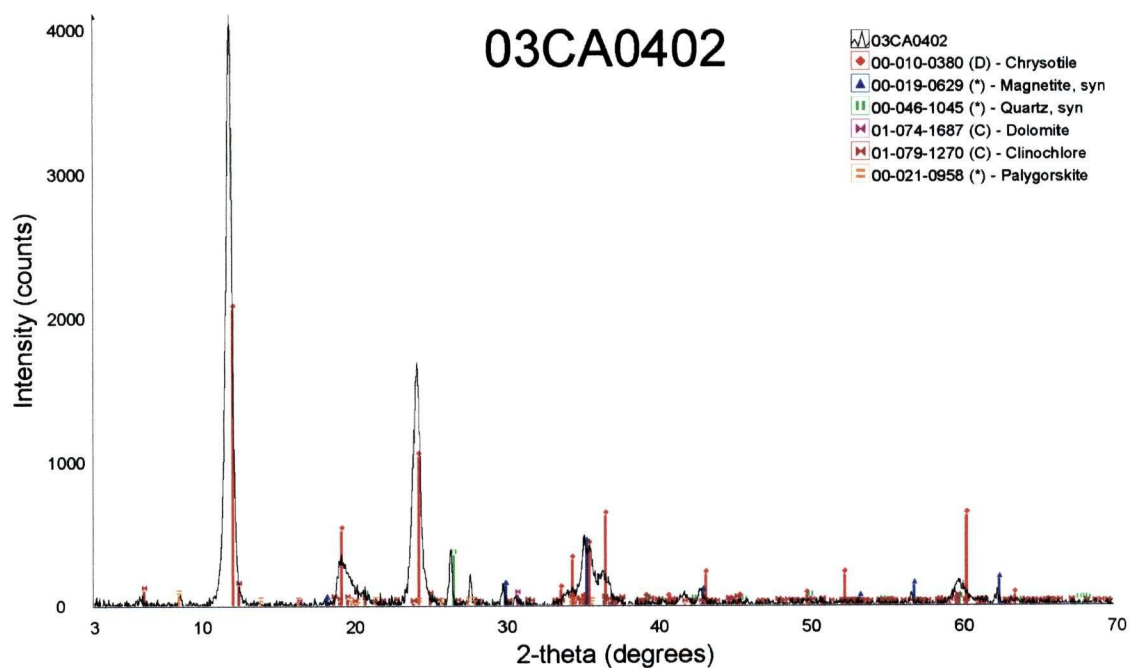


FIGURE B22: X-ray diffractogram for 03CA0402.

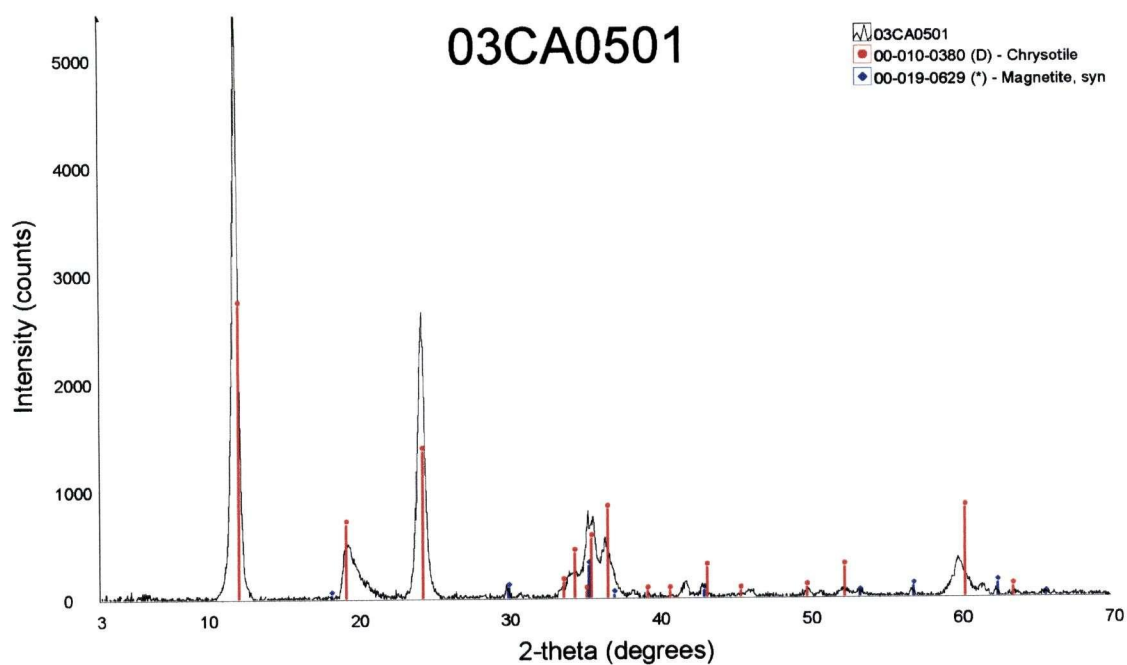


FIGURE B23: X-ray diffractogram for 03CA0501.

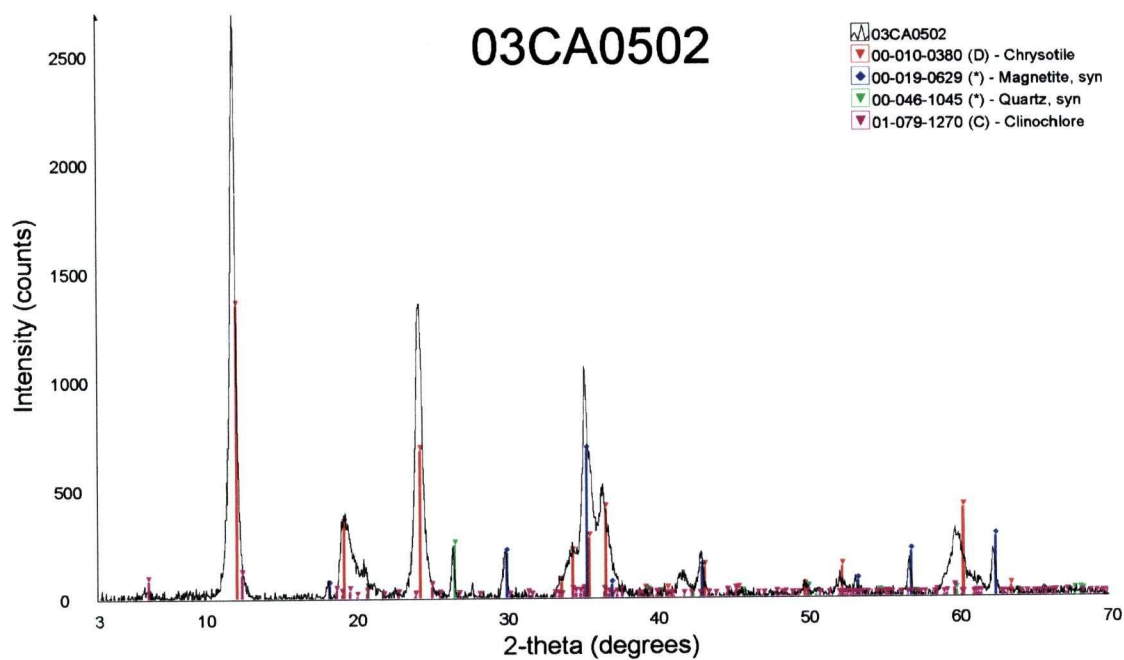


FIGURE B24: X-ray diffractogram for 03CA0502.



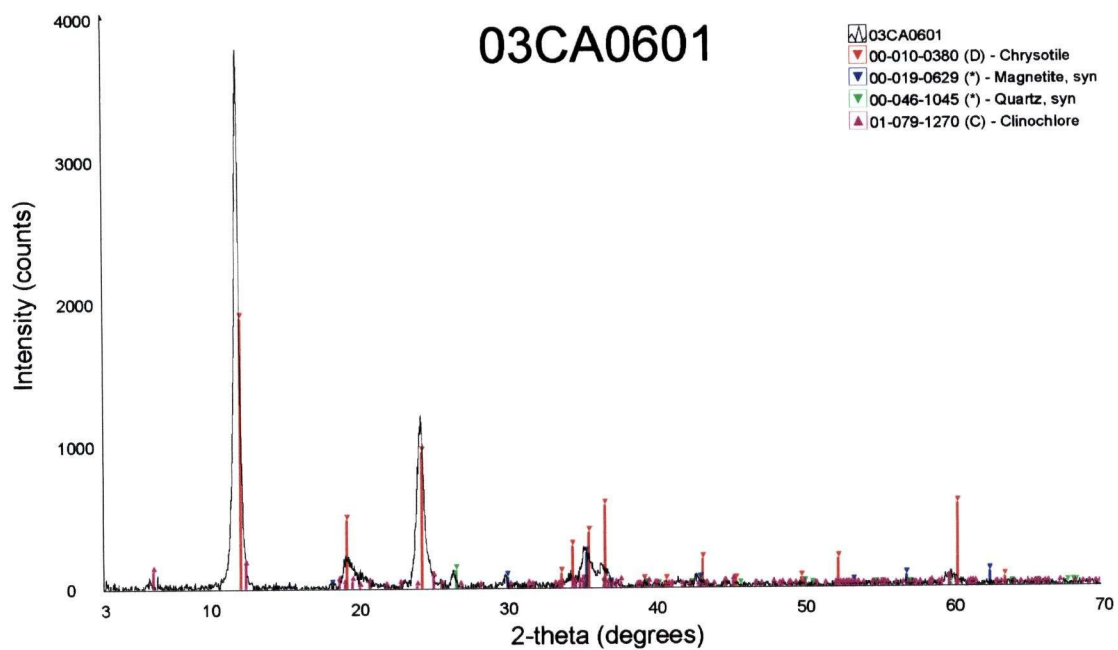


FIGURE B25: X-ray diffractogram for 03CA0601.

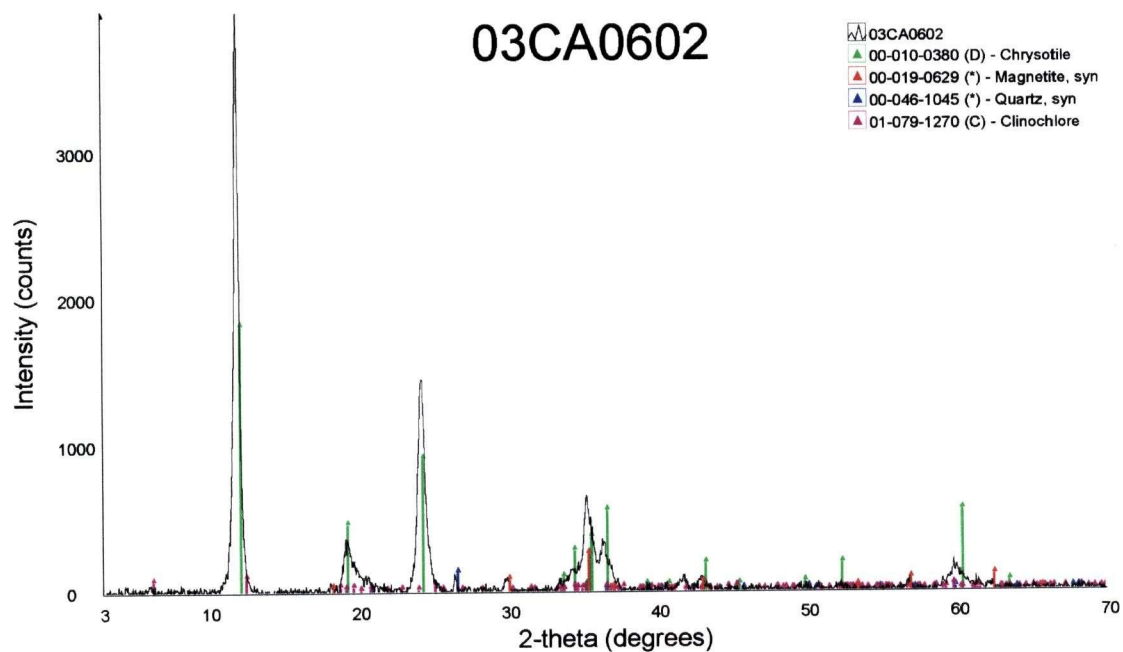


FIGURE B26: X-ray diffractogram for 03CA0602.



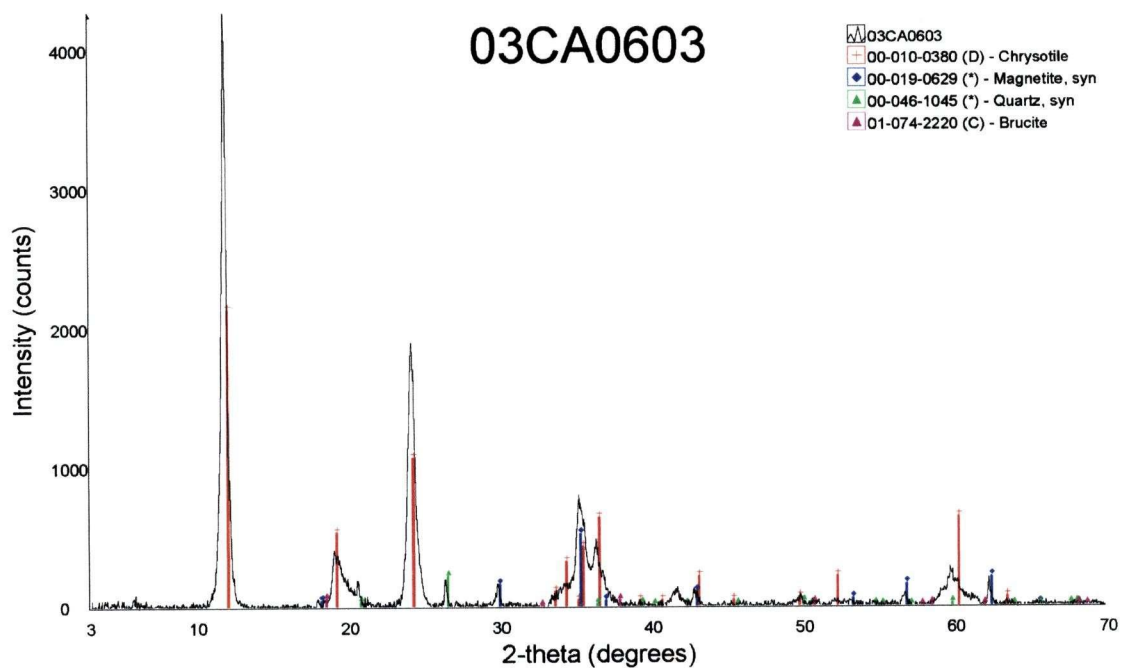


FIGURE B27: X-ray diffractogram for 03CA0603.

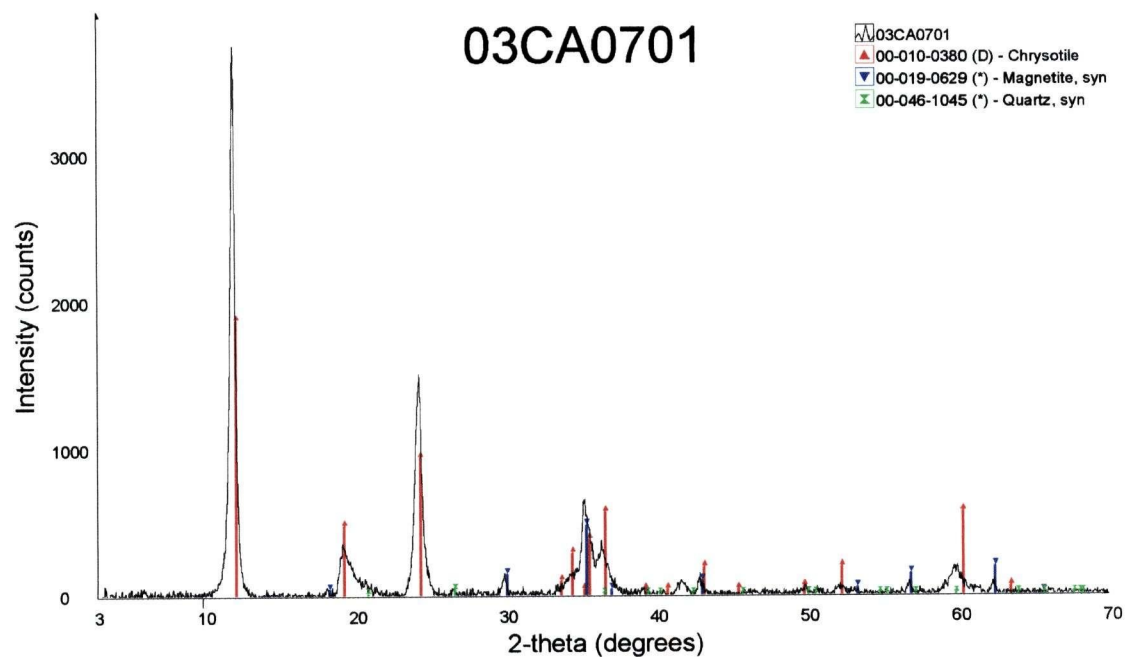


FIGURE B28: X-ray diffractogram for 03CA0701.

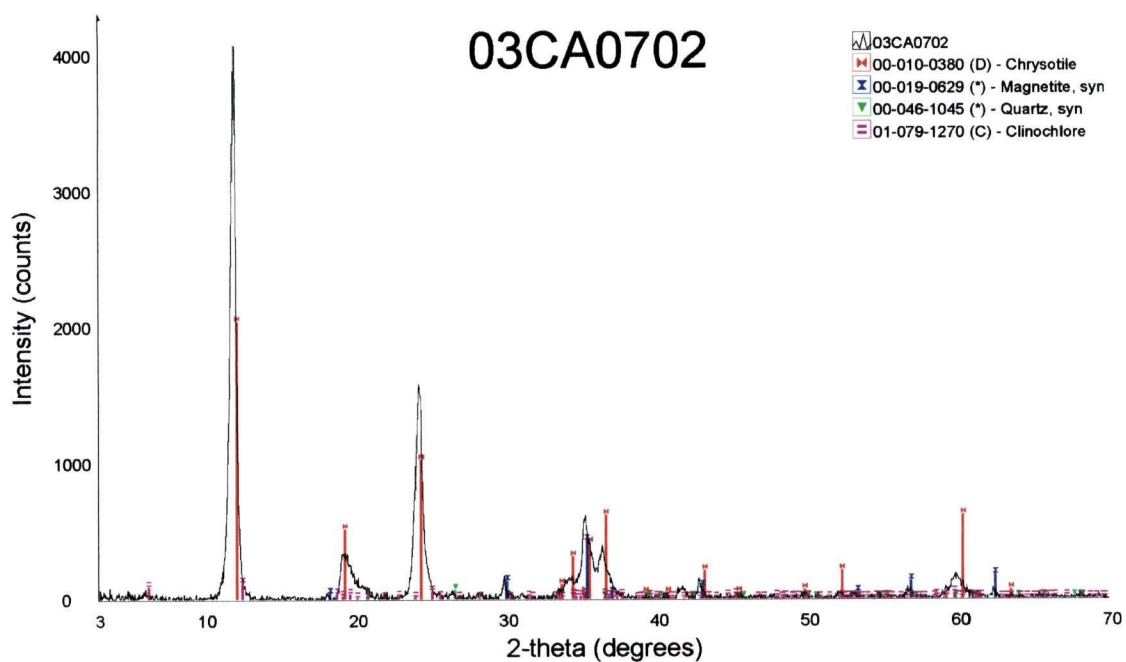


FIGURE B29: X-ray diffractogram for 03CA0702.

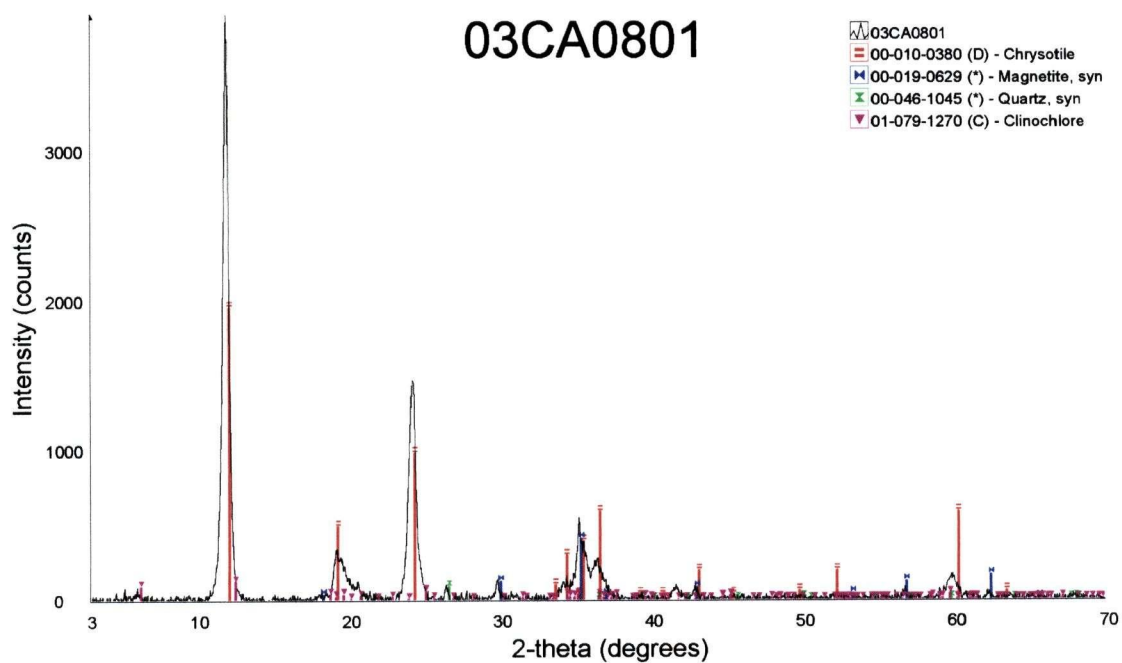


FIGURE B30: X-ray diffractogram for 03CA0801.

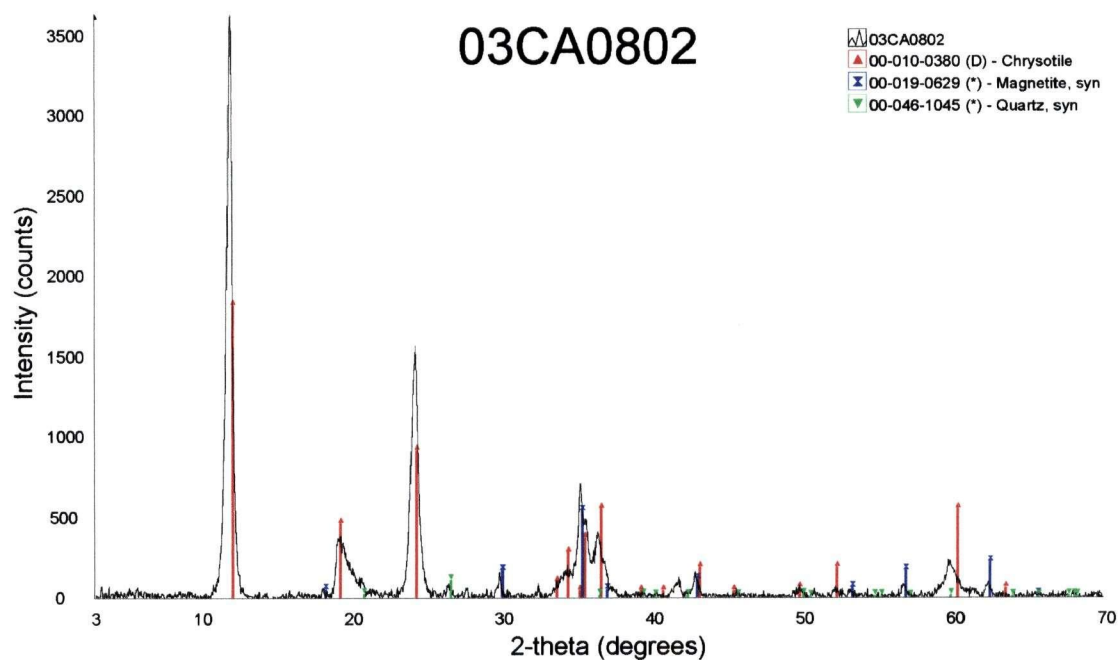


FIGURE B31: X-ray diffractogram for 03CA0802.

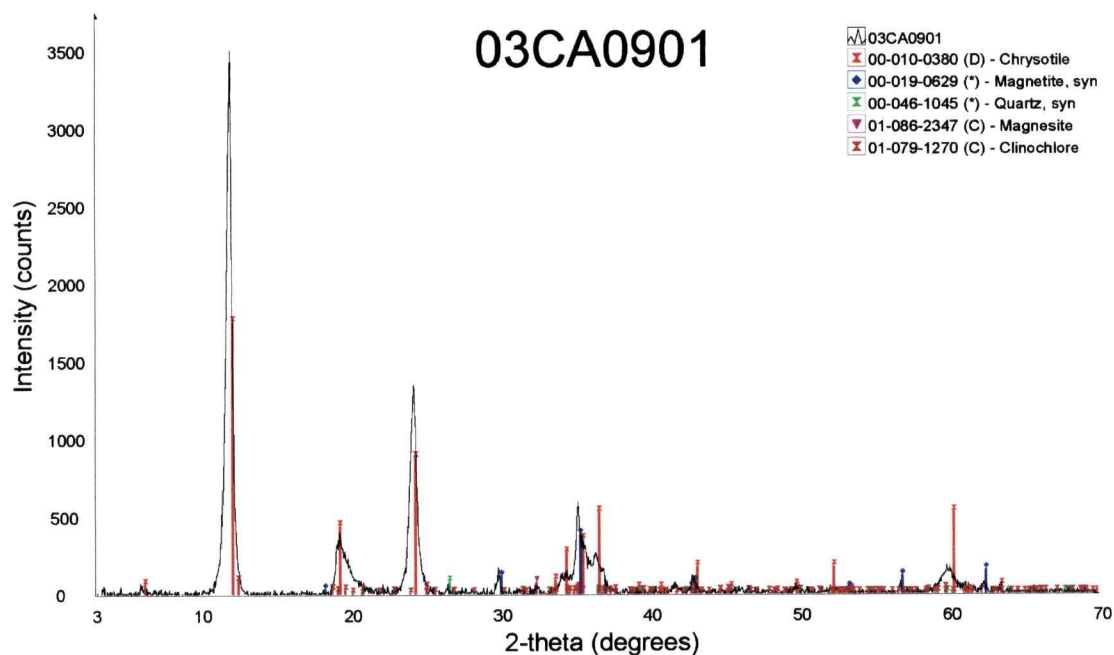


FIGURE B32: X-ray diffractogram for 03CA0901.

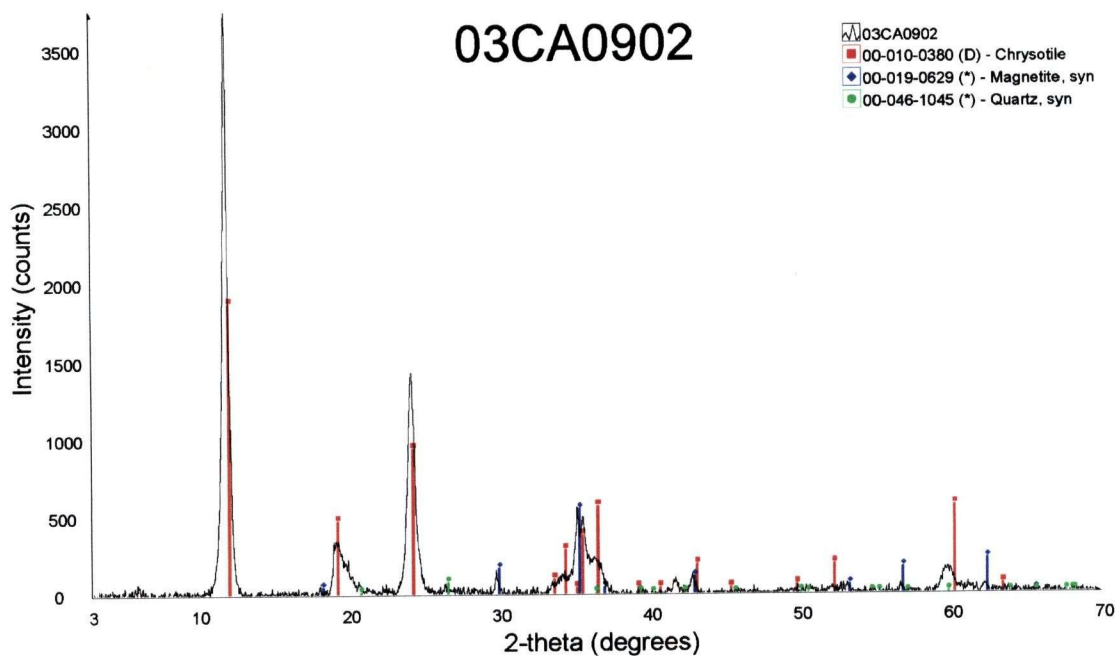


FIGURE B33: X-ray diffractogram for 03CA0902.

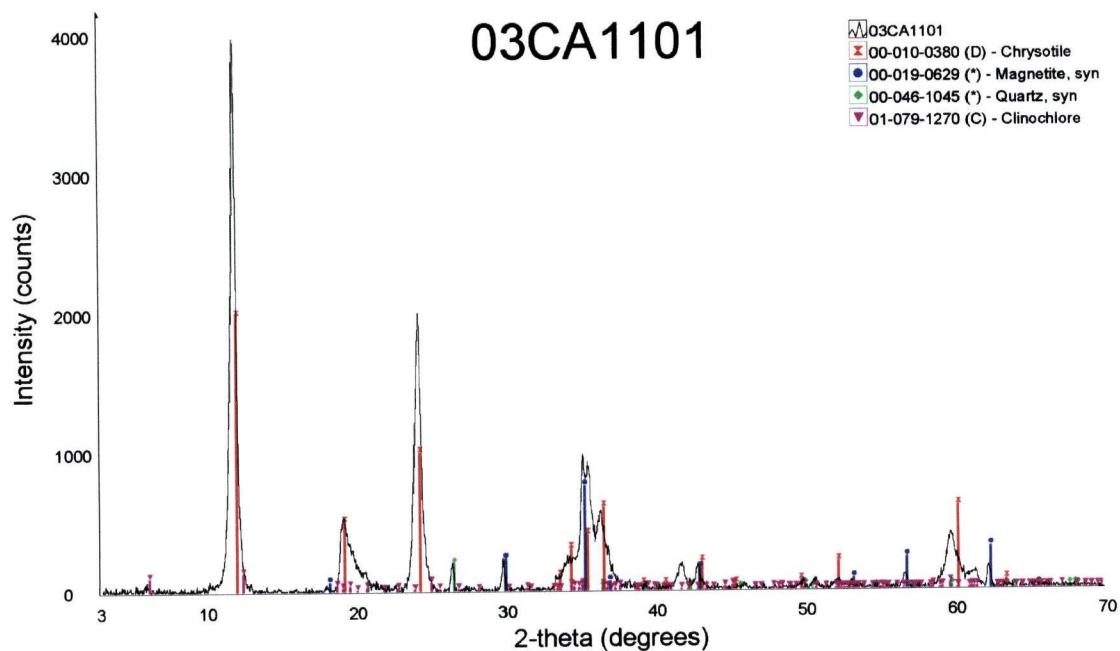


FIGURE B34: X-ray diffractogram for 03CA1101.

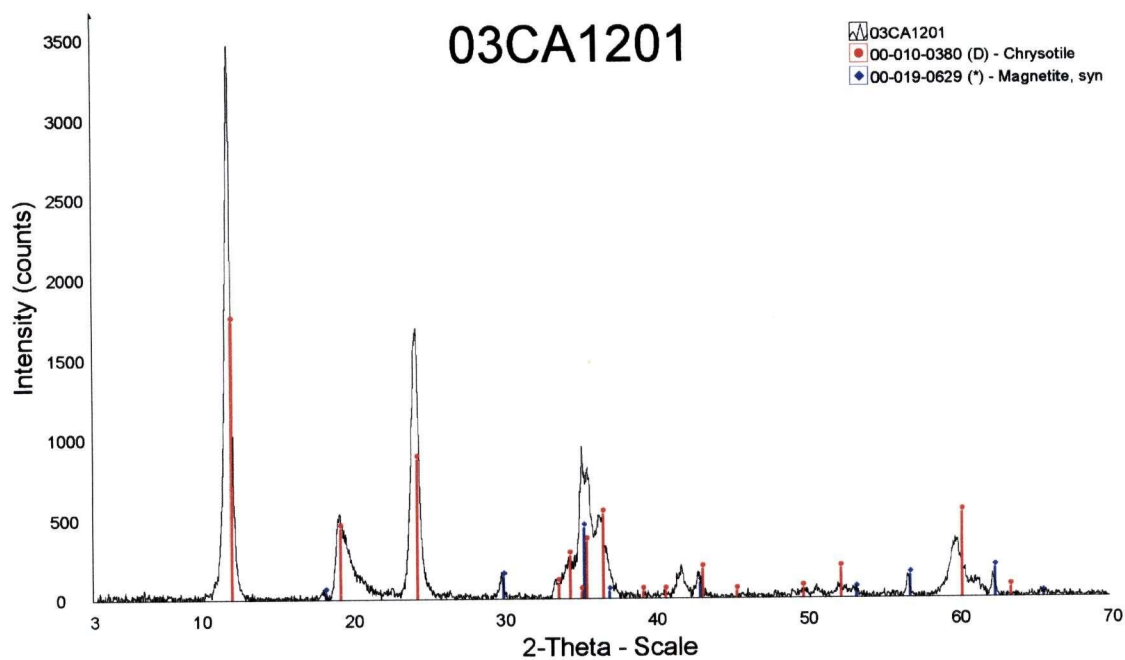


FIGURE B35: X-ray diffractogram for 03CA1201.

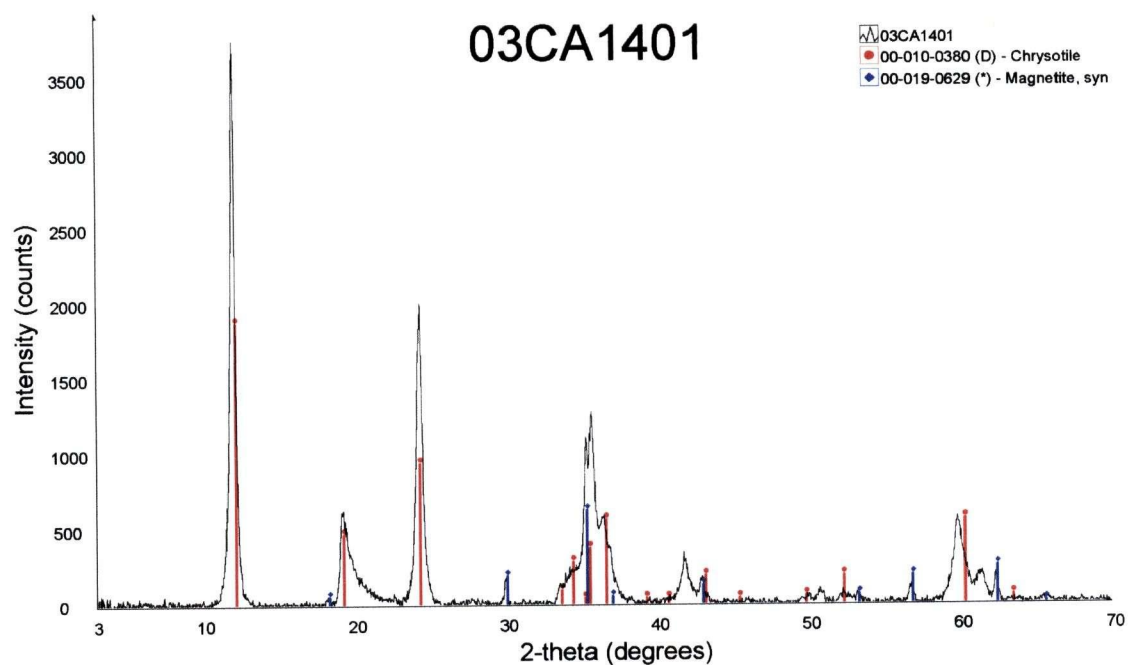


FIGURE B36: X-ray diffractogram for 03CA1401.

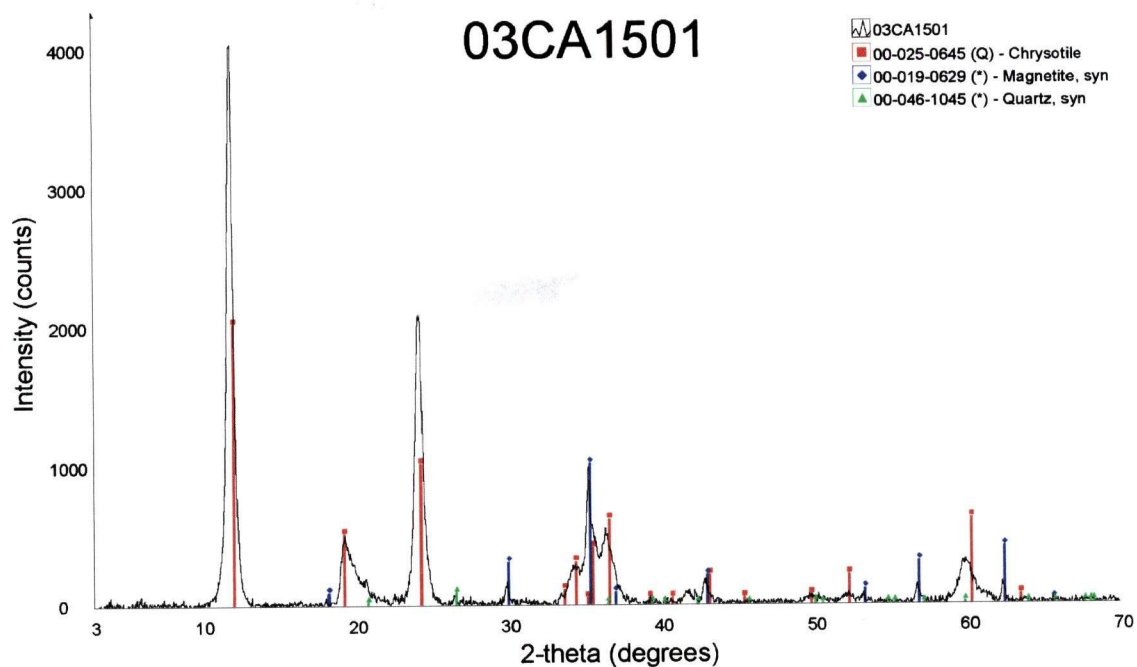


FIGURE B37: X-ray diffractogram for 03CA1501.

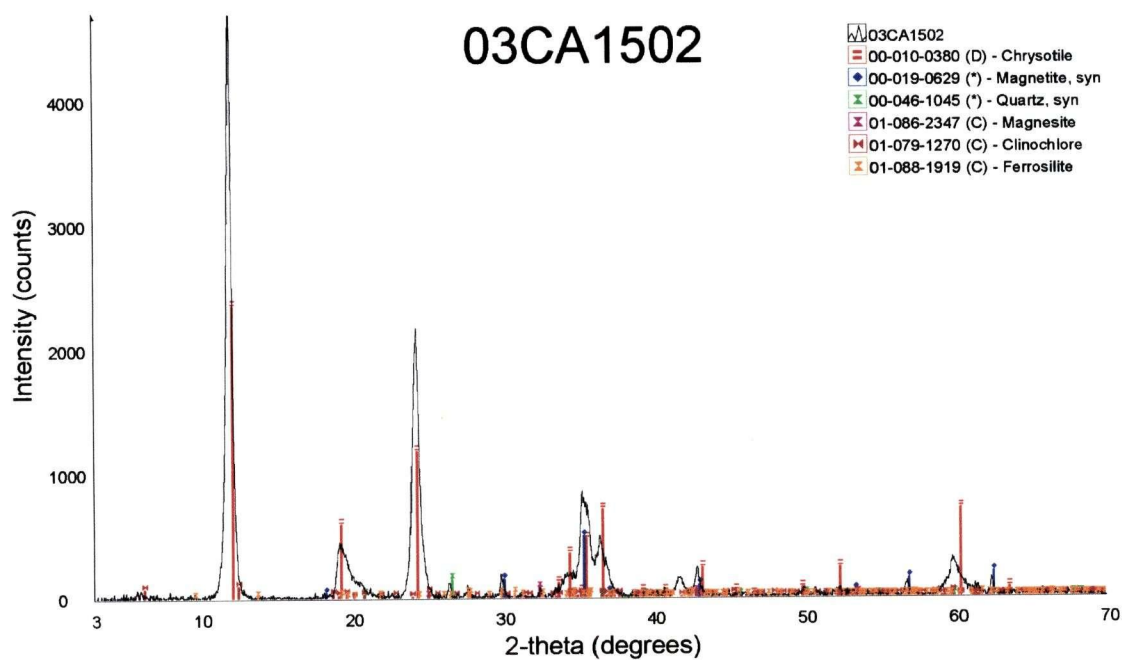


FIGURE B38: X-ray diffractogram for 03CA1502.

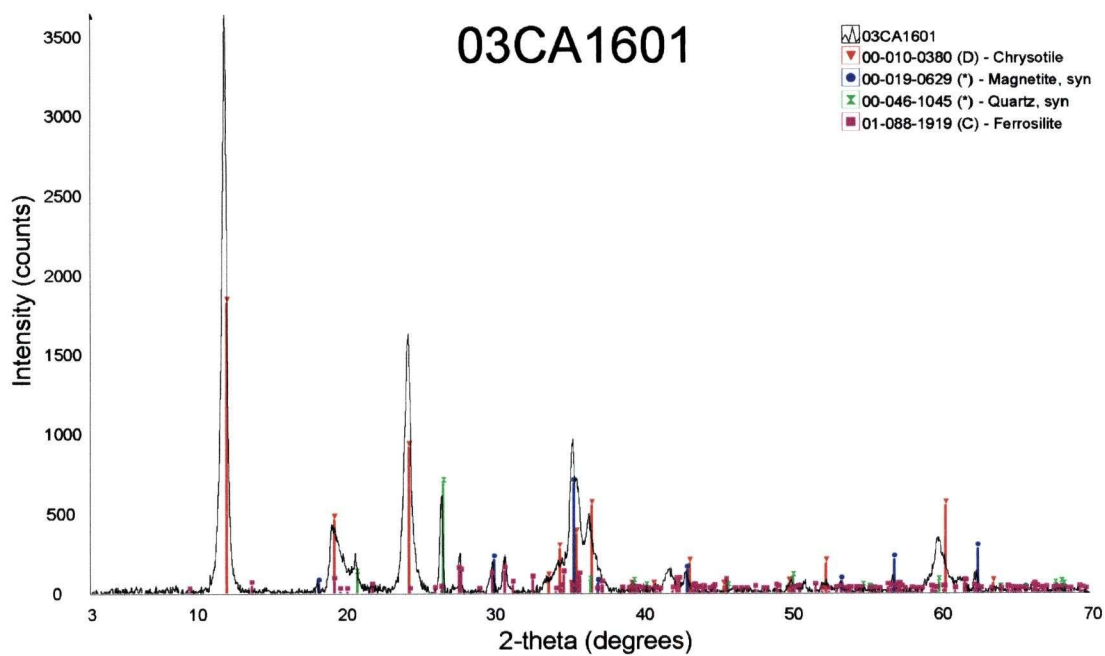


FIGURE B39: X-ray diffractogram for 03CA1601.

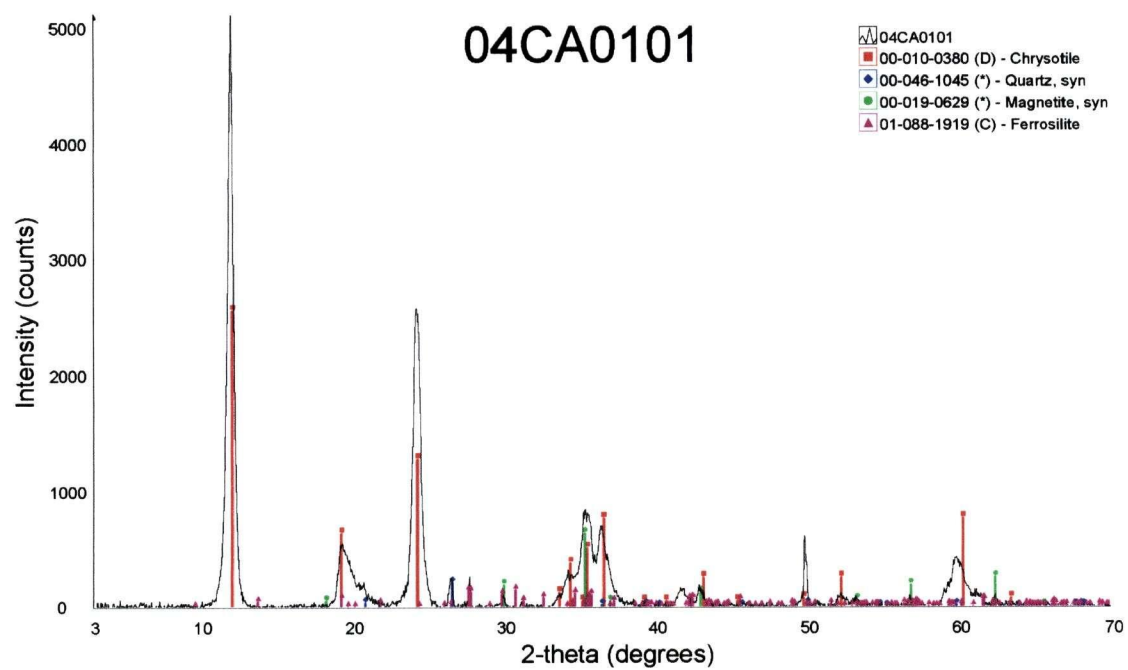


FIGURE B40: X-ray diffractogram for 04CA0101.



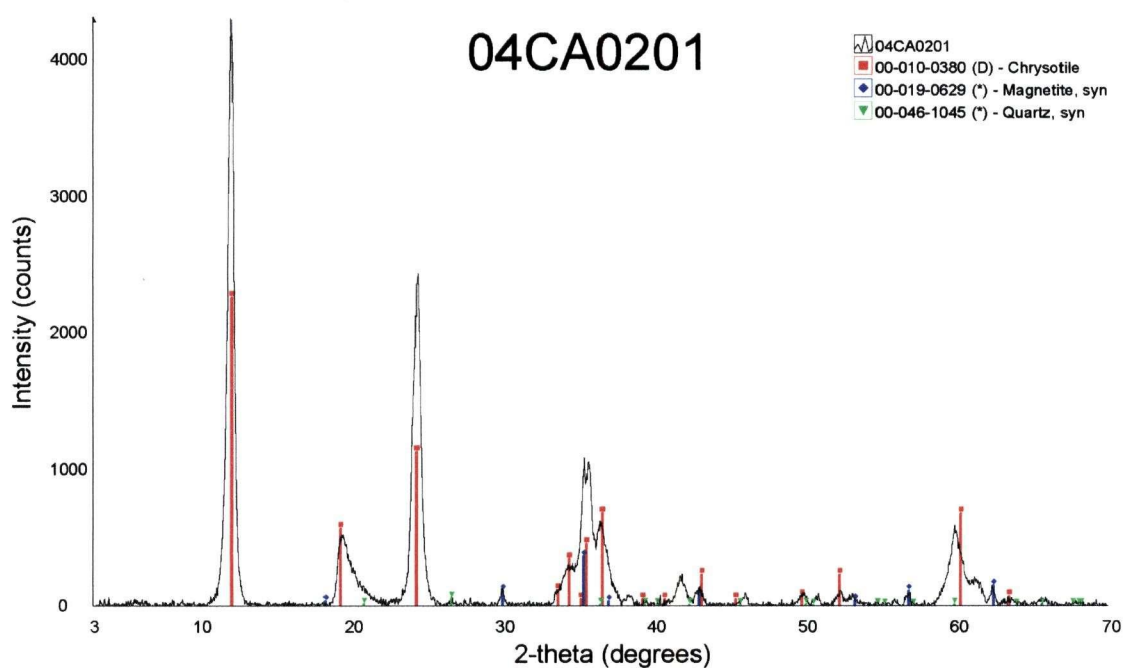


FIGURE B41: X-ray diffractogram for 04CA0201.

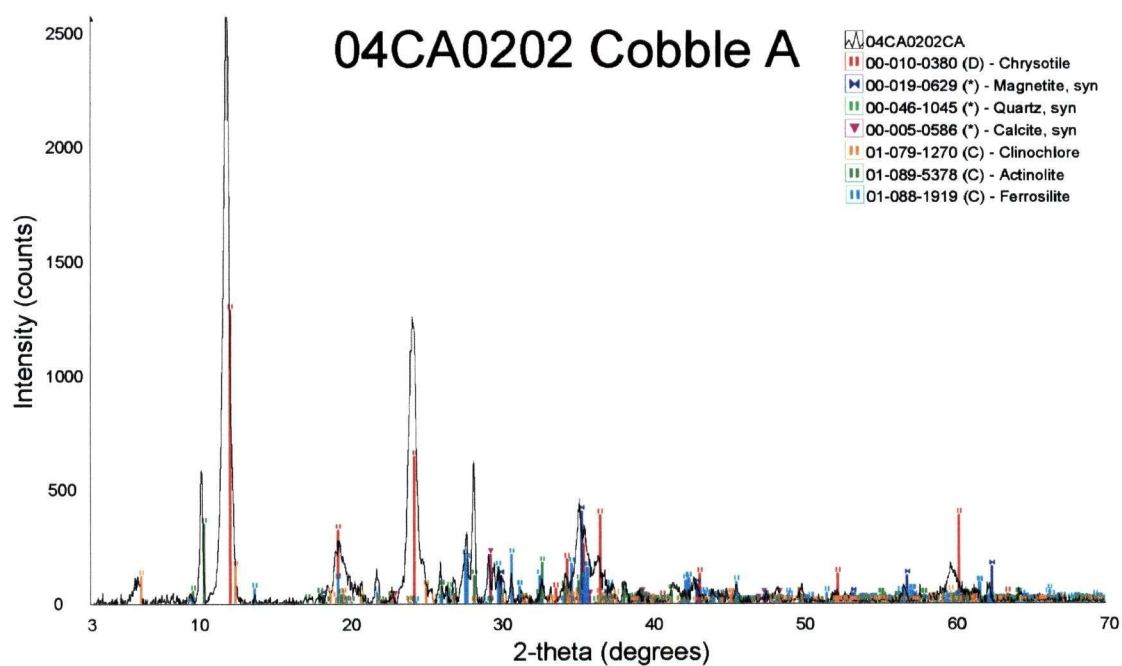


FIGURE B42: X-ray diffractogram for cobble coating from 04CA0202 cobble A.



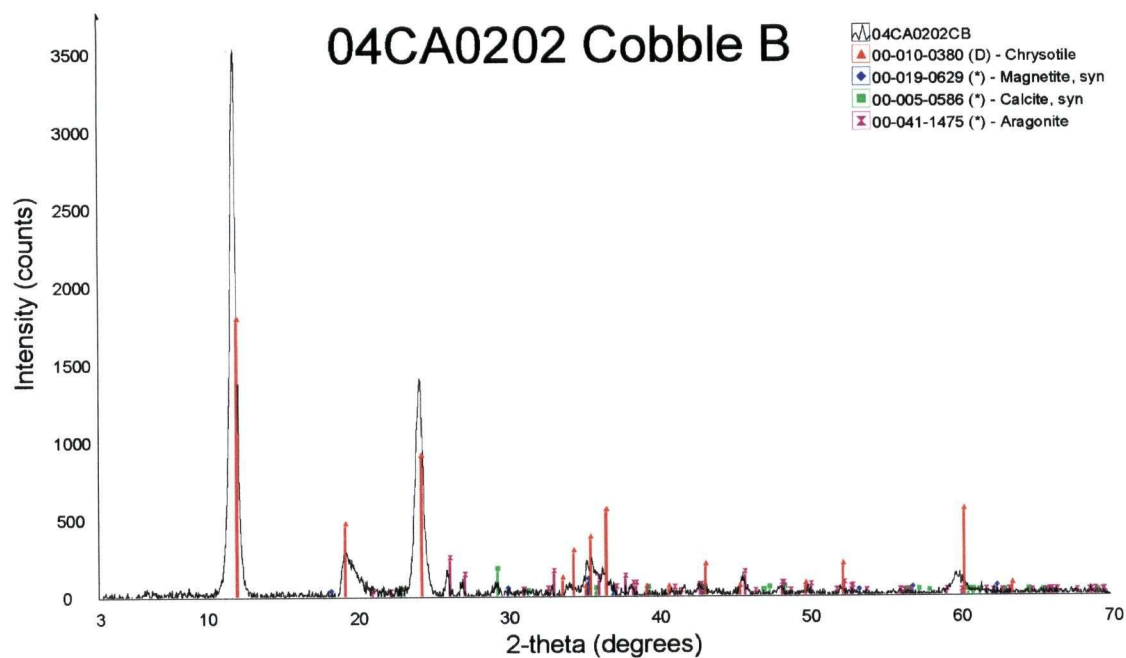


FIGURE B43: X-ray diffractogram for cobble coating from 04CA0202 cobble B.

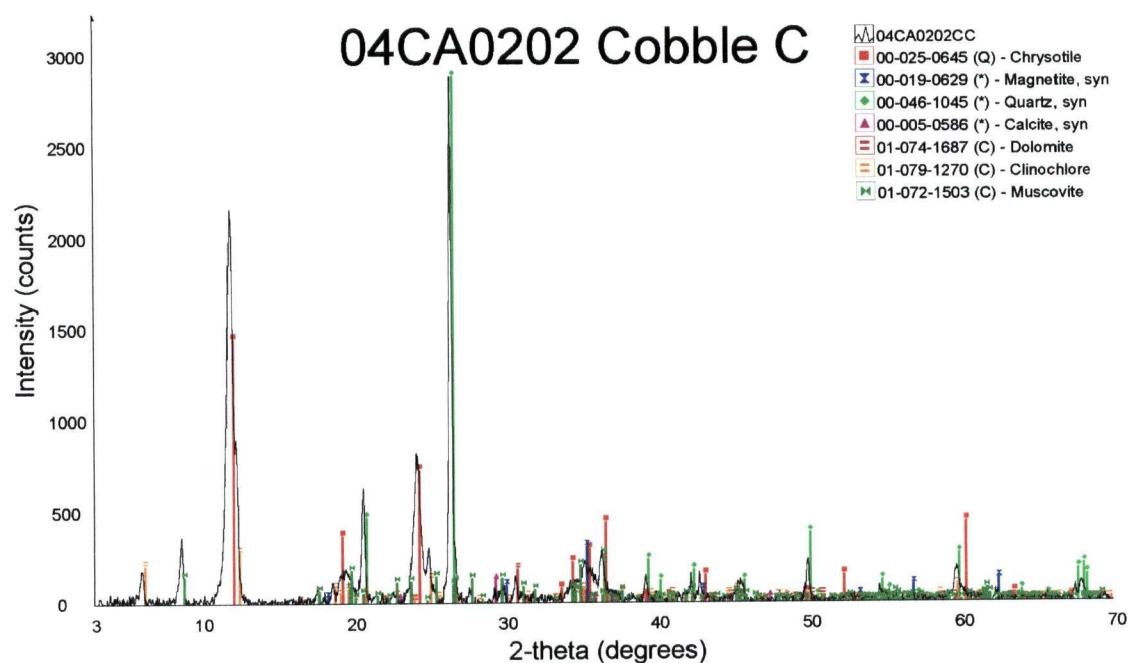


FIGURE B44: X-ray diffractogram for cobble coating from 04CA0202 cobble C.

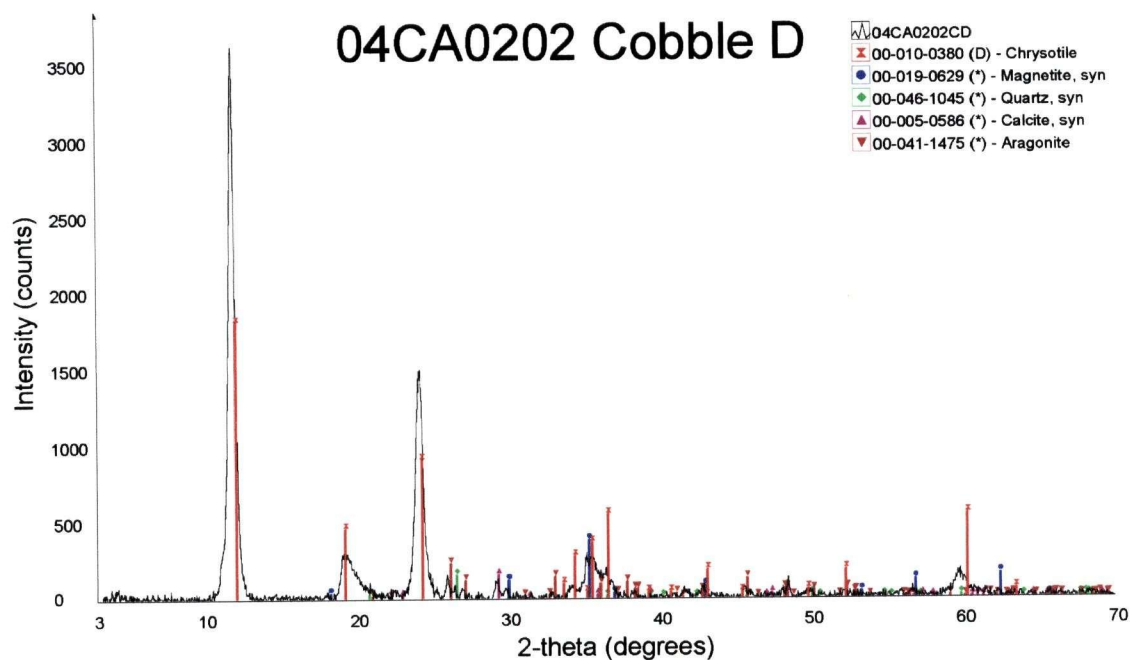


FIGURE B45: X-ray diffractogram for cobble coating from 04CA0202 cobble D.

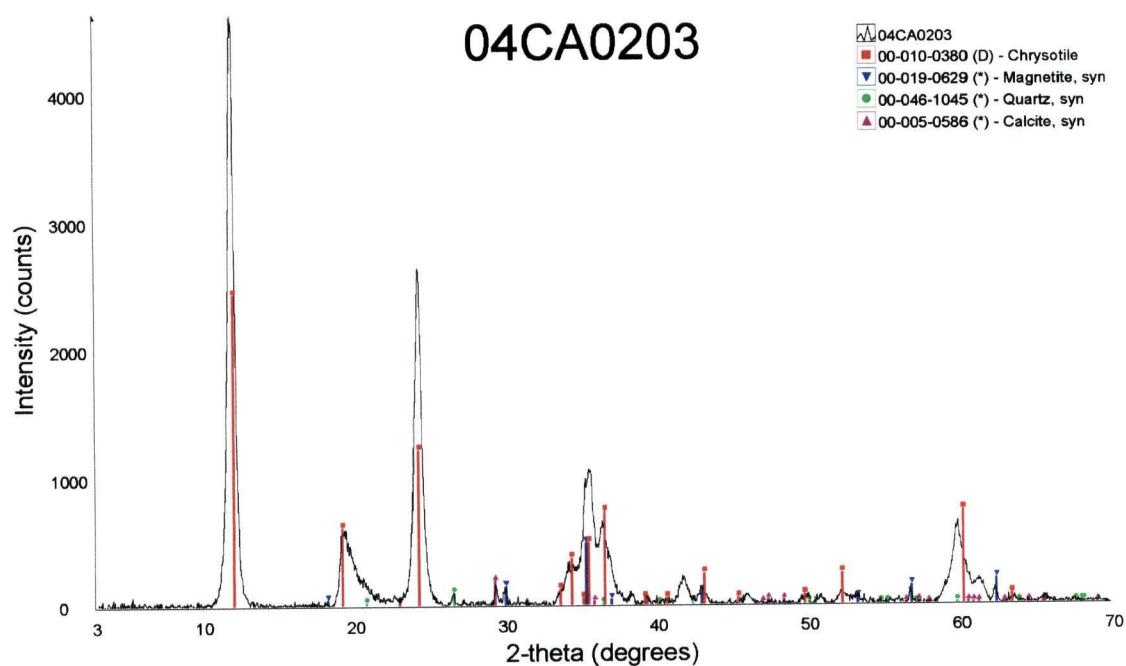


FIGURE B46: X-ray diffractogram for 04CA0203.

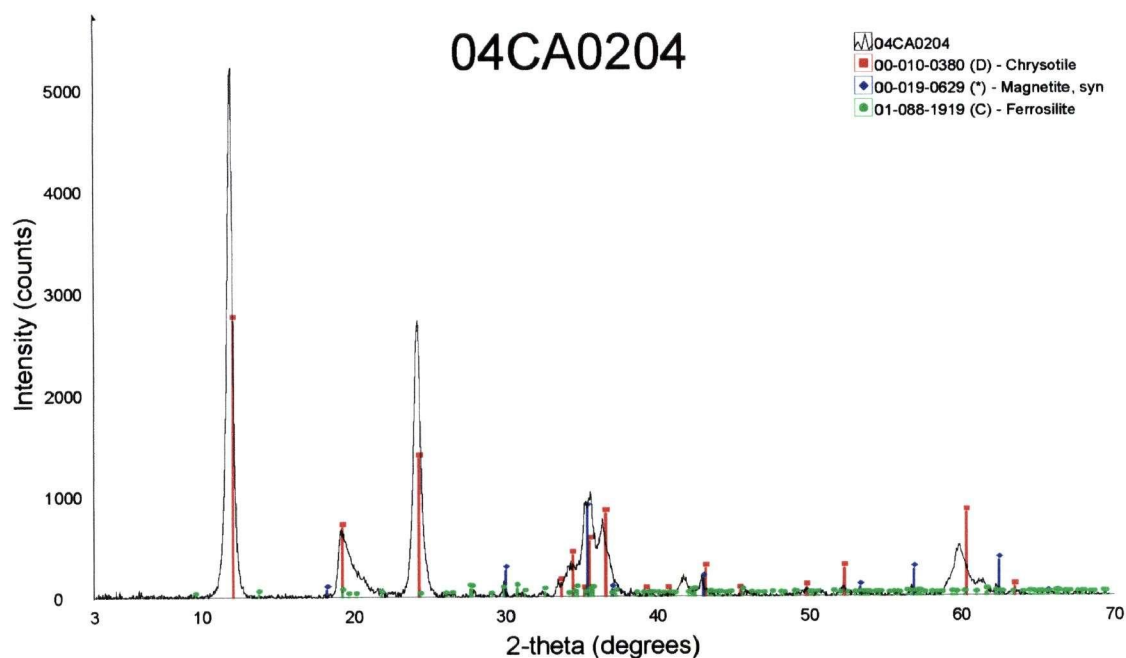


FIGURE B47: X-ray diffractogram for 04CA0204.

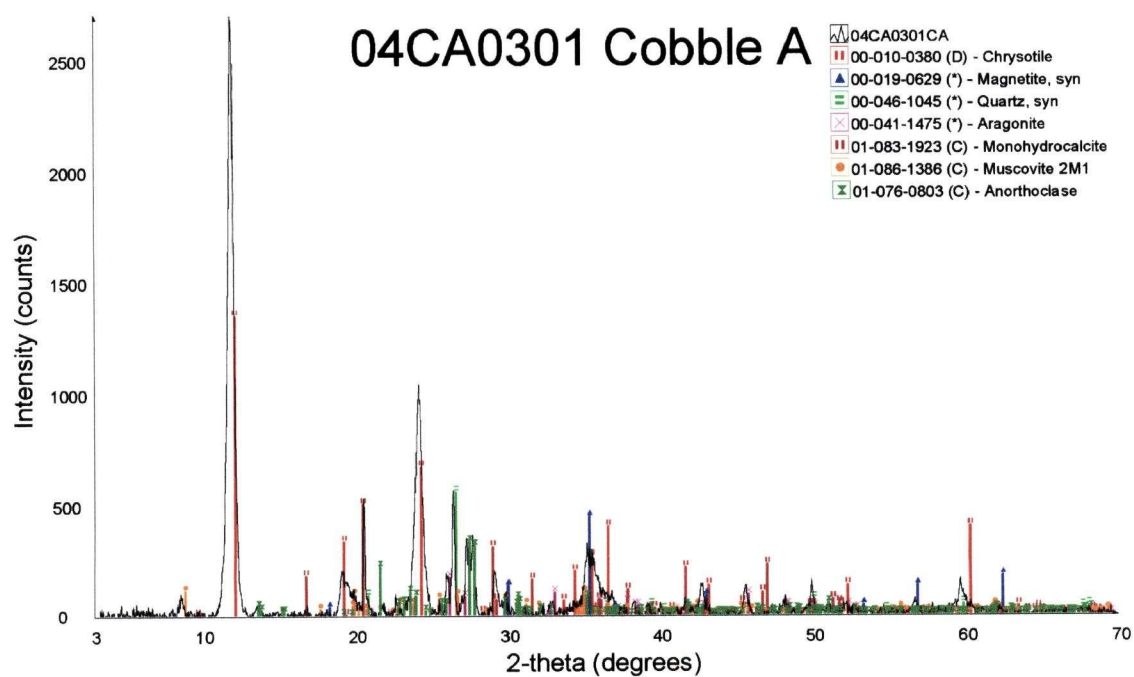


FIGURE B48: X-ray diffractogram for cobble coating from 04CA0301 cobble A.

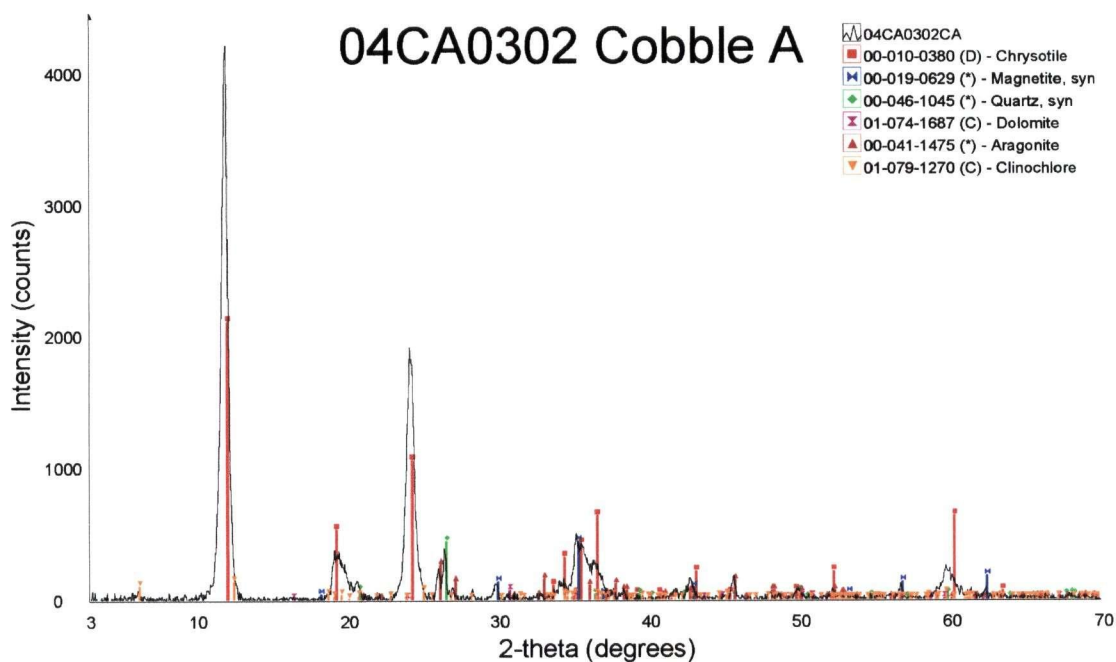


FIGURE B49: X-ray diffractogram for cobble coating from 04CA0302 cobble A.

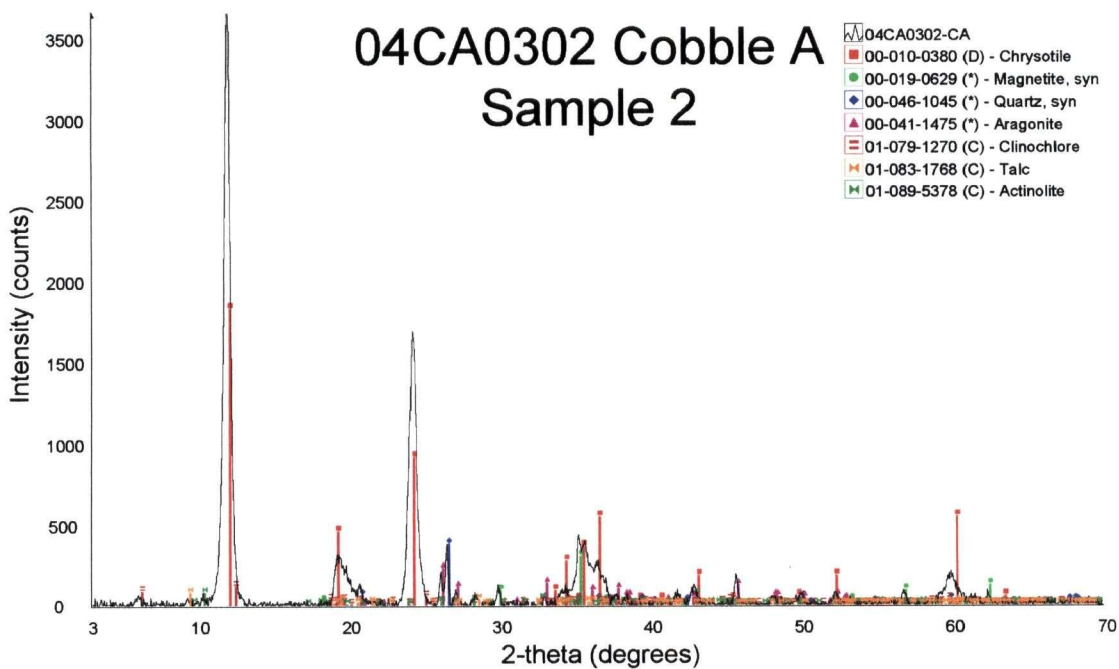


FIGURE B50: Duplicate X-ray diffractogram for cobble coating 04CA0302 cobble A.

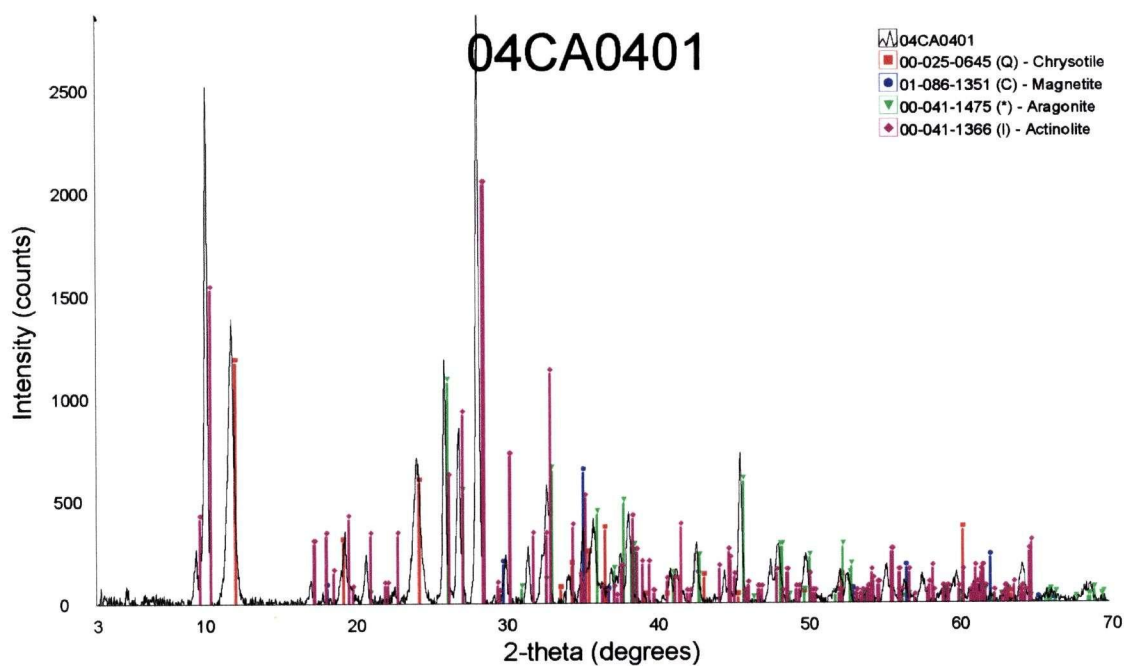


FIGURE B51: X-ray diffractogram for 04CA0401.

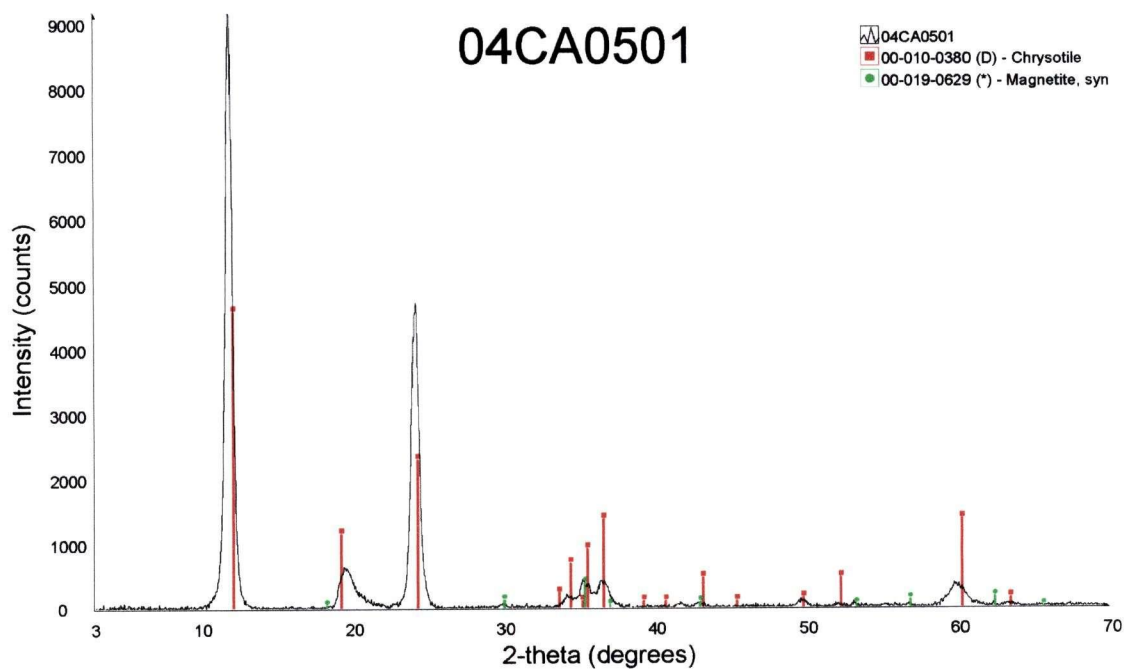


FIGURE B52: X-ray diffractogram for 04CA0501.

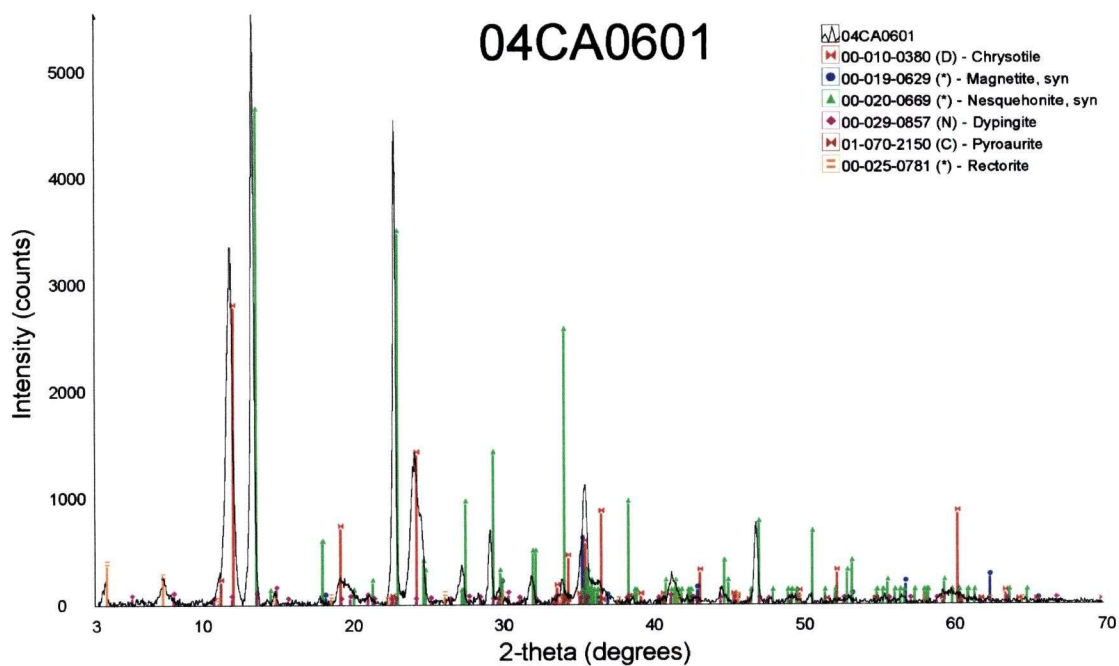


FIGURE B53: X-ray diffractogram for 04CA0601.

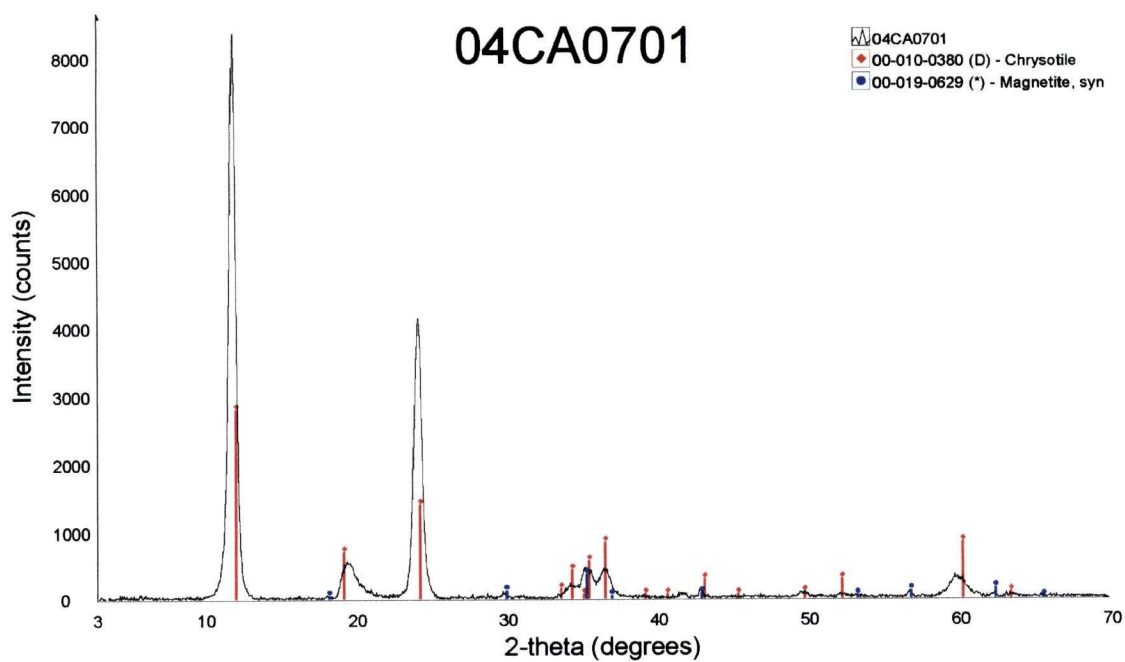


FIGURE B54: X-ray diffractogram for 04CA0701.

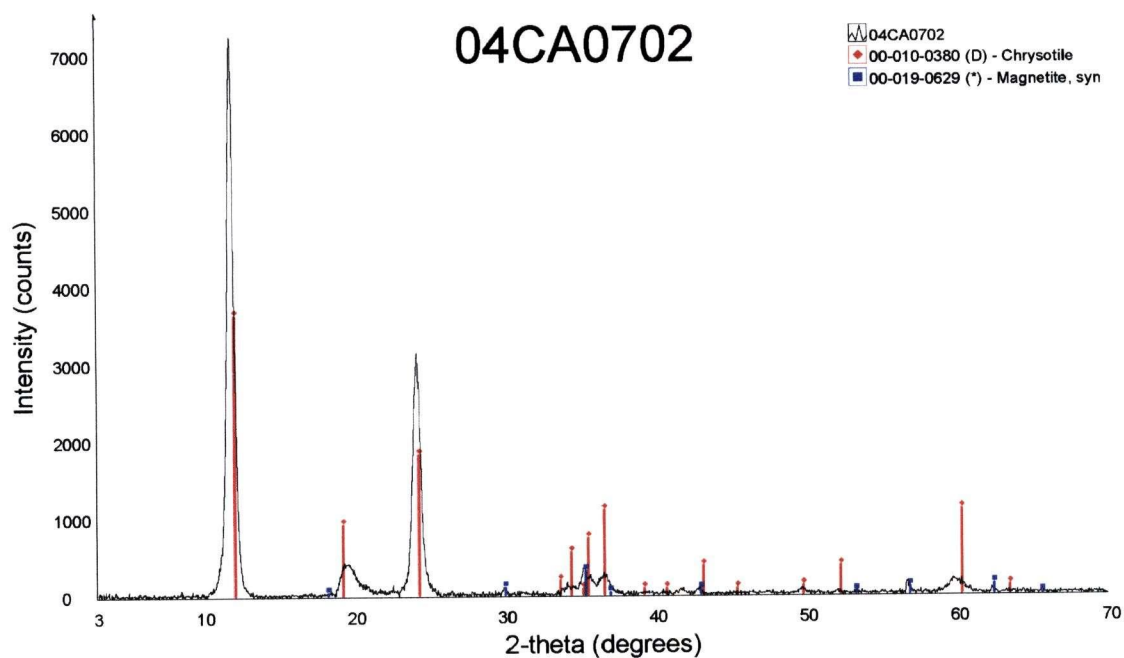


FIGURE B55: X-ray diffractogram for 04CA0702.

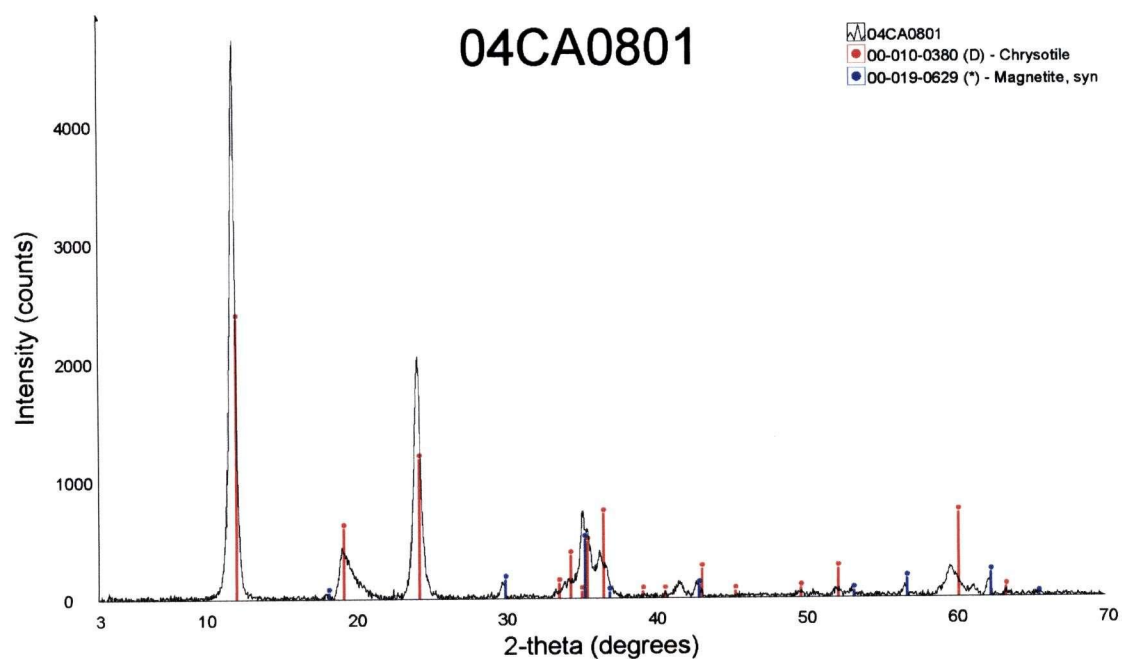


FIGURE B56: X-ray diffractogram for 04CA0801.



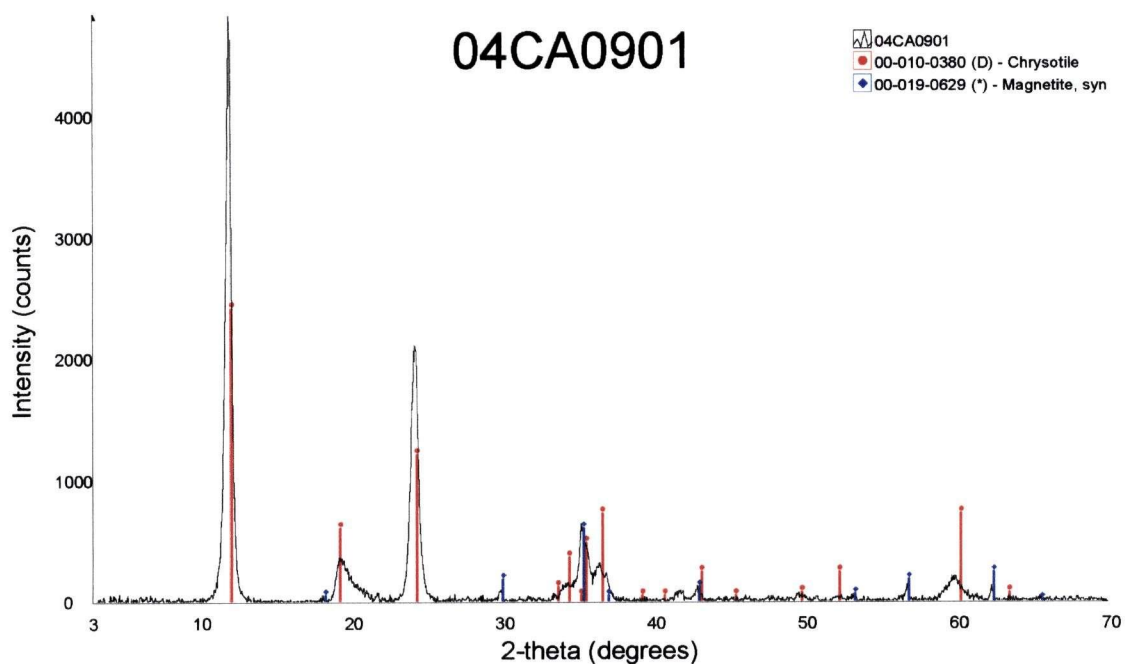


FIGURE B57: X-ray diffractogram for 04CA0901.

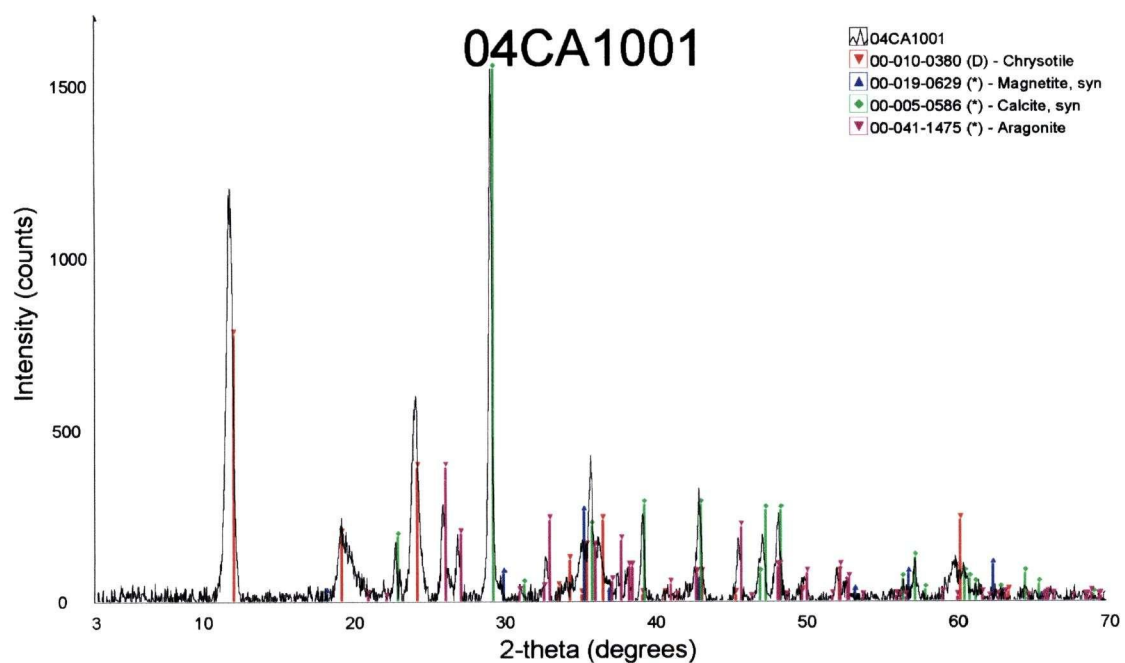


FIGURE B58: X-ray diffractogram for 04CA1001.



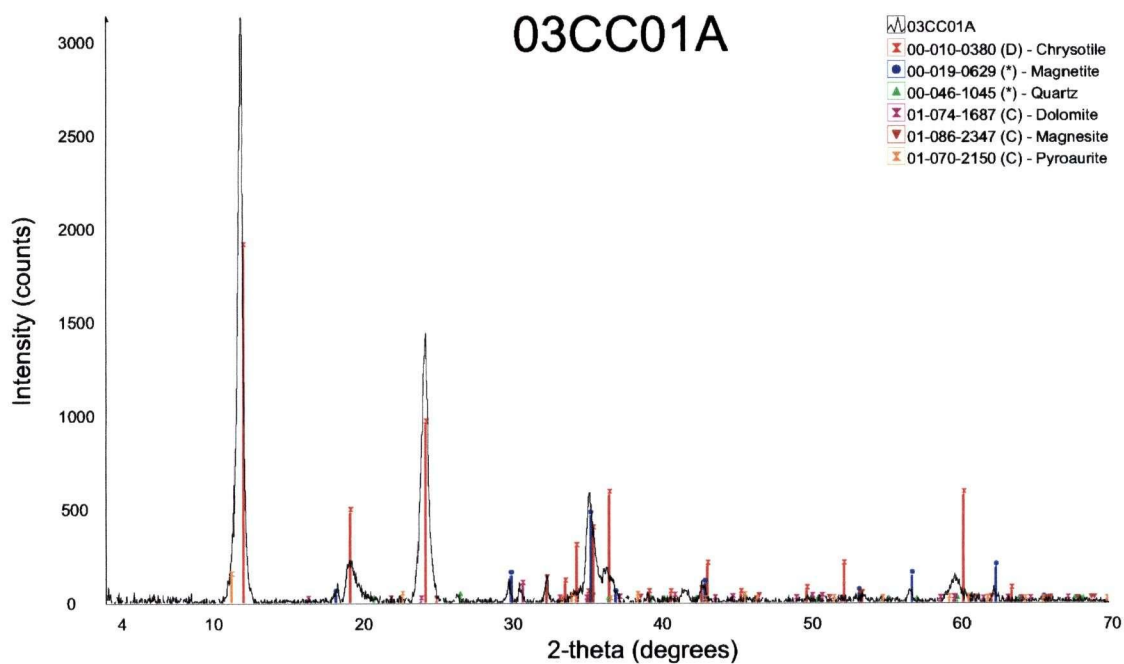


FIGURE B59: X-ray diffractogram for 03CC01A.

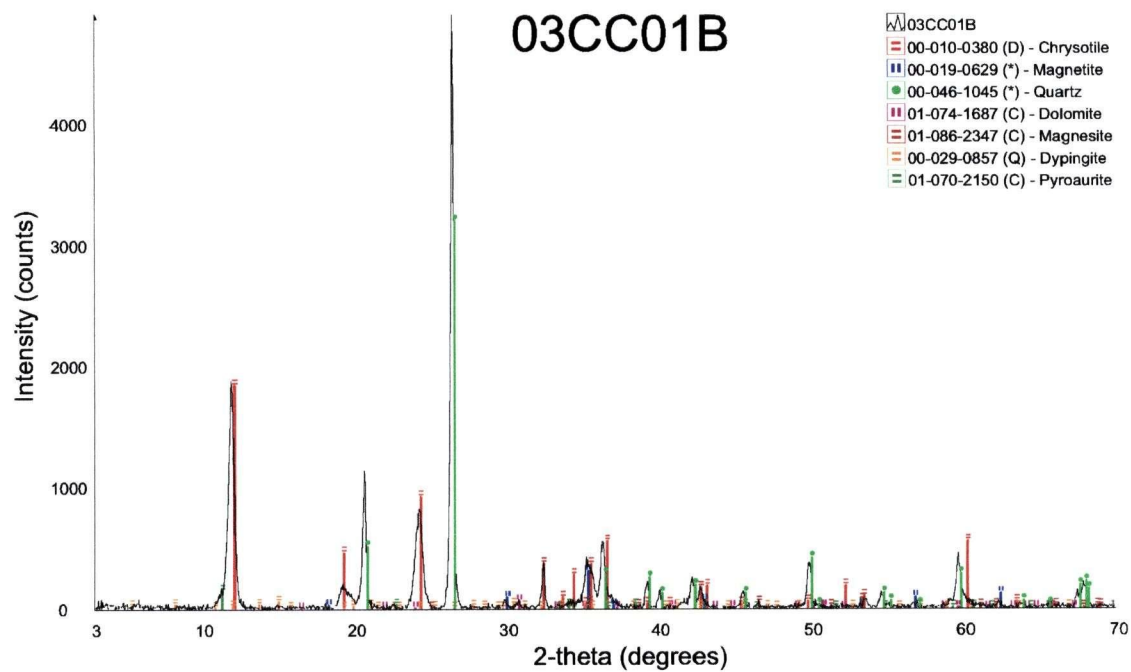


FIGURE B60: X-ray diffractogram for 03CC01B.

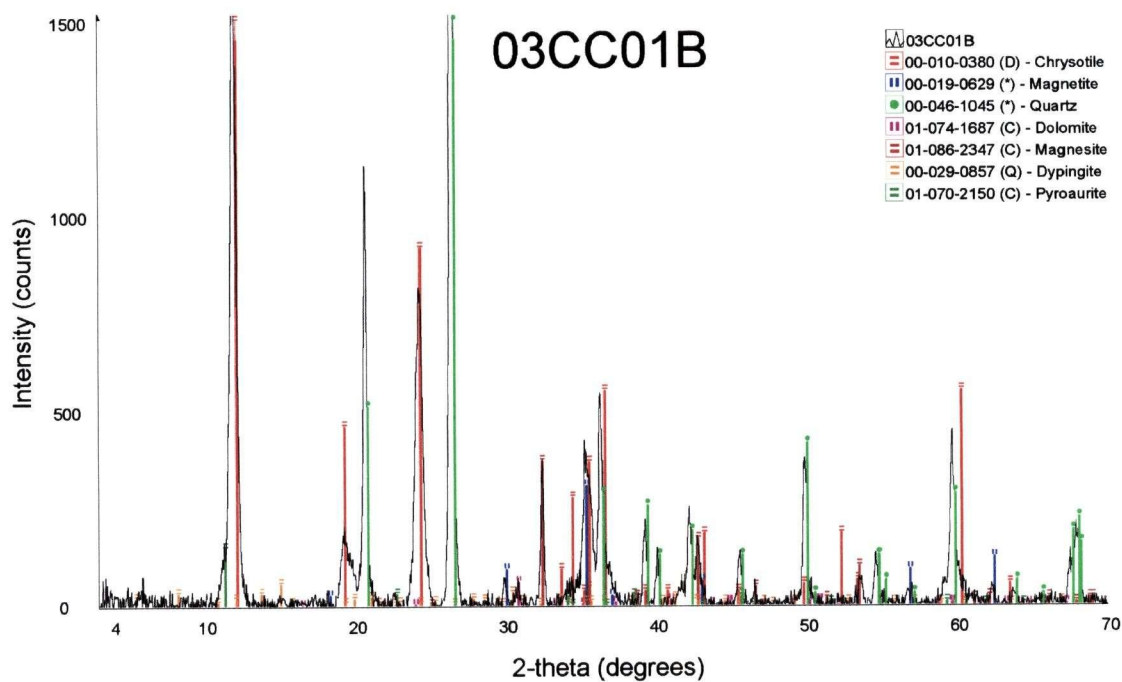


FIGURE B61: Close-up of X-ray diffractogram for 03CC01B.

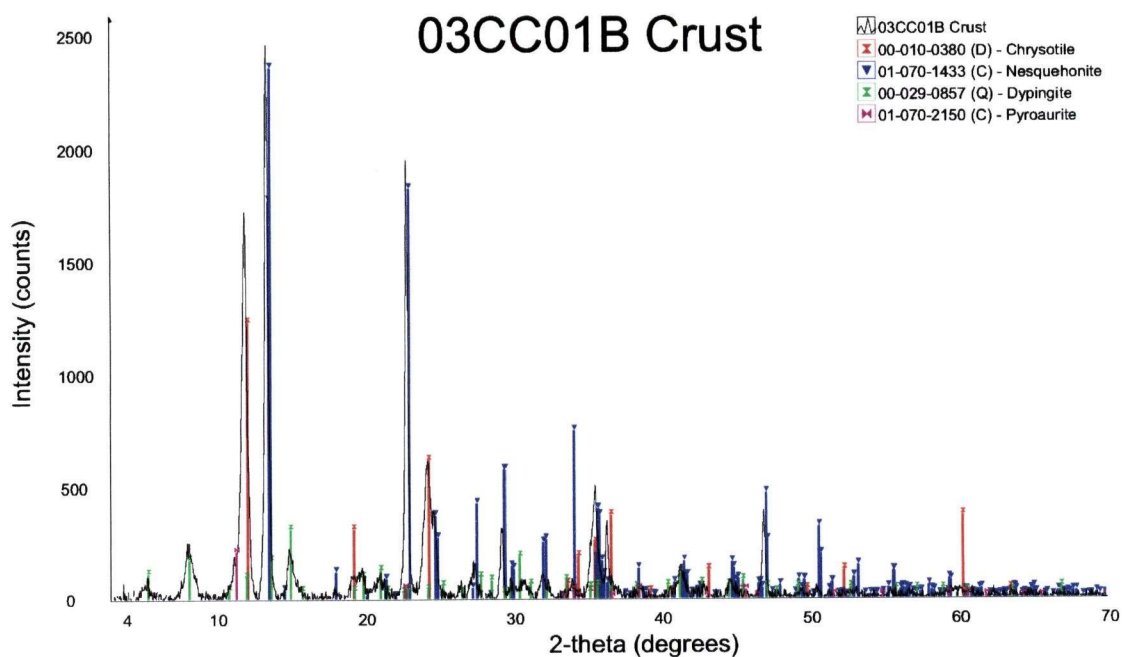


FIGURE B62: X-ray diffractogram for vertical crust from 03CC01B.

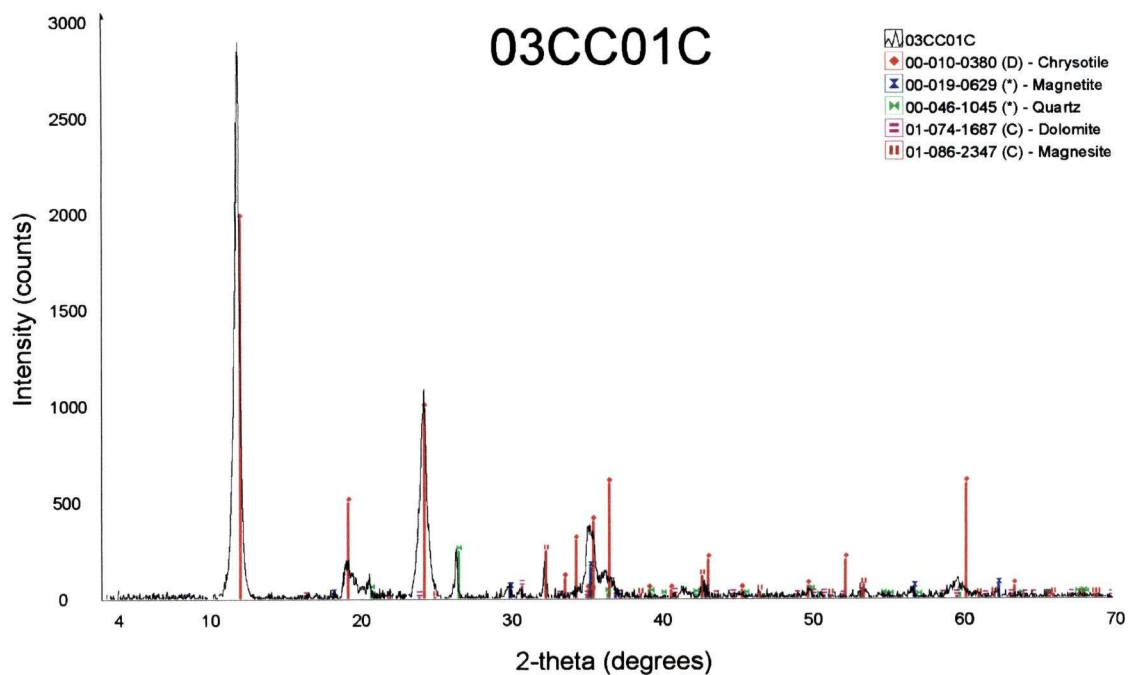


FIGURE B63: X-ray diffractogram for 03CC01C.

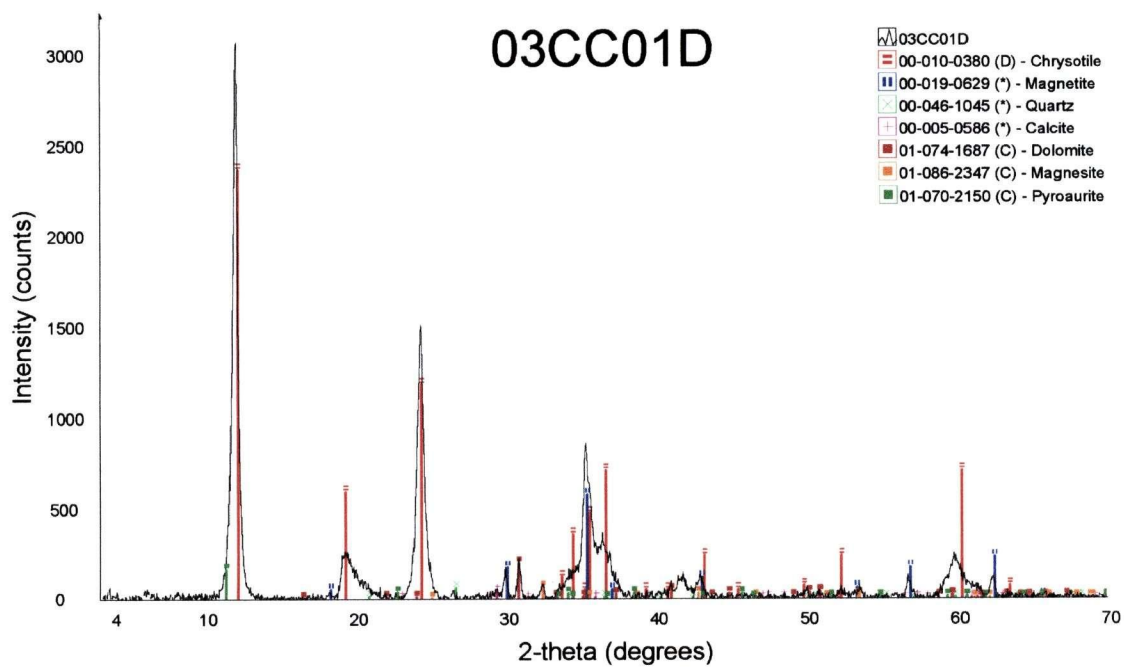


FIGURE B64: X-ray diffractogram for 03CC01D.

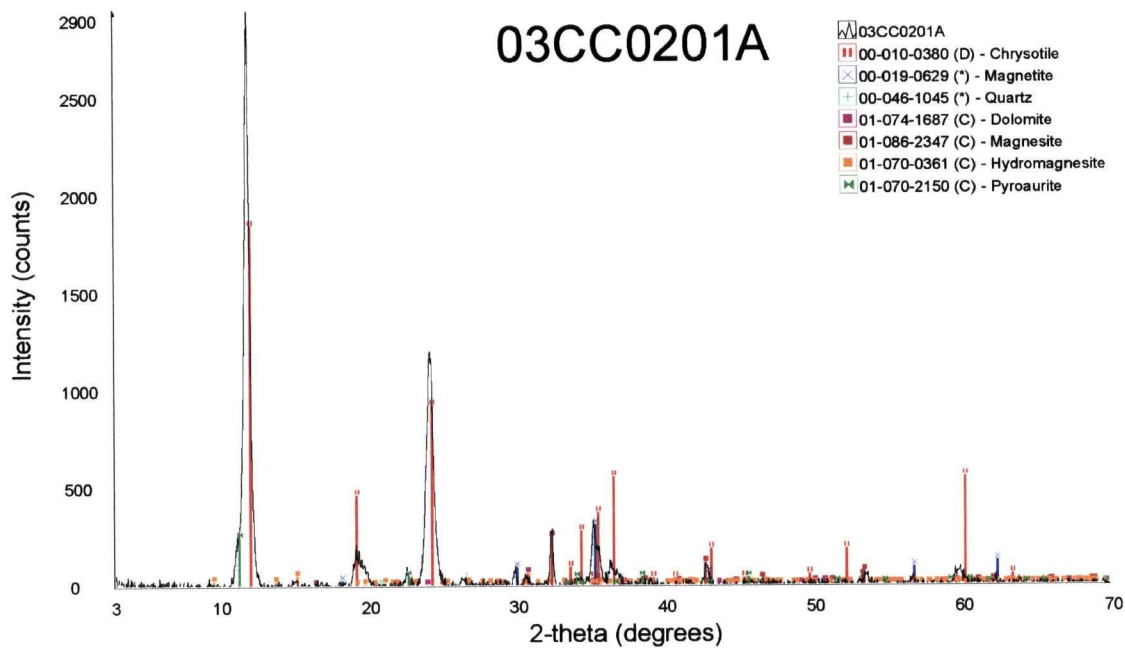


FIGURE B65: X-ray diffractogram for 03CC0201A.

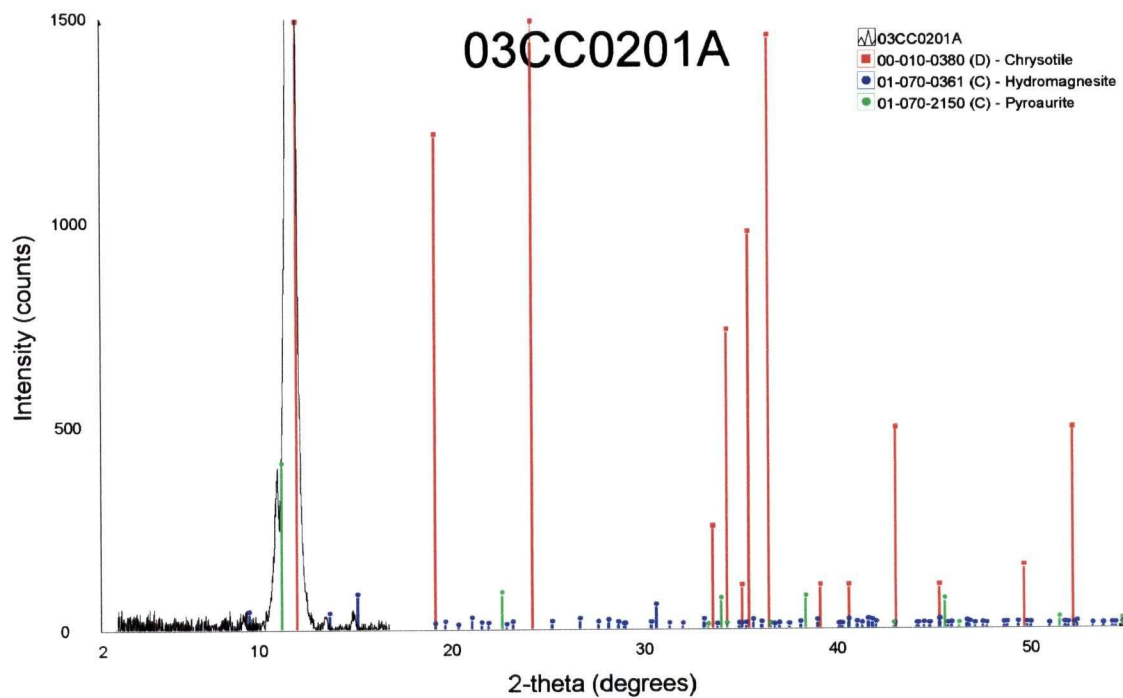


FIGURE B66: Close-up of X-ray diffractogram for 03CC0201A using higher count rate.

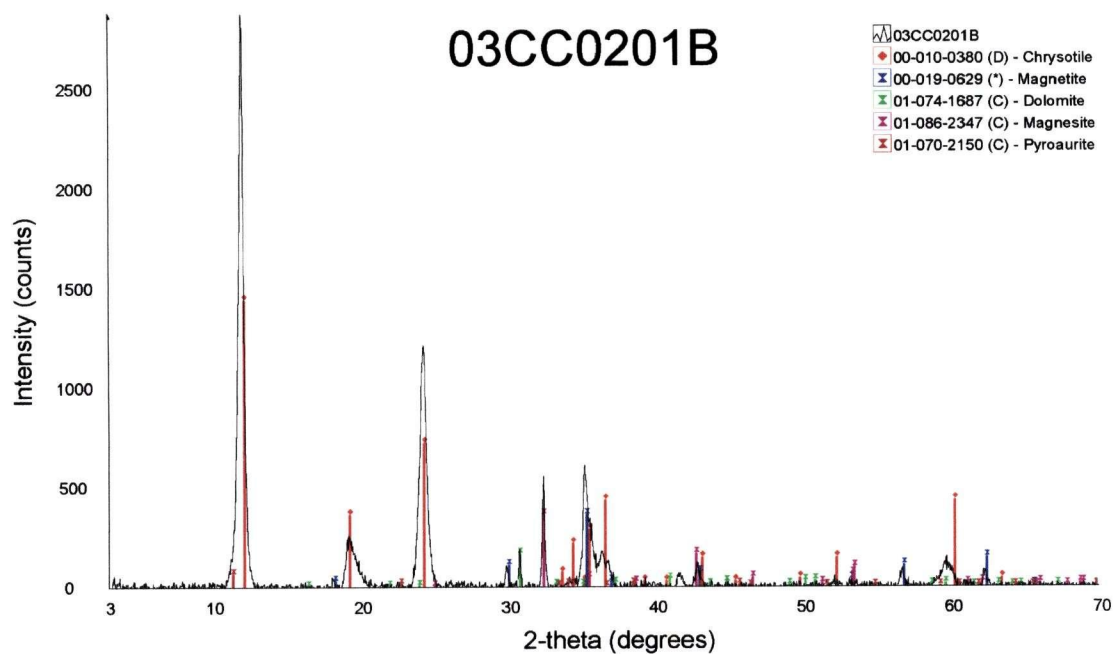


FIGURE B67: X-ray diffractogram for 03CC0201B.

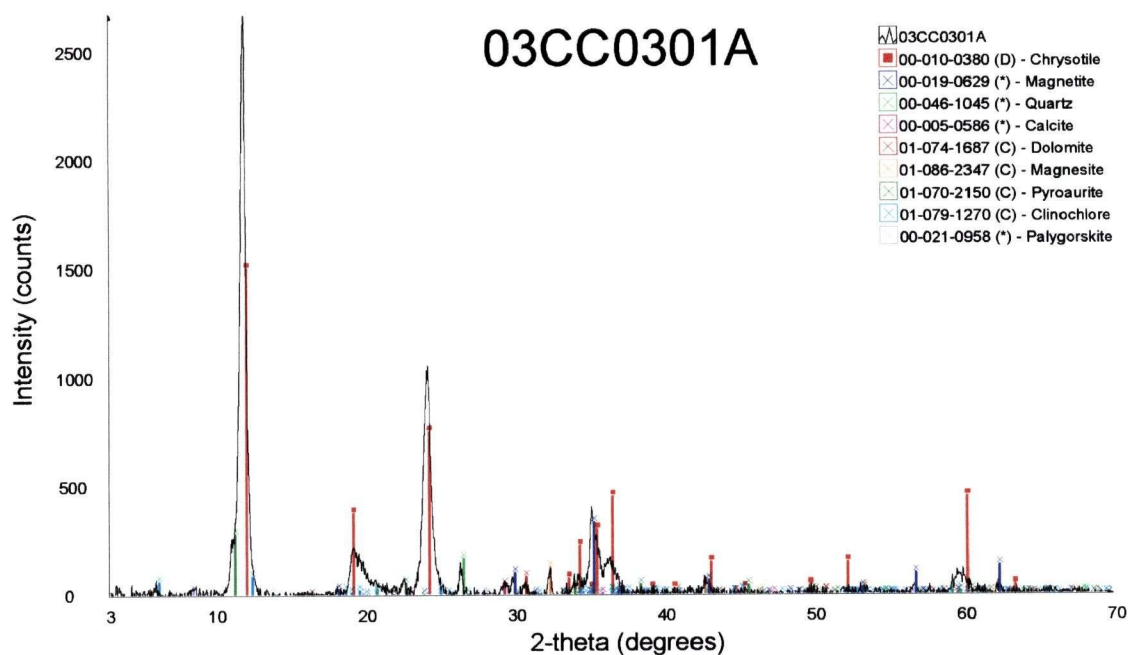


FIGURE B68: X-ray diffractogram for 03CC0301A.

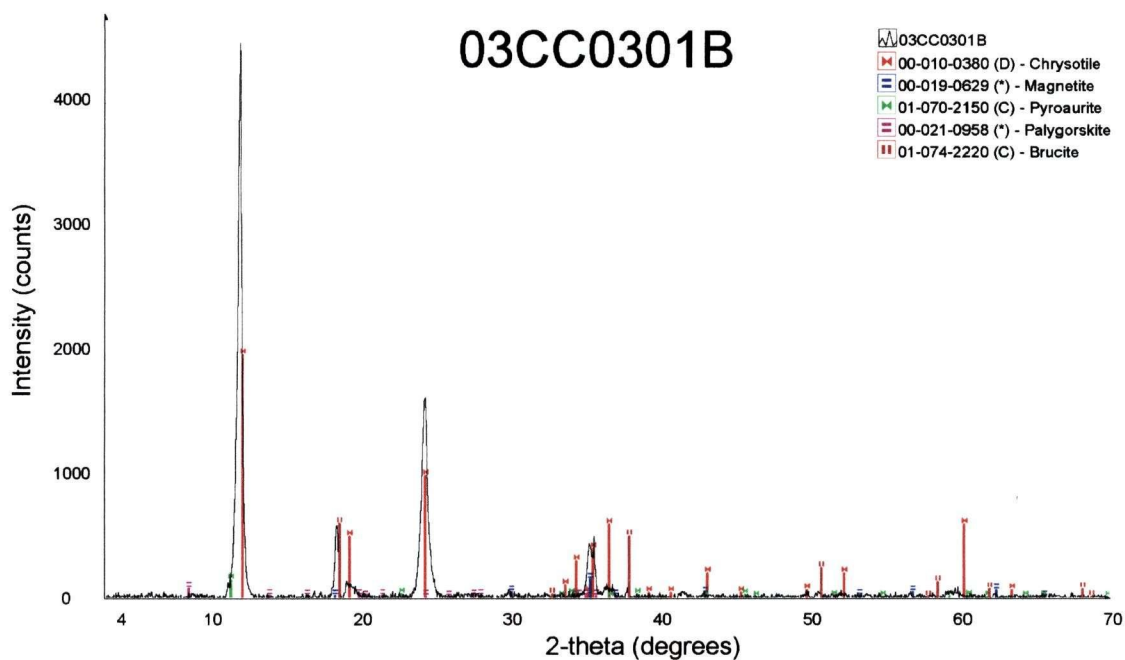


FIGURE B69: X-ray diffractogram for 03CC0301B.

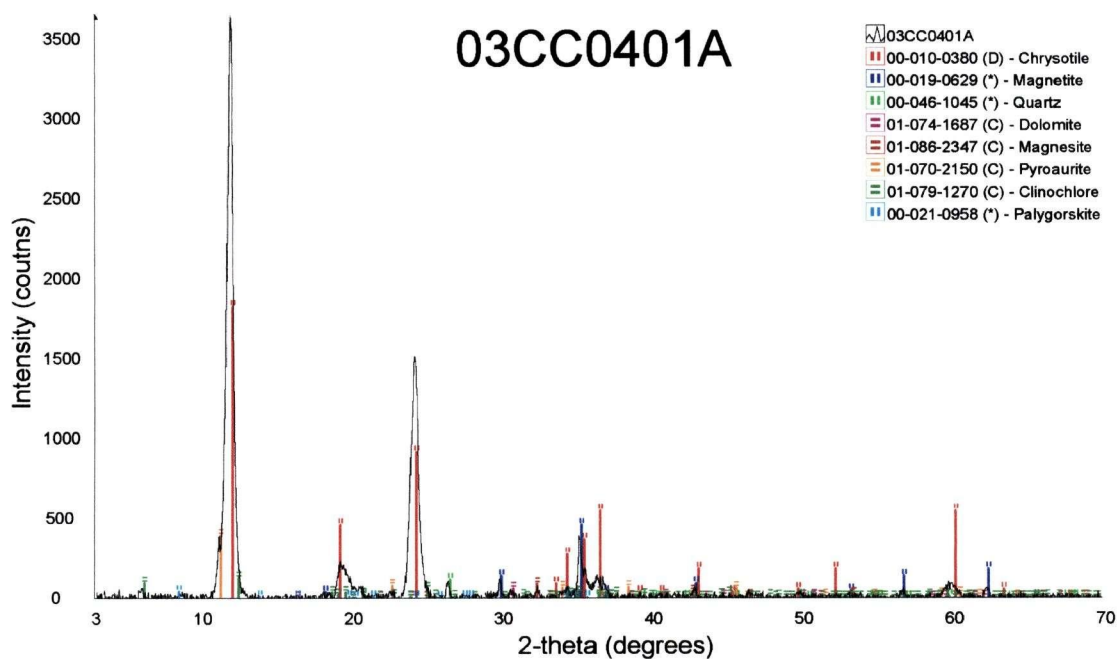


FIGURE B70: X-ray diffractogram for 03CC0401A.

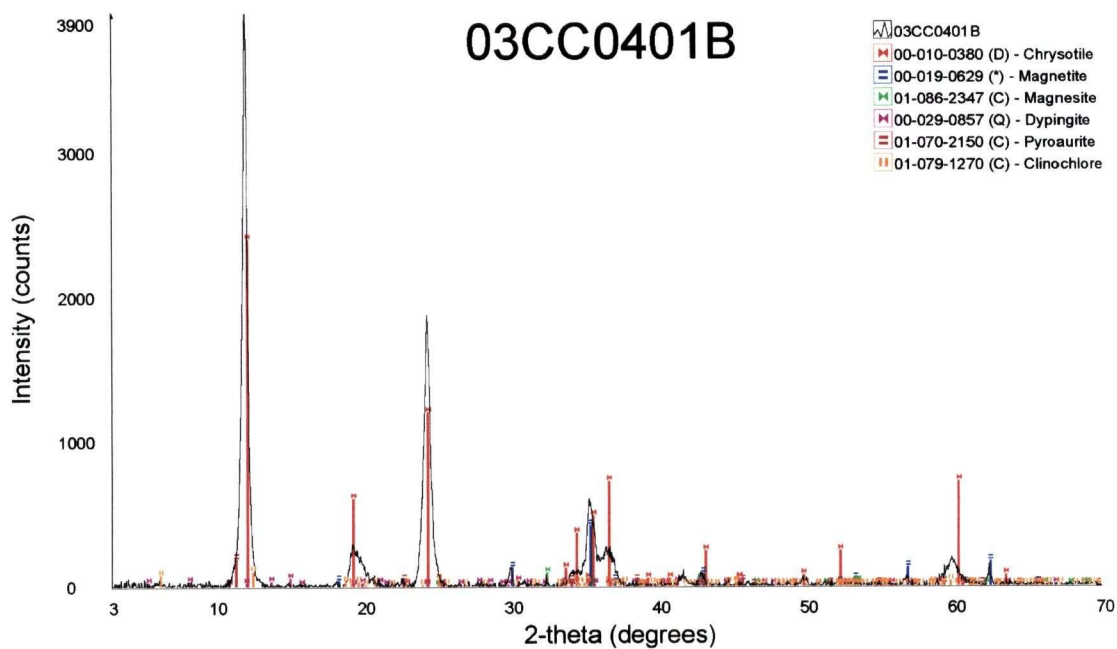


FIGURE B71: X-ray diffractogram for 03CC0401B.

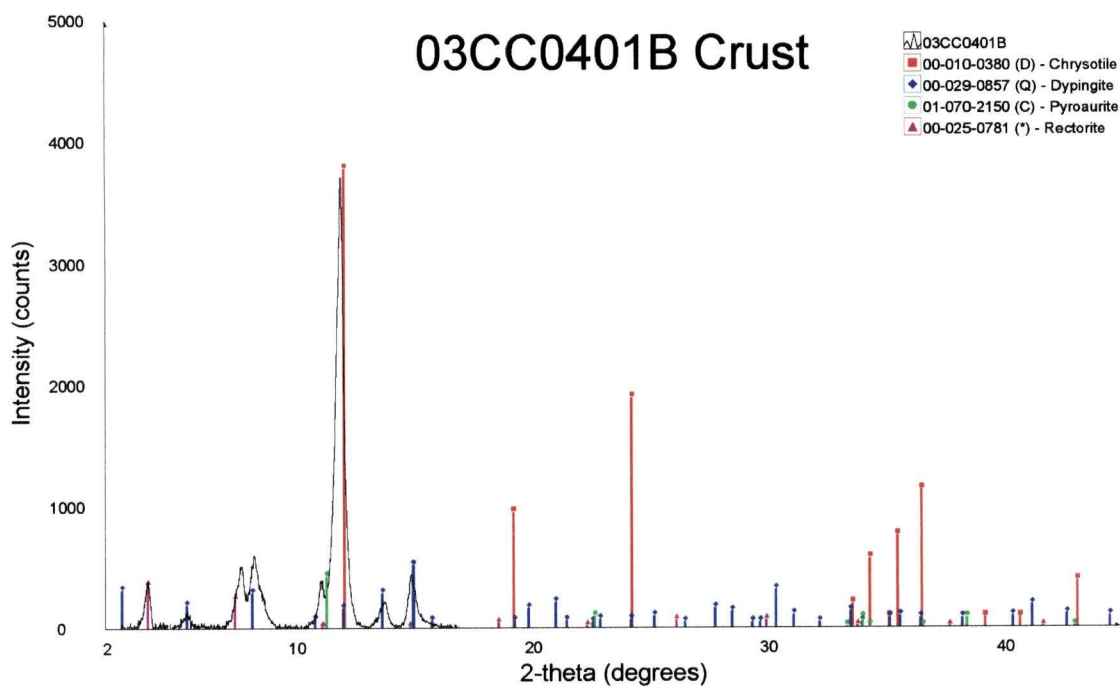


FIGURE B72: X-ray diffractogram for 03CC0401B using higher count rate.



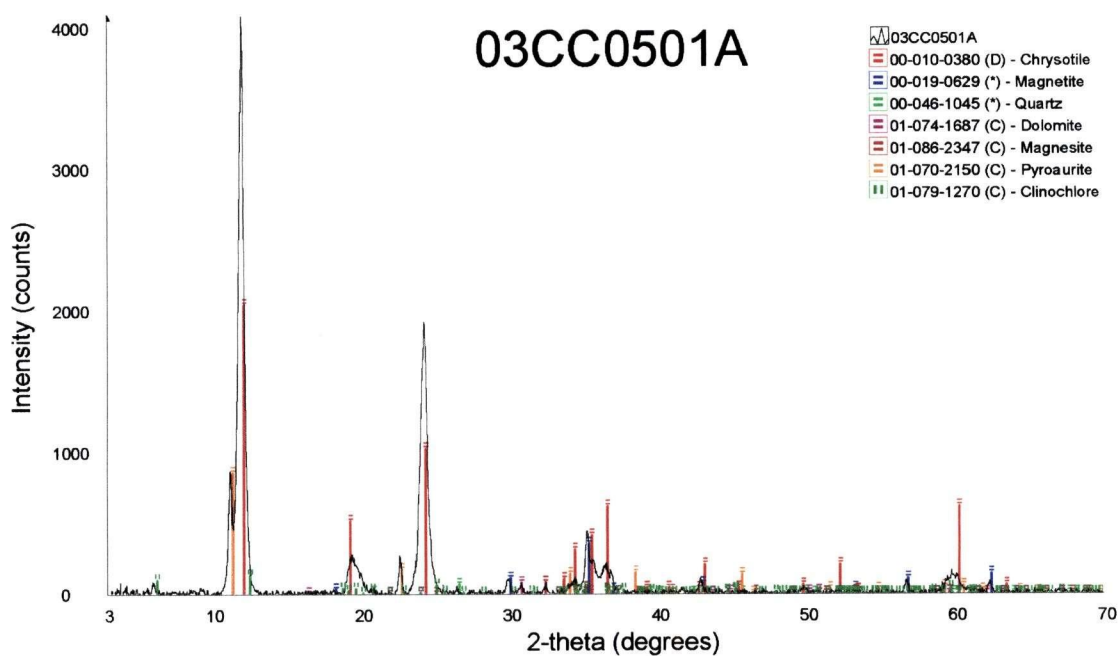


FIGURE B73: X-ray diffractogram for 03CC0501A.

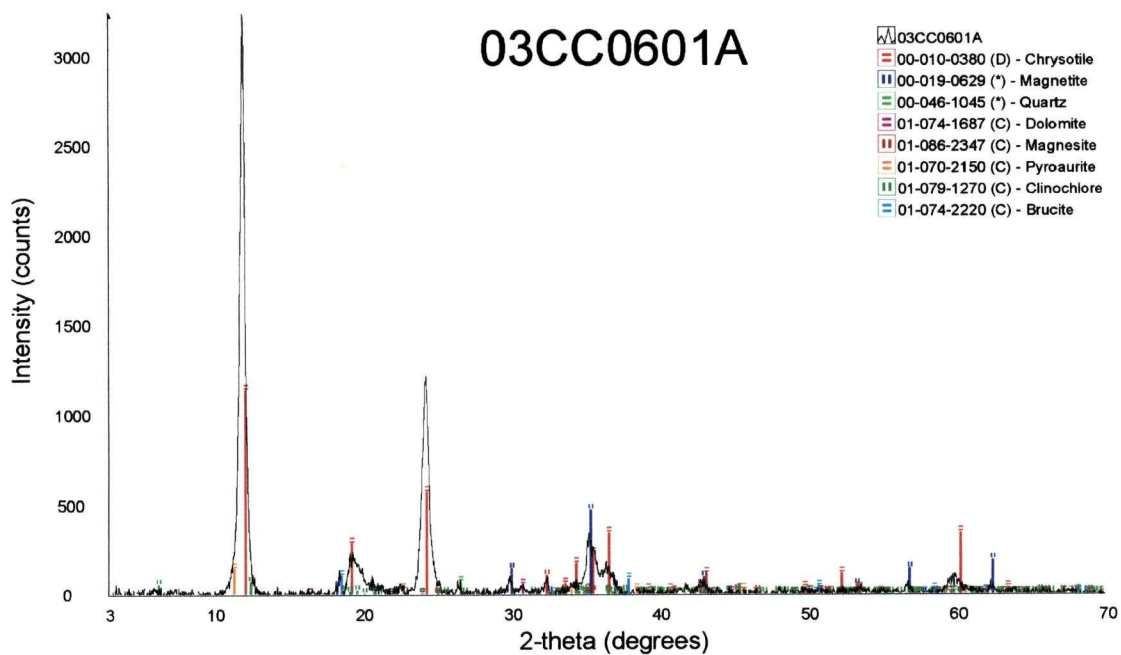


FIGURE B74: X-ray diffractogram for 03CC0601A.



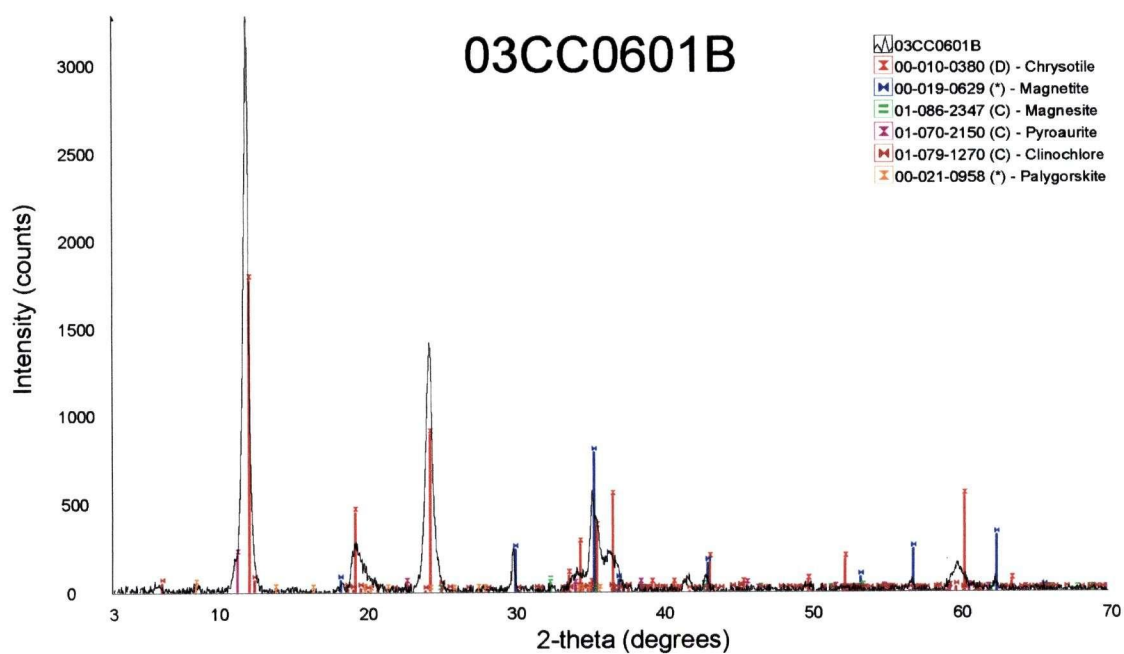


FIGURE B75: X-ray diffractogram for 03CC0601B.

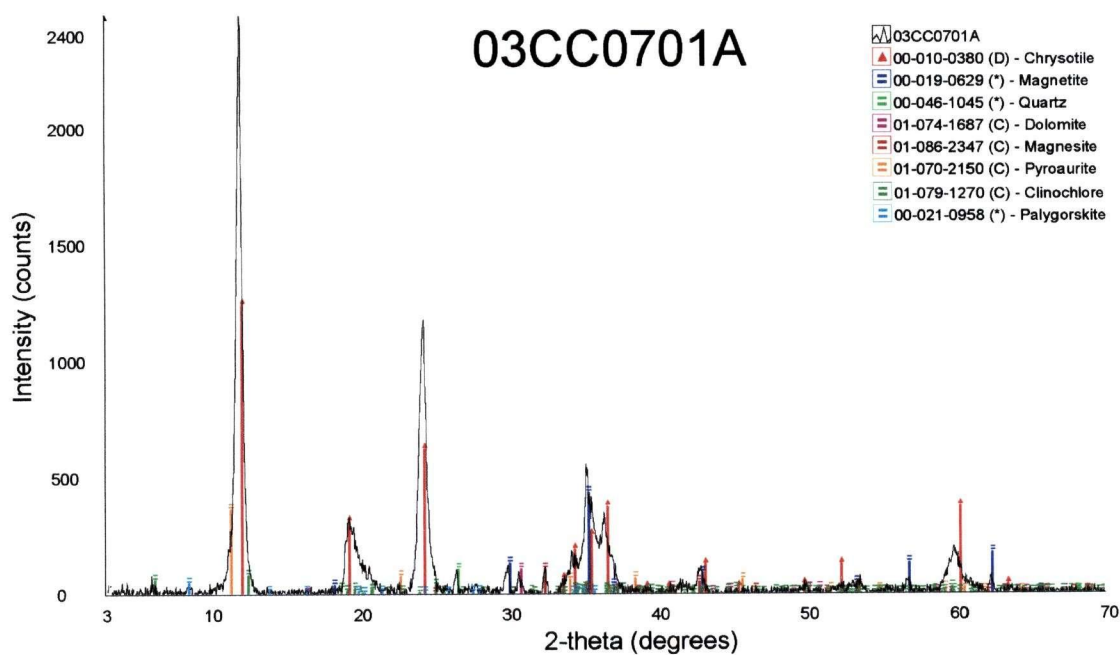


FIGURE B76: X-ray diffractogram for 03CC0701A.

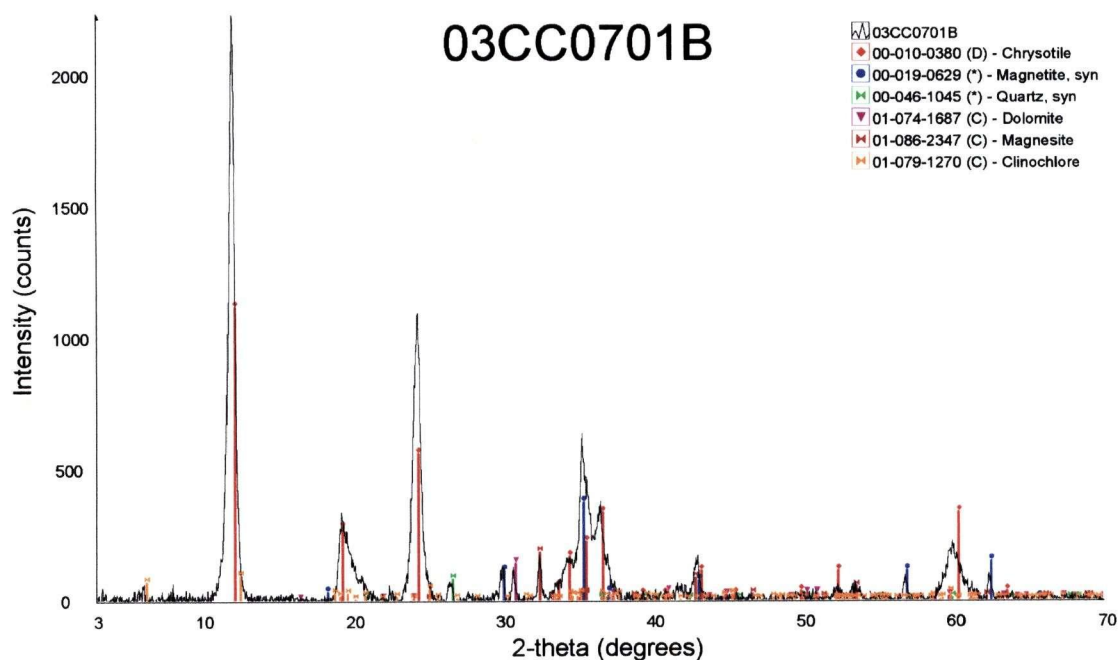


FIGURE B77: X-ray diffractogram for 03CC0701B.

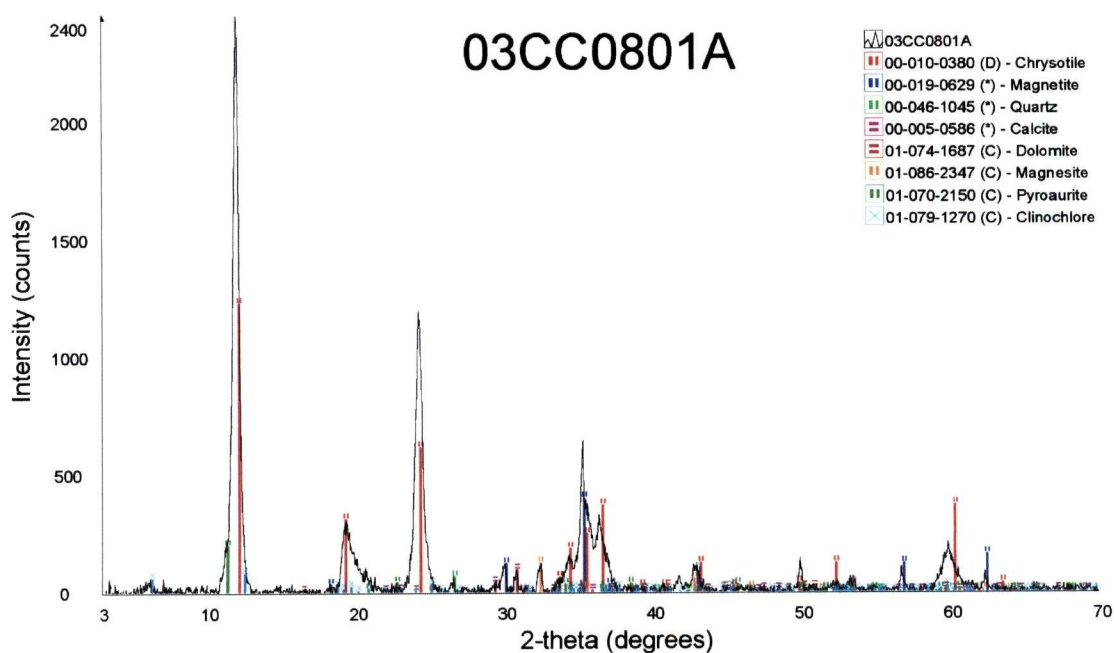


FIGURE B78: X-ray diffractogram for 03CC0801A.

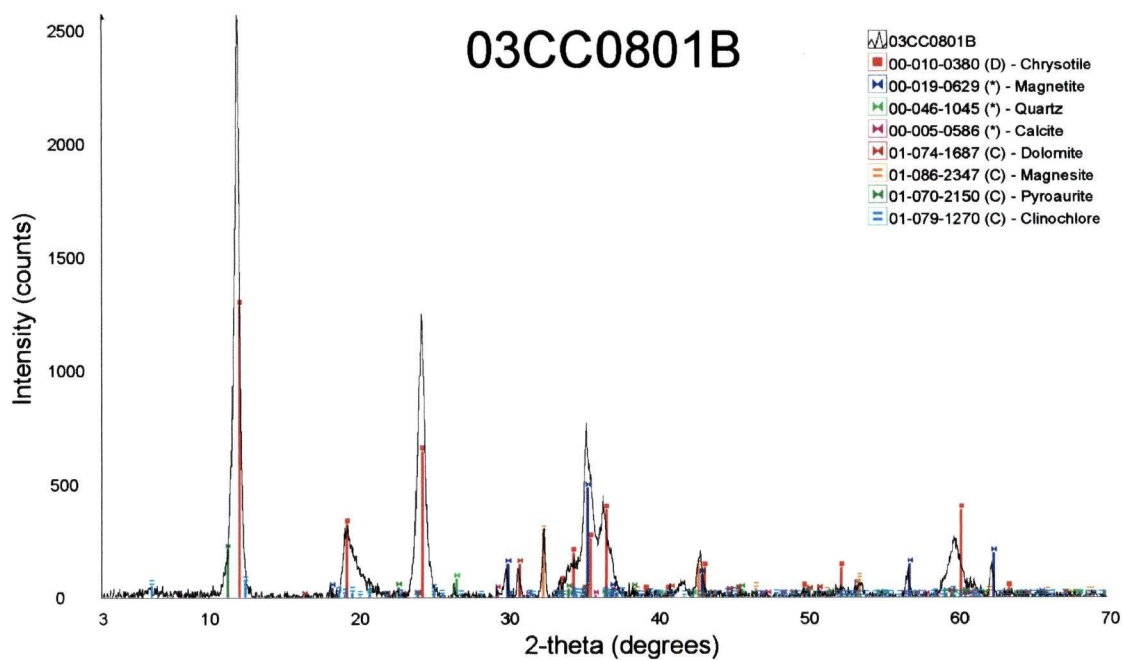


FIGURE B79: X-ray diffractogram for 03CC0801B.

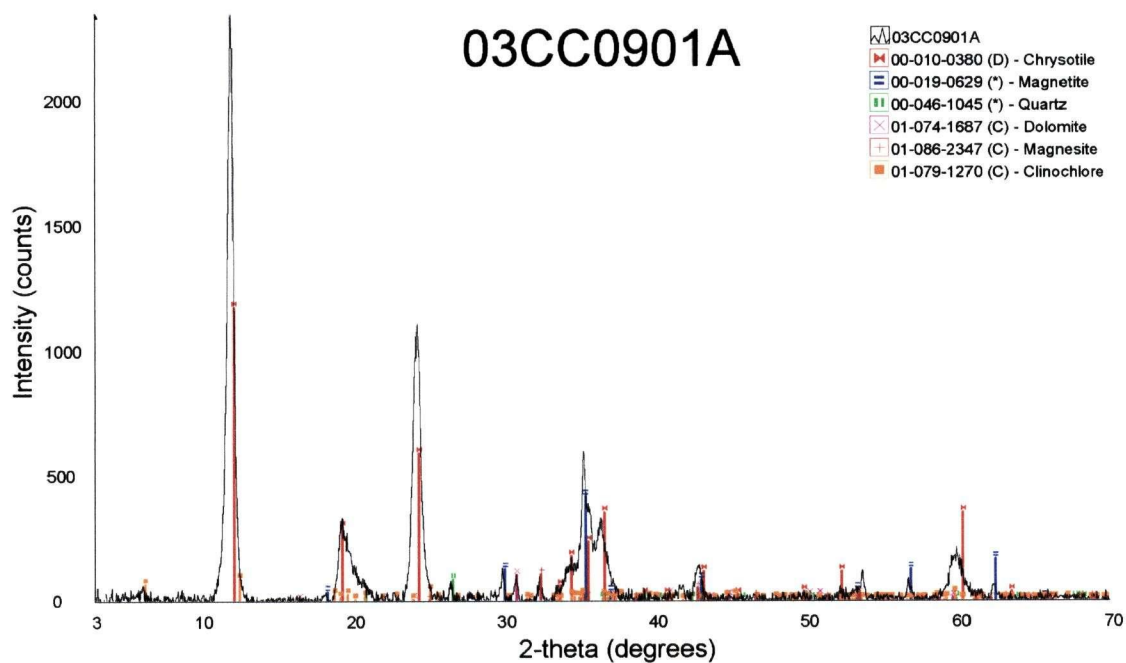


FIGURE B80: X-ray diffractogram for 03CC0901A.

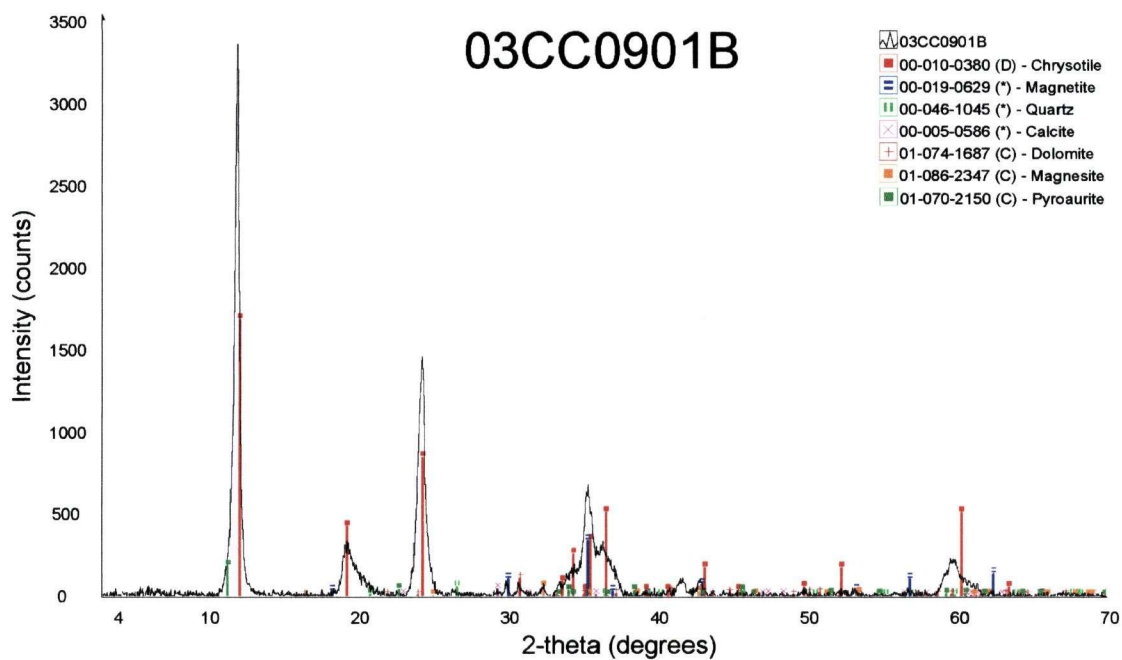


FIGURE B81: X-ray diffractogram for 03CC0901B.

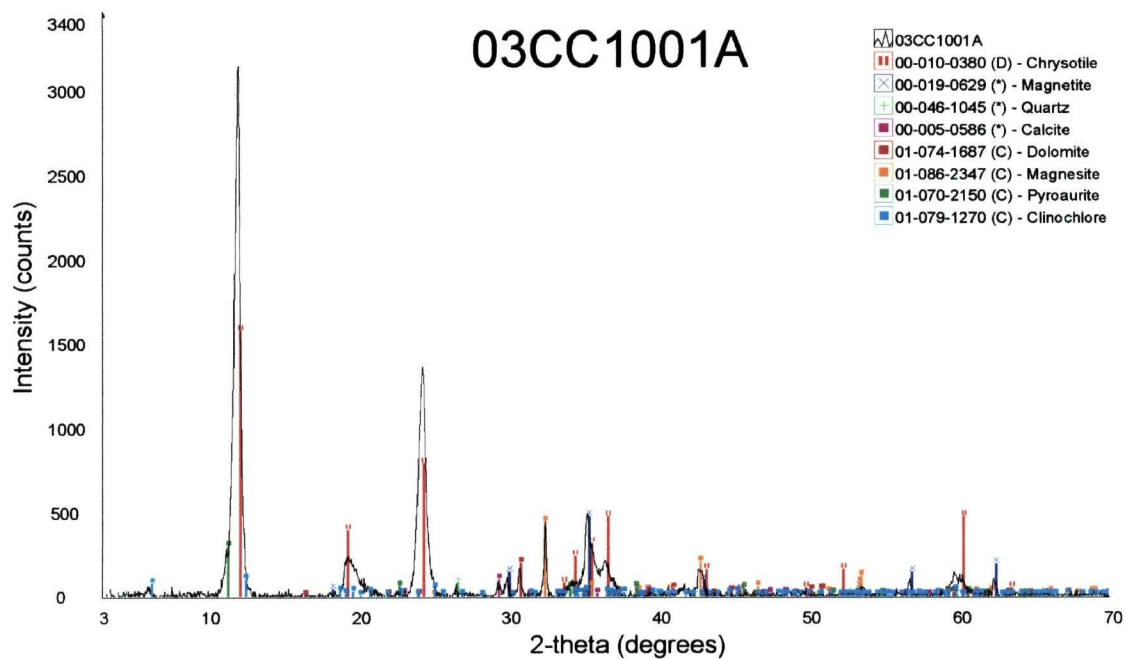


FIGURE B82: X-ray diffractogram for 03CC1001A.

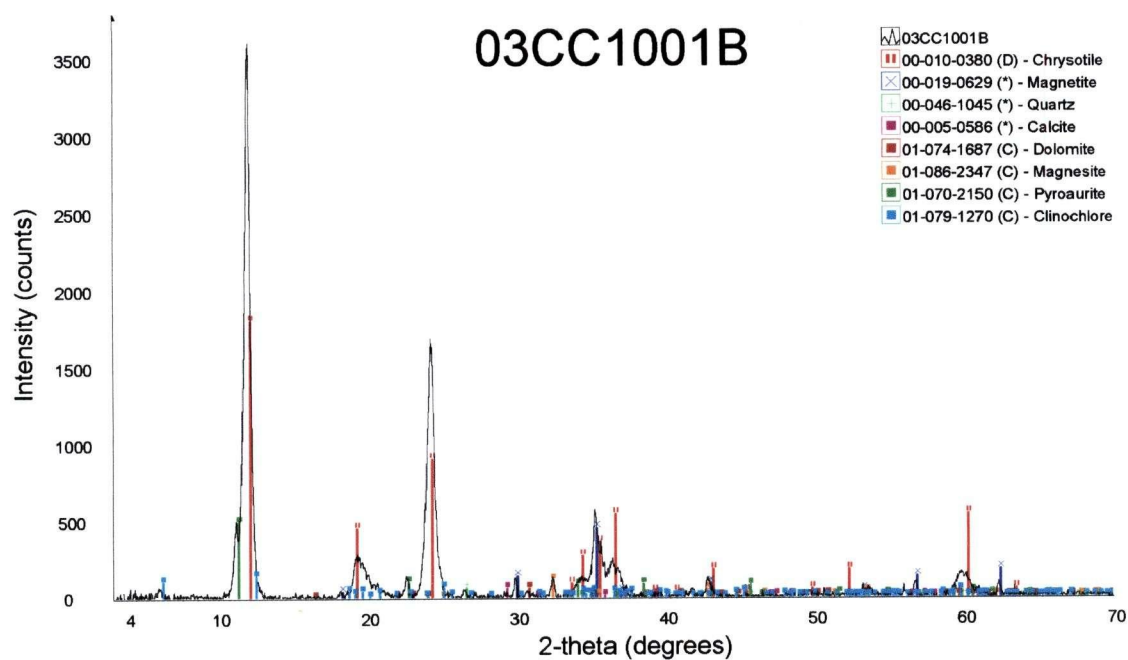


FIGURE B83: X-ray diffractogram for 03CC1001B.

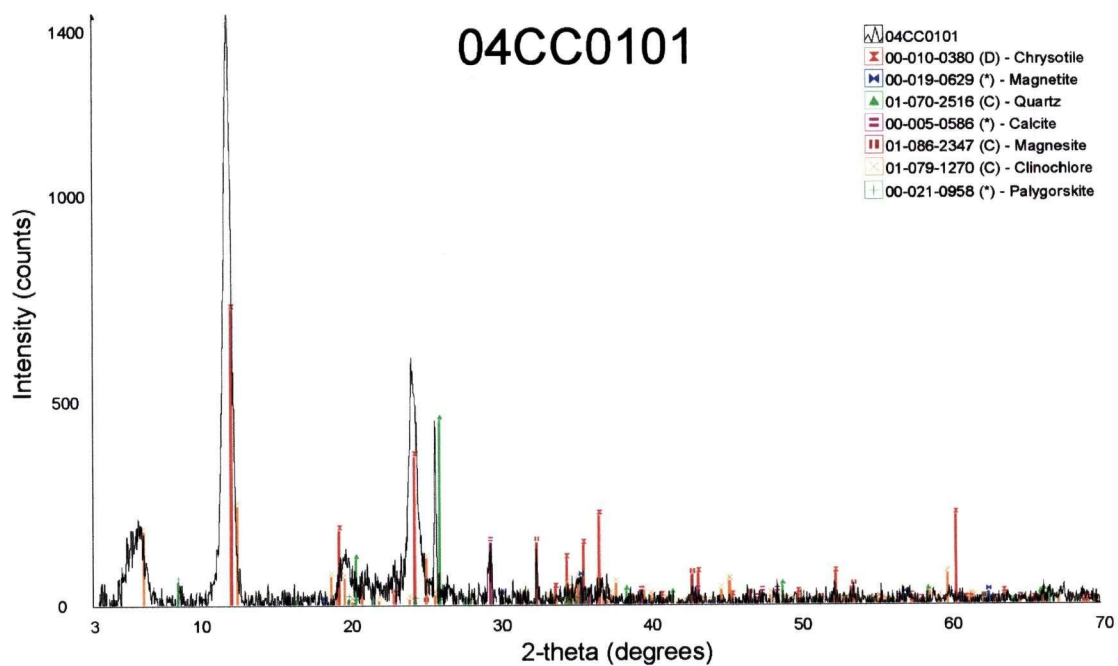


FIGURE B84: X-ray diffractogram for 04CC0101.

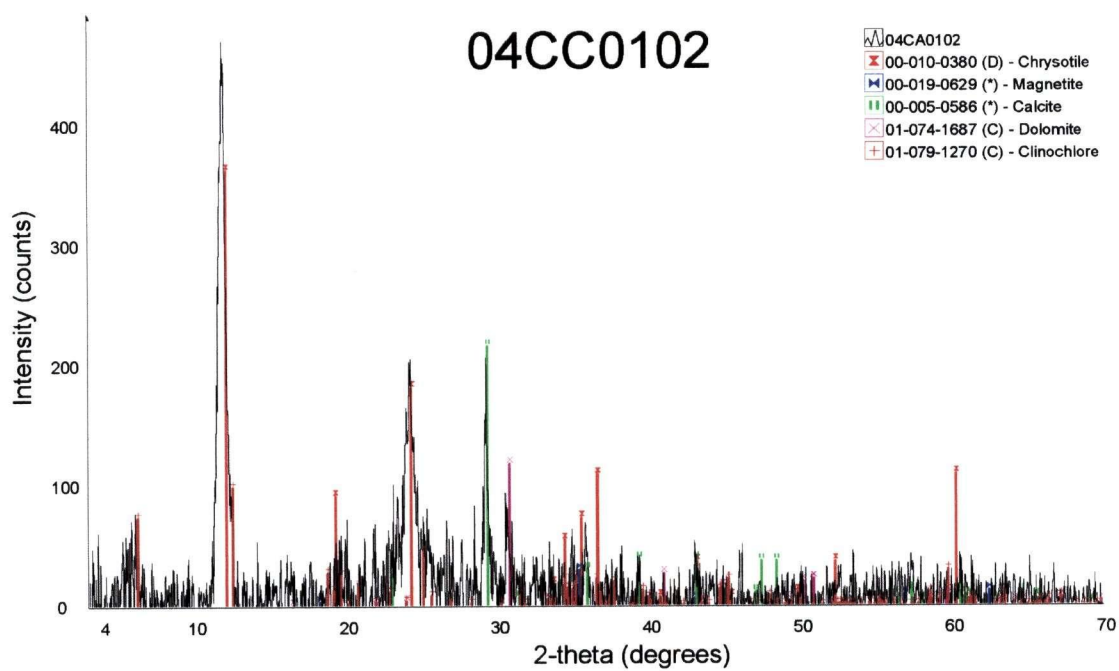


FIGURE B85: X-ray diffractogram for 04CC0102.

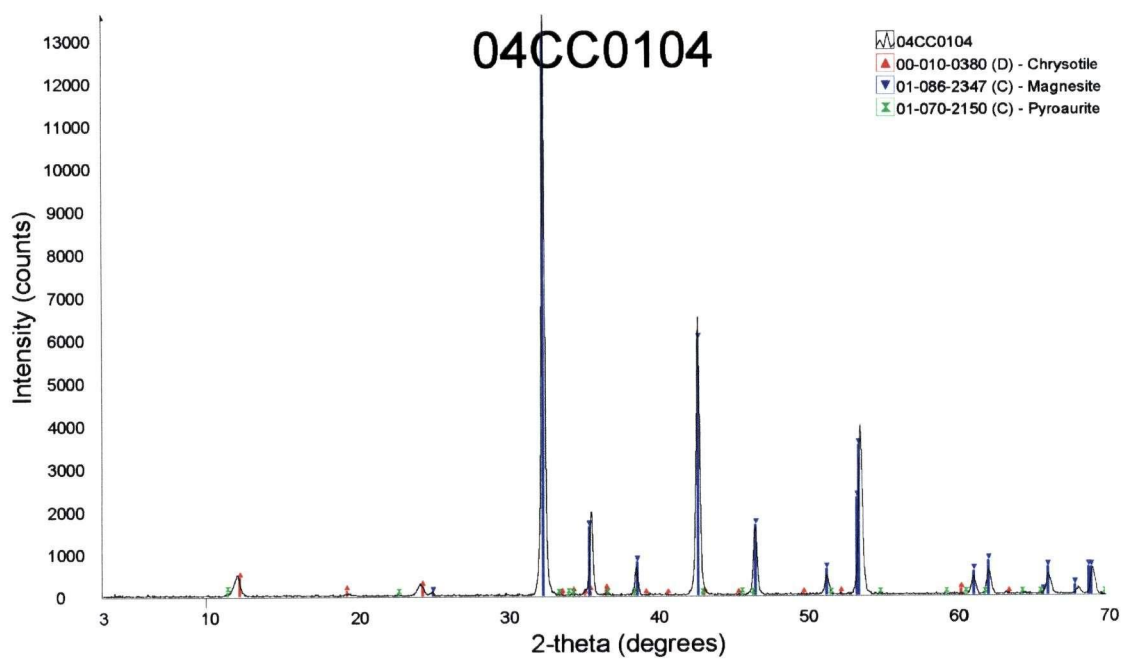


FIGURE B86: X-ray diffractogram for 04CC0104.



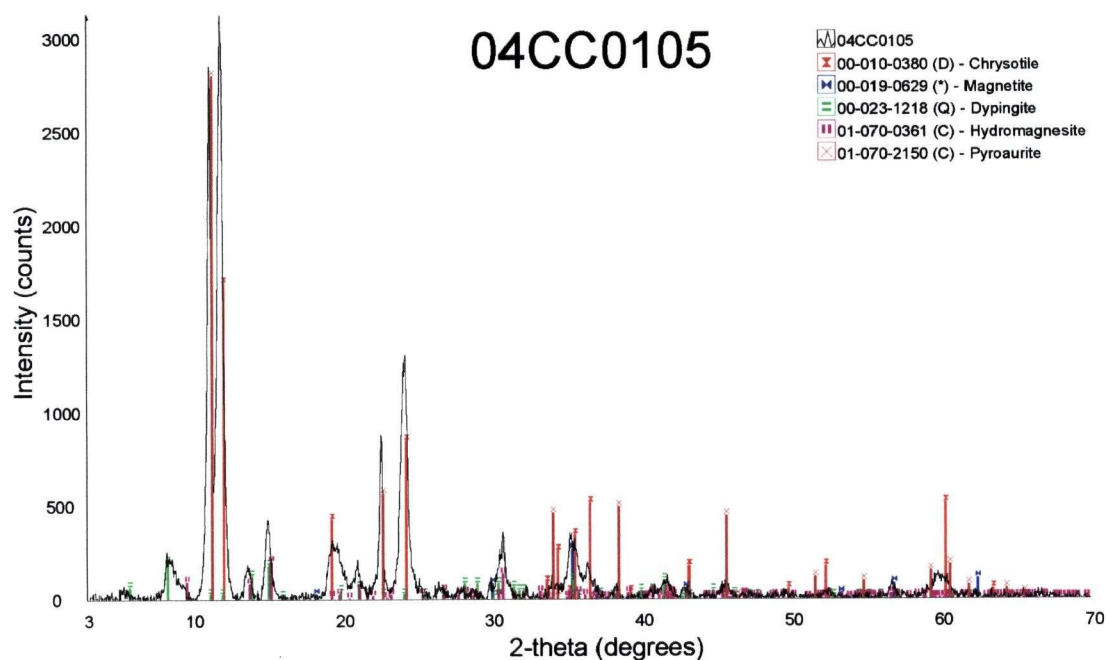


FIGURE B87: X-ray diffractogram for 04CC0105.

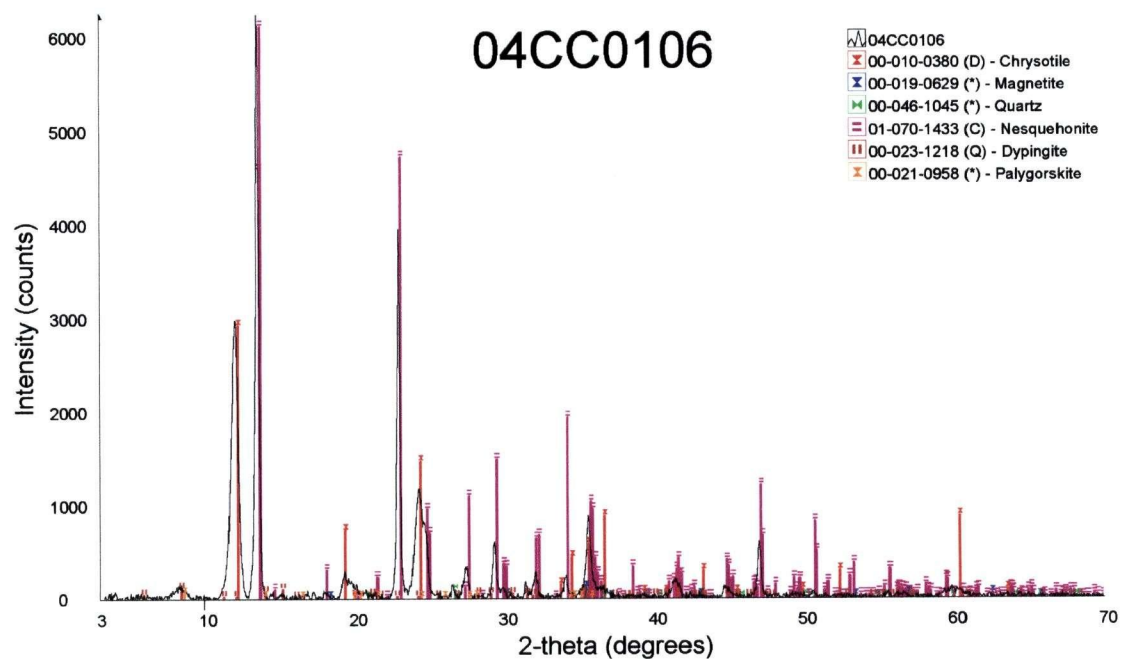


FIGURE B88: X-ray diffractogram for 04CC0106.

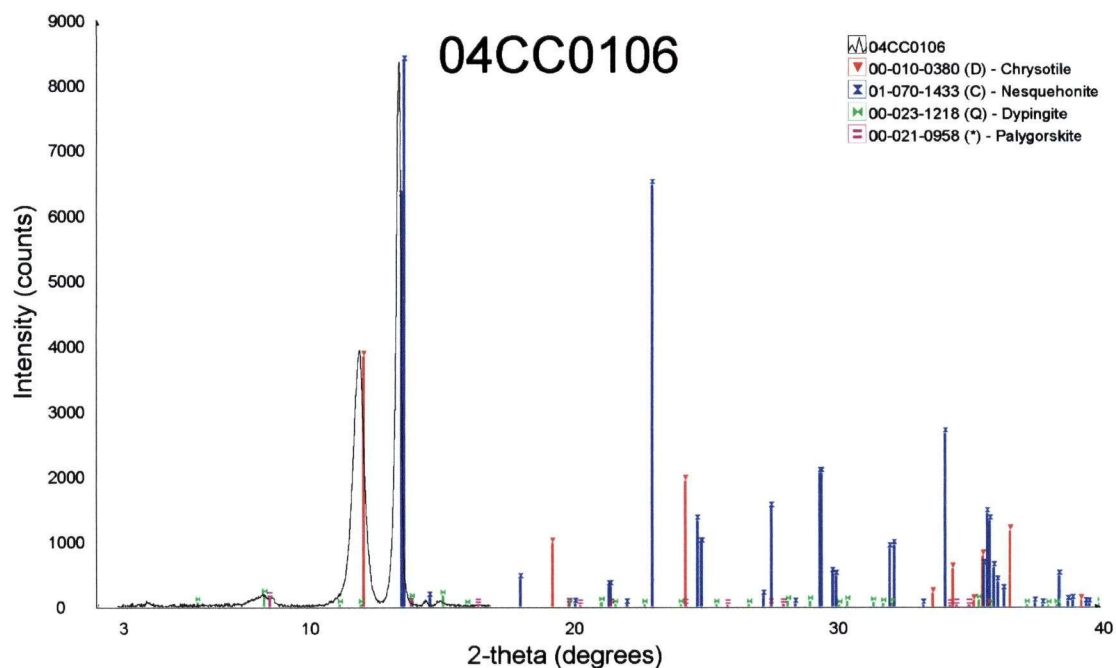


FIGURE B89: Close-up of X-ray diffractogram for 04CC0106 using higher count rate.

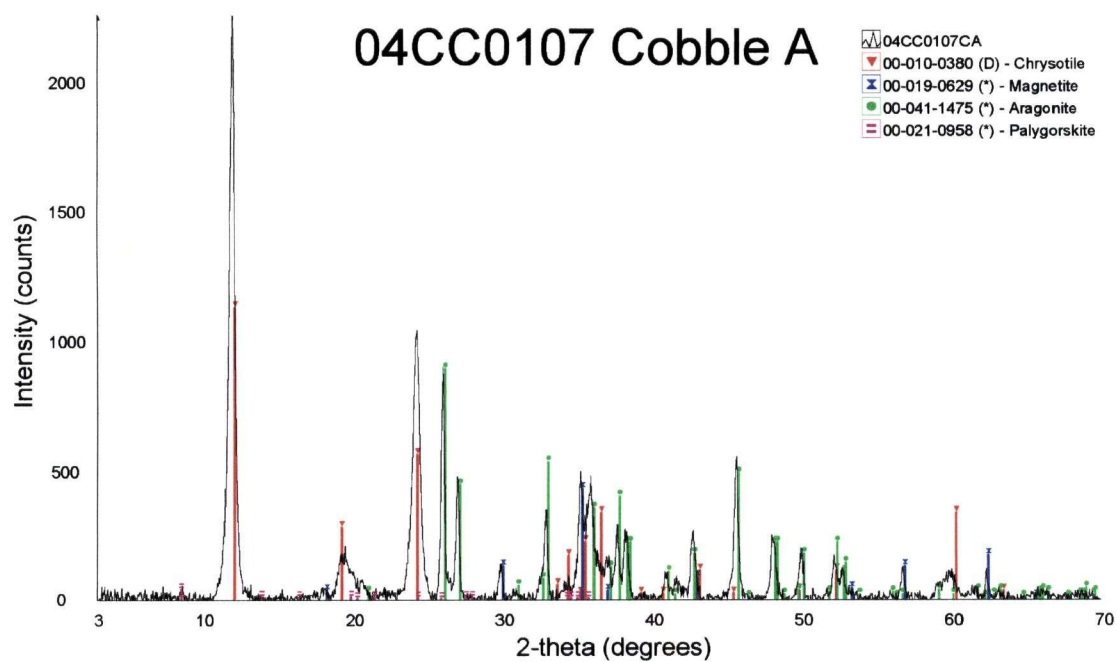


FIGURE B90: X-ray diffractogram for cobble coating from 04CC0107 cobble A.



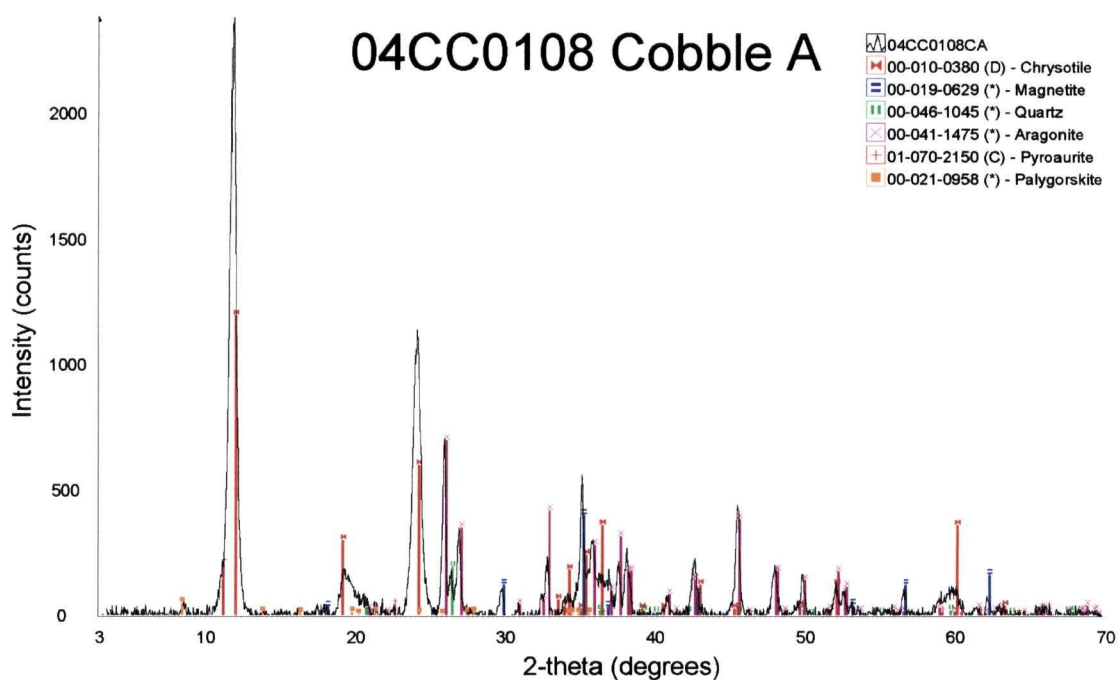


FIGURE B91: X-ray diffractogram for cobble coating from 04CC0108 cobble A.

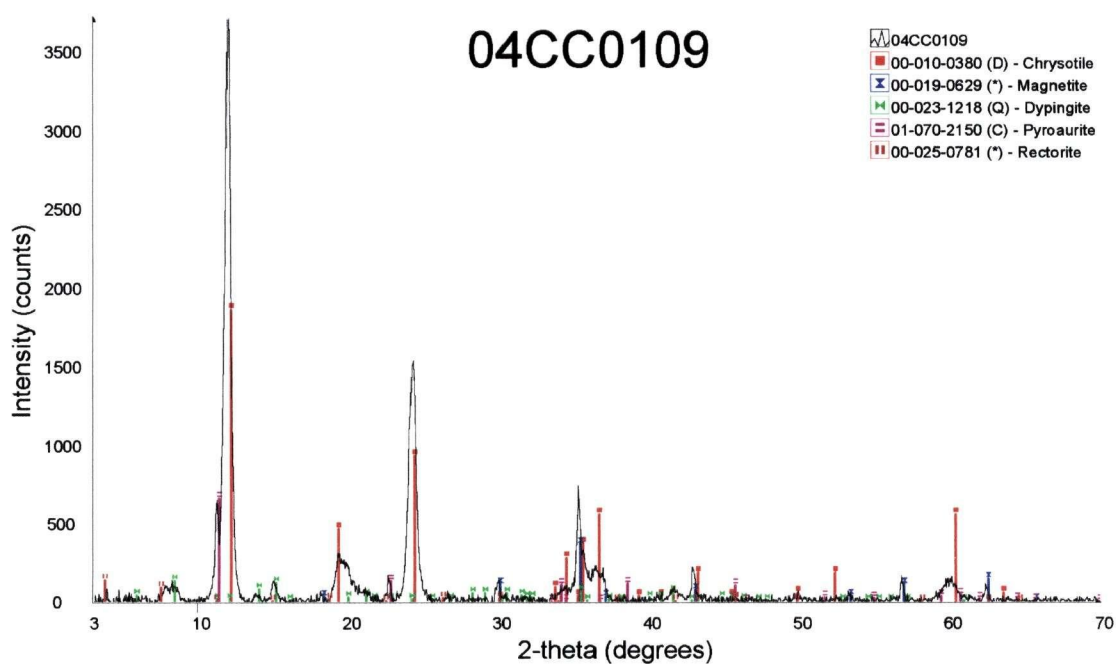


FIGURE B92: X-ray diffractogram for 04CC0109.

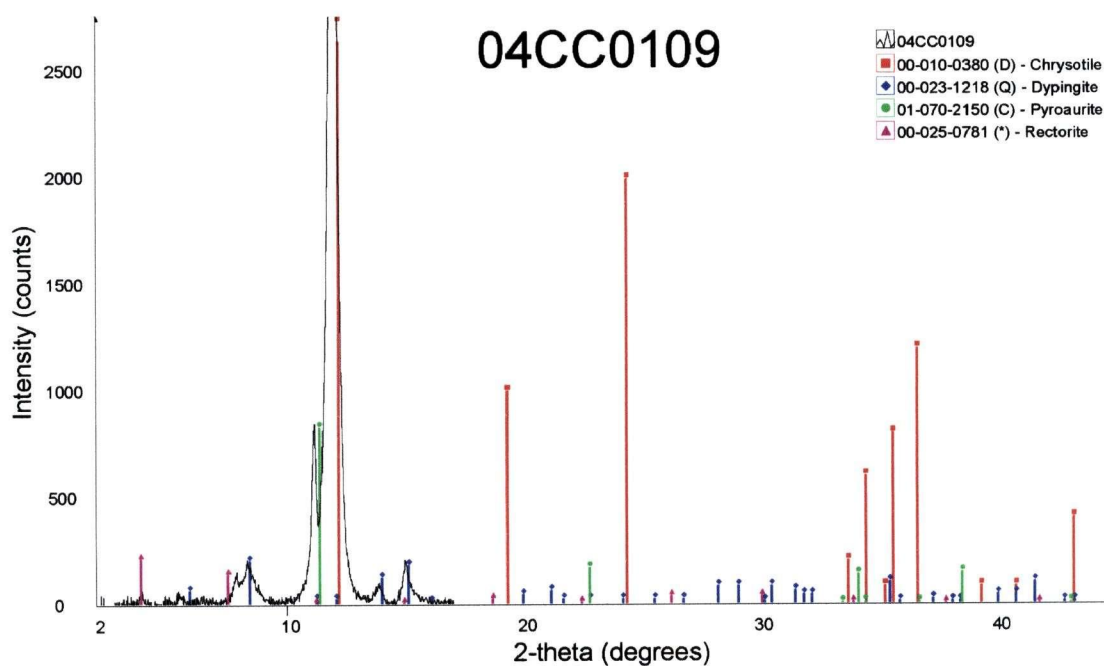


FIGURE B93: Close-up of X-ray diffractogram for 04CC0109 using higher count rate.

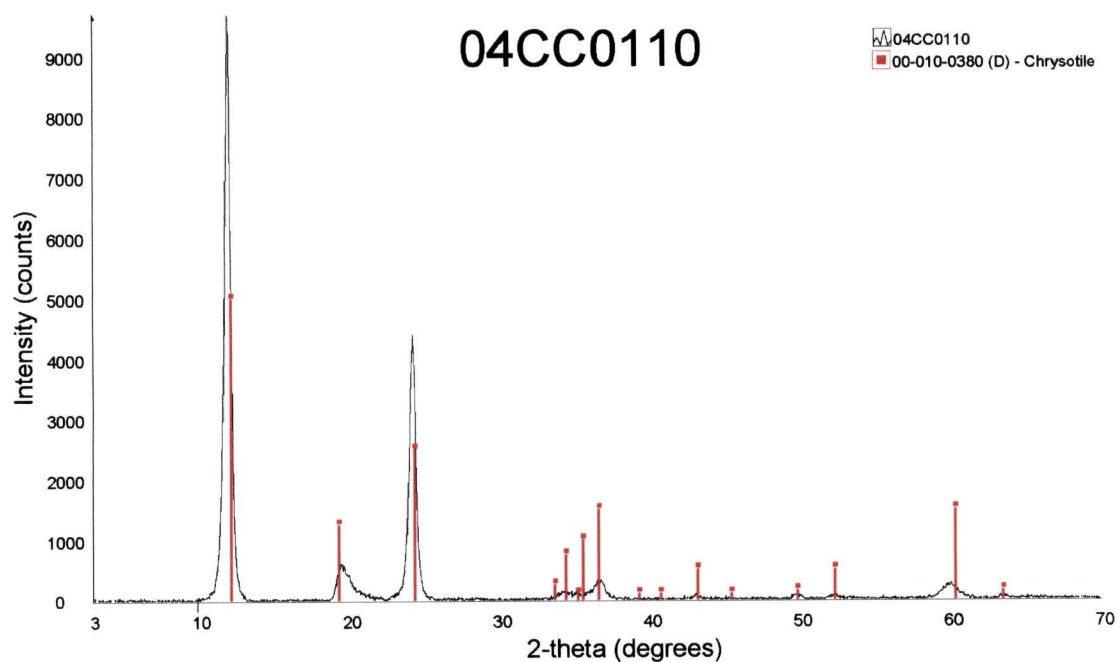


FIGURE B94: X-ray diffractogram for 04CC0110. Pure chrysotile used in synthetic tailings (Chapter 4).

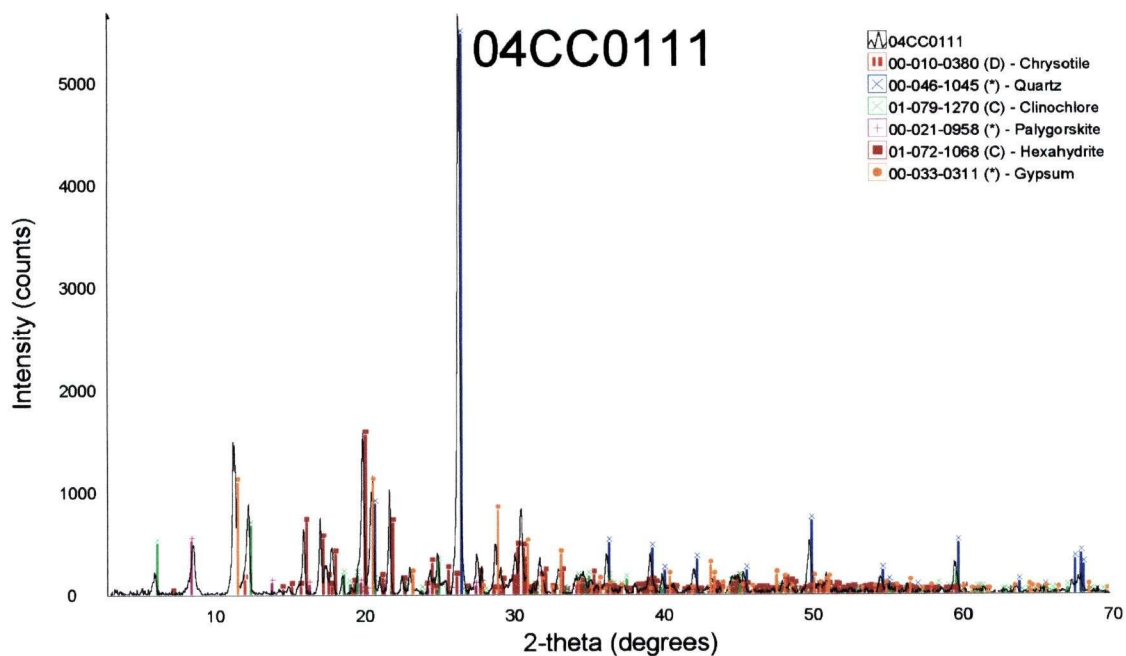


FIGURE B95: X-ray diffractogram for 04CC0111.

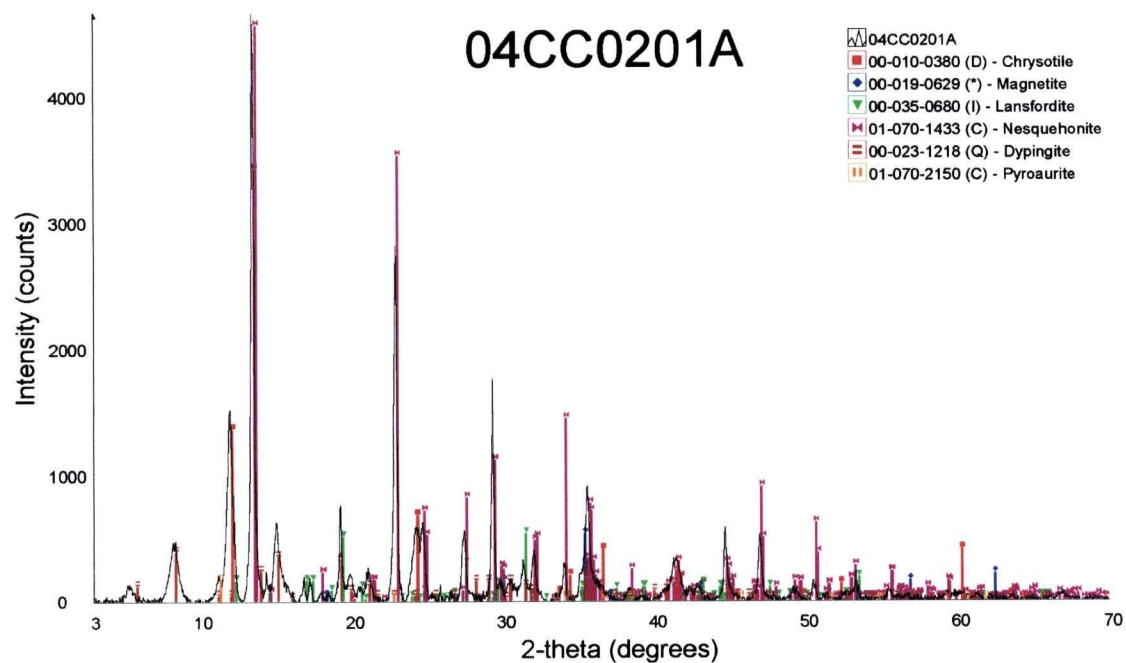


FIGURE B96: X-ray diffractogram for 04CC0201A.

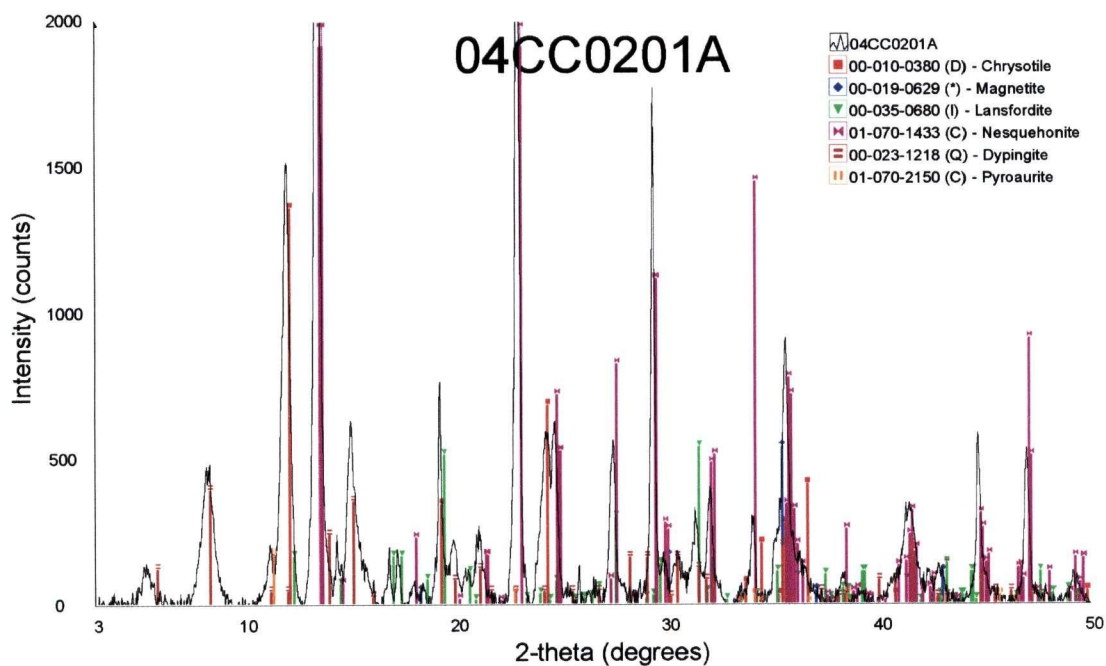


FIGURE B97: Close-up of X-ray diffractogram for 04CC0201A.

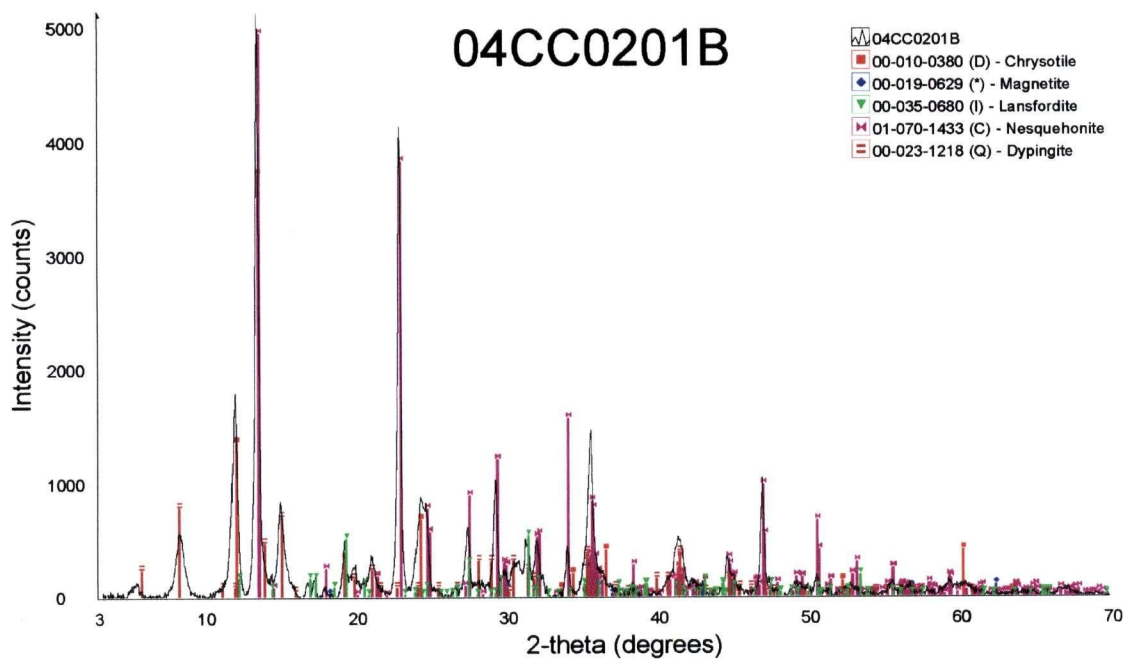


FIGURE B98: X-ray diffractogram for 04CC0201B.

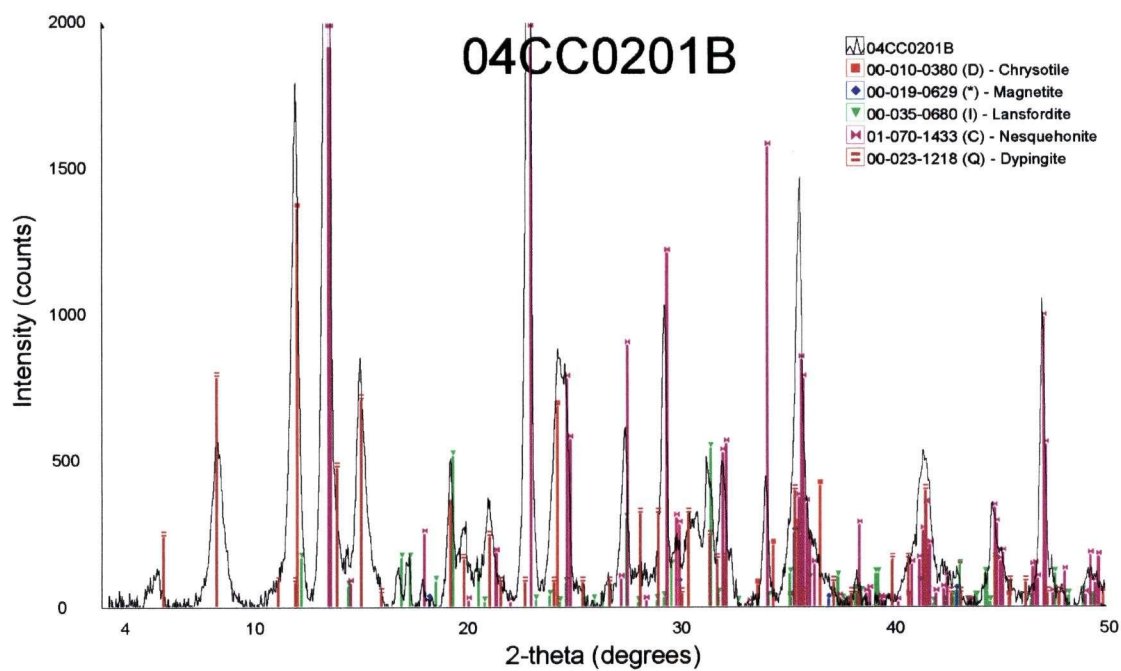


FIGURE B99: Close-up of X-ray diffractogram for 04CC0201B.

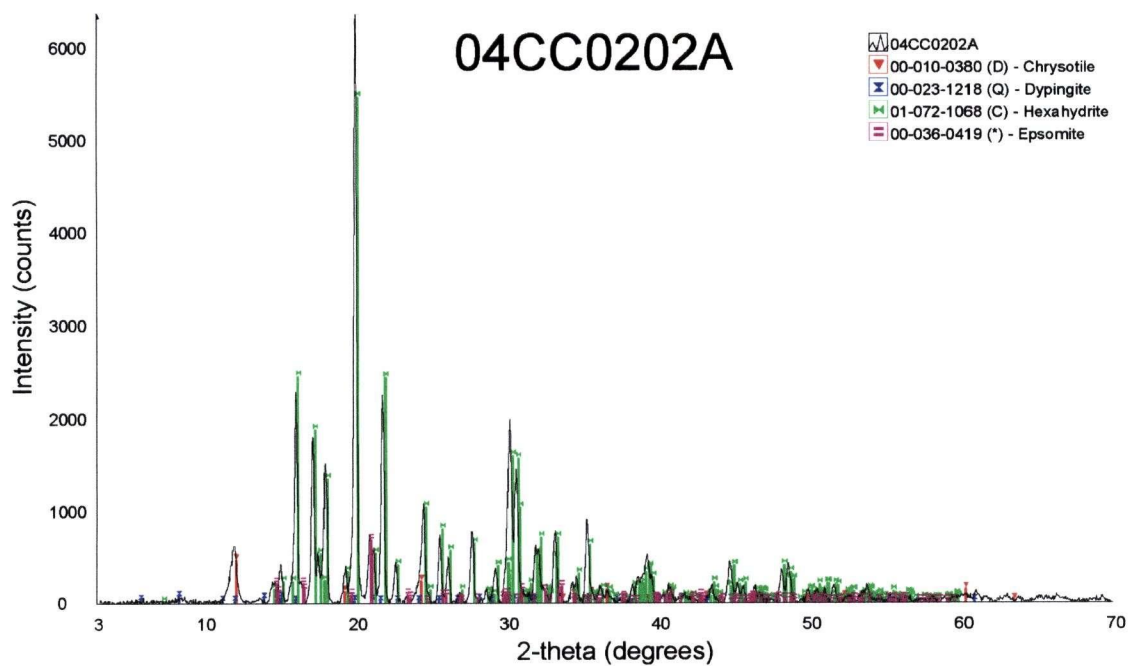


FIGURE B100: X-ray diffractogram for 04CC0202A.

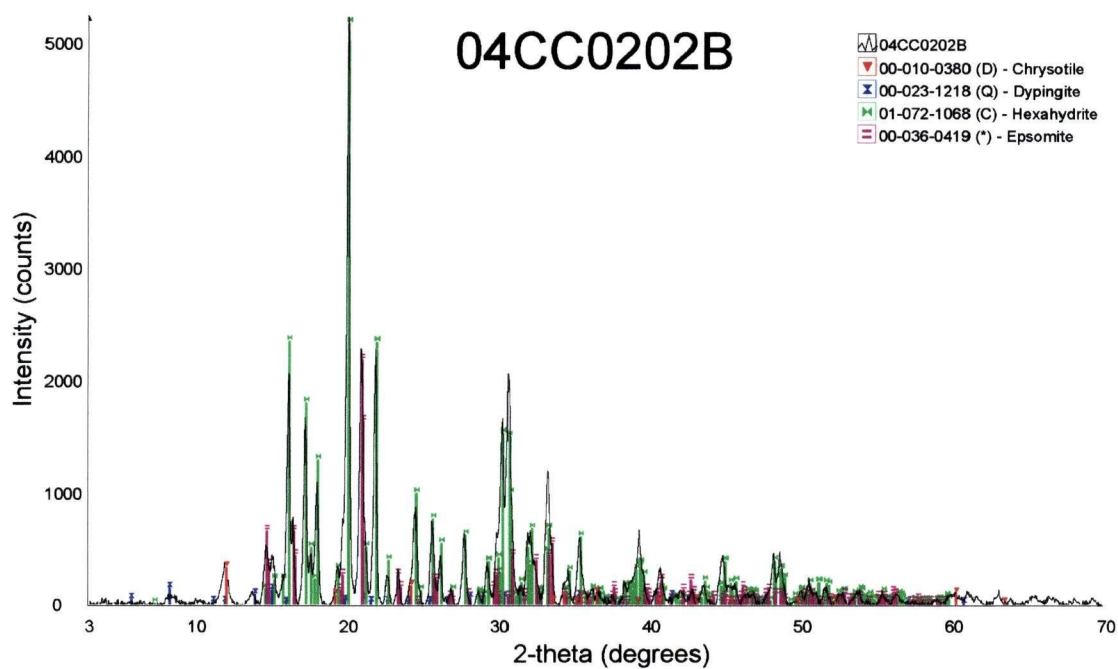


FIGURE B101: X-ray diffractogram for 04CC0202B.

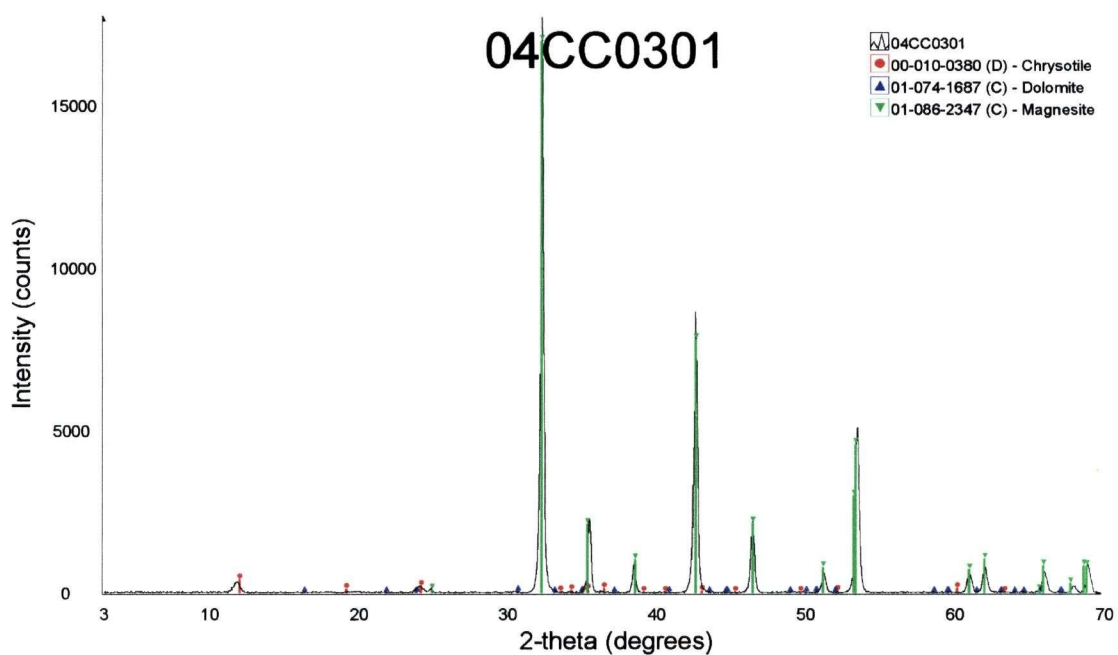


FIGURE B102: X-ray diffractogram for 04CC0301.



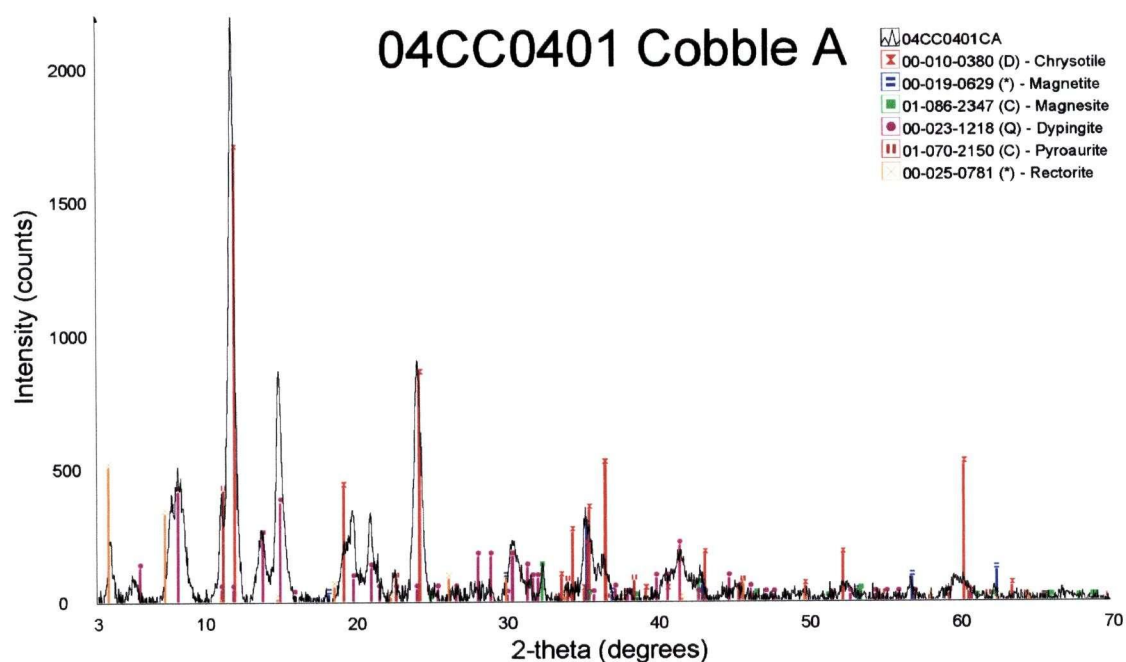


FIGURE B103: X-ray diffractogram for cobble coating from 04CC0401 cobble A.

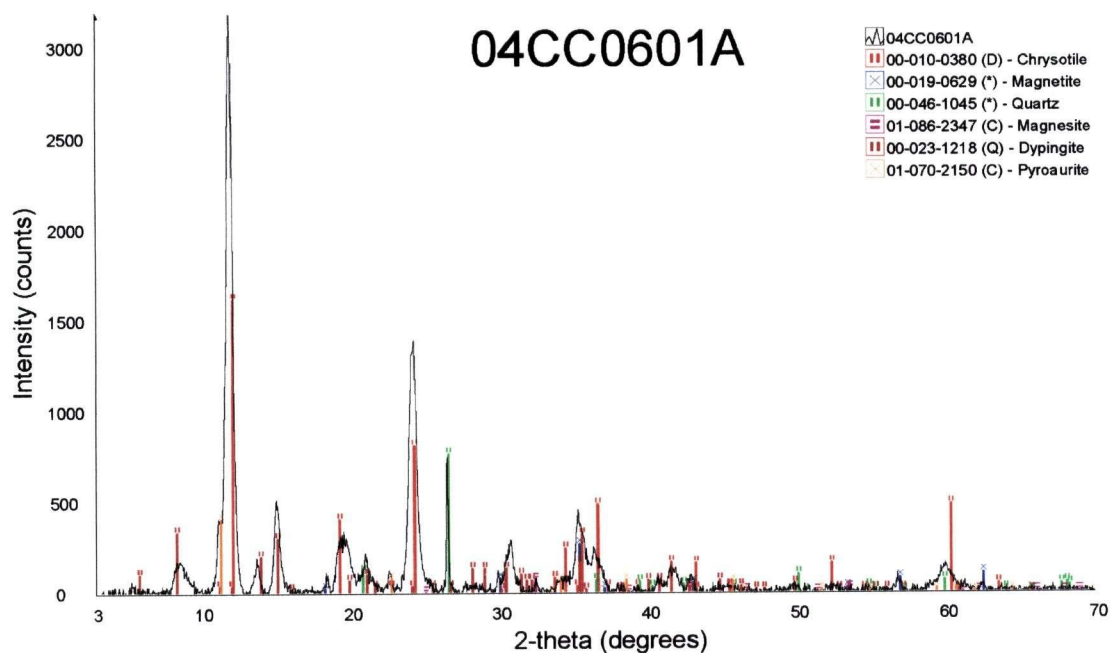


FIGURE B104: X-ray diffractogram for 04CC0601A.

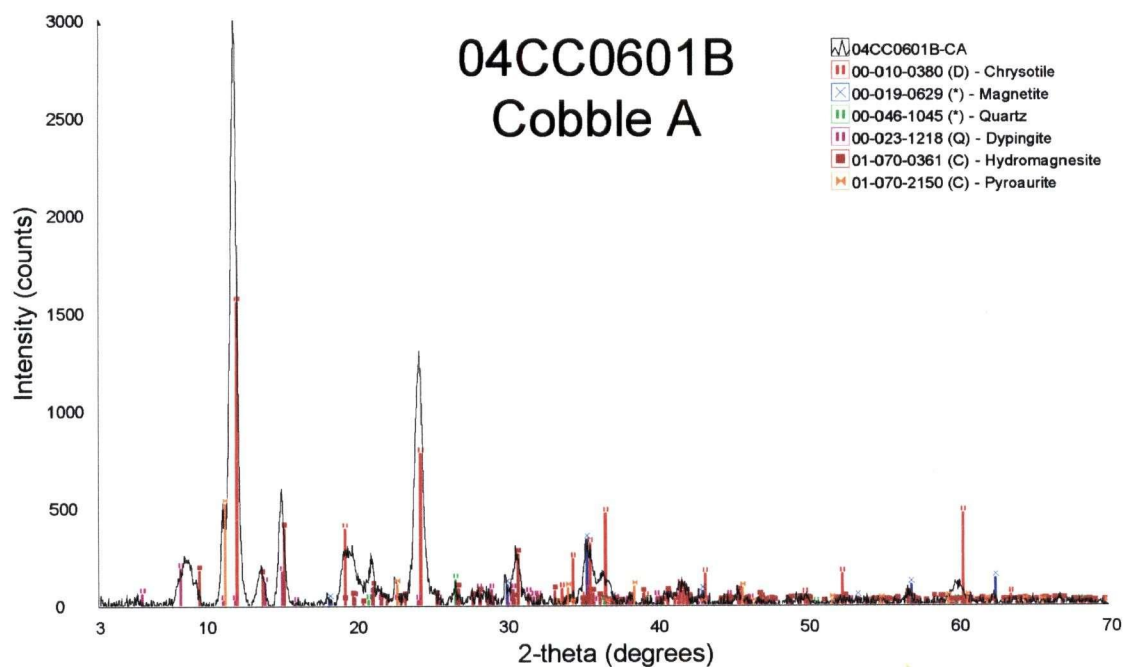


FIGURE B105: X-ray diffractogram for cobble coating from 04CC0601B cobble A.

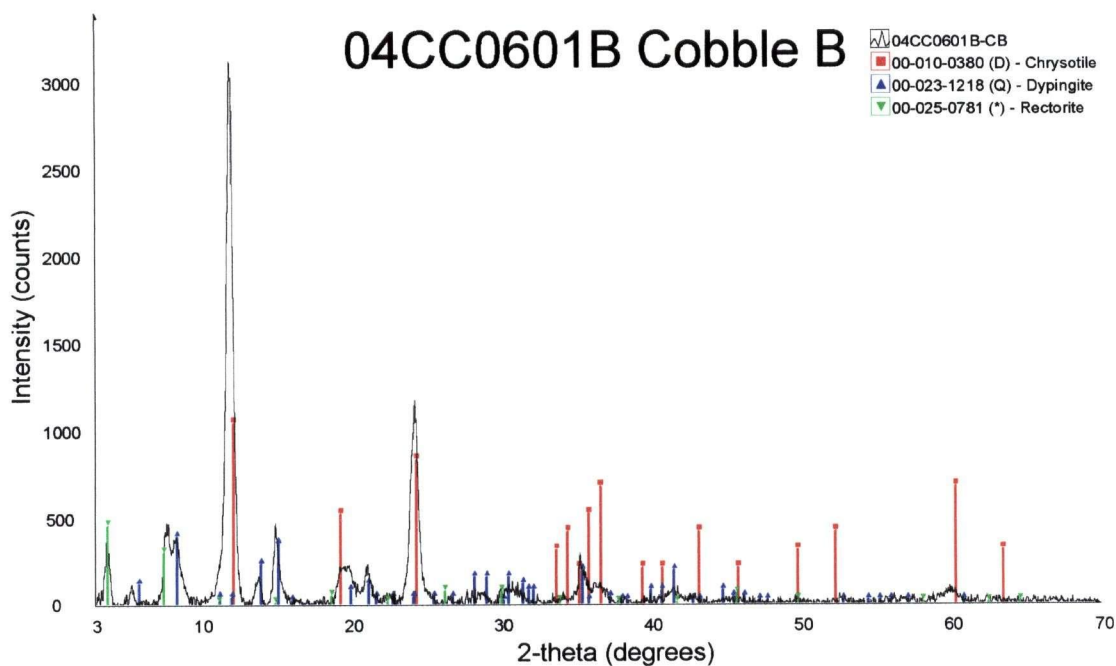


FIGURE B106: X-ray diffractogram for cobble coating from 04CC0601B cobble B.



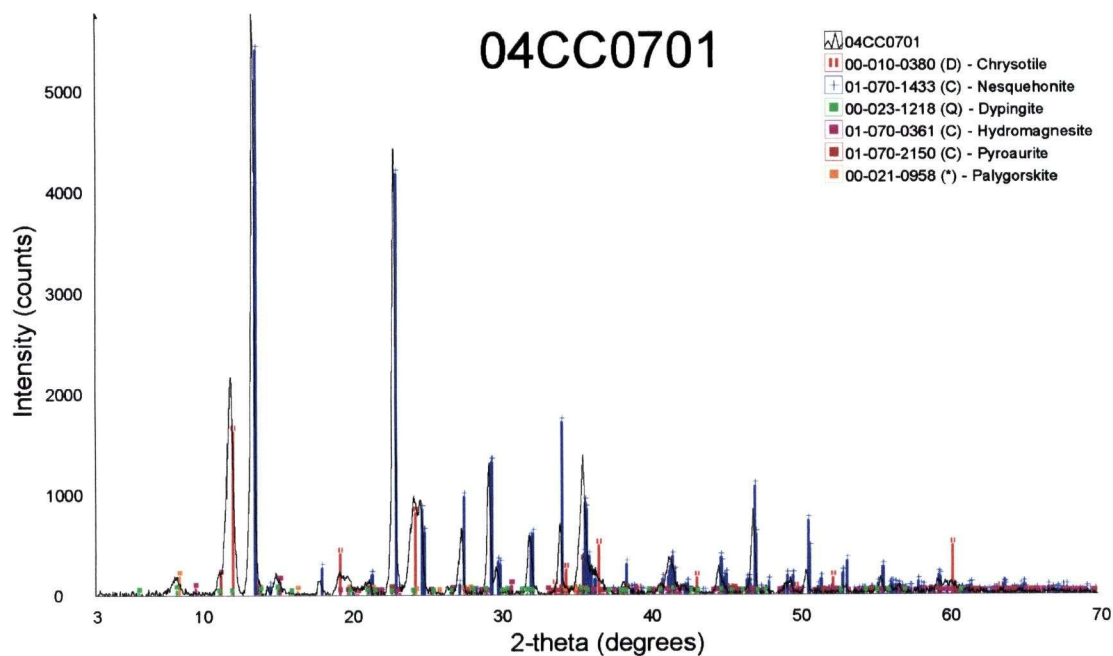


FIGURE B107: X-ray diffractogram for 04CC0701.

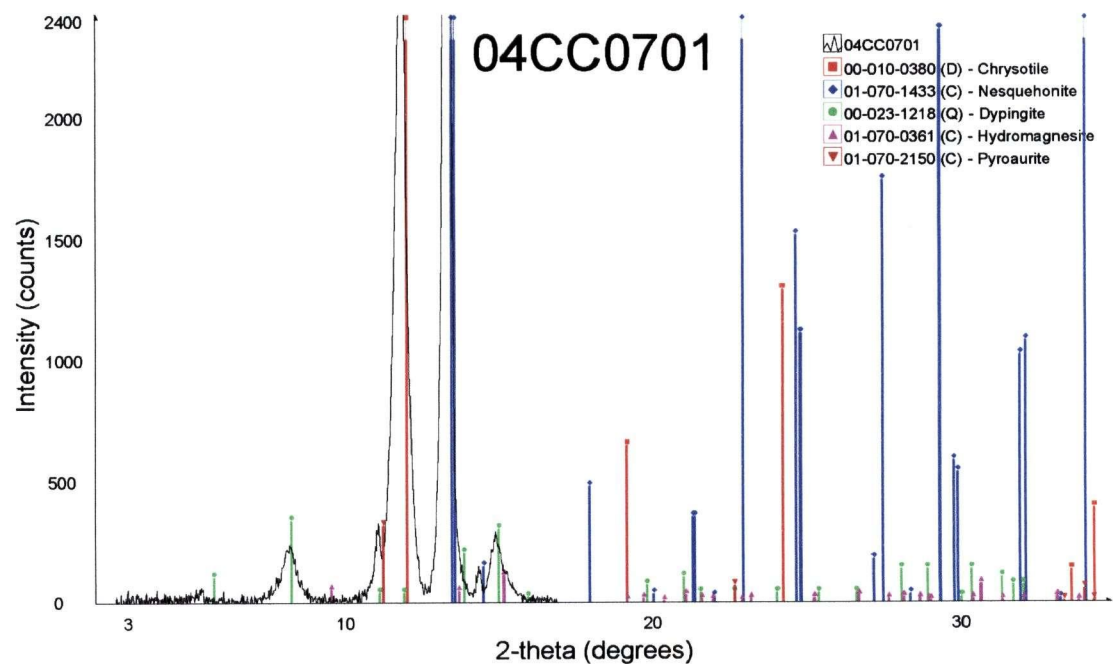


FIGURE B108: Close-up of X-ray diffractogram for 04CC0701.

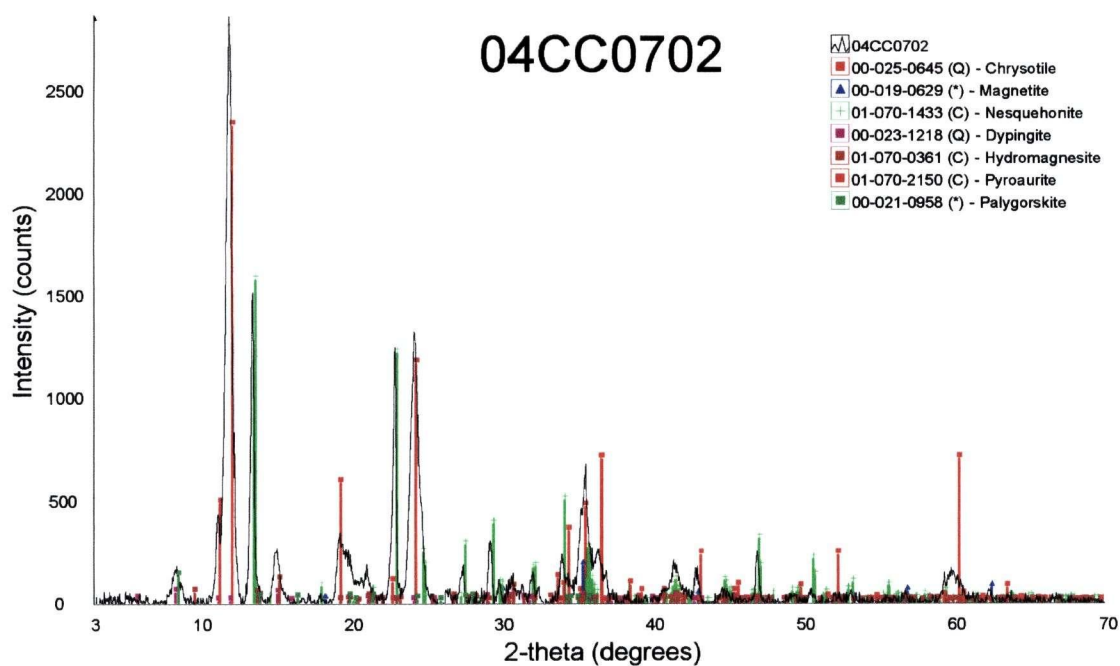


FIGURE B109: X-ray diffractogram for 04CC0702.

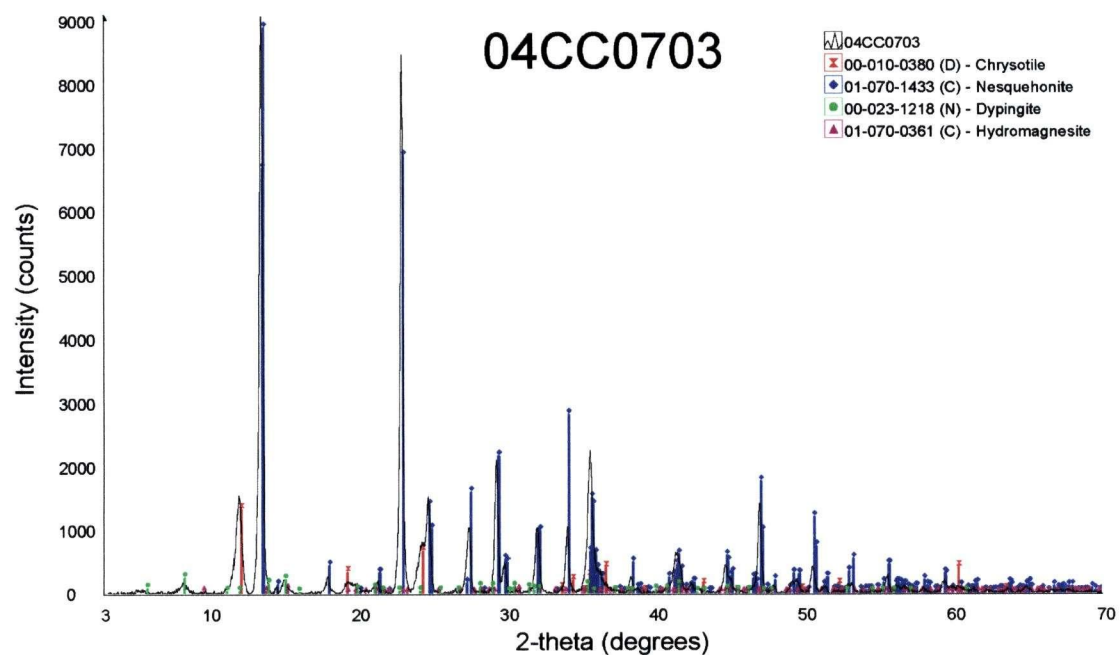


FIGURE B110: X-ray diffractogram for 04CC0703.

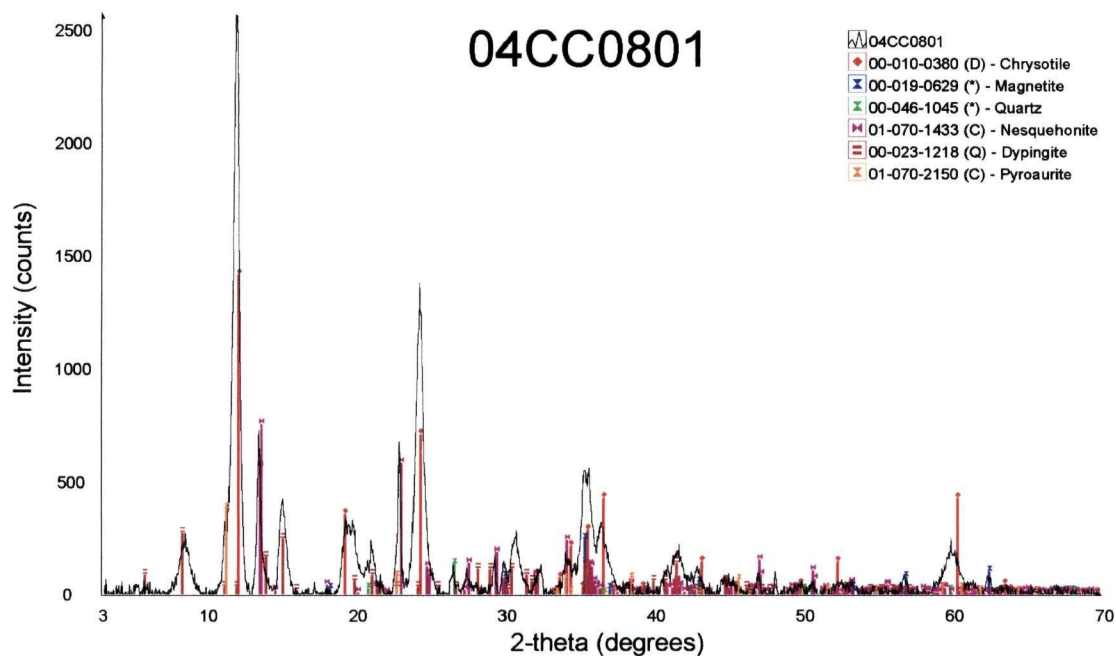


FIGURE B111: X-ray diffractogram for 04CC0801.

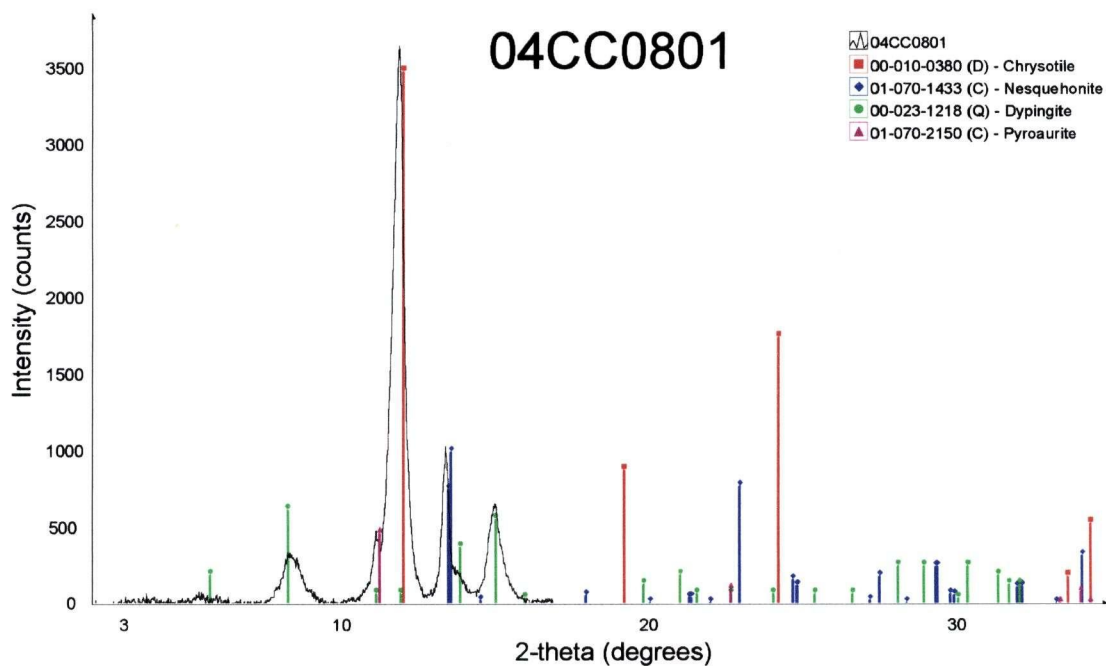


FIGURE B112: X-ray diffractogram for 04CC0801 using higher count rate.

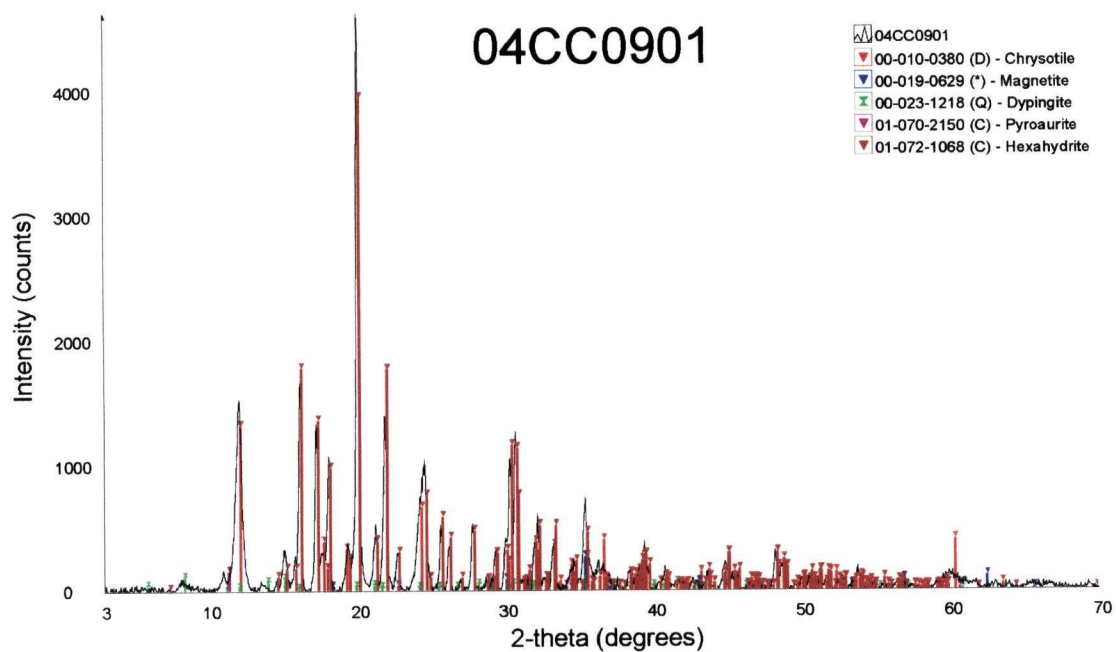


FIGURE B113: X-ray diffractogram for 04CC0901.

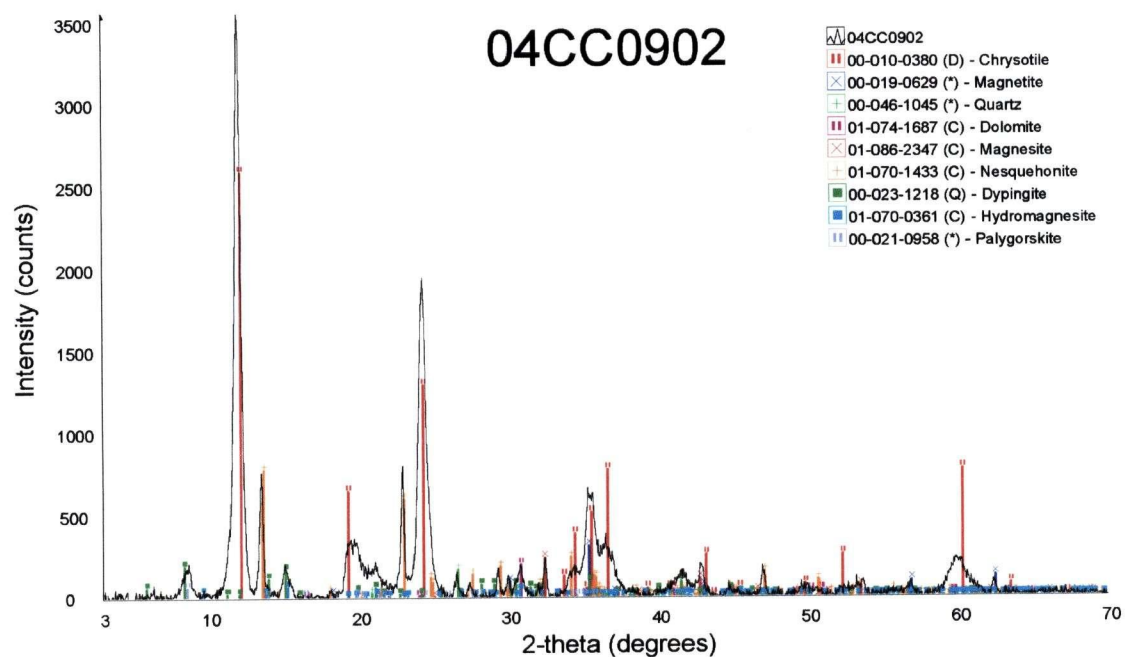


FIGURE B114: X-ray diffractogram for 04CC0902.

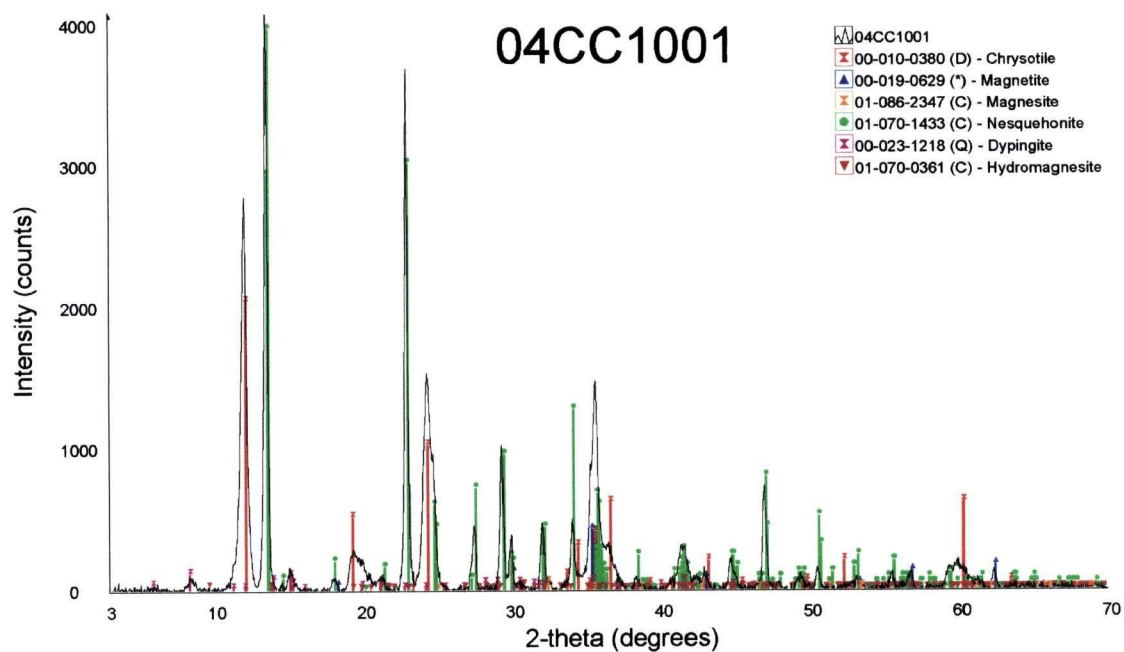


FIGURE B115: X-ray diffractogram for 04CC1001.

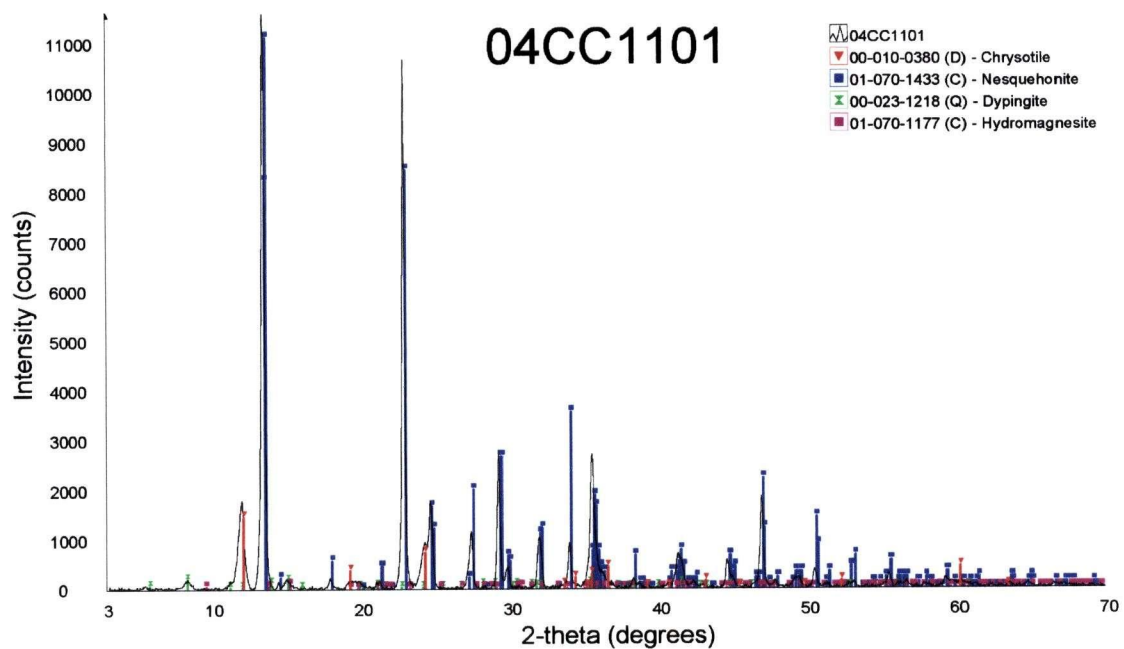


FIGURE B116: X-ray diffractogram for 04CC1101.

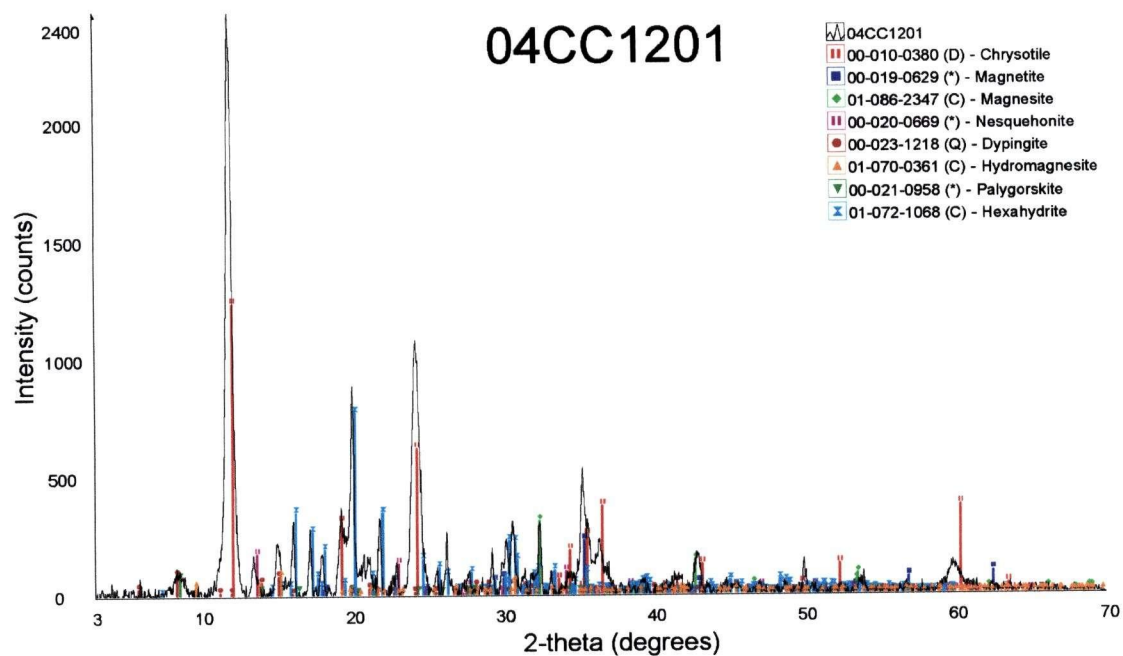


FIGURE B117: X-ray diffractogram for 04CC1201.

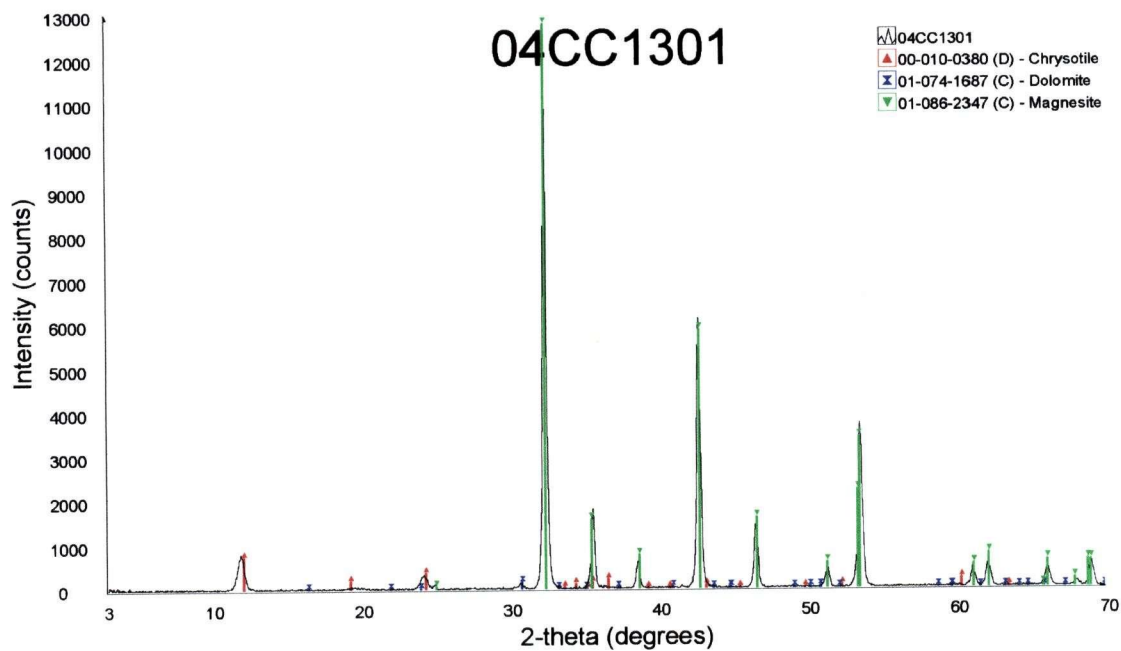


FIGURE B118: X-ray diffractogram for 04CC1301.



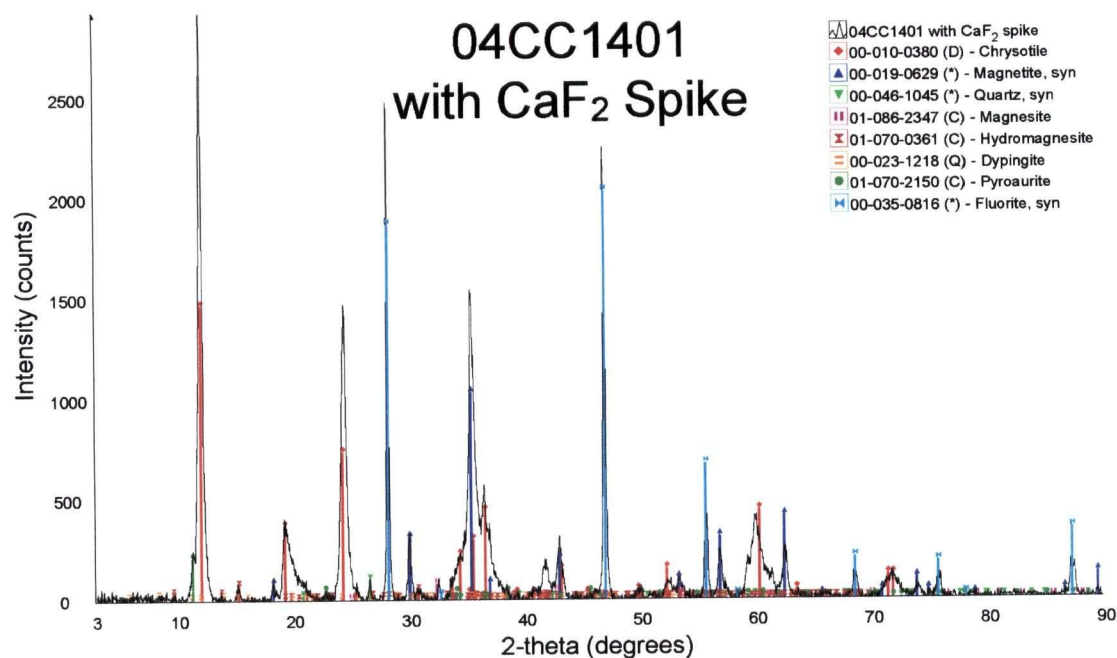


FIGURE B119: X-ray diffractogram for 04CC1401 with 10 wt.% spike for Rietveld refinement.

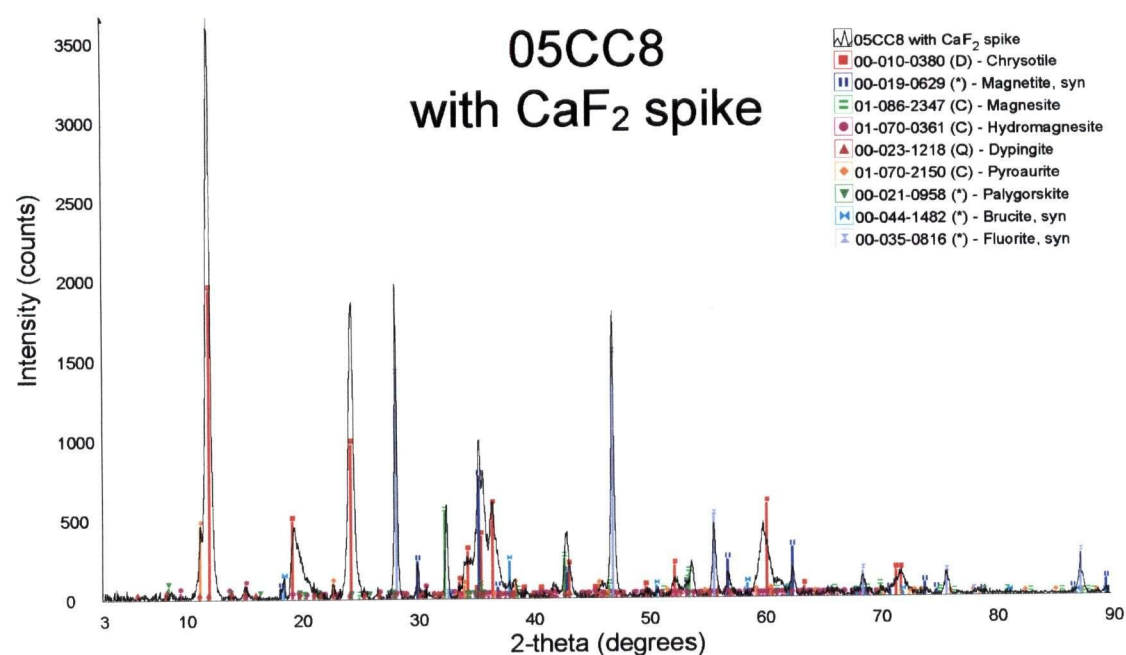


FIGURE B120: X-ray diffractogram for 05CC8 with 10 wt.% spike for Rietveld refinement.

**APPENDIX C:*****Sieving data***

Grain size analysis was performed by dry-sieving 60 bulk tailings samples collected during the 2003 field season (Tables C1, C2, and C3). Standard sieve sizes ranging from 16 mm to 0.053 mm were used. Chrysotile-rich samples do not give particularly accurate grain size data due to the fibrous nature of the mineral. Long fibres do not pass easily through sieves and as such are generally included in larger size fractions which do not reflect the higher surface area associated with fibres.

A separate method of wet sieving, developed by James Thom at the department of Earth and Ocean Sciences at UBC, was used to determine the "fibre fraction" of one bulk sample from each sample locality (Table C4). Accounting for the fibre fraction allows for improved quantification of surface area within chrysotile-rich samples. For each locality, the bulk sample was dry-sieved and bundles of fibres were hand-picked from the larger size fractions. The remaining, predominantly non-fibrous material was washed in deionised water in an ultrasonic bath and mechanically stirred to disaggregate small fibres. The fibre-rich water was decanted from the bath and passed through filter-cloth to collect the fine fibre fraction. Surface-area analysis was done on A65-grade chrysotile from Cassiar with the BET N-gas absorption isotherm technique.

The data presented in Tables C1, C2, and C3 was collected by Elizabeth Castle. Wet-sieving of sample 03CA1601 (Table C4) was done by James Thom. Sample 04CC1601 was wet-sieved by the author with the assistance of Joanne Woodhouse.



TABLE C1: Results of grain size analyses for the 03CC series of samples from Clinton Creek.

Size (mm)	03CC01A		03CC01B		03CC01C		03CC01D	
	wt. %	% passing	wt. %	% passing	wt. %	% passing	wt. %	% passing
>16.0	21.54	78.46	38.64	61.36	25.29	74.71	13.47	86.53
>9.51	13.54	64.92	9.12	52.24	9.30	65.42	9.85	76.68
>4.76	25.87	39.04	18.03	34.21	22.93	42.49	14.14	62.54
>2.00	19.21	19.84	15.28	18.93	17.29	25.19	20.04	42.50
>0.850	8.50	11.34	8.98	9.94	9.03	16.16	19.30	23.20
>0.425	5.64	5.70	5.12	4.83	7.60	8.56	12.99	10.21
>0.212	3.54	2.15	3.06	1.77	5.19	3.37	7.30	2.91
>0.180	0.14	2.01	0.14	1.63	0.61	2.76	0.56	2.34
>0.150	0.51	1.50	0.42	1.20	0.70	2.05	0.57	1.77
>0.106	0.91	0.59	0.85	0.35	1.46	0.60	1.42	0.35
>0.075	0.45	0.14	0.27	0.08	0.49	0.10	0.26	0.09
>0.053	0.08	0.05	0.04	0.03	0.07	0.04	0.07	0.02
<0.053	0.05	0.00	0.03	0.00	0.04	0.00	0.02	0.00
TOTAL	100.00		100.00		100.00		100.00	

Size	03CC0201A		03CC0201B		03CC0301A		03CC0301B	
	wt. %	% passing	wt. %	% passing	wt. %	% passing	wt. %	% passing
>16.0	4.09	95.91	3.14	96.86	0.00	100.00	31.17	68.83
>9.51	4.16	91.75	15.33	81.54	0.00	100.00	20.89	47.94
>4.76	5.04	86.71	12.31	69.23	0.49	99.51	20.23	27.71
>2.00	17.26	69.46	17.88	51.34	2.87	96.64	10.72	16.99
>0.850	24.91	44.55	20.61	30.74	14.77	81.86	5.49	11.51
>0.425	24.02	20.52	15.38	15.36	15.47	66.40	5.10	6.40
>0.212	14.66	5.86	10.15	5.21	16.58	49.82	2.03	4.37
>0.180	1.22	4.64	0.69	4.52	5.40	44.42	0.39	3.98
>0.150	1.50	3.14	1.50	3.03	6.93	37.49	0.66	3.32
>0.106	2.35	0.78	2.26	0.76	12.19	25.30	1.09	2.23
>0.075	0.64	0.15	0.63	0.14	14.08	11.22	1.06	1.18
>0.053	0.12	0.03	0.10	0.03	7.86	3.36	0.73	0.45
<0.053	0.03	0.00	0.03	0.00	3.36	0.00	0.45	0.00
TOTAL	100.00		100.00		100.00		100.00	

Size	03CC0401A		03CC0401B		03CC0601A		03CC0601B	
	wt. %	% passing	wt. %	% passing	wt. %	% passing	wt. %	% passing
>16.0	7.49	92.51	0.00	100.00	4.28	95.72	24.69	75.31
>9.51	0.00	92.51	63.80	36.20	9.34	86.39	14.52	60.79
>4.76	1.82	90.69	12.91	23.29	13.92	72.46	15.59	45.20
>2.00	2.94	87.75	5.51	17.78	8.47	63.99	14.22	30.98
>0.850	20.52	67.24	2.93	14.85	10.28	53.71	10.69	20.29
>0.425	9.06	58.18	2.36	12.49	17.81	35.90	9.09	11.20
>0.212	10.67	47.51	2.55	9.94	8.21	27.69	5.60	5.60
>0.180	2.17	45.34	0.58	9.36	1.41	26.28	0.88	4.72
>0.150	3.30	42.03	0.93	8.43	2.29	23.99	0.96	3.76
>0.106	8.59	33.44	1.98	6.45	5.79	18.20	1.58	2.18
>0.075	15.66	17.77	2.60	3.85	8.69	9.51	1.26	0.92
>0.053	11.26	6.51	2.64	1.21	8.97	0.54	0.66	0.26
<0.053	6.51	0.00	1.21	0.00	0.54	0.00	0.26	0.00
TOTAL	100.00		100.00		100.00		100.00	

TABLE C1 (continued): Results of grain size analyses for the 03CC series of samples from Clinton Creek.

Size	03CC0701A		03CC0701B		03CC0801A		03CC0801B	
	wt. %	% passing	wt. %	% passing	wt. %	% passing	% passing	wt. %
>16.0	25.82	74.18	0.00	100.00	0.00	100.00	9.91	90.09
>9.51	22.42	51.76	5.32	94.68	2.56	97.44	14.69	75.40
>4.76	11.28	40.48	27.46	67.21	6.09	91.35	17.81	57.59
>2.00	10.44	30.04	32.18	35.03	8.94	82.41	18.13	39.46
>0.850	5.41	24.62	12.37	22.66	8.96	73.45	11.20	28.26
>0.425	6.47	18.15	8.22	14.44	17.23	56.21	9.45	18.81
>0.212	4.29	13.86	4.49	9.95	2.90	53.31	7.83	10.98
>0.180	0.47	13.39	0.42	9.52	1.98	51.33	1.40	9.58
>0.150	0.79	12.60	0.89	8.63	10.75	40.59	1.64	7.94
>0.106	2.39	10.20	2.20	6.43	9.73	30.85	2.66	5.29
>0.075	3.37	6.83	2.61	3.82	12.41	18.44	2.63	2.66
>0.053	3.74	3.09	2.79	1.03	12.92	5.52	1.82	0.84
<0.053	3.09	0.00	1.03	0.00	5.52	0.00	0.84	0.00
TOTAL	100.00		100.00		100.00		100.00	

Size	03CC0901A		03CC0901B		03CC1001A		03CC1001B	
	wt. %	% passing	wt. %	% passing	wt. %	% passing	% passing	wt. %
>16.0	1.18	98.82	49.33	50.67	0.00	100.00	2.29	97.71
>9.51	4.55	94.27	4.39	46.28	4.71	95.29	4.65	93.05
>4.76	6.51	87.76	10.50	35.78	13.62	81.67	9.71	83.34
>2.00	6.71	81.04	9.21	26.56	11.23	70.45	16.45	66.89
>0.850	12.62	68.42	6.52	20.04	12.91	57.53	9.43	57.46
>0.425	21.28	47.14	7.26	12.78	18.83	38.70	15.84	41.62
>0.212	10.78	36.36	5.68	7.10	16.45	22.25	14.10	27.53
>0.180	2.44	33.91	0.87	6.22	3.07	19.18	2.82	24.71
>0.150	3.43	30.49	1.01	5.21	3.44	15.75	5.92	18.79
>0.106	8.69	21.79	1.63	3.58	5.84	9.91	5.59	13.20
>0.075	13.06	8.73	1.55	2.03	5.97	3.94	5.92	7.27
>0.053	7.97	0.76	1.15	0.88	3.70	0.24	5.29	1.99
<0.053	0.76	0.00	0.88	0.00	0.24	0.00	1.99	0.00
TOTAL	100.00		100.00		100.00		100.00	

TABLE C2: Results of grain size analyses for the MMI03 series from Cassiar.

Size (mm)	MMI031-1		MMI031-2		MMI031-3		MMI031-4	
	wt. %	% passing	wt. %	% passing	wt. %	% passing	wt. %	% passing
>16.0	0.00	100.00	4.79	95.21	7.71	92.29	7.10	92.90
>9.51	7.56	92.44	5.90	89.31	1.14	91.16	29.43	63.47
>4.76	20.55	71.89	19.35	69.96	12.00	79.16	19.88	43.59
>2.00	19.69	52.20	28.11	41.84	26.06	53.09	13.29	30.31
>0.850	21.41	30.79	17.14	24.70	25.81	27.28	11.40	18.90
>0.425	14.00	16.79	11.83	12.87	18.48	8.80	7.70	11.20
>0.212	9.17	7.62	7.14	5.73	1.89	6.91	5.28	5.92
>0.180	1.02	6.60	0.72	5.00	1.05	5.85	0.77	5.15
>0.150	1.45	5.15	1.21	3.79	1.47	4.38	1.38	3.77
>0.106	2.41	2.74	1.83	1.97	2.23	2.15	1.85	1.92
>0.075	1.34	1.39	1.07	0.90	1.22	0.93	0.98	0.94
>0.053	1.02	0.38	0.52	0.38	0.55	0.38	0.57	0.37
<0.053	0.38	0.00	0.38	0.00	0.38	0.00	0.37	0.00
TOTAL	100.00		100.00		100.00		100.00	

Size	MMI031-5		MMI031-6		MMI031-7		MMI031-8	
	wt. %	% passing	wt. %	% passing	wt. %	% passing	wt. %	% passing
>16.0	10.49	89.51	0.00	100.00	3.51	96.49	7.57	92.43
>9.51	2.14	87.36	16.67	83.33	9.78	86.71	5.66	86.76
>4.76	11.84	75.52	13.73	69.61	15.39	71.32	9.70	77.06
>2.00	17.39	58.13	7.32	62.28	19.08	52.23	22.49	54.57
>0.850	19.17	38.96	17.36	44.93	16.21	36.03	21.26	33.31
>0.425	17.19	21.77	19.78	25.14	14.43	21.59	16.32	16.99
>0.212	11.71	10.06	13.61	11.53	10.82	10.78	9.93	7.07
>0.180	1.48	8.58	1.33	10.21	1.59	9.19	0.84	6.23
>0.150	1.85	6.73	1.90	8.30	2.25	6.94	1.63	4.60
>0.106	2.74	3.99	3.75	4.56	3.06	3.88	2.30	2.30
>0.075	1.62	2.38	1.44	3.11	1.44	2.44	1.18	1.12
>0.053	1.29	1.09	2.83	0.29	1.29	1.14	0.62	0.50
<0.053	1.09	0.00	0.29	0.00	1.14	0.00	0.50	0.00
TOTAL	100.00		100.00		100.00		100.00	

Size	MMI031-9		MMI031-10		MMI031-11		MMI031-12	
	wt. %	% passing	wt. %	% passing	wt. %	% passing	wt. %	% passing
>16.0	0.00	100.00	0.00	100.00	0.00	100.00	0.00	100.00
>9.51	5.80	94.20	0.00	100.00	0.00	100.00	1.32	98.68
>4.76	3.88	90.32	12.45	87.55	17.90	82.10	20.14	78.53
>2.00	15.82	74.50	16.80	70.74	16.45	65.65	26.70	51.83
>0.850	26.09	48.41	11.58	59.16	17.35	48.30	19.89	31.94
>0.425	24.75	23.66	20.94	38.23	26.78	21.52	15.37	16.57
>0.212	13.73	9.93	23.44	14.79	16.18	5.35	9.84	6.73
>0.180	1.63	8.31	3.43	11.36	1.22	4.12	0.98	5.75
>0.150	2.21	6.09	4.30	7.07	1.50	2.63	1.49	4.26
>0.106	3.13	2.96	2.66	4.40	1.68	0.95	2.09	2.17
>0.075	1.38	1.59	1.69	2.72	0.23	0.72	0.89	1.28
>0.053	0.88	0.71	1.58	1.14	0.32	0.41	0.72	0.55
<0.053	0.71	0.00	1.14	0.00	0.41	0.00	0.55	0.00
TOTAL	100.00		100.00		100.00		100.00	

TABLE C3: Results of grain size analyses for the 03CA series of samples from Cassiar.

Size (mm)	03CA0101		03CA0201		03CA0202		03CA0203	
	wt. %	% passing	wt. %	% passing	wt. %	% passing	wt. %	% passing
>16.0	18.92	81.08	49.22	50.78	8.77	91.23	14.92	85.08
>9.51	10.74	70.34	10.12	40.67	12.82	78.41	19.66	65.42
>4.76	16.75	53.58	10.10	30.57	15.44	62.97	15.78	49.64
>2.00	19.07	34.51	10.46	20.10	19.30	43.67	15.11	34.53
>0.850	11.72	22.80	7.36	12.74	17.13	26.54	12.95	21.58
>0.425	9.55	13.24	5.43	7.31	12.25	14.29	9.69	11.89
>0.212	6.59	6.65	3.67	3.64	7.79	6.50	6.81	5.08
>0.180	0.90	5.76	0.54	3.10	1.01	5.48	0.67	4.41
>0.150	1.15	4.61	0.64	2.46	1.22	4.27	1.20	3.21
>0.106	1.63	2.98	0.91	1.55	1.86	2.41	2.11	1.10
>0.075	1.81	1.17	0.88	0.68	1.31	1.10	0.43	0.67
>0.053	0.93	0.24	0.50	0.18	0.63	0.46	0.38	0.29
<0.053	0.24	0.00	0.18	0.00	0.46	0.00	0.29	0.00
TOTAL	100.00		100.00		100.00		100.00	

Size	03CA0301		03CA0302		03CA0303		03CA0304	
	wt. %	% passing	wt. %	% passing	wt. %	% passing	wt. %	% passing
>16.0	9.13	90.87	0.00	100.00	3.29	96.71	5.30	94.70
>9.51	10.20	80.67	12.35	87.65	12.60	84.12	4.94	89.77
>4.76	12.15	68.52	10.72	76.93	10.24	73.87	8.06	81.71
>2.00	16.67	51.86	17.96	58.96	18.49	55.38	16.69	65.02
>0.850	18.33	33.53	18.12	40.84	16.25	39.13	19.14	45.88
>0.425	16.17	17.36	18.05	22.79	17.05	22.08	19.23	26.65
>0.212	9.80	7.56	12.40	10.39	11.39	10.68	13.17	13.48
>0.180	1.28	6.28	1.89	8.49	1.71	8.97	2.00	11.48
>0.150	1.48	4.80	2.00	6.49	2.03	6.94	2.35	9.13
>0.106	1.99	2.81	3.05	3.44	2.82	4.12	3.64	5.49
>0.075	1.43	1.38	2.13	1.30	2.91	1.21	2.45	3.04
>0.053	0.92	0.46	0.92	0.38	0.89	0.32	1.80	1.24
<0.053	0.46	0.00	0.38	0.00	0.32	0.00	1.24	0.00
TOTAL	100.00		100.00		100.00		100.00	

Size	03CA0305		03CA0401		03CA0402		03CA0501	
	wt. %	% passing	wt. %	% passing	wt. %	% passing	wt. %	% passing
>16.0	0.40	99.60	9.28	90.72	1.54	98.46	79.75	20.25
>9.51	0.56	99.05	7.11	83.61	3.12	95.34	0.80	19.45
>4.76	13.48	85.57	16.84	66.77	11.96	83.38	1.92	17.53
>2.00	26.74	58.83	20.00	46.77	18.87	64.51	4.86	12.67
>0.850	24.14	34.68	16.87	29.90	24.68	39.84	3.66	9.01
>0.425	16.27	18.41	12.80	17.11	18.19	21.65	3.60	5.41
>0.212	9.97	8.44	8.84	8.26	11.03	10.61	2.74	2.68
>0.180	1.27	7.17	1.15	7.11	1.32	9.29	0.29	2.39
>0.150	1.55	5.62	1.47	5.65	1.85	7.44	0.51	1.88
>0.106	2.17	3.45	2.22	3.42	2.78	4.66	0.82	1.06
>0.075	1.43	2.02	1.39	2.03	1.71	2.95	0.53	0.53
>0.053	1.07	0.95	1.14	0.89	1.52	1.43	0.35	0.18
<0.053	0.95	0.00	0.89	0.00	1.43	0.00	0.18	0.00
TOTAL	100.00		100.00		100.00		100.00	

TABLE C3 (continued): Results of grain size analyses for the 03CA series of samples from Cassiar.

Size (mm)	03CA0502		03CA0601		03CA0602		03CA0603	
	wt. %	% passing	wt. %	% passing	wt. %	% passing	wt. %	% passing
>16.0	6.96	93.04	0.00	100.00	0.00	100.00	0.00	100.00
>9.51	3.20	89.83	0.00	100.00	0.69	99.31	0.00	100.00
>4.76	11.92	77.91	4.25	95.75	10.62	88.69	21.23	78.77
>2.00	17.73	60.19	15.63	80.12	19.70	69.00	37.05	41.72
>0.850	15.83	44.36	23.35	56.77	32.41	36.58	24.20	17.52
>0.425	15.34	29.01	20.73	36.04	19.46	17.12	9.72	7.80
>0.212	13.15	15.87	17.46	18.57	10.85	6.27	5.00	2.80
>0.180	1.94	13.93	2.42	16.15	1.42	4.85	0.47	2.33
>0.150	2.68	11.25	3.34	12.82	1.39	3.46	0.63	1.70
>0.106	3.80	7.45	6.74	6.08	2.04	1.42	0.92	0.77
>0.075	3.28	4.17	2.55	3.53	0.66	0.76	0.31	0.46
>0.053	2.61	1.56	1.90	1.64	0.45	0.31	0.24	0.22
<0.053	1.56	0.00	1.64	0.00	0.31	0.00	0.22	0.00
TOTAL	100.00		100.00		100.00		100.00	

Size	03CA0701		03CA0702		03CA0801		03CA0802	
	wt. %	% passing	wt. %	% passing	wt. %	% passing	wt. %	% passing
>16.0	1.21	98.79	0.00	100.00	0.00	100.00	6.72	93.28
>9.51	0.87	97.91	3.43	96.57	6.31	93.69	8.64	84.63
>4.76	16.45	81.46	18.82	77.75	10.29	83.40	15.63	69.01
>2.00	20.13	61.33	20.77	56.98	19.21	64.19	22.59	46.41
>0.850	15.09	46.25	14.94	42.04	21.29	42.90	20.23	26.18
>0.425	16.54	29.71	16.36	25.68	18.75	24.16	13.20	12.98
>0.212	15.70	14.01	14.33	11.35	11.72	12.44	7.35	5.63
>0.180	2.78	11.23	2.36	8.99	1.92	10.52	0.73	4.89
>0.150	4.10	7.13	2.07	6.92	1.92	8.60	1.02	3.87
>0.106	2.83	4.30	3.22	3.70	3.54	5.06	1.54	2.33
>0.075	1.62	2.68	1.43	2.27	1.73	3.33	1.03	1.30
>0.053	1.56	1.12	1.24	1.03	1.78	1.55	0.72	0.58
<0.053	1.12	0.00	1.03	0.00	1.55	0.00	0.58	0.00
TOTAL	100.00		100.00		100.00		100.00	

Size	03CA0901		03CA0902		03CA1001		03CA1002	
	wt. %	% passing	wt. %	% passing	wt. %	% passing	wt. %	% passing
>16.0	70.61	29.39	9.26	90.74	0.00	100.00	5.08	94.92
>9.51	3.69	25.70	17.30	73.43	0.53	99.47	11.34	83.58
>4.76	3.99	21.71	20.86	52.57	5.67	93.80	18.65	64.93
>2.00	3.54	18.17	11.27	41.30	11.92	81.87	21.76	43.17
>0.850	3.94	14.23	14.12	27.17	12.64	69.23	18.10	25.08
>0.425	4.54	9.69	12.24	14.94	21.53	47.71	9.99	15.08
>0.212	3.59	6.10	8.09	6.85	22.29	25.41	8.09	6.99
>0.180	0.42	5.68	1.37	5.47	3.55	21.87	1.00	5.99
>0.150	0.67	5.01	1.33	4.15	3.93	17.93	2.04	3.95
>0.106	1.66	3.35	2.15	2.00	6.82	11.11	0.76	3.19
>0.075	0.92	2.43	0.64	1.36	3.51	7.61	0.71	2.48
>0.053	1.16	1.26	0.76	0.60	3.97	3.63	0.42	2.06
<0.053	1.26	0.00	0.60	0.00	3.63	0.00	2.06	0.00
TOTAL	100.00		100.00		100.00		100.00	

TABLE C3 (continued): Results of grain size analyses for the 03CA series of samples from Cassiar.

Size (mm)	03CA1101		03CA1102		03CA1201		03CA1202	
	wt. %	% passing	wt. %	% passing	wt. %	% passing	wt. %	% passing
>16.0	0.00	100.00	9.63	90.37	5.86	94.14	15.46	84.54
>9.51	1.03	98.97	9.86	80.51	5.18	88.96	13.05	71.49
>4.76	7.20	91.76	12.92	67.59	9.58	79.38	23.28	48.21
>2.00	19.70	72.06	21.17	46.42	12.78	66.60	19.39	28.82
>0.850	15.04	57.02	18.57	27.85	11.01	55.59	10.82	18.00
>0.425	17.31	39.71	13.40	14.45	17.82	37.78	7.89	10.11
>0.212	16.86	22.85	8.16	6.28	17.41	20.36	5.31	4.80
>0.180	2.70	20.15	1.12	5.17	2.55	17.82	0.73	4.07
>0.150	2.94	17.21	1.19	3.98	3.17	14.64	0.78	3.29
>0.106	6.15	11.06	1.82	2.16	6.09	8.55	1.52	1.77
>0.075	3.35	7.71	0.96	1.20	2.72	5.83	0.75	1.02
>0.053	3.88	3.84	0.73	0.48	3.00	2.83	0.59	0.43
<0.053	3.84	0.00	0.48	0.00	2.83	0.00	0.43	0.00
TOTAL	100.00		100.00		100.00		100.00	

TABLE C4: Wet-sieving data for bulk samples from Clinton Creek (04CC1401) and Cassiar (03CC1601)

Sieve Size (mm)	04CC1401					
	Sample		Non-fibrous		Fibrous	
	wt. %	%passing	wt. %	%passing	wt. %	%passing
>9.51	13.38	86.62	14.29	85.71	0.18	99.16
>1.68	44.37	42.25	45.09	40.61	2.17	64.75
>1.41	6.02	36.23	6.00	34.62	2.96	58.37
>0.850	11.21	25.02	11.64	22.97	1.30	53.15
>0.595	7.38	17.64	7.38	15.59	2.79	45.78
>0.350	8.61	9.03	8.70	6.89	2.37	38.48
>0.212	4.96	4.07	4.51	2.38	6.27	27.34
>0.180	0.74	3.33	0.59	1.79	10.95	24.42
>0.106	1.93	1.40	1.26	0.53	16.03	13.36
>0.053	1.06	0.34	0.42	0.11	25.84	3.53
<0.053	0.34	0.00	0.11	0.00	29.15	0.00
TOTAL	100.00		100.00		100.00	

Sieve Size (mm)	04CC1601					
	Sample		Non-fibrous		Fibrous	
	wt. %	%passing	wt. %	%passing	wt. %	%passing
> 16.0	4.30	95.70	4.83	95.17	0.00	100.00
> 9.50	8.13	87.56	9.13	86.04	0.00	100.00
> 4.76	18.44	69.13	20.68	65.36	0.17	99.83
>2.00	22.50	46.63	23.07	42.28	17.83	82.00
>0.850	20.60	26.02	18.35	23.93	38.93	43.07
>0.425	10.43	15.59	8.31	15.62	27.73	15.34
>0.212	7.21	8.38	6.21	9.41	15.34	0.00
>0.150	2.10	6.28	2.36	7.06	0.00	0.00
>0.106	2.02	4.26	2.27	4.79	0.00	0.00
>0.075	1.62	2.65	1.82	2.97	0.00	0.00
>0.053	1.16	1.48	1.30	1.67	0.00	0.00
<0.053	1.48		1.67		0.00	
TOTAL	100.00		100.00		100.00	